The Generation of Transverse and Longitudinal Vortices in Low Speed Wind Tunnels

by

C.M. Copland, M.Eng.

Dissertation submitted to the University of Glasgow
for the degree of Doctor of Philosophy
October 1997

The research documented in this dissertation was funded by the British Ministry of Defence through the Defence Evaluation Research Agency (DERA) under extra-mural agreement ASF/2163U.

Acknowledgements

The work described in this dissertation was carried out by the author whilst a full-time student in the Department of Aerospace Engineering at the University of Glasgow during the period October 1994 to October 1997. The dissertation is original in content except where otherwise stated.

The author wishes to express his gratitude for the excellent advice and encouragement given by his supervisors, Dr F.N. Coton and Prof. R.A.McD. Galbraith, during the course of this work.

The help and advice of the following people, at Glasgow University, is also gratefully acknowledged, Mr. R. Gilmour, Mr. T.Smedley, Mr. D. Perrins, Mr. D. Howie, Mr. J. Kitching, Mr A. Masson.

The financial support of the British Ministry of Defence through the Defence Evaluation Research Agency (DERA) is also gratefully acknowledged.

Abstract

The present study documents an experimental and numerical investigation into the feasibility of generating longitudinal and transverse vortices in low speed wind tunnels. The longitudinal vortex system is that of a co-rotating vortex pair which, if substituted for a classical single tip vortex, may produce a beneficial modification to Blade Vortex Interaction. The transverse vortex mimics the tip vortex of a typical helicopter rotor and may be used to assess its effect when interacting with other aerofoils or fuselage components.

Experiments have been conducted to investigate the flow field associated with two co-rotating vortices which represent the idealised vortex system associated with a novel rotor blade tip planform - the Westland Helicopters Vane Tip. These vortices were generated by two rectangular NACA 0015 half wings positioned upstream of the working section of a low speed wind tunnel. Hot-wire measurements were conducted downstream of the generators using x-wire probes to document the strength, position and size of the vortices. A numerical model was utilised to provide an accurate means of determining vortex strength, position and size. Finally, the model was successfully extended to consider the rotation of the vortex system.

The transverse vortex was generated by a rotating blade placed in the contraction of a low speed wind tunnel. A numerical model was utilised in the conceptual design of the experimental facility to model the flow through the settling chamber, contraction, working section and diffuser. This numerical model consisted of a three dimensional source panel method, used to calculate the constrained flow through the low speed tunnel, and a free wake model representing the wake generated by the vortex generator. Convection of the wake was determined by superposition of the undisturbed tunnel velocity and the induced velocity components from the wake itself. Results, obtained via a parametric analysis, illustrate the relationship between the geometry of the wake and basic physical design parameters. On this basis, two possible operational strategies for the upstream rotor are examined with reference to development of the experimental facility. It is concluded that,

while a short duration finite rotor traverse may be the optimum vortex generation strategy, a continuous running rotor is a more cost effective and viable option.

On completion of the numerical study, a new experimental facility for the generation of a transverse vortex, akin to that experienced by a tail rotor during perpendicular Blade vortex interactions, was constructed. The design of the transverse vortex generator is presented together with preliminary results. These results document the success of the facility and clearly show the strong periodic nature of the convecting transverse vortex.

Contents

Chapter 4 - Hot-Wire Anemometry.

Chapter 5 - Twin Vortex Configuration.

Chapter 6 - Transverse Vortex Configuration.

Chapter 7 - Conclusions and Recommendations.

List of Figures

List of Tables

List of Results

Nomenclature

b	.....	Span
c	.....	Chord
C_L, c_l	.....	Lift Coefficient
d	.....	Characteristic Length,
		Diameter of sensor (cylindrical element)
E	.....	Voltage
f	.....	Frequency (Hz) (Rotational)
k, h	.....	Yaw, Pitch Coefficients
k	.....	Thermal conductivity of the fluid
h	.....	Heat-transfer coefficient,
		Separation distance
I	.....	Electrical current in the sensor
L, l	.....	Lift
l	.....	Length (of Vortex Element)
M	.....	Number of acquired points (per revolution)
N	.....	Number of digital time series records (files),
		Number of samples in a time series
Nu	.....	Nusselt number (hd/k)
n	.....	Specific file containing a digital time series record,
		Specific sample in a time series
$\boldsymbol{n}$	.....	Unit Normal Vector
P	.....	Pressure
r	.....	Radial position (co-ordinate)
r_c	.....	Vortex core radius
R	.....	Rotor radius
Re	.....	Reynolds Number
S	.....	Area
t	.....	Time
T_a	.....	Temperature of ambient fluid
T	.....	Period (=1/f),

		Total sampling time (secs)
Tu	.....	Turbulence Intensity
V	.....	Velocity Vector
V_e	.....	Effective Velocity
U,V,W	.....	Velocity components in Cartesian co-ordinates
$\overline{U},\overline{V},\overline{W}$	.....	Mean velocity components in Cartesian co-ordinates
u,v,w	.....	Velocity components in Cartesian Co-ordinates, Fluctuating velocity components
u_θ,u_r,u_z	.....	Velocity components in Cylindrical Co-ordinates
U_N,U_T,U_B	.....	Velocity components in Wire Co-ordinate System
x,y,z or X,Y,Z	.....	Cartesian Co-ordinates

Greek symbols

α	.....	Angle of Incidence, hot-wire sensor inclination
β	.....	Yaw Angle
ϕ	.....	Velocity Potential
γ	.....	Vorticity (shed or trailed in rotor wake)
μ	.....	Constant of Viscosity
ν	.....	Kinematic Viscosity
ν_T	.....	Eddy Viscosity
ρ	.....	Density
σ	.....	Source Strength or Standard Deviation.
ψ	.....	Azimuth Angle
ω	.....	Vorticity, Angular velocity
Γ	.....	Circulation
Ω	.....	Rotational velocity (rads/sec)

Subscripts

b	.....	Blade, Bridge
c	.....	Core

eff	Effective
geom	Geometric
o	Reference Position
1	Reference Position
w	Wing
W	Wire
v	Vortex
N,T,B	Normal, Tangential, Bi-normal Components
θ,r,z	Angular, Radial, Axial Components
∞	Conditions at Infinity (Freestream)
$\perp$	Perpendicular
ind , *i*	Induced
loc	Local
tot	Total
tun	Tunnel
1,2	Sensor identification for x-wire probes

Abbreviations

A/D	Analogue to Digital Converter
ALP1	Azimuthal position 1 corresponding to AOA1
ALP2	Azimuthal position 2 corresponding to AOA2
AOA1	Angle of Attack(Incidence) at ALP1
AOA2	Angle of Attack(Incidence) at ALP2
AZI1	Azimuthal position1 corresponding to TV1
AZI2	Azimuthal position 2 corresponding to TV2
WSVEL	Working Section Velocity
TV1	Tip Velocity Position 1
TV2	Tip Velocity Position 2
RC	Core Radius
SR	Sampling Rate (Hz)

CHAPTER 1

Introduction

1.1 Background

One of the oldest subjects in fluid mechanics concerns the study of flows with concentrated vorticity in free motion. Concentrated vortices, consisting of layers or cores of vorticity, occur in many types of fluid motion ranging from small eddies to large scale atmospheric vortices such as tornadoes and hurricanes. This work will be limited to one particular aerodynamic problem, that of lift generated vortices. A complete survey of the subject of vortex motion and the history is omitted due to the extensive research, in many diverse fields, that comes under the general heading of vortex motion.

It is well known that any finite lifting surface produces a system of vortices as a result of the lift distribution decreasing to zero at the tips. The interaction of such vortices with an object (wing, rotating blades of a helicopter, complete aircraft) is encountered in many areas within the aerodynamic and fluid mechanic fields. These interactions, in the majority of cases, result in some kind of unwanted phenomena. In fixed wing aerodynamics this

can manifest itself as large trailing tip vortices which (during landing) can have a hazardous effect on any subsequent aircraft and disrupt flight operations near an airfield (Bushnell(1992), Beard(1991), Mullins(1996)). In rotorcraft operations, the complex aerodynamic flow field, again, contains strong trailing vortices which convect and interact with other blades, the fuselage and tail rotor. In the case of a trailing vortex interacting with a following rotor blade (commonly termed Blade Vortex Interaction- BVI), high radiated noise levels may result which can also limit flight operations around the airfield (Sheridan & Smith (1979)).

This work addresses the generation of the interacting vortices for, primarily, rotorcraft implementation. It is based (as is all work on vortices) on what is now regarded as one of the most important contributions in fluid mechanics from the 'founders' of what is commonly termed vortex dynamics, H. von Helmholtz and Lord Kelvin (Chapter 2). It will be a fundamental study into the generation of longitudinal and transverse vortices in the working section of wind tunnels. The longitudinal vortex will be that of a vortex pair representing a possible beneficial modification to main rotor Blade Vortex Interaction when compared to the classical single tip vortex. The transverse vortex will be generated by a rotating blade placed in the contraction of a low speed wind tunnel for use in the investigation of tail rotor BVI. To investigate these complex phenomena, a detailed knowledge of the behaviour of the interacting vortex or vortices is required.

1.2 Vortex Flows in Aerodynamics

Of the wide ranging topics available, no single area has attracted more attention than that of the lift generated vortices which are trailed from the tips of aircraft. From the early days of fixed wing flight to the modern helicopters and high performance jets, the dynamics of vortex structures have proved frustrating and perplexing.

The greatest impetus for the study of vortices came from the study of finite wings where the existence of the lift generated vortex had a significant negative effect. Although the presence of the vortices was known (Lanchester (1907)- Fig. 1.1) and much valuable work was carried out up until the 1930's, the problem of trailing vortices ceased to be one of the

leading areas of aerodynamic research. Mass interest in such flows only really started in the late 60's early 70's with the introduction of the Boeing 747 'Jumbo Jet'. This interest stemmed primarily from the possible hazardous effect a large vortex would have on following aircraft when approaching landing.

To date, there are many theoretical, experimental and numerical studies in the literature which are devoted entirely to the understanding of such flows encompassing large aircraft wakes. In spite of this, the present understanding of such flows remains qualitative - in particular at large downstream distances (Crow Instability (1970)). In all these studies, the detailed knowledge of the mechanics of the formation and subsequent roll-up of the tip vortices and their destruction have been precluded. No single work has addressed the complete life of the vortex from formation to destruction and this is unlikely to happen in the near future due to the intractable nature of the flow field.

In addition to the fixed wing aircraft, the operating characteristics of helicopters are strongly influenced by the vortex wakes of the rotating blades. The dominant feature of such wakes is the helical vortices which have their origin at the tips of the rotor blades. The interaction of these blades with the vortex wake changes their aerodynamic loads and thus affects their operating performance, vibration and acoustic characteristics. Although a detailed knowledge of the formation and the initial roll-up of such concentrated vortices is not used for typical wake analyses, such a knowledge is essential to modify the structure of these vortices and, hence, investigate any beneficial effects that may result from any modification. It is important to study, in detail, the flow field in the vicinity of the tip of a finite wing or a helicopter rotor blade to understand the behaviour of the vortex and its subsequent trajectory.

1.2.1 Fixed Wing Aerodynamics

The flow field associated with any fixed wing aircraft is dominated by the two tip vortices generated by the wings (Fig. 1.2). These vortices are trailed from the wing tips and form a counter-rotating pair which convect downward away from the aircraft. Of the extensive literature available, work can generally be split up into that associated with the advent of

the 747 (1970's) and work carried out in the 1990's related to a new generation of large body commercial aircraft. Over the last few years there has been a resurgence of interest in the flow field associated with flapped wings due, primarily, to the hazardous wake which is generated.

The flurry of basic and applied research in the 70's (Olsen et. al.(1970), NASA SP-409 (1975), Donaldson (1975)) produced a better understanding of the far-wake structure and its unwanted persistence. However, little success was achieved in reducing the hazard. The only solution documented was to maintain a suitable large spacing between aircraft during takeoff and landing. This spacing requirement, especially for landings, limits the operational capacity at a growing number of commercial airports around the world due to the continual increase in air traffic.

When an aircraft is in landing configuration, with the flaps deployed, each wing generates not one but two primary vortices: one at the wing tip and one at the outer tip of the flap (Fig. 1.3). The flap vortex is the stronger of the two and the tip vortex rotates around it. Figure 1.4 depicts the vector field associated with this configuration which was detailed by Bruin et al.(1996). These two vortices are of unequal strength and size and after a short period (around three quarters of a revolution) they merge to form a single vortex.

It has been documented by Rossow (1977) that the manner in which the vortices combine determines whether the wake will have its circulation concentrated (with high rotational velocities) or dispersed. The actual mechanism of why the vortices persist for such a long time (which provides a hazard to following aircraft) is not fully understood. Today, wake vortices are at the centre of massive research programmes in Europe and the US. Rossow stated (AGARD CP-584) that there is not, at present, a satisfactory solution for the reduction of the intensity or hazard caused by the wake (vortices) of subsonic transport aircraft.

In fixed wing aerodynamics a distinction must also be drawn between vortex wakes created by flow separation from highly swept wings, such as delta wings, and vortex wakes associated with typical subsonic transport aircraft. An extensive discussion of the

former is provided in AGARD CP-494 ("Vortex Flow Aerodynamics", 1990) but, unfortunately, this symposium did not address the wakes associated with transport aircraft in detail which was the primary impetus for the proceedings. This was addressed in AGARD CP-584 ("The Characterisation and Modification of Wakes from Lifting Vehicles in Fluids", 1996) which documents the latest approach to the vortex wakes associated with the fixed wing aircraft and the relevant regulatory action concerning aircraft spacing. Here, a detailed discussion of the initial wake formation and roll-up to the final instability, decay and breakdown is addressed. However, effective ways of modifying the vortical wake structure of fixed wing aircraft to counteract the hazardous effect were still not achieved.

1.2.2 Helicopter Aerodynamics

Despite early investigations, the development of a practicable helicopter lagged far behind that of fixed wing aircraft. The early stages of helicopter development floundered due to difficulties of stability in forward flight, which were caused by the asymmetric nature of the lift distribution acting on the rotor disk. It was only after the fully articulated rotor hub came into being that helicopter flight really started in earnest. An extensive history of helicopter aviation is provided in the excellent texts by Johnson(1980), Bramwell(1976) and in AGARD R-481 (*Aerodynamics of Rotorcraft*, 1990).

The helicopter industry was initially dominated by the military but, due to the ability of the helicopter to hover and take-off and land in confined areas, it has proven to be of significant value in civil aviation. In fact, it was predicted that the number of civil helicopters in service would overtake the number of military helicopters in use by the mid 80's (Lowson 1980). This increase in civil helicopter traffic resulted in one of the most significant recent events (in relation to helicopter noise) which concerns the regulatory action -rather than any technological breakthrough- implemented by the Civil Aviation Authorities. Up until this time the specification of external noise limits were either made by the individual customer or by the designer and manufacturer. The ongoing imposition of more severe noise limitations means that future helicopters are required to be substantially quieter (Lowson 1992).

With the increasing requirement for the military to avoid detection and for civil helicopters to be more "environmentally friendly", aero-acoustics has become a major field of study (Strenfeld 1979). Extensive discussions are documented in AGARD-CP-552 (*Aerodynamics and Aero-Acoustics of Rotorcraft*,1995) which provides a comprehensive discussion of the field at the present moment. As the acoustic feature is produced by aerodynamic effects at the blade, valuable information on the performance might come from the study of acoustic data as well as the aerodynamic data.

Naturally, the significance of the noise sources will vary from design to design, but for a typical helicopter it has been documented, Lowson (1992), that the order of importance of these sources is:

1. High speed impulsive noise from compressibility effects on advancing side
2. Blade vortex interaction noise during manoeuvre or low speed descent
3. Turbulence induced noise
4. Tail rotor noise
5. Other main rotor discrete frequency noise
6. Other sources such as engine or gearbox

As can be seen from the above the four most important aspects of noise generation on a helicopter are aerodynamic in nature with mechanical noise playing only a minor role.

1.2.2.1 General Flow Field

The aerodynamic environment around a rotorcraft is, in comparison to fixed wing aircraft, extremely complex (Figs. 1.2 & 1.5). The helicopter rotor in forward flight experiences rapid changes in the local effective velocity, ranging from Mach 0.2 on the retreating side to near Mach 1 on the advancing side. On the retreating side the blades pitch up to high incidence which results in dynamic stall. The helicopter operates in conditions of flow separation and in its own wake where the blade tip vortices and wake structure interact with the rotor blades of the main and tail rotors, and the fuselage itself. All these complex issues result in noise, vibration and structural loads which have an adverse effect on helicopter performance. Excellent discussions of the above are provided by Prouty (1985) and AGARD R-481 which also details the complex design issues experienced in rotorcraft

aerodynamics. Future rotorcraft technological developments have also been documented by Tyler and Vincent (1996).

Of considerable importance are the concentrated trailed tip vortices generated by the main rotor which convect. The roll-up of the trailing tip vortex is in principle the same as that of the fixed wing but, in contrast, the developed vortex experiences many strong interactions with fuselage, rotor blades and tail rotor. Sheridan and Smith (1979) provide a good overview of all the "Interactional Aerodynamics" associated with the helicopter.

For the particular case of a single helicopter rotating blade, vortices trail from its root and tip regions, as illustrated in Fig. 1.6. For the rotor blade, however, the bound circulation is not symmetric about the half-span and for typical cases the maximum circulation occurs between 80 to 95 % radius. Thus, although the circulation drops to zero at the tip, the rate of decrease is still very high. This results in strong trailing vorticity at the outer edge of the wake which rapidly (within 60° of rotation - Simons, Pacifico and Jones (1967)) rolls up into a concentrated tip vortex. The strength of such a vortex has been documented to be almost equal to the maximum bound circulation of the blade (Johnson - Helicopter Theory (1980)). On the inboard section of the blade, the bound circulation decreases gradually to zero at the root and is of the opposite sense. The gradient of the circulation in this region is small, resulting in a root vortex which is considerably weaker than that of the tip vortex. Hence, it is the strong concentrated tip vortex which is by far the most dominant feature of a helicopter's rotor wake.

1.2.2.2 Blade Vortex Interaction

Due to the translatory motion during flight, a rotor blade may encounter a tip vortex trailed from either itself or another blade, in both slow and high forward flight conditions. It has been established (Kokkalis (1988), Horner et al.(1991-95)) that when a tip vortex passes close to a blade its effect results primarily from the vertical velocity component induced by the vortex. This produces a time-dependent change in the blade's effective angle of incidence which corresponds to a variation in the blade circulation and hence blade loading (lift). Such vortex induced loads have been identified as being the principle source of rotor and fuselage vibration as well as high radiated noise.

In most flight conditions, the tip vortices trailed by the rotor blades of a helicopter tend to pass under its rotor disc. Under certain flight conditions, however, (e.g. steady descending flight) the resulting inflow tends to force the wake into the rotor disc plane, thus causing strong blade-vortex interactions. There may be up to seven possible areas (Fig. 1.7) where blade-vortex interaction may occur and these are dependent on flight path. Also, depending on the position of the vortex in relation to the rotating blade, the angle at which they meet varies from near parallel through what is commonly termed oblique interactions to near perpendicular (Fig. 1.8). These interactions are all characterised by the interacting vortex lying in a plane parallel to the plane of the blade.

It is well documented, Schmitz and Yu (1983), that the severity of such interactions is governed by:

1. Strength of tip vortex
2. Core size of tip vortex
3. Local interaction angle between the blade and the tip vortex (Fig. 1.8)
4. Vertical Separation between the tip vortex and the blade

A considerable amount of research has been conducted into the phenomenon of BVI over the last 20 years. Excellent reviews on the occurrence of BVI and its aerodynamic effects within the helicopter rotor environment are given by Gessow (1985) and Pillippe et al. (1985) and concepts for the reduction of BVI noise are discussed in Hardlin and Lamkin (1987).

1.2.2.3 Rotor Tip Profile/Vortex System

Rotorcraft have, over the last few years, started to use different planforms to alter the aerodynamic flow in the tip region. Due to the high loads that occur on the tip of the rotating blade during flight it is documented that the rectangular tip profile in unlikely to be the optimum, Seddon (1990). The alteration of the tip geometry is not a new concept and has been employed extensively in the fixed wing environment by the use of winglets to reduce vortex induced drag. Helicopter tips, however, have been designed to different specifications. Instead of trying to limit vortex induced drag, the majority of helicopter

rotor tips have been designed for high speed flow to reduce compressibility effects on the advancing side and (dynamic) stall effects on the retreating side of the rotor disk. They are specifically designed to address point 1 in the list of noise radiation sources.

An extensive discussion of available blade geometries and tip planforms is documented in AGARD R-481. Here we will only discuss four of the more 'exotic' types of tip planform. These are,

1. Vane Tip (Westland Helicopters Ltd.)
2. BERP (Westland Helicopters Ltd.)
3. Free Tip (NASA)
4. Muller Winglet (sometimes referred to as the Aachen Tip)

The Vane Tip (Fig. 1.9) was developed by Westland Helicopters Ltd to specifically address the noise generation originating from a BVI event. Brocklehurst & Pike (1993) documented that, if the strong single tip vortex could be split up into two vortices of equal strength (each half the strength of the original tip vortex) separated by half a chord length or greater, the interaction of this twin vortex system with a rotating blade would result in a weaker BVI encounter and hence reduce noise radiation. Due to the passive nature of such a device, noise reduction of in-service aircraft could easily be accomplished by simply re-blading existing helicopters. Tyler & Vincent (1996) present a general discussion of the Vane Tip in relation to future technological developments. They state that wind tunnel tests have demonstrated a 6 dB reduction in radiated noise.

The use of such a wing tip extension is not new. Tangler (1975,1978) attempted to modify the structure of the tip vortex with the use of a small sub-wing attached to the rotor tip (Fig.1.10). This tip was much smaller than the Vane Tip and it is unlikely that it would be capable of generating two distinct vortices. However, the sub-wing tip would, most likely, severely alter the size of the core (increasing its size) and, thus, reduce the peak velocities. This may have resulted in a beneficial reduction in the radiated noise due to BVI. Hoad (1980) details an experimental investigation to determine the overall character of noise induced by blade vortex interactions as affected by tip configuration (including the sub-wing). Virtually no work was done on the sub wing for about 15 years but, recently, there seems to be a resurgence of interest (primarily due to advances in CFD

and acoustic/aerodynamic measurement techniques). This was discussed by Jenkins (1997) and he stated (during a presentation) that this tip would be implemented on a model helicopter rotor for acoustic testing in the near future (October 1997).

The BERP (British Experimental Rotor Program) Tip is well documented (Seddon (1990), Hansford(1987), Perry(1987)) due to its use in attaining the World Helicopter Speed Record (Hopkins(1986), Wanstall(1986)). Experimental work carried out by Bell Helicopter Inc. (Scott et. al.(1991)) on the BERP showed that at medium to high incidence the tip would generate at pair of unequal counter rotating vortices (Fig. 1.11) . The flow field measurements associated with this are depicted in Fig. 1.12. Lowson (1992) also includes a discussion of the benefits of the BERP tip in high speed (compressible) flow. The combination of sweep and reduced thickness allows the flow field around the tip to remain below Mach 1. Lowson states that this form of tip also reduces the noise in low speed descent (strong BVI flight condition) by up to 5 dB. Unfortunately, there is no discussion of the reasons for this reduction and the results were obtained from in-flight testing. It is possible that the BERP tip may 1) significantly alter the tip vortex structure to provide a beneficial effect in a BVI encounter and/or 2) generate a twin vortex flow field which may have a beneficial effect during BVI.

In the United States during the 80's a considerable amount of effort went into the free-tip concept (Fig. 1.13). The free-tip design incorporated a tip that was free to pitch independently from the rest of the blade. The concept was primarily aimed at reducing oscillatory rotor loads, vibration and hence increase performance. This tip was able to pivot and so could have a different incidence with respect to the rest of the blade. Stroub et al. (1986) document the design of the blade and control system of the rotor blade and the benefits in power reduction. They state that the aerodynamic design of the free-tip was selected primarily to maximise pitch acceleration in response to changing lift and so maintain nearly constant lift around the azimuth. The resulting vortex system was documented by Martin and Fortin (1988) who conducted a numerical analysis of the tip. However, even though the free tip concept was shown to reduce power and oscillatory loads in the control system, there was no discussion of the flow field development or of the effect of these unusual aerodynamics on BVI or noise radiation.

Muller (1990) employed an out of plane winglet (Fig. 1.14) device to try and increase the separation of tip vortex and interacting blade. This increase in separation would reduce the vortex induced loads which act on the blade and so correspondingly reduce the impulsive noise. The winglet was designed to reduce the influence of BVI by increasing the distance between tip vortices and rotor blades at their first encounter. Muller conducted both experimental and numerical studies on the winglet and discussed both the existence of the mid-vortex resulting from a blade vortex interaction (noted also by Horner (1994) - Figs. 1.19 & 1.20) and the double vortex flow field found in the downward pointing winglet configuration. The second vortex, which has the same sense as the tip, is generated from a concentration of the circulation in the region where the winglet starts to bend down. It was also stated that both parts of the double vortex may have the same strength depending on the circulation distribution and the winglet shape. Vortex merging of the two vortex system was also noted, which resulted in a very smooth vortex core with low tangential velocities.

1.2.2.4 Main Rotor Tip Vortex/Tail Rotor Interaction

Despite its extensive use in helicopter designs, the aerodynamics of the tail rotor have been minimally researched when compared to its companion main rotor. As an increase in main rotor efficiency has a greater effect on the overall performance than a comparative tail rotor improvement, resources expended on the main rotor have been easier to justify. There is a universal lack of understanding of the many interactional mechanisms that affect helicopter tail rotor performance. Experimental research has, to date, targeted the problem of interactions on the main rotor blade but there is currently a considerable dearth of information on interactions associated with the tail rotor environment.

The tail rotor has three primary functions: to provide a moment to counteract the main rotor torque reaction on the fuselage; to enable the pilot to select a desired heading whilst in the hover; or to select a desired sideslip angle in flight. The operating regime of the tail rotor is seldom uniform. The flow field around the tail rotor is affected by the main rotor downwash, the influence of the rear fuselage and fin and, under certain flight conditions, the proximity of the ground (Wiesner & Kohler (1974)). The relative proportions of these vary significantly with flight condition. Three critical factors that can contribute to loss of

tail rotor directional control have been identified. These are: tail rotor operating in the vortex ring state (which can result from sideways flight); the influence of the main rotor tip vortices on the flow at the tail rotor; and fuselage weathercock instability in rearward flight. These are all clearly documented in Prouty and by Srinivas et al. (1993).

The effects of the main rotor tip vortex interacting with the tail rotor are considerably less understood than those of main rotor interactions. In Fig. 1.15, a helicopter in level flight forms a pair of large wing tip vortices somewhat akin to those trailed behind a fixed wing aircraft. These vortices are generated from the individual blade tip vortices rolling around each other to form these larger trailed vortices. In forward flight the tail rotor will be in the centre of the main rotor wake and, where they affect the tail rotor, will cut each main rotor blade trailing tip vortex in sequence as they are trailed from the rear of the disc. In quartering flight (Fig.1.16) the tail rotor can become immersed in these large rolled up tip vortices trailed from the edge of the main rotor disc. This flight condition has the most significant effect of tail rotor performance. Depending of the relative rotation of the vortices and tail rotor, the net effect can be a dramatic loss in tail rotor performance.

When compared to the vortex configuration during main rotor BVI (Fig. 1.8), documented in section 1.2.2.2, the interacting vortex lies in a plane perpendicular to that of the blade (Fig.1.17). The convecting main rotor vortex can interact with the tail rotor itself during the roll-up of the trailing tail rotor tip vortex, or with the fully rolled up tip vortex. Unfortunately, there is no apparent work documented on the specific mechanisms that are associated with these particular phenomena and the only discussions have been documented in respect to in-flight tests (Ellin (1993)). These only document the overall effects rather that the interactions themselves.

The direction of the rotor rotation, the type (pusher or puller) and the position relative to the main rotor disk, all have a significant effect on tail rotor performance. It is likely that all these design factors are related to the interaction with the main rotor tip vortices and wake. It is not understood why this is the case. The final tail rotor design is primarily down to trial and error but the general consensus is that top blade forward gives the best tail rotor performance. In many cases it is only when the yaw handling of a helicopter is unsatisfactory that research has been carried out. Although understanding of the tail rotor

has improved over the years, new tail rotor designs are regularly proving to be deficient, necessitating re-working either before or after the aircraft enters service.

1.3 Review of Previous Work

As one can imagine, the scope of work published on vortex flows associated with fixed and rotary winged aircraft is extensive. Here, relevant papers which are of particular importance to Blade Vortex Interaction, the Vane Tip and Tail Rotor Interactions are discussed. The papers which document the experimental work carried out at Glasgow University on Blade Vortex Interaction, work carried at Westland Helicopters on the 'Vane Tip' and work conducted in the investigation of tail rotor interaction are of most importance in the present study. Other papers documented in this section provided additional information on primarily in-flight and computational studies conducted into BVI.

A number of experimental studies have been carried out into the fundamental mechanism for a vortex approaching a rotating blade. In this respect the studies conducted by Surendraiah (1969) and subsequently Padakannaya (1971) using an upstream wing tip to generate a vortex that interacted with a downstream rotor are seminal work. This work enabled the gross features of the blade-vortex interaction to be illustrated. Researchers at NASA Ames (Caradonna et al. (1988)) developed this approach further in the late 80's using a similar facility but with better resolution in the pressure data which allowed a "convective disturbance" in the aerofoil pressure distribution to be identified. Further studies at Glasgow University improved on previous pressure and aerodynamic load measurements but also provided vital flow field information through the use of Particle Image Velocimitry (PIV). The PIV results provided high quality images of the local blade flow field at various stages of the interaction process.

The work conducted by Kokkalis et al. (Fig.1.18) employed a set-up similar to Surendraiah's. In these experiments a vortex generated upstream of the horizontal rotor disk convected towards the rotor hub. However, the method of generating the interaction vortex was different. They utilised a differential incidence of two wings meeting near the

tunnel centre line to generate the interacting vortex. This work initiated the investigation into Blade Vortex Interaction at Glasgow University. The major improvement over the study conducted by Surendraiah was in the spacial resolution achieved in the pressure measurements. Kokkalis was able to suggest that the effects of varying the intersection height were not symmetric above and below the blade. The interactions in which the vortex passed above the blade were stronger than those in which the vortex passed below, particularly during close interactions.

In the study by Kokkalis the interacting vortex was measured using a triple hot wire probe to obtain vortex strength and core size. Horner continued with this research with an improved acquisition system. The work concentrated on oblique BVI and involved the use of Particle Image Velocimitry to investigate the trajectory of the vortex under the influence of the passing blade. Horner was also able to obtain the vortex strength for the interacting vortex but there is a discrepancy between the PIV data and the triple hot wire data. This thesis addresses this discrepancy (Chapter 5) and provides a discussion of the two prior interacting vortex measurement results.

Horner documented the flow field associated with the oblique interaction and noted that, due to the induced velocities acting on the rotor blade, there would be a tip vortex and a 'mid' vortex generated (Fig. 1.19). Muller also commented on the influence of the mid vortex as detailed in section 1.2.2.3 and stated that the mid vortex is weak when compared to the interacting vortex. It was mentioned that the mid vortex has the opposite sign to that of the tip vortex and starts at about 85-90 percent of the rotor radius. Figure 1.20 depicts the different vortex structures which are generated on a zero incidence blade when influenced by an oblique interacting vortex occurring in different quadrants. On the left is a caricature of a second quadrant BVI and on the right a third quadrant oblique BVI event. As can be seen the interactions are very different and result in substantial differences in the evolution of the three-dimensional flow structures which occur during interactions.

Caradonna et al. (1988) also utilised a technique similar to that employed by Surendraiah. They used a two-bladed teetering rotor, again interacting with a vortex generated from an upstream finite wing. This study utilised pressure transducers about the aerofoil at three spanwise locations in order to document the nature of the unsteady pressure distributions

generated when the rotating blade experiences BVI. This study documented the rise and collapse of the leading edge suction peak and allowed the identification of two pressure disturbances, designated the convective and propagative disturbance. The first disturbance was a ripple of lower pressure seen to cross the aerofoil (also seen by Kokkalis). The second disturbance was associated with the high speed environment and it was stated that it could be associated with an acoustic wave originating from the leading edge vortex interaction.

In wind tunnel tests of a model MBB BO-105 rotor, Van der Wall (1993) successfully measured the pressure distribution around one instrumented rotating blade of a complete rotor system to concentrate on BVI locations and noise radiation. Tests were conducted in high and low speed cases representing descent flight conditions with a high noise level. The low speed BVI case was characterised by very strong vortex interactions at the blade tip which cause the extreme noise producing state known as blade slap. This enabled the BVI locations for the complete rotor to be determined and then comparison drawn to the aerodynamic lift and moment distributions. Whilst not concentrating on the fundamental fluid dynamic aspect of BVI, the study identified that, in the full rotor environment, many blade vortex interactions involve pairs of trailed vortices. These pairs of vortices occur on the advancing side of the rotor, rotating in different directions, in the high speed case. There is still a need for continual research into twin vortex interactions as, at present, only the mechanism for the generation has been noted and not the detailed influence on the local blade flow field and noise radiation. The BO-105 model has subsequently been used in extensive laser doppler velocimetry measurements and aeroacoustic testing documented by Splettstoesser et al. (1997) and Schultz et al. (1997).

Other studies have used different experimental set-ups to investigate the fundamental aspects of blade vortex interactions, notably Seath et al. (1987), Booth et al. (1984) and Straus et al. (1988). Booth et al. (1984) utilised an oscillating aerofoil to generate the transverse vortices. However, the wake behind the aerofoil contained pairs of vortices which resembled a Karman vortex street. It was pointed out that there are some inherent limitations in this experimental method. Firstly, the vortex pairs cannot be considered to be exactly equivalent to an isolated tip vortex encountering a rotor blade on a helicopter. Since the vortices occur in pairs, they influence each other. Secondly, in the presence of a

blade, the spacing between the filaments becomes important. As stated, the blade can be said to have an isolated encounter only if the spacing between the vortices is greater than the blade model chord. Such a requirement may conflict with the need for a well defined vortex and consequently the condition for an isolated encounter is not always met.

Straus et al. (1987) utilised a similar facility to Booth but limited the pitching motion to a single ramp up profile rather than a continuously oscillating motion. The aerofoil was rapidly pitched to try and obtain a single two-dimensional shed vortex. However, as stated by Straus, the response time of the pitching system is crucial to produce a single rolled-up shed vortex. The required time of motion of the pitching aerofoil should be less than the time it takes the air to travel one chord length. If the time is too long the shed vorticity will not roll-up into the required vortex. As expected, at low velocities the time to pitch the aerofoil is short - a threshold time of 21ms is quoted at a freestream velocity of 12.2 m/s. However, if the freestream velocity were to be increased, the threshold time to attain a single vortex would decrease and so mechanical actuation problems may arise which could limit the operational range of the generator. Another problem, which may occur, is flow separation from the leading edge resulting in the generation of another vortex of opposite sense to the original shed vortex. Control of the size and strength of the vortex is also difficult with a pitching aerofoil, as you are limited to a finite range of operation.

Of the computational studies conducted into BVI, a distinction between the fluid dynamic approach based on the Navier-Stokes equations, and acoustic approaches based on the Ffowcs-Williams and Hawkings (FWH) equations and the Kirchoff method, can be drawn. These methods are interlinked (the FWH equations is a rearrangement of the N-S equations) and it is necessary to know the blade surface pressure and the flow around the blade before an acoustic analysis can be conducted. It has been argued (Farassat & Brentner (1987)) that the requirement of aerodynamics input data is viewed by some as a weakness of the acoustic analogy. Lyrintzis et al. (1997) provides a good discussion of the two acoustic approaches (in relation to BVI) and stated that the prediction methods require similar computational resources but these requirements are small compared with those of the CFD flow solver (for the Euler equations). There, is at present, considerable attention being paid to the numerical prediction of aeroacoustics primarily due to the advances in CFD.

McCroskey (1988) documented the growing application of computational aerodynamics (CFD) to rotorcraft problems with particular emphasis on the development of new methods. The discussion presented by McCroskey, even though it is dated when consideration is given to recent advances in computational power, does still highlight the primary deficiencies in these methods. Caradonna (1994) also presents a discussion of recent methods for the computational prediction of rotor-wake problems. He states that there is a particular need to investigate (both experimentally and computationally) the generation, convection and interaction of lifting surface wakes. This is a difficult problem for most CFD methods because numerical dissipation is rapid (accumulation of numerical errors). Trying to eliminate these errors by increasing grid sizing in still computationally prohibitive.

Computational studies have also been conducted to try to numerically model the experimental configurations (particularly those of Padakannaya, Caradonna and Kokkalis). The first study, by Padakannaya (1974), detailed the use of a lifting surface method to predict the unsteady aerodynamic forces induced on a model rotor with a vortex lattice method to represent the convecting wake generated by the interacting vortex. A method similar to this was implemented by Coton (1994) and De la Iglesia (1993) (documented in Chapter 3). This method utilised lifting line theory with a two dimensional panel representation to predict the unsteady spanwise loads. A free wake model was also utilised to represent the wake generated under the influence of an interacting vortex from an impulsively started unloaded blade (at zero incidence). Caradonna et al. (1988) provided a comparison of their experimental and computational studies. The numerical model was constructed using a three dimensional full-potential rotor code and, as stated, gave excellent comparisons with the experimental data for a wide range of conditions.

In-flight studies have also been conducted and the most recent of which is documented by Kufeld (1997). This investigation utilised a pressure instrumented rotor on a UH-60A to document the airloads and so provide information for code validation. Kufeld states that the complete program involves comparison of flight test data with both small and full scale wind tunnel tests (similar to tests conducted on the MBB BO-105 rotor).

Unfortunately, there have been few experimental studies conducted on the main rotor vortex/ tail rotor interactions. The most notable investigation was the in-flight study conducted by Ellin (1993) on the DRA Research Lynx with an instrumented tail rotor designed to obtain pressure data. This study noted six distinct regions on the main rotor vortex/ tail rotor interaction, each corresponding to a different mechanism in the low speed envelope. The tests were carried out in hover, forward flight and in quartering flight. Ellin stated that further experimental work was required into blade vortex interaction with the vortex perpendicular to the blade surface to investigate these phenomena.
The Vane Tip (Brocklehurst & Pike (1994)) is a new novel helicopter tip that could be beneficial in the reduction of noise by the generation of two co-rotating vortices. The tip was designed to satisfy several requirements:

1. generate two vortices
2. these vortices spaced half chord apart
3. near equal strength (in 2nd quadrant)
4. pitching moment balance must be maintained
5. sweep desired to minimise compressibility effects
6. reasonably high incidence performance

Initially, lifting line theory was implemented, which showed that the same reduction in bound circulation was required at the blade/vane junction and at the tip of the vane to generate the two vortices. Lifting surface theory was then used to develop the geometry of the final tip with a leading edge extension to increase the area at the junction region and so reduce the local lift which was a result of the induced upwash from the inboard vortex. Twist and sweep were also added to ensure no significant changes would be seen in the pitching moment. Wind tunnel tests were conducted on a fixed wing model of the vane tip to verify the existence of the two vortices and document their persistence downstream. These tests were conducted using flow visualisation techniques and no detailed flow field measurements were documented even though it was stated that measurements were made using a five hole probe to assess the strength and positions of the vortices over a range of sideslip and incidence.

All the experimental, computational and in-flight investigations detailed here provide a small summary of the type of work that has been and is being carried out into the complex field of rotor and helicopter aerodynamics. The experimental investigations range from fundamental studies into single vortex interactions with a single rotating blade, to complex small scale fully articulated rotor systems to detail specific regions of BVI and their acoustic influence.

At Glasgow University there is an investigation, being conducted at present, into the behaviour of a single interacting vortex with a loaded blade. This is based on the previous investigations of both Kokkalis and Horner. Investigations are also scheduled to be conducted utilising the twin vortex system (documented here) on an unloaded blade (Masson (1997), to be published at time of writing). The work presented in Chapter 5 addresses the initial vortex measurement on the single and twin vortex generator implemented on the BVI rig at Glasgow University.

1.4 Scope of Present Study

This study is an investigation into the generation and convection of trailing tip vortices for future studies into vortex interactions. The two main areas of interest are related to helicopter aerodynamics. The first, an investigation into the idealised flow field associated with the Vane Tip and the second, an investigation into the generation of a transverse vortex in a low speed wind tunnel for implementation in an investigation into main rotor tip vortex/ tail rotor interaction. This work tries to address some of the conclusions stated by Ellin with respect to tail rotor interactions and Brocklehurst's discussion of the Vane Tip.

The crucial factor in all experiments to date has been the manner in which the interacting vortices have been generated and their subsequent trajectory through the wind tunnel's working section. These two features are of critical importance in interpreting the resultant data collected and in the application of such interpretations to real aircraft. When data pertaining to blade vortex interactions are acquired from experiments in which the generation of the interacting vortex differs, there are clear differences in the flow

development. How important these differences are is not clear, and it may be that they simply affect the peripheral response and not the fundamental interaction. Nonetheless, whatever system is used, it is essential that the detailed structure of the interacting vortex is known. It is also important to have a good knowledge of the vortex trajectory, stability and tendency to wander from its mean path. This applies irrespective of the method of generation.

One of the interactions concerned with the present study is a vortex orthogonal to the plane of the aerofoil (Fig. 1.21). This interaction models that of a main rotor tip vortex interacting with the tail rotor (Fig. 1.17) and, as such, requires a transverse vortex travelling in a stable fashion through the wind tunnel's working section. The conventional generation method for such a vortex is to place an aerofoil at the entrance of the working section and subject it to a rapid change in incidence (Fig. 1.22). Although this procedure is fraught with difficulty, it does produce a vortex, but one in which the structure (size and strength) may not comprehensively mimic the trailing vortex from the tip of a rotor see page 16). Accordingly, it was proposed to investigate the generation of a tip vortex via a rotor placed in the settling chamber of a wind tunnel (Fig. 1.23) such that the blade tip enters the contraction. Whether or not such a procedure is feasible is an aim of this present study.

The other main task, is an investigation into the generation of unconventional trailing vortex structures which may have beneficial noise reduction characteristics. This vortex structure will be that of a vortex pair wrapping round each other for a range of separation distances (Fig.1.24). The generation of the twin vortices should satisfy criteria 1-3, documented above, for the Vane Tip. The success of this particular study may lead to a detailed appreciation of one aspect of BVI noise reduction by an alteration of the rotor tip vortex structure.

The culmination of this study is the present thesis, which details the development of the two prototype vortex generation systems. These were built and tested in the Department of Aerospace Engineering's 1.15m x 0.8m low speed wind tunnel. Whilst the low Reynolds numbers (approximately $2x10^5$) are lower than those achievable in larger tunnels this was considered less important than the generation and subsequent convection. The

results from this study will be used to assess the worthiness of expenditure to develop facilities in a larger tunnel.

Additional work was also conducted into the implementation of the twin vortex generator in the larger 2.1m x 1.6m Handley Page wind tunnel. This study provided vital information in discussion to a significant discrepancy between the single vortex data acquired Kokkalis and subsequently Horner. This additional work is documented in the present thesis as a prelude to single vortex loaded BVI and twin vortex BVI investigations (Masson (1997)).

This work will document the fundamental study into the generation of transverse and longitudinal vortices in the working section of a wind tunnel. At the outset of the project the proposed work could be split into four main tasks:

1. Numerical modelling of the transverse vortex configuration for design purposes
2. Design of twin/ transverse vortex generators and hot-wire calibration facility
3. Measurement of the vortex structure and convection of the twin vortex and transverse vortex in Glasgow University's 1.15m x 0.8m low speed wind tunnel using hot-wire anemometry
4. Measurement of single and twin vortex generators in the 2.6m x 1.6m Handley Page Wind Tunnel

It should be noted that the object of this feasibility study was to simply validate the techniques adopted and not to necessarily produce the structure of the vortices that will eventually be utilised in a larger wind tunnel.

1.5 Outline of Dissertation

The main body of the dissertation is divided into seven chapters headed by this introduction.

In Chapter 2, a description of the fundamental aspects of vortex dynamics and trailing tip vortices is described. This chapter is included at the start of the main text, rather than as an

Appendix, to provide an introduction to some of the fundamental theory on which this thesis is based.

Chapter 3 documents the numerical model of the transverse vortex generator for design purposes. This chapter details the implementation of a simple panel method code to represent the wind tunnel with a free wake model to represent the trailing tip vortex and wake convecting through the tunnel. The results and discussion are included in this chapter due to the experimental design (documented in Chapter 6) relying completely on these.

In Chapter 4, a discussion of hot-wire anemometry is provided and, more specifically , the use of x-wire probes which are used in the experiments documented in Chapters 5 and 6. The design of a calibration facility and procedure is discussed along with data acquisition and data analysis. A discussion of the traverse is provided as this is also common between the two experiments.

In Chapter 5, a detailed discussion of the design of the Twin Vortex Configuration for both the 1.15m x 0.8m and 2.1m x 1.6m tunnels is provided. Extensive results for the former are provided with subsequent tests in the latter addressing a discrepancy between the triple wire data of Kokkalis and the PIV data of Horner.

In Chapter 6, a detailed discussion of the design of the Transverse Vortex Configuration is given and also the original BVI rig on which it was based. Initial tests document the success of the facility and the feasibility study.

In Chapter 7 the Conclusions of all the work in Chapters 3-6 are provided and recommendations for future work documented.

CHAPTER 2

Fundamental Concepts

2.1 Introduction

When modelling the structure and convection of vortices or conducting experimental measurements, it is important to understand the fundamental equations which determine their behaviour. In this chapter the fundamental aspects of vortex flows are briefly presented. The theory documented here is readily available, and more fully covered, in many excellent texts but is included in this chapter both for completeness and to introduce the reader to some of the theory on which this thesis is based. The numerical models detailed in this thesis (Chapters 3 & 5) rely on these fundamental principles.

Many fluid regions are characterised by regions of concentrated vorticity imbedded in irrotational (potential) fluid. By the theorems of Helmholtz and Kelvin we know that the inviscid motion of the vorticity in these regions is given by the local fluid velocity which in turn is determined from the vorticity field. The required local velocities are determined as the solution to a Poisson equation for the velocity field often in terms of the Biot-Savart

integration. In addition, we know that for a uniform-density (incompressible), inviscid fluid, tubes or elements of vorticity retain their identity and move as material objects. However, the inviscid theory presented here does have some severe limitations. Vortices have a tendency to dissipate with time under the influence of viscosity and their behaviour at large downstream distances long after their generation, is almost impossible to predict or to measure.

The connection between trailing streamwise vortices and the forward motion of an aerofoil was clarified by Lanchaster (1907). He documented that the circulation of the wings bound vortex must equal that of the trailing vortices. Prandtl was the first to provide a practical theory for predicting the aerodynamic properties of a finite wing during the 1st World War (Prandtl's Classical Lifting Line Theory). The amount of available information on the generation, behaviour and breakdown/dissipation of trailing vortices is extensive. More research has (probably) been conducted on this single topic in the aerodynamics field than any other. Here the foundations for the ideal behaviour of vortices are laid down.

2.2 Governing Laws for Vortex Flow

The generation and behaviour of convecting vortices is unfortunately not as straight forward as the ideal theory which tries to represent them. This thesis is concerned completely with the behaviour of vortices in a low speed environment. Hence, the first assumption made is the flow is incompressible. The complete form and derivation of the Navier-Stokes equations is documented in any good fluids text e.g. Kuethe and Chow (1986), Acheson (1990), Anderson (1991). The velocity-pressure description of an incompressible flow of a Newtonian fluid has the following governing equations-

Conservation of Mass $\quad \text{div } \boldsymbol{V} = \nabla.\boldsymbol{V} = 0$

Conservation of Momentum $\quad \dfrac{D\boldsymbol{V}}{Dt} = \dfrac{\partial.\boldsymbol{V}}{\partial.t} + \boldsymbol{V}.\nabla\boldsymbol{V} = -\dfrac{1}{\rho}\nabla p + \nu.\nabla^2\boldsymbol{V}$

Euler's equation can be derived simply from above by assuming the flow is inviscid and neglecting the last term.

Potential flow is yet another simplification (steady, inviscid, incompressible, irrotational Flow) to the full Navier-Stokes equations and every potential flow solution in classical hydro-aerodynamics is an exact solution of the Navier-Stokes equations. If the flow is considered to be incompressible and irrotational($\nabla \times V = 0$) then the continuity equation reduces to,

$$\nabla^2 \phi = 0 \text{ (Laplace's equation)}$$

where the velocity is related to the velocity potential by,

$$V = \nabla \phi$$

Vorticity(ω) is of vital interest in fluid dynamics and is related to velocity by,

$$\omega = \text{curl } V = \nabla \times V$$

and is a measure of rotational effects due to it being equal to twice the local angular velocity of a fluid element. In this thesis (Chapter 5) we will only deal with streamwise vorticity. In an inviscid fluid, vorticity is a kinematic property and like matter it can neither be created or destroyed i.e. Vortex lines are material lines. Thus, they can only undergo convection and deformation. Excellent discussions of the generation of vorticity and vortex motion are given by Moore (1976), Morton (1984) and Sarpkaya (1989).

The governing equation for the motion of vortices in a fluid is derived (by simply taking the curl) from the momentum equation above. The (Helmholtz) vorticity transport equation for an incompressible homogeneous fluid, is therefore,

$$\frac{D\omega}{Dt} = \frac{\partial \omega}{\partial .t} + V.\nabla \omega = \omega.\nabla V + \nu.\nabla^2 \omega$$

where	$V.\nabla \omega$	Rate of change due to convection of the fluid.
	$\omega.\nabla V$	Rate of deformation of the vortex lines (exists only in a three-dimensional flow).
	$\nu.\nabla^2 \omega$	Rate of diffusion of vorticity.

The two terms on the right hand side provide the physical mechanisms by which the vorticity of a fluid particle can change. The inviscid incompressible version of the above is,

$$\frac{D\omega}{Dt} = \frac{\partial\omega}{\partial.t} + V.\nabla\omega = \omega.\nabla V$$

For two dimensional and uni-directional flows the vorticity equation reduces to,

$$\frac{D\omega}{Dt} = \nu.\nabla^2\omega$$

and the vorticity is now perpendicular to the flow direction and is transported with the fluid. For two-dimensional incompressible and inviscid flow the vorticity of a fluid element remains constant with time and is represented by,

$$\frac{D\omega}{Dt} = \frac{\partial\omega}{\partial.t} + V.\nabla\omega = 0$$

where the stream function can be determined from the vorticity by $\omega = -\nabla^2\Psi$ (Poisson's equation). The stream function is also related to the two-dimensional velocity components by $u = \partial\Psi/\partial y$ and $v = -\partial\Psi/\partial x$.

Helmholtz summarised some of the properties of vortices in 1858 with his vortex theorems which follow directly from the inviscid vorticity transport equation. These three theorems govern the behaviour of inviscid three-dimensional vortices:

I. Fluid particles originally free of vorticity remain free of vorticity.
II. Fluid particles on a vortex line at any instant will be on a vortex line at all subsequent times. Alternatively, it can be said that vortex lines and tubes move with the fluid.
III. The strength of a vortex tube does not vary with time during the motion of the fluid.

Of course, in a real viscous fluid, the vorticity is diffused through the action of viscosity. This corresponds to an expansion of the vortex core and a reduction of the induced angular velocity. However the rate of diffusion is, in practice, much faster due to the addition diffusive effect of turbulence in the flow.

The concept of circulation was used independently by Lanchester, Kutta and Joukowski to create a breakthrough in the theory of aerodynamic lift at the turn of the twentieth century. The relationship between circulation and lift is documented here in section 2.5 and the

historical circumstances surrounding this breakthrough are discussed in Anderson (1991). The circulation is defined as, and related to vorticity by,

$$\Gamma = \oint_C \boldsymbol{V}.d\boldsymbol{s} = \iint_S (\boldsymbol{\omega}.\boldsymbol{n})dS$$

Here the integral should be carried out in a counter-clockwise (+ve) sense. Sometimes the above equation is stated with a minus sign. This is simply due to a clockwise direction of integration for the circulation which is convenient in the analysis of aerofoil and wing theory (documented in Kuethe & Chow (1986)).

Kelvin's circulation theorem states that the time rate of change of circulation around a closed curve consisting of the same fluid elements is zero, which mathematically is,

$$\frac{D\Gamma}{Dt} = 0$$

This theorem helps to explain the generation of circulation around an aerofoil. If initially an aerofoil is at rest the velocity is zero and hence the circulation around the aerofoil is zero. When the aerofoil starts to move a circulation is generated around the aerofoil due to the flow leaving the trailing edge smoothly (Kutta Condition); correspondingly circulation must be shed which is opposite and equal to the circulation around the aerofoil (termed the shed vortex). If a closed curve was placed around both aerofoil and shed vortex the total circulation would be zero. A more detailed discussion of the initial formation of the starting vortex from the first instant of motion of an impulsively started blade- where there is an almost potential type of flow around the aerofoil- until it is fully formed and equal in strength to the aerofoil circulation is detailed in Prandtl and Tietjens (this admirably depicts the shed vortex). So in general, if there is a time dependent change in the circulation around the blade, there must correspondingly be a counter vortex shed in the wake equal to the change in circulation. This is the mechanism for the shed vortex used in perpendicular BVI illustrated in Fig. 1.21.

The fundamental relation required for the determination of the induced velocity due to any type of vortex or bounded region of concentrated vorticity is given by the Biot-Savart Law (see Batchelor 1967) which was found experimentally by Biot and Savart in 1820 in

connection with the determination of the magnetic field intensity induced by an element of electric current. A general formulation, with the solution of Poisson's equation, is documented by Katz & Plotkin (1991) and Batchelor (1967) for a general bounded region of vorticity. This general formulation is simplified for the induced velocity of a vortex element, which may be visualised as a thin tube in which all the vorticity is confined (sometimes called the thin filament approximation). The Biot-Savart Law relates the velocity induced by a vortex filament to its strength and orientation. The velocity field induced by an element of a vortex of length dl is expressed by the Biot-Savart Law as,

$$dV = \frac{\Gamma}{4\pi} \cdot \frac{d\boldsymbol{l} \times \boldsymbol{r}}{|\boldsymbol{r}|^3}$$

and for a line vortex of arbitrary length AB the total induced velocity of the entire vortex filament is,

$$V = \int_A^B \frac{\Gamma}{4\pi} \cdot \frac{d\boldsymbol{l} \times \boldsymbol{r}}{|\boldsymbol{r}|^3}$$

The induced velocity is directed normal to the plane formed by the vortex element and the point and the direction is consistent with the sense of the vortex circulation.

The induced velocity due to a vortex element at an arbitrary point P by a straight vortex element of circulation Γ, as depicted in Fig. 2.1, is,

$$V_{ind} = \frac{\Gamma}{4\pi} \int_A^B \frac{\boldsymbol{r}}{d^3} . dl$$

which then reduces to,

$$V_{ind} = \frac{\Gamma}{4\pi r} \left(\cos\alpha + \cos\beta \right)$$

A derivation of the above equation is provided in the text by Stepniewski (1984). Thus, the velocity induced at a point is simply a function of the circulation strength of the element and the relative geometry of the vortex element and point. For a vortex of infinite length (two-dimensional potential vortex) the Biot-Savart law reduces to,

$$u_\theta = \frac{\Gamma}{2\pi r}$$

and for a semi-infinite vortex to,

$$u_\theta = \frac{\Gamma}{4\pi r}$$

These simple derivations are, also, documented in Anderson (1991).

It is easily shown that a vortex flow is a physically possible incompressible flow and that the vortex flow is irrotational at every point except the origin. To avoid the mathematical singularity when a point lies on the vortex *(r=0)* a finite core for the vortex must be introduced. These core models are documented in the next section.

A discussion of these governing laws and their application to the general field of inviscid vortex modelling is given, in more detail, by Sarpkaya(1989), Leonard (1985), Moore (1976), and Widnall (1975).

2.3 Vortex Core Models

In this section different types of vortex model are documented. These range from simple analytical models which are used extensively, to more complex diffusive vortices determined from the solution of the vorticity transport equation. All the models (apart from Burgers model) are two dimensional in nature and all are laminar vortex models as they take no account of the influence of turbulence.

The rule that u_θ is proportional to r^{-1} must break down for small values of r to avoid unphysical singularities on the axis itself. The fluid velocity can never be infinite in the real world and in so far as it reverses direction between two points, which lie close to the axis but on opposite sides, the change cannot be a discontinuous one. Thus every free vortex line must have a core of *some* sort. Figure 2.2, adapted from a figure presented by Bradshaw (1971), illustrates the general distribution of velocity and vorticity associated with a simple line vortex.

The immense complexities associated with concentrated vortices have prevented the derivation of a theoretically rigorous vortex model which describes the phenomenon in every detail. For this reason several empirical formulae for the tangential velocity have

been used by many to study different aspects of concentrated vortices. The best known among these are the Rankine and Lamb-Oseen models. The Rankine vortex rotates as a solid body within its core, $r < r_c$, and is characterised by a potential flow outside, $r > r_c$ (determined by the Biot-Savart Law), i.e. all the vorticity is confined to the core region. The Rankine vortex can be expressed, dimensionally, by

$$u_\theta = \frac{\Gamma}{2\pi}.\frac{1}{r} \qquad (r > r_c)$$

$$u_\theta = \frac{\Gamma}{2\pi}.\frac{r}{r_c^2} \qquad (r < r_c)$$

Vatistas et. al. (1991) proposed an equation which represents a series of general velocity profiles for rectilinear vortices. This core model links Rankine's model and the Scully's model, and Vatistas also presents a comparison with Burgers Model. The tangential velocity in the core can be expressed, non-dimensionally, by

$$\bar{u}_\theta = \frac{\bar{r}}{(1+\bar{r}^{an})^{1/n}}$$

For maximum at

$$\bar{u}_\theta = 2\pi.r_c u_\theta/\Gamma \qquad \bar{r} = r/r_c$$

Scully documented a distinct difference between his Fixed Wing Core Model (FWCM) and Rotary Wing Core Model (RWCM). The FWCM was derived from LDV measurements detailed by Orloff and the RWCM from the experimental results Cook (1972). The FWCM model follows from the Vatistas model with $a = 2$ and $n = 1$ and is usually expressed in dimensional form as,

$$u_\theta = \frac{\Gamma}{2\pi r}.\frac{r^2}{r^2 + r_c^2}$$

Scully stated that, for the rotary wing core model, the magnitude of the measured peak tangentially induced velocity is about the same but the core radius is an order of magnitude smaller when compared to fixed-wing measurements. Scully documented the RWCM curve fit to Cook's data as,

$$u_\theta = 0.4\frac{\Gamma}{2\pi r}\cdot\frac{r^2}{r^2+r_c^2} \qquad \bar{r} \le 1.0$$

$$u_\theta = 0.2\frac{\Gamma}{2\pi r}\left[10-9e^{-0.075\left(\frac{r}{r_c}-1\right)}\right] \qquad \bar{r} \ge 1.0$$

However, other measurements discussed by Scully showed that the tip vortex properties of a model rotor are closer to the fixed wing data than the rotor wing data which was used to gain the above curve fit. Full-scale rotor measurements mentioned by Scully were also closer to the FWCM and so some doubt was placed on the validity of the RWCM.

These equations documented by Scully were presented in a slightly different form, with the number 2 (for infinite line (two-dimensional) vortex) replaced by a 4 (for a vortex element). The standard convention used in the majority of experimental vortex investigations is to curve fit the two-dimensional (infinite) version of the above. All the core models presented here are for a two-dimensional vortex.

Leishman & Bagia have recently utilised a specific form of the Vatistas model in rotor vortex Laser Doppler Velocimetry measurements. This experimental analysis determined the tip vortex profile for a rotating blade could be approximated by,

$$u_\theta = \frac{\Gamma}{2\pi r}\cdot\frac{r^2}{\sqrt{r^4+r_c^4}}$$

Lamb considered the problem of the diffusion of a laminar line vortex with time. The Lamb model involves a Gaussian vorticity distribution and a circumferential velocity given by (Batchelor (1967), Lamb (1932)). The vorticity transport equation reduces to the single equation for vorticity $\omega(r,t)$

$$\frac{\partial\omega}{\partial t} = \nu\nabla^2\omega$$

An exact solution to the above is

$$\omega = \frac{\Gamma_o}{4\pi\nu t}e^{-r^2/4\nu t}$$

$$u_\theta = \frac{\Gamma_o}{2\pi r}\left(1 - e^{-r^2/4\nu t}\right) \qquad t = \frac{z}{w_\infty}$$

where Γ_o represents the initial strength of the trailing vortex and so the circulation in the vortex core Γ at a time t is,

$$\Gamma = \Gamma_o\left(1 - e^{-r^2/4\nu t}\right)$$

This model satisfies the Navier-Stokes equations for the two-dimensional, axisymmetric flow in an incompressible fluid which is represented in terms of vorticity (documented in section 2.2). The Lamb vortex illustrates the time-dependent growth (decay) of a laminar vortex under the influence of (molecular) viscosity. No account is taken for the effect of turbulence on vortex decay. The radius at which the tangential velocity is a maximum is,

$$r_m = 2.24\sqrt{\nu t}$$

For the above it is easily shown that at $t = 0$ the vortex core velocity distribution is equivalent to the result from the Biot-Savart law with a discontinuity at $r = 0$ for an infinite line vortex.

The Burgers vortex (Burgers (1948), documented in the texts by Acheson (1990) Saffman (1995)and Batchelor (1967)), is another exact solution of the vorticity equation. It is a steady, three dimensional axisymmetric vortex represented in a cylindrical co-ordinate system by,

$$u_r = -\frac{\alpha r}{2} \qquad u_z = \alpha z \qquad u_\theta = \frac{\Gamma}{2\pi r}\left(1 - e^{-\alpha r^2/4\nu}\right)$$

Burgers vortex involves the convection , intensification and diffusion of vortex lines which represent the second third and fourth terms in the (Helmholtz) vorticity equation. This representation has the diffusion of vorticity countered by a second term representing a secondary flow which forces the vorticity towards the axis and intensifies it by stretching fluid elements. This results in a steady rather than a decaying vortex. The vorticity is represented by,

$$\omega = \frac{\alpha\Gamma}{4\pi\nu t}e^{-\alpha r^2/4\nu}$$

and is confined to a core which is small for large secondary flows and small values of viscosity. This is, as stated by Acheson, untypical of real vortices in respect to the core radius being dependent on the secondary flow whereas the constants Γ and α are free parameters independent of this secondary flow.

A comparison of the Rankine, Lamb, Vatistas and Scully vortex models are presented in Figs. 2.3-2.5. In Fig. 2.3 the Rankine model is compared with the Biot-Savart Law. All the other Figures use the Rankine model for comparison. In Fig. 2.4, the non-dimensional representation of the previously documented Lamb model is shown which can be expressed (see Newman(1959)), as

$$\bar{u}_\theta = \frac{1}{\bar{r}}\left(1 - e^{-\bar{r}^2}\right)$$

These simple models, and, in particular, the Scully and Vatistas models, are the most widely used in numerical analysis, to remove the singularity which occurs on application of the Biot-Savart law, and for the curve fitting of experimental vortex data.

2.4 Twin Vortex Configurations

Vortices placed close to one another can mutually interact, and generate interesting motions. To examine these interactions, the vortex will be idealised as a concentrated point vortex in two dimensions. A real vortex, with a core within which vorticity is distributed, can be idealised this way with a strength equal to the average vorticity in the core times the core area. Motion outside the core (off the line) is assumed irrotational and inviscid. Irrotational (Potential) flow is governed by the linear Laplace equation and therefore the principle of superposition holds. This means that the flow at any point x,y can be obtained by adding the contribution of all (the two) vortices in the field. To determine the mutual interaction of line vortices, the important principle to keep in mind is the Helmholtz vortex theorem which states that vortex lines move with the flow.

The flow induced by a spinning vortex pair can be assumed as inviscid and incompressible. The two point vortices separated by a distance $2r_o$ with circulation intensity of Γ, as

illustrated in Fig. 2.6, results in co-rotation along a path with radius r_o and

Rotating Speed $\omega = \dfrac{\Gamma}{4\pi r_o^2}$ Period $T = \dfrac{8\pi^2 r_o^2}{\Gamma}$

Rotating Mach Number $M_r = \dfrac{\Gamma}{4\pi r_o a_o}$

In Fig. 2.7, there are two point vortices of unequal strengths Γ_1 and Γ_2. The strengths of the vortices are positive which corresponds to an anticlockwise rotation (vorticity). The distance between these two vortices is $h = h_1 + h_2$. In this 2-dimensional flow field the velocity at point 2 due to vortex 1 is directed upward and equals,

$$V_1 = \frac{\Gamma_1}{2\pi h}$$

where V_1 is the velocity induced by vortex 1 on vortex 2 and can be calculated from the Biot-Savart law provided the distance h is greater than the core size. Similarly, the induced velocity at point 1 due to vortex 2 is downward, and equals

$$V_2 = \frac{\Gamma_2}{2\pi h}$$

The vortex pair therefore rotate anticlockwise around the centre of gravity G which is stationary. This description of the motion of two co-rotating vortices is of utmost importance to Chapter 5.

In Fig. 2.8, the two vortices have the same magnitude of circulation but the opposite sense of rotation. Here, the magnitude of the velocity of each vortex at the location of the other is,

$$V = \frac{\Gamma}{2\pi h}$$

and the velocities are in the same direction. This results in the two counter-rotating vortices translating with the velocity (V) relative to the fluid. If Figure 2.8 were inverted (change the sign of the two point vortices) the flow could represent the idealised flow-field generated by a straight finite wing where the two counter rotating point vortices represent the trailing tip vortices.

2.5 Aerofoils - Generation of Lift

The circulation distribution is obtained by application of the Kutta-Joukowski theorem In 1906 Joukowski published the lift theorem

> "If an irrotational two-dimensional fluid current, having at infinity the velocity V_∞, surrounds any closed contour on which the circulation of velocity is Γ, the force of the aerodynamic pressure acts on this contour in a direction perpendicular to the velocity and has the value
>
> $$l = \rho . V_\infty \Gamma$$
>
> The direction of this force is found by causing to rotate through a right angle the vector around its origin, in an inverse direction to that of the circulation."

The above relationship between lift and circulation can be expressed slightly differently by using the non-dimensional lift coefficient

$$l = \tfrac{1}{2}\rho . V_\infty^2 c . c_l \qquad \text{so that} \qquad \Gamma = \tfrac{1}{2} V_\infty c . c_l$$

Aerodynamic lift depends on the generation of circulation. When an aerofoil generates lift, the average pressure on the upper surface must be less than on its lower. It follows from Bernoulli's theorem that the velocity over the upper surface must be higher than that over the lower and therefore, by the definition of circulation given previously, we should expect that the circulation around a closed curve surrounding the aerofoil to be non-zero. The method of its generation is related to potential flow by the Kutta condition at the sharp trailing edge, as mentioned previously. The circulation around the aerofoil is commonly termed the bound circulation or bound vortex because it is attached to the body (aerofoil) and departs from the characteristics of a free vortex in the external flow because it does not remain attached to the same fluid particles. A bound vortex of the proper strength in a uniform stream is equivalent to a body with circulation in a uniform stream.

At the trailing edge of a two-dimensional aerofoil, subject to a freestream velocity, there will exist the boundary layers from the surfaces on either side. These boundary layers will join up and move downstream in the form of a wake with a reduced velocity distribution.

The velocity profile will change with downstream position under the influence of viscosity. The wake cross section will increase in size as the magnitude of its mean velocity defect decreases. At a sufficient distance downstream, the streamlines will all be parallel and the velocity will be constant and equal to the freestream value.

2.6 Wing/Rotor Trailing Tip Vortices and Wakes

This thesis deals with the feasibility of generating a pair of co-rotating vortices (fixed wing trailing tip vortices) and a transverse vortex (rotary wing trailing tip vortex) and so a clear understanding of the method of generation and fundamental finite wing theory is required.

It is well known that a finite-span wing trails a vortex sheet that rolls up downstream of the wing to form two counter rotating vortices. Near the wing tips the flow tends to curl around the tip due to the pressure equalisation from the lower to the upper (suction) surface. This flow establishes a circulatory motion which trails downstream of the wing and thus satisfies Helmhotz vortex theorem which states that a vortex filament (the bound vortex of the wing) cannot end in a fluid; it must extend to the boundaries (or infinity) or form a closed path (in the form of the rolled-up trailing tip vortex). The spanwise distribution of lift is based on the 2D aerofoil theory with the addition of the non-uniform spanwise downward induced velocity due to the existence of the tip vortex. This downwash combines with the freestream velocity to produce a local relative velocity (often expressed as a change in geometric angle of incidence), which varies along the span. This fundamental wing theory applies to both fixed and rotary (finite) wings. Vorticity and viscous forces are assumed to be confined to the thin boundary layer around the aerofoil, a thin wake emanating from separation at the trailing edge of the wing and the core of the trailing vortex as depicted in Fig. 2.10.

In the fixed wing case, the bound circulation (lift distribution) is symmetric about the mid-span station and can be assumed constant when the freestream velocity and incidence do not change. With a rotating wing there is an additional velocity component from the rotation of the blade. This rotary motion results in higher velocities closer to the tip and hence a higher loading in this region. This produces a loading distribution which is

concentrated in the tip region with a maximum at approximately 80 % span. Due to the time-dependent change in the loading at each azimuthal blade position, vorticity is also shed into the wake (from Kelvins theorem). Excellent discussions of the wake generated by rotorcraft are presented in texts by Bramwell (1976), Johnson(1980), Stepniewiski & Keys (1984), and Prouty (1985). These texts provide extensive coverage of rotary wing aerodynamics and discuss numerical methods for the prediction of blade loading and wake geometry. A discussion of numerical methods, to represent the vortical wake generated by a rotating blade, is presented in the next Chapter.

According to inviscid theory, a vortex sheet emanates from the trailing edge of a lifting wing and rolls up under the action of its self-induced velocity field. The initial strength of the vortex sheet is determined by the shape and incidence of the wing. The steady three-dimensional problem is intractable and it is normal to replace it by a conceptually and numerically simpler unsteady two dimensional problem where the initial strength of the vortex sheet is given, either by lifting surface theory or by the further approximation of lifting-line theory.

The first practical theory for predicting the aerodynamic properties of a finite wing was developed by Prandtl around the time of the 1st World War. Prandtl replaced the finite wing by a bound vortex (situated on the lifting line). The lift on the finite wing was related to the bound vortex strength via the Kutta-Joukowski theorem. Since the bound vortex cannot end in the fluid (satisfying Helmholtz theorem), the vortex continued as two free vortices which trailed downstream from the tips to infinity (commonly called the horseshoe vortex). An extension of this, was to represent the wing as an infinite number of horseshoe vortices and so determine a relationship between the circulation distribution along the wing (lifting line) and the induced angle of attack (which results from the induced effect from the trailing vortices which form the horseshoe vortices). A detailed discussion of Prandtl's lfting line theory is provided in the texts by Kuethe & Chow (1986) and Anderson (1991).

Early theoretical treatment of the rolling up of the trailing vortex sheet are generally based on the papers of Kaden, Betz and Spreiter & Sacks. Betz presented the first calculation method which described quantitatively the velocity and vorticity fields far behind an

elliptically span loaded wing. This method is a two-dimensional, inviscid analysis of the roll-up process. This entailed relating the circulation around a finite wing to the final state of a trailed tip vortex. The vortex sheet trailed from the wing was ultimately shown to roll up into a pair of trailing counter rotating tip vortices. Rossow (1973) extended this method to account for arbitrary load distributions. Brown (1973) discusses the effect of the variation of span loading on the development of fully rolled-up wing trailing vortices (based on the method of Betz). Widnall & Wolf (1980) used this method to estimate the strength of a rolled up helicopter tip vortex when numerically modelling blade vortex interaction. The Betz method was implemented in this case, to calculate the velocity profile in a trailing vortex, which was determined from the spanwise distribution of the (rotating) blade tip loading. This was used to investigate a number of tip loading cases and documented that the BVI acoustic signal was sensitive to changes in tip vortex structure and hence blade tip loading. This is important in the present investigation due to the significant change in blade tip loading with the Vane Tip. Unfortunately, this analysis provides no mechanism for the actual roll-up process and the main inaccuracies are well documented by Williams (1974).

The Spreiter & Sacks (1951) approach consisted of equating the kinetic energy inside and outside of the core to the induced drag of the wing which resulted in an expression relating cores radius to the induced drag. This method was coupled to the Betz model by Staufenbiel (1984), and compared with experimental results analysed using a modified Lamb model. Graham(1996) also discusses a proposed extension to the Betz model and presents an experimental assessment of its validity. He states that the two dimensional inviscid approximation to the wake flow is valid and that the simple Betz model is a good approximation for single vortex roll-up.

Aft of the trailing edge the vortex grows quickly with streamwise distance on the suction side of the tip. Its high rate of rotation produces low pressures in its core that accelerate incoming fluid to produce a large axial velocity surplus. As the core leaves the trailing edge substantial changes occur due to the lack of solid boundaries. The axial velocity surplus (greater than the freestream velocity) usually reverses to become a deficit. The development of the vortex is well documented in velocity measurements by McCormick, Chigier & Corsiglia (1971,1972), Cliffone & Orloff (1974) and others, but these

investigations have documented both increases and deficits in core axial velocity. Saffman (1995), also, provides a mathematical proof which details that the velocity in the core should be higher than the freestream velocity. Modern CFD methods have been applied to investigate the wing tip vortex in the near field. Dacles-Mariani et al. (1995) provide a good discussion of this approach in relation to any inaccuracies which result from grid resolution and turbulence modelling for a finite difference solution.

Current concern with vortex flows stems from increased flight speeds. Higher speeds and the pursuit of efficiency leads to higher wing loading. A higher wing loading means both a higher lift coefficient at the relatively low speeds associated with take-off and landing. Higher lift coefficients in turn require either systems of slats and flaps, involving regions of vortex flow or large angles of incidence on the wings of low aspect ratio involving leading-edge and nose vortices. This also applies for helicopter rotor blades where consistent increases in disk loading results in stronger trailed tip vortices which interact and produce stronger blade vortex interactions.

2.7 Vortex Dissipation and Merging

The previous section primarily deals with the generation of the trailing tip vortex and the roll-up close to the blade. However, at large downstream distances there are highly complex changes in the trailing vortex structures which have not attracted the same amount of attention as the initial formation. This primarily arises from the difficulty in conducting experimental investigations at large downstream distances.

The strictly inviscid theory of Helmholtz and Kelvin is important in the generation of the vortices (see previous discussion). However, in any experimental analysis the viscous nature of the flow must always be appreciated. The roll-up phase of vortex generation can be assumed inviscid , however, at large downstream distances viscous forces cause the dissipation and breakdown of the vortex structure. A general assumption is that there are three main regions of vortex development consisting of the roll-up a period of little change in vortex parameters followed by diffusion/dissipation (and possible instabilities associated with counter rotating vortices and merging with co-rotating vortices). The vortex may

after rolling up immediately start to decay and so these time-dependent regions of vortex development are somewhat uncertain.

In discussion of the persistence of tip vortices at airports, it has been speculated that these vortices are laminar in nature and, thus, provides one explanation of their unusually long existence. Other influences such as the ground, surrounding buildings, prevailing weather conditions etc. all add to the complexity when trying to investigate these phenomena. Turbulence must also be considered, though its precise influence on the dynamics of the vortex structure is unclear.

The growth of a line (trailing) vortex with time under the influence of viscosity is a well known example of viscous flow (Lamb vortex documented above). However, the influence of turbulence on the development of the trailing vortex results is a more rapid change in the vortex structure than predicted. Unfortunately, all these models (apart from the models based on the vorticity transport equation) take no account of the time dependent change in core size or vortex strength. Lamb's model only documents the time dependent change in vortex strength and size under the influence of viscosity. Squire (1954) was the first to attempt to calculate the decay rate of the vortex system as a function of time after generation, by trying to take into account the effect of turbulent mixing, and proposed an adaptation of the laminar (Lamb's) solution using an eddy viscosity (ν_T).

$$\nu_T = a\Gamma_o \qquad\qquad \omega = \frac{\Gamma_o}{4\pi\nu t} e^{-r^2/4\nu t}$$

This work was extended by Owen (1964), and Hall (1966) discusses the effects of turbulence in some detail. Newman (1959), Dosanjh et al. (1962) and Iversen (1976) carried out experimental studies on turbulent line (trailing) vortices to determine the 'eddy viscosity' term.

Another method assumes a profile similar to that applied to turbulent boundary layers and is documented by Corsiglia et al. (1973). There are other investigations based on this analogy with turbulent boundary layers and these are extensively documented by Hoffman & Joubert (1963), Saffman (1973) and in the text edited by Olsen et al.(1971).

Most vortex cores, even in a laboratory, are turbulent. The motion is irregular and the rate of diffusion much greater than if the flow were laminar. In the previous section the vortex models can be described as laminar vortex models. The structure of a turbulent line vortex is a problem of considerable interest, but the status of the present understanding is unclear. There have been a few discussions on the existence of laminar and turbulent vortices with the majority of vortex investigations utilising a 2-D inviscid core model to analyse the data.

The diffusion of the vortex can also be accompanied by instabilities at very large downstream distances in the case of two counter rotating vortices. This instability was initially detailed by Crow (1970). The latest work on the Crow instability is discussed in AGARD CP-584. These discussions state that if just vortex diffusion, caused by viscosity, were present, the trailing (counter rotating) vortices would exist for a very long time. Very often the trailing vortices undergo a symmetric instability in the early stages of growth before they decay by "simple" vortex diffusion. A detailed discussion of aircraft trailing tip vortices in relation to their formation, structure(laminar/turbulent), decay, motion and stability is provided by Widnall (1975).

There is very little documented work of the flow field associated with two co-rotating vortices and all the work is related to fixed wing aircraft. The documented work only concentrates on the two dimensional numerical modelling of twin and multiple vortex systems. The most relevant twin vortex study was conducted by Rossow (1977,1987) when investigating the merging of twin, fixed wing, co-rotating vortices (as illustrated in Fig. 2.9). This study was based on the previous work of Christiansen & Zabusky (1973), Chrstiansen (1973) and Roberts & Christiansen (1972). Rossow documented that simple flow visualisation techniques had been applied to investigate this type of flow field structure but there is no apparent experimental flow field measurements into the idealised vortex system associated with two co-rotating vortices.

There is more interest, at present, due to the landing configuration of large commercial aircraft like the Airbus A3XX where the predicted tip vortices will be 15-20% stronger than those associated with the Boeing 747. At present, the experimental work seems to be concentrating on scale model aircraft with multiple wing and juncture vortices, where complex vortex motions and merging occur. There is still a need to investigate,

experimentally, the fundamental process of vortex merging which occurs with co-rotating vortices. There is no documented experimental investigations into the fundamental merging process of two vortices and, as stated, the only documented twin vortex investigations are numerical in nature. With the advent of the Vane Tip more experimental work is required on both fixed wing and rotary wing twin and multiple vortex systems to ascertain where and how these vortices merge.

CHAPTER 3

Numerical Model of Transverse Vortex Configuration

3.1 Introduction

One of the main aims of this thesis is to examine the feasibility of the generation of a transverse vortex. To aid in the experimental design, development and verification of this experimental facility, it was initially decided to model the convecting vortex numerically. This model was then used to determine design parameters for the subsequent manufacture of the test facility. The design of the experimental facility is documented in Chapter 6 and relies completely on the numerical model for operating and design parameters.

The transverse vortex was to be produced by a rotating blade placed in the contraction of the 1.15m x 0.8m low speed wind tunnel (Fig. 3.1) at Glasgow University. This configuration, illustrated in (Fig. 3.2), posed a number of complex problems which could only be overcome with the aid of the numerical model. The first, and most significant problem, was the accelerating flowfield associated with the contraction of the tunnel. This

had to be modelled to determine the effect of the velocity gradient on the convecting tip vortex and wake. Secondly, the motion of the rotating blade had to be determined, for a specified wind tunnel velocity, to attain the desired transverse vortex.

Of particular interest in this study were the relevant geometrical parameters of the blade, and the operating conditions of the blade and wind tunnel, to attain a good representation of a transverse vortex. The developed code, therefore, had to be adaptable to enable a comprehensive analysis of the fundamental input parameters such as position, size and motion of the blade, and working section velocity. Results had to illustrate the three dimensional development of the wake (and related tip vortex) through the wind tunnel with enough clarity to isolate the specific effects of a particular design parameter.

The features of the experimental facility that had to be modelled were the vortical wake structure generated from the rotating blade and the main flow through the wind tunnel. The rotor wake was represented by a free wake model consisting of a lattice of shed and trailed vortex elements which were generated using classical lifting line theory. This vortex system was then convected through the contraction and working section of the wind tunnel with the superposition of the local velocity, calculated via a three dimensional source panel method, and the induced velocity components from the vortex elements. Due to the inviscid nature of this model, no account was taken for vortex dissipation or the change in vortex strength due to deformation of the vortex element, and so the strength of each vortex element was invariant with time. This chapter details the derivation and operation of the numerical model.

3.2 Numerical Model of the Wind Tunnel

A source panel method was used to calculate the incompressible, inviscid, potential flow through the 1.15m x 0.8m low speed wind tunnel at the Dept. of Aerospace Engineering, University of Glasgow. This method was based on the work of Hess and Smith (1967). The method was chosen for its relative simplicity and adaptability to internal flows. A considerable amount of theory is available on the topic of panel methods and the choice of which type of formulation to implement is primarily determined by the case in question,

geometric limitations and experience. Due to the simple geometry of the modelled portion of the wind tunnel and the non-lifting nature of the body, a plane quadrilateral element with constant source distribution was deemed sufficient for this case.

3.2.1 Introduction - Panel Methods

Integral-equation methods for solving potential flow problems became feasible with the advent of digital computers. Their initial effectiveness was proven by consideration of two-dimensional and axi-symmetric problems in the late 1950's. However, three dimensional methods have been of principle concern for the past 30 years with the pioneering work of Hess and Smith (1967). A panel method is a numerical method for predicting the flow around an arbitrary body in inviscid, irrotational, incompressible (potential) flow and the theory behind them has been well documented by Katz & Plotkin (1991), Hoeijmakers(1992) and Rom (1992). The theory behind the formulation of three-dimensional panel methods is not presented in this dissertation due to the excellent coverage by the previous authors and general introductory discussions on panel methods by Hess (1990) and Bristow (1980). Here, a brief introduction to panel methods is provided and the method of solution for the present application.

In a panel method, the geometry of a three dimensional body is represented (approximated) by a series of panels. These panels are usually quadrilaterals, although more complex geometries can be implemented. The corners of each panel are referred to as the vertices. In most panel methods the vertices form flat plates but some higher order panel methods use parabolic curvature to increase the accuracy of the approximation.

The flow over the body is then simulated by placing singularities, of some strength, at the centre of each panel to represent the flow field around the body. This point is usually called the centroid or collocation point. The flow singularity may be sources, doublets (made up of a source and sink), vortices or any combination of these. The singularity can be distributed with constant strength across a panel (a low-order panel method) or have some linear or quadratically varying strength across the panel (high-order panel method). Typically, high order panel methods require significantly longer computational times and,

care must be taken to ensure that all the panels match up exactly due to the requirement that the singularity strength be continuous across panels.

There are extensive reviews about the relative advantages/disadvantages of low and high order methods relating to the required computational time and accuracy (Maskew 1981/2). Comparisons of the most commonly utilised codes are given by Youngren et al. (1983), Margason et al. (1985), and in Katz & Plotkin (1991, Section 12.4). In recent years, there has been a tendency towards low order methods with simpler geometric specifications (quadrilateral elements) purely due to an increase in computational efficiency with faster computers handling an ever larger numbers of panels.

The velocity at the collocation point of each panel may be calculated from the strength of the singularity situated on that panel and the influence of all the other panel singularities in the numerical model at that collocation point. The effect of one panel on all the others is determined mathematically (see Katz & Plotkin (1991)) and is referred to as the influence coefficient. The unique matrix of influence coefficients (for all the panels) is dependent on the singularity type used, its distribution and the specified panel geometry. To solve this matrix, boundary conditions (Neumann or Dirichlet) must be specified which result in zero normal velocity on each panel.

Due to their very nature, the implementation of panel methods have some obvious limitations. With potential flow (panel method) calculations, viscosity is not, directly, taken into account. However, these calculations can be adapted, by a coupling of panel methods and boundary layer solvers (discussed by Katz & Plotkin),to account for viscosity. The inability to model compressibility also limits their use, being unsuitable as a design tool for transonic flows. However, a derivation of the subsonic PAN AIR code called TRAN AIR (Erickson et al. 1987), which utilises surface panels and a flow field grid (CFD), can account for these compressibility effects.

Other numerical methods, based on the Navier-Stokes equations (CFD), can resolve these problems, however, there are also limitations here. For a panel method, only the surface of the body needs to be geometrically represented and the required input geometry is easier and quicker to formulate than a CFD solver (where the entire flow field must be

discretised). Panel codes also offer the designer the ability to model the complete aircraft (Tinoco et al. 1987) which, for CFD, is still in its infancy. Roggero & Larguier (1993) illustrate what is possible with three dimensional complex aerodynamic calculations around a complete aircraft in take-off configuration. Katz & Maskew (1988)also detail a complete aircraft model and present an application of a vortex wake model to represent the wake from a hovering helicopter rotor.

The typical methodology for any panel method is depicted in the diagram below. Each of the steps required for a panel method solution are discussed, for the present application, in the following sections. The method of Hess & Smith, which was applied here, allows the reversal of the normal to the panel to solve for an internal flow.

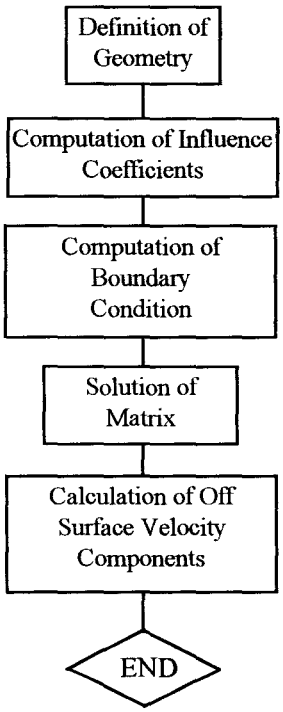

Diagram - Typical flow chart for the numerical solution of the surface singularity distribution problem (Katz & Plotkin (1991)).

With respect to other investigations into internal flows, Ashby & Sadlin (1985) present an analysis of the ability of a low order panel method to predict complex three-dimensional internal flow fields. Browne & Ashby (1989) continue the work and present a detailed discussion of the integration of wind tunnel and computational methods for aerodynamic configurations. Their study documents the effectiveness of using a low-order panel code

to estimate the wind tunnel wall corrections needed on test models. Application of this method is detailed by Browne & Katz (1990) with the method applied to a two element, two-dimensional high lift wing section, and a complete fighter aeroplane model up to high angles of attack. Nathman & Frank (1987) also document the application of VSAERO, (VSAERO documented by Maskew (1982,1987)) to internal flows with discussion of specific applications (wind tunnel probe, wind tunnel vane set and turbofan bypass duct). In addition, Mokry et al. (1987) discuss the application of a doublet panel method for the determination of wall corrections on a wind tunnel half model transport aircraft.

3.2.2 Discretisation of Tunnel Geometry

The wind tunnel, depicted in Fig. 3.1, must be discretised into a number of quadrilateral panels so the influence coefficients may be calculated. The panels do not have to be of the same size or have to form a uniform geometry. However, as with all panel methods the more panels used results in a corresponding increase in computational time and improvements in accuracy.

The internal surface of the wind tunnel was discretised into approximately 1000 individual quadrilateral elements representing the settling chamber, contraction, working section and diffuser (Fig.3.3). This representation gave sufficient distance upstream of the vortex generator location to ensure accurate predictions there, and extended far enough downstream to allow the vortex system to convect through and out of the working section. Since the accuracy of the calculation depends not only on the number of quadrilateral elements used but also on the manner in which these elements are distributed over the surface, a non-uniform distribution of panels was used. In particular, panels were concentrated in the region of the contraction (area of high curvature) and the working section (area of interest). Each panel consists of four corner points which have three dimensional co-ordinates. From these corner points the centriod or collocation point is calculated by simply determining the intersection of the two diagonals of the quadrilateral. A simple transformation was used to transform from the three-dimensional tunnel co-ordinate system into a panel co-ordinate system - thus enabling the influence coefficients to be determined.

3.2.3 Formulation of Matrix of Influence Coefficients

The formation of the matrix of influence coefficients is comprehensively detailed by Hess and Smith (1964,1967). The numerical equations which are used to determine the influence coefficients which make up the matrix are detailed (with derivations) in Katz & Plotkin (1991) for three dimensional constant strength singularity elements and, in particular, quadrilateral source elements. These equations are the same as those derived by Hess & Smith. The derivation is performed in a local frame of reference and so all panels are rotated from the global (wind tunnel) co-ordinate system into a panel co-ordinate system via a simple transformation.

Initially, the model requires the specified geometry of the tunnel and from this calculates the corner points of the quadrilateral elements. The control point of each panel , where the fluid velocity normal to the elements is require to vanish (Neumann boundary condition), is then determined. This is then followed by the determination of the influence coefficients. The matrix of influence coefficients depends solely on the geometry of the quadrilateral elements and is independent of the onset flow. The matrix contains the components of velocity induced at a point in space by a plane quadrilateral having a constant unit value of source density. This is evaluated for the normal velocities induced by all the quadrilateral elements at each other's control points. Multiplying the normal velocity induced by an element at a particular control point for a unit source density, by the constant but unknown value of the source density on that element; summing over all the elements, and repeating for each control point, gives the set of total normal velocities at the control point due to the entire approximated body surface.

3.2.4 Surface Boundary Condition

The continuity equation is given in chapter 2 and in this equation V is the total velocity. This total velocity consists of the freestream velocity and a disturbance created by the body (velocity induced by source panels). The Neumann boundary condition is applied, in this case, which states that the condition of no flow through the surface of the body must be satisfied, i.e.

$$\boldsymbol{V}.\boldsymbol{n} = 0$$

This entails equating the induced normal velocities and the normal components of the onset flow at the control points of the panels to zero. The variation of onset velocity through the wind tunnel, as a result of the changing cross sectional area, is obtained by application of the conservation of mass equation based on a specified working section velocity. Hence, at each panel, the representative onset (freestream) velocity at each panel can be applied. Once the normal velocities of this onset flow have been calculated at each control point, the Neumann boundary condition in then applied.

There are problems associated with applying the Neumann boundary condition to internal flows (documented by Ashby & Sadlin (1985)). This was primarily due to the leakage which results from applying the boundary conditions at a single control point. However, the main problem with this formulation is the additional velocities which would be induced by the rotating blade and the wake vortex elements. The wake from the rotating blade will induce a velocity component on the wall and, hence, alter the onset velocity which in specified in the boundary conditions. This was not taken into account in this formulation. This was due to the increasing number of wake elements which are generated each time step in the free wake model. This would necessitate an implementation of the panel method each iteration due to the time-dependent change in the wake structure and hence a change in onset velocities (boundary condition). For the present design application a wake model, loosely coupled with the simple source panel code, proved satisfactory and the added time and effort to develop a more robust numerical model was not considered necessary.

3.2.5 Iterative Solution

The method in which the induced velocity matrix and the surface boundary condition are solved, to determine the source strength of the panels, is a simple matrix problem.

$$\begin{pmatrix} a_{11} & a_{12} & \cdots & a_{1N} \\ a_{21} & a_{22} & \cdots & a_{2N} \\ \vdots & \vdots & \ddots & \vdots \\ a_{N1} & a_{N2} & \cdots & a_{NN} \end{pmatrix} \begin{pmatrix} \sigma_1 \\ \sigma_2 \\ \vdots \\ \sigma_N \end{pmatrix} = \begin{pmatrix} V.n_1 \\ V.n_2 \\ \vdots \\ V.n_3 \end{pmatrix}$$

where σ_i are the unknown (source strengths) in the equations,

a_{ij} the matrix of influence coefficients

$V.n_i$ the normal freestream onset velocity on each panel calculated from continuity.

Two approaches can be applied for the solution of the large system of equations presented above. These are a direct solution or an iterative solution. The direct solution, usually based on the Gaussian Elimination method, is a reliable approach but it does have the disadvantage that it requires a computing time which is proportional to the number of unknowns cubed. As originally developed by Hess & Smith, the Douglas-Neumann 3-D panel method employed a direct matrix solution, however, iterative techniques were also discussed. An iterative technique usually requires much less computational time for the large numbers of unknowns. Iteration techniques have also been developed to speed up standard (Gauss-Seidel) methods for more advanced lifting panel formulations (Clark 1985). For the present application the system of linear algebraic equations were solved using a Gauss-Seidel iterative solution. Convergence for the source strengths takes approximately 20 iterations. This method is documented in any numerical methods text (e.g. Borse (1991)) and by Hess & Smith.

3.2.6 Calculation of Off-Surface Velocity

Once the source density distribution is known, the three velocity components at any point in the modelled tunnel can be calculated. This is done in exactly the same way as for the induced velocities at a control point, but the point now rests off the tunnel surface. The velocities induced by all the panels are then calculated and added to the local onset flow velocity to get the final total velocity at that prescribed point.

All off surface points are computed in the tunnel co-ordinate system. When dealing with the rotating blade and the wake there is a hub fixed co-ordinate system and so the relative points must be transformed into the tunnel co-ordinate system to determine the velocity components. As a priori, the position of the hub is specified in the input parameter list and so, for the wake nodes, there is a simple translation from the tunnel axis to the hub axis. This is specified in the input parameters to the numerical model as a rotor axis position

with respect to the tunnel co-ordinate system. Normally the rotor hub position is 2.5m - 3.5m from the origin of the wind tunnel co-ordinate system.

A matrix of off surface points were selected within the settling chamber, contraction and working section to investigate the magnitude and direction of the individual velocity vectors. This was carried out primarily to ascertain whether the tunnel model was providing an adequate representation of the accelerated flow through the contraction and the influence of the tunnel walls. This was done prior to the coupling of the tunnel model with the rotating blade model.

3.3 Numerical Model of Rotating Blade

Wake models and their related lifting line/surface models have been applied to a range of differing aerodynamic problems, from simple fixed wing applications to modern tilt-rotor configurations. Here, a rotating blade model which is a derivation of the model used by Coton & Iglesia (1994) to investigate Blade-Vortex Interaction, is discussed. Their work examined how a streamwise convecting vortex interacts with a rotating blade of fixed incidence running at a specified constant blade tip speed. For the present study, it was necessary to remove the convecting vortex and make provision for the variation of the blade incidence and angular velocity. These features, together with the inclusion of the wind tunnel wall influence were incorporated by substantial modification of the existing code.

The single blade rotor with a NACA 0015 profile was modelled using a lifting line positioned at the quarter chord line. This line was discretised into several sections (10) and the bound circulation determined via two-dimensional lift curve data for the aerofoil section. Shed vorticity appears as the variation of the bound circulation with time; and trailed vorticity as the difference in the circulation between two adjacent spanwise sections. This vorticity is represented in the wake by discrete trailed and shed vortex filaments which are added at each time step. The manner in which these wake filaments move is then determined by a free wake approach. In it, the wake shape is modified at

each time step by integration of the velocity field. An essential feature of this approach is the calculation of the velocity induced at each node point by all wake filaments and bound vorticity elements. This, together with an increment in the angle of incidence induced at the blade by the wake is evaluated by application of the Biot-Savart Law (Chapter 2).

Within the numerical model, the blade is positioned relative to the wind tunnel co-ordinate system at a location in the contraction. All the rotor and wake calculations are relative to a hub fixed co-ordinate system but are easily transformed into a tunnel fixed co-ordinate system for calculation of the local velocity components. The model allows input specification of azimuthal blade tip velocity and geometric angle of incidence functions. There is also an option to run the blade continuously or for a short period with a specified acceleration/deceleration tip velocity profile. The blade is assumed to be rigid along its span and no allowance was made for any blade flap.

3.3.1 Introduction - Wake Models

The direct consequence of the lift on a wing in three-dimensional unsteady flow is a wake of trailed and shed vorticity. This wake vorticity in turn induces a velocity at the wing surface which has a major influence on the loading. The calculation of the wake induced velocity is therefore an important part of rotary wing aerodynamics analyses. Considering both the accuracy and efficiency of the calculation of wake induced velocity, it is best to represent the continuous wake vorticity as a series of discrete wake (vortex) elements in which all the vorticity is confined. For each vortex in the wake the induced velocity can be evaluated via the Biot-Savart Law and then the total induced velocity may be determined by a simple summation of all the induced velocities from all the elements at a specified point in space.

As a blade rotates through the air, trailed and shed vorticity is left in the wake. After each vortex element is created, it is convected with the local velocity of the flow field which consists of the forward (or climb) speed of the rotor plus an induced velocity component from the wake itself. There are a number of different types of wake models which are currently available. These vary from the fairly 'simple' prescribed wakes to sophisticated

free wake models. Many models in use are semi-empirical in nature, for example, Landgrebe (1969). In these prescribed wake models, the wake trajectory is described by functional modifications to the classical (rigid) wake.

The classical or rigid wake model consists of an undisturbed helical geometry in which all the wake elements are convected with the same mean velocity. In forward flight, the helical vortices trailed from each blade tip are carried rearward by the freestream velocity parallel to the disk, as well as downward by the component normal to the disk. Thus the wake geometry consists of concentrated vortices trailed in skewed, interlocking helixes. Since no account of the mutual interaction of wake vortices is taken, the classical wake model is not representative. A comparison of the classical rigid wake and distorted wake for fixed and rotary wings is detailed in Figs. 3.4 & 3.5.

In prescribed wake models the wake geometry is specified a priori and can include wake roll-up and deformation details. The predetermined geometry is usually based on simple analytical expressions as well as experimental results. Distortion functions are specified in terms of rotor geometric and operational factors with the aid of wake geometry measurements from small scale isolated rotors. The induced velocity field from the rotor wake is then calculated through the application of the Biot-Savart law integrated along the prescribed trajectory of each tip vortex filament. Although computationally efficient and of considerable use in routine rotor design work, prescribed wake models do not fully capture the physical nature of the rotor wake. Also, their applicability is generally restricted to conditions bounded by the experimental data from which they were derived.

Due to the unknown geometry of the wake as it convects through the contraction and working section of the wind tunnel, the free wake method was the only available option for the present application. In a free wake analysis, the induced velocity at each element which constitutes the wake, is evaluated at each time step by summation of the contributions of all the elements in the wake and the contribution of the bound vorticity of the blade. The total convection velocities (induced and freestream components) may then be integrated to obtain the new positions of the wake elements at the next time step. The wake is modelled as a vortex lattice grid (illustrated in Fig. 3.6) composed of vortex elements. The strength of each line segment in the wake is determined from the blade

bound circulation which can be evaluated at a finite number of azimuthal and radial positions. Continuity of vorticity requires that the trailed vortex strength is given by the difference in bound circulation between adjacent radial stations. Similarly, the shed vorticity strength is obtained from the difference in bound circulation at successive azimuthal stations. Free wake models solve for the wake geometry directly and, in principle, do not require experimental data for formulation purposes. However, since the strengths and positions of the individual wake elements are now part of the solution process, free-wake models are obviously computationally more intensive. Pioneering work on free-wake models was performed by Clark & Leiper (1970) and Sadler(1971), and many variations and developments have followed in the last fifteen years (e.g. Quackenbush et al. (1990,1995), Felker et al. (1990), Ramachandran (1989), Rosen et al. (1988), Favier et al. (1987), Morino et al. (1985), Rosen et al. (1984,1985), Miller (1983)).

Excellent reviews of wake modelling, as applied to helicopter configurations, are readily available in texts by Bramwell (1976), Johnson(1980), Stepniewski & Keys(1984) and describe, in detail, the formulation of both rigid wake and free-wake analyses. Gray (1991) provides a discussion of the application of vortex modelling to rotor aerodynamics and AGARD-R-781 "Aerodynamics of Rotorcraft" includes a summary of the status of aerodynamic prediction codes and experimental work up until 1990. Also,Davis & Chang (1987) provide a more general discussion of 'current' trends in the rotor aerodynamics field by examining recent advances in lifting line/surface theory, wake modelling, panel methods, and finite difference models.

3.3.2 Lifting Line Theory

The classical lifting line theory, for predicting the aerodynamics properties of a finite wing, was developed by Ludwig Prandtl and his colleagues around 1911-1918. The utility of Prandtl's theory is so great that it is still in use today. The method consists of representing a wing as a large number of horseshoe vortices, each one with a different strength of bound vortex, but with all the bound vortices coincident along a single line (called the

lifting line). Accordingly, due to Helmholtz vortex theorems, a vortex cannot end in a fluid and so two free vortices must be trailed downstream. An excellent discussion of the use of lifting-line theory for rotary wing applications is provided by Johnson (1990) and a detailed derivation for fixed wings is available in any aerodynamics text (e.g. Anderson (1991), Kuethe & Chow (1986)).

The assumption of high aspect ratio splits the three-dimensional wing aerodynamic problem into inner and outer problems i.e. wing and wake models. The inner problem is a two-dimensional aerofoil, or more correctly an infinite wing with a specified onset velocity. The outer problem is the wake, consisting of trailed and shed vorticity behind the lifting-line (bound vortex). The inner and outer problems are linked together by the calculation of the bound circulation (blade loading) via the determination of the effective angle of incidence and onset velocity. The blade is discretised into 10 segments each with a control point. At these control points all the velocity components, effective incidence, blade lift and bound circulation for each azimuthal position (time step) are calculated.

The loading near a rotating wing drops to zero at the tip very rapidly. The maximum loading occurs at approximately 80% blade radius. On a rotor blade where the loading is concentrated at the tip due to the higher velocities in this region, the gradient of the lift at the tip is particularly high. To attain a suitable representation of the distribution of blade load the approximation of a number of equally spaced blade segments would result in significant errors. As such, the blade is discretised with smaller segments toward the tip where the bound circulation gradient is highest. This is illustrated in Fig. 3.7.

3.3.3 Velocity Components on Rotating Blade

The velocity components which act at the rotating blade (and wake) can be determined from the Biot-Savart law (for induced velocities) and the panel method (for the three components of local flow velocity). The velocities which act on the blade (in a blade fixed co-ordinate system) can, therefore, be expressed as,

chordwise velocity $u(r) = \Omega r + (u_t + v_{ind})\sin\psi - (-v_t + u_{ind})\cos\psi$

spanwise velocity $v(r) = (u_t + v_{ind})\cos\psi + (-v_t + u_{ind})\sin\psi$

vertical velocity $w(r) = w_t + w_{ind}$

where u_t, v_t, w_t are the velocity components from the panel method in the wind tunnel co-ordinate system.

$u_{ind}, v_{ind}, w_{ind}$ are the induced velocity components from the Biot-Savart law in a hub fixed co-ordinate system.

$u(r), v(r), w(r)$ are the velocity components acting in a blade fixed co-ordinate system.

This is slightly more complicated than the simple rotating blade in a uniform flow as depicted in Fig. 3.8.

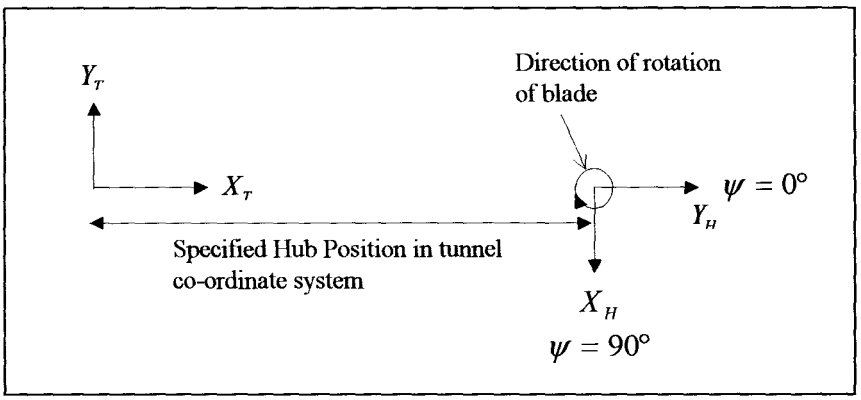

Diagram - Illustration of hub and tunnel co-ordinate systems with specification of blade azimuth.

The equations above represent the transformation of the wind tunnel velocities into a blade fixed co-ordinate system where the azimuthal position (ψ) of the rotating blade varies with time (co-ordinate systems depicted in the above diagram). Hence, the local velocity at each spanwise station on the blade must be calculated via the panel code. This is done by simply specifying the location of each spanwise blade control point in the tunnel co-ordinate system for the off surface panel calculation.

The above representation is for the case where the blade is operated in a continual running mode with a constant angular velocity. However, the numerical model can also be run in a

single rotation mode with acceleration, constant velocity and deceleration phases. These phases are specified by functions of azimuthal position and tip velocity. All this does is change the Ωr term. By specification of the variation of tip velocity with azimuthal position, the blade can accelerate from zero up to a constant tip velocity and then decelerate back down to zero.

3.3.4 Effective Angle of Incidence

The effect of the wake and the wind tunnel on the blade is considered as an increment in the angle of attack which is calculated via,

$$\alpha_i(r) = \tan^{-1}\left(-\frac{w(r)}{u(r)}\right)$$

The effective angle of incidence can the be determined from the specified geometric incidence and the above increment in angle of attack by,

$$\alpha_{eff}(r) = \alpha_{geom} - \alpha_i(r)$$

Once the effective angle of incidence is determined, from all the induced effects of all the vortex elements (v_{ind}) and the vertical velocity component ($u_{z.t}$) from the wind tunnel model, the lift coefficient is calculated from the two dimensional c_l *vs.* α graph for a NACA 0015 aerofoil. A discussion of effective and geometric incidence is provided in Kuethe & Chow (1986) and Anderson (1991) in relation to finite wing theory.
It must be pointed out that the geometric angle is specified as a function of the azimuthal variation. Commonly, when the blade is positioned pointing into the flow (towards the Settling Chamber), the incidence is zero. As the blade rotates towards the working section, the geometric incidence increases linearly as a function of azimuthal position. When the blade crosses the entrance to the working section the geometric incidence is (usually) held constant and when rotating back towards the settling chamber the incidence returns to zero, again via a linear function with respect to azimuthal position.

3.3.5 Calculation of Bound Circulation

The circulation distribution is obtained by application of the Kutta-Joukowski theorem expressed by,

$$l(r) = \rho.V\Gamma(r)$$

where r is the radial position of the control point of each blade segment and V is the resultant velocity determined from the chordwise and vertical velocities (expressed previously).

The above equation is altered slightly to express the bound circulation as a function of lift coefficient which results in,

$$\Gamma(r) = \tfrac{1}{2}Vc.c_l(r)$$

where

$$l(r) = \tfrac{1}{2}\rho.V^2c.c_l(r)$$

This calculation utilises two-dimensional $c_l vs.\alpha$ data for the NACA 0015 aerofoil (documented in Abbott & Doenhoff (1959)) at the appropriate blade tip Reynolds Number.

3.3.6 Free Wake Model

In the current study the blade is discretised into 10 segments with a control point located in the middle of each segment. The strengths of the trailed vortex elements trailed from the blade are determined from the change in the circulation distribution between two consecutive radial positions (depicted in Fig. 3.7) i.e.

$$\gamma_t = \Gamma(\psi, r_{i+1}) - \Gamma(\psi, r_i)$$

and the strengths of the shed vortex elements are determined from the time dependent change in the vortex circulation which corresponds to the azimuthal change in bound circulation i.e.

$$\gamma_s = \Gamma(\psi, r_i) - \Gamma(\psi + \Delta\psi, r_i)$$

The summation for the induced velocity, V_{ind}, at any point in the flow field is carried out using the Biot-Savart Law (Chapter 2) over all the vortex filaments. Further discussions of the free wake model and the vortex lattice method can be found in the texts by Stepniewski & Keys (1984) and Johnson (1980).

3.3.7 Determination of Wake Node Positions

The calculation of the circulation, velocity and node displacements are evaluated at each time step. To determine the local velocity at each node, the induced velocity is summed with the freestream wind tunnel velocity from the panel method. As detailed by Iglesia (1992), a 2nd order Adams-Bashorth multi-step integration is then used on the basis of this resultant velocity to determine the node displacements.

3.4 Parametric Analysis

The numerical model initially reads in an input parameter file which contains all the relevant variables for use in the parametric analysis. The file simplifies alteration of test conditions when running numerous different cases. A description of the parameters contained within this file are given below.

3.4.1 Discussion of Input Parameters

The rotor blade axis was positioned relative to the wind tunnel co-ordinate system whose x-axis lies along the centre-line and z-axis is positive upwards. The origin of the tunnel co-ordinate system was located at the entrance to the settling chamber which corresponds to the start of the modelled portion of the tunnel. Although the blade position could be varied in all three co-ordinate directions, only significant movements in the x-direction were considered. Typical x-values ranged from 2.5-3.5 metres relative to the wind tunnel origin. In Tables 3.1 and 3.2, the X and Y values represent the position of the rotor hub in wind tunnel co-ordinates.

The geometry of the blade was specified by the radius (R) and the chord length (c). These were primarily determined from the maximum allowable radius available wherever the blade was positioned in the contraction. Values range between 0.8 and 0.55 metres. Changes in chord length provide adjustment of the bound circulation strength and hence the strength of the trailed tip vortex.

The working section velocity (WSVEL) is specified and used to calculate the required source density. The source density distribution is then used to calculate the local velocities in the wake and on the lifting line due to the wind tunnel geometry. In this study, the wind tunnel working section velocity was varied between 10 and 30 m/s which represented the operational limits of the 1.15m x 0.8m low speed wind tunnel which was modelled.

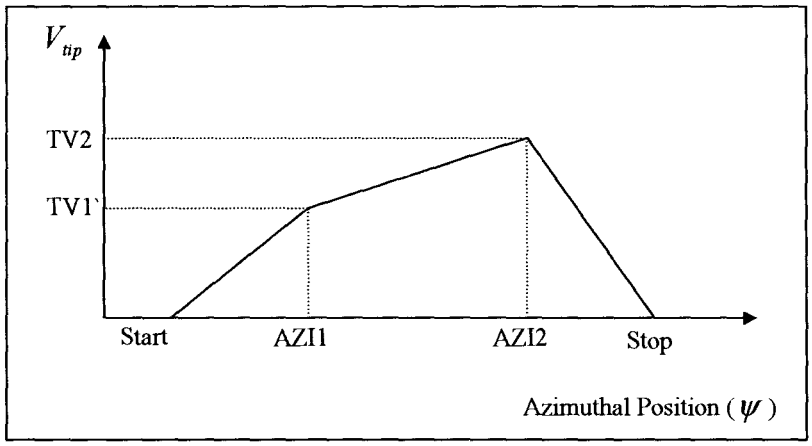

The blade tip speed can be specified either as a constant (TV1) for continuous running or as a tip velocity distribution in relation to azimuth for single rotation cases. In the single rotation cases, azimuthal positions of the rotating blade must be specified as a series of motion defining blade positions. The first phase consists of an initial acceleration up to a specified tip speed (TV1) which is sufficient to overcome reversed flow problems. In the second phase, the blade is either accelerated again (up to TV2) or held at a constant tip speed (TV1=TV2). Finally, the blade is decelerated to rest. This is depicted in the above diagram.

The geometric angle of incidence is specified in a similar way to the above, for both the single rotation and continuous running configurations. This involves a pitch-up phase from zero incidence, a constant pitch or ramp down phase (to control tip vortex strength)

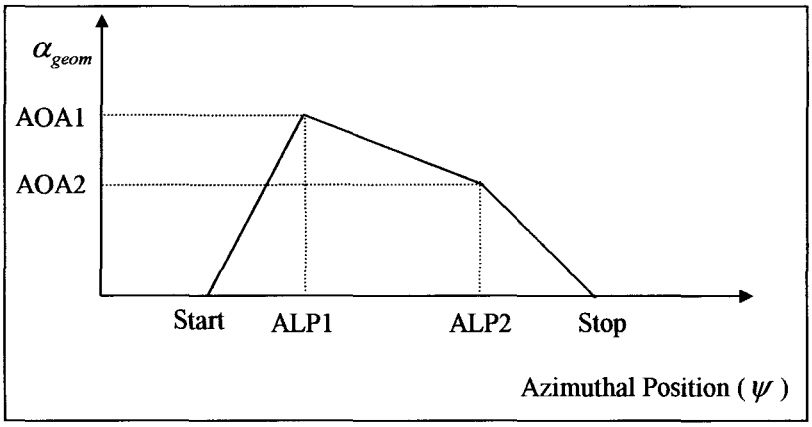

and a final pitch down phase to zero incidence (depicted in the above figure). Values up to a maximum of 10 degrees geometric incidence were considered although, for the majority of cases, a maximum geometric angle of incidence of 5 degrees produced and adequate tip vortex representation.

To eliminate any numerical instability caused by the rotor hub arrangement, a root cut-off is required for the rotor blade. This is set at 20% of the rotor radius. In the experimental set-up (Chapter 6) this portion of the blade is taken up by the pitch mechanism and the rotor hub. Consequently, it will contribute little to the aerodynamic behaviour of the blade.

A Scully vortex (documented in Chapter 2) was adopted for the vortex filaments with the core radius set at 15% of the blade chord. This corresponds to typical values obtained from experimental measurements carried out at Glasgow University. To enhance the computational efficiency, there is a cut-off distance beyond which the influence of a vortex filament is assumed negligible. This can be varied, but a value of 1.5 metres was found to be suitable.

For a given distance of wake travel, the duration of the simulation is related to the working section velocity. A slower working section velocity corresponds to a longer simulation time. Similarly, to retain a given level of detail in the rotor wake, the time step is necessarily related to the rotational speed of the blade. The time step is chosen primarily to balance the level of wake detail with the computational time. More wake elements due

to a shorter time step will increase the overall computational time of the simulation significantly.

3.4.2 Input Configurations

The input parameters documented above were varied to determine their influence on the wake trajectory. The single rotation cases are documented in Table 3.1 and the continual running cases are documented in Table 3.2.

Initial tests at fixed incidence and constant rotational speed, were conducted to determine an appropriate range of each parameter and to identify numerical instabilities in the model. The results from these tests were compromised by a strong vortex shed at the impulsive start-up of the blade. Subsequent tests, therefore, all utilised variations of blade incidence and tip velocity as described above. Thus, by setting the initial blade incidence and/or tip velocity value to zero and allowing it to increase thereafter, it was possible to eliminate the initial strong starting vortex associated with an impulsively started blade.

3.5 Results

In the course of the present study, a large number of possible configurations were considered. In this section, selected results are presented to illustrate the main influences on the geometric features of the tip vortex and wake. The results are presented in two sections corresponding to the modes of operation of the rotor i.e. the limited azimuthal range and the continual running cases. The figures show the plane of the wake and the tunnel walls as viewed from above. In each case, the blade axis is indicated and the blade rotates in a clockwise direction. Three dimensional views of the wake and tunnel are not presented, as the wake lattice was found to exhibit little wander in the cross sectional plane along which it convected.

3.5.1 Acceleration/Deceleration Cases

The complete set of tests which were investigated for this operational mode are given in

Table 3.1. As stated previously, these cases are characterised by a specified function of tip speed versus azimuth which may be sub-divided into three different phases of motion. These were initially confined within one revolution to minimise the disturbance which the rotor may have on the tip vortex. It was, however, also possible to extend the acceleration and deceleration phases if required. In each case the pitch motion did not necessarily have the same prescribed azimuthal break-points as the acceleration/deceleration phases and was independently prescribed in the input parameter file.

The analysis first concentrated on the variation of blade speed and working section velocity. Figure R3.1 illustrates one of the first cases examined. The blade tip speed was set at 70 m/s using a blade of radius 0.6 metres positioned at 3.3 metres relative to the wind tunnel origin. This corresponds to a blade position in the contraction close to the working section. The tip speed was held constant through the second phase of motion during which the blade incidence was set at five degrees. For this case, the working section velocity was set at 30 m/s which is the highest velocity attainable in the wind tunnel. From this figure, it is noticeable that the wake lattice is fairly sparse as a consequence of the 'large' time step (0.0035 seconds) used in the calculation. This value was chosen purely to minimise computational time in the initial stages of the study. This value is, however, sufficient to provide enough detail to illustrate the effect which the blade speed and tunnel velocity have on the wake geometry. The figure shows that the wake structure is skewed because of its high convection speed. To study perpendicular BVI, a near symmetrical wake structure would be preferred. There are two possible ways of achieving this. It could be done by either increasing the blade tip speed or decreasing the working section velocity. It would be inadvisable to increase the blade tip speed too much due to mechanical design considerations, and so a reduction in the tunnel velocity would be the most appropriate action.

Figure R3.2 represents a similar case where the working section velocity is reduced to 20 m/s. All other parameters are unchanged from the previous case. As can be seen from the figure, the wake is more symmetrical and much less skewed. The tunnel velocity could be reduced further to 10 or 15 m/s but the time taken for the wake to convect through the working section would be higher. With due consideration being given to the practical

problem of vortex dissipation with time, it was decided to fix the working section velocity at 20 m/s for future calculations using the same rotor dimensions.

Although the reduction in wind tunnel speed produced a more symmetric wake structure, it was evident that scope still existed to improve symmetry by varying the rotor speed. For this reason, the next stage in the work was to alter the second phase of the blade motion, from the constant tip velocity previously used, to a linearly increasing velocity. Figure R3.3 illustrates one such case. The blade is accelerated up to 50 m/s then accelerated again across the entrance to the working section up to 90 m/s. For this calculation, the time step was decreased to 0.0025 seconds and so there is an increase in the number of vortex filaments in the figure. As before, the motion of the blade was restricted to one revolution during which the blade was pitched up to five degrees whilst accelerating. Its incidence was then held constant until the blade was approximately pointing in the downstream direction and then it was pitched down to zero degrees. As may be observed in the figure, the changing incidence generated a strong tip vortex on the right side of the wake with weaker tip vortex elements on the left.

As the blade changes from travelling with the flow to moving against it, the relative velocities which it experiences increase as a result of its orientation to the local flow velocity. Consequently, if the blade velocity was held constant across the working section, there would initially be a stronger vortex strength on the left side of the wake compared with the right side when looking upstream. It may, therefore, be concluded that obtaining a constant tip vortex strength across the working section (whilst ensuring that the wake shape is symmetrical) is only possible through the control of the tip vortex strength by pitching the blade to counter the increase in relative velocities experienced by the blade. Subsequent analysis concentrated on determining this pitching motion profile so a constant tip vortex strength would span the working section.

Figure R3.4 is typical of results incorporating pitch down motion as the blade crosses the entrance of the working section. Here the blade is still accelerated in the second phase of motion but, the final tip velocity is 100 m/s as compared to 90 m/s in the previous example. The blade axis has also been moved slightly forward from 3.3 to 3.45 metres. Since the blade axis is now closer to the working section in this case, the increase in

mainstream velocity at the blade has to be offset by an increase in tip velocity to counter wake skewing. Also, with the blade being positioned further forward, with no reduction in blade radius, there is less clearance between the blade tip and tunnel wall. This enables the wake to occupy more of the working section and creates a better tip vortex profile. For the case presented, the pitch profile is characterised by an initial increase to five degrees followed by a linear reduction to 2.75 degrees as the blade travels across the working section. The incidence is then finally reduced to zero and the blade brought to rest. The tip vortex strength depicted in the diagram is now fairly constant across the width of the tunnel.

In Fig. R3.5, a larger blade of 0.75 metres was located slightly further back in the contraction at 3.2 metres. The working section velocity was also reduced to 15 m/s to improve the symmetry of the wake. The blade was initially accelerated up to 50 m/s and, as in the previous case, accelerated again across the working section but only up to 90 m/s before decelerating back to zero. Even though the tip velocity profile was not altered from previous examples, the increase in blade radius did reduce the rotational speed of the blade. It is pertinent to note that the separation distance between the tunnel walls and the blade tip was small enough in this case that some doubt must be cast on the validity of the potential flow model within this region.

Before conducting the continual running cases, a single rotation case with a blade of radius 0.65 metres positioned at 3.45 metres from tunnel origin was examined for a working section velocity of 20 m/s (Fig. R3.6). In this case, the blade was accelerated up to a tip speed of 50 m/s which was then held constant across the working section before bringing the blade to rest. Once again, the pitching motion comprised an initial pitch-up to five degrees, then a reduction to 2.75 degrees across the working section and finally back to zero. Due to the lower resultant velocities incurred on the left side of the diagram by holding the tip velocity constant, there is a lower tip vortex strength in this area compared with the previous cases. It was evident from this result that the continual running case would not produce as good a transverse vortex as the single rotation but, as discussed later, the mechanical advantages of such an arrangement may be significant.

3.5.2 Continual Running Cases

The continual running cases are characterised by a series of wake lattice structures generated by each revolution of the blade. All continual running configurations are listed in Table 3.2. The main reason for considering continuous running is to simplify the design of the actual facility. As in the previous section, it is necessary to determine the optimum position of the rotor and the most appropriate setting for the working section velocity. In this configuration, however, the influence which these have on the separation between each individual convecting wake becomes an important factor.

Figure R3.7 depicts a continuous running case with a constant tip speed of 50 m/s. All parameters are the same as the previous single rotation case although a larger time step has been used. This was necessary as a result of the increased computational time required to run the simulation over a longer duration together with the increased number of vortex filaments compared with the single rotation cases. The geometry of the lattice in Fig. R3.7 is consistent with the previous single rotation depicted in Fig. R3.6. In both cases, the incidence of the blade section varied linearly between 5 and 2.75 degrees as it crossed the working section. This resulted in non-symmetry of the tip vortex strength which was subsequently overcome, to some extent, by keeping the blade incidence constant when crossing the working section. This also had the practical advantage of simplifying the pitch motion profile. It should be noted, however, that this does not result in the generation of a constant strength tip vortex. An exact function for incidence variation could be calculated for each azimuth position to attain a constant tip vortex strength but this would only result in a highly complex pitch/azimuth profile which may be difficult to implement experimentally.

Further continuous running cases concentrated on blade position. In Fig. R3.8, the blade was moved back to 2.5 metres. The diagram shows the distortion that occurs in the wake with the blade so far back in the contraction/settling chamber. This is exactly the same phenomenon that was noted in an earlier single rotation case. As may be observed, lower streamwise velocity in this region of the tunnel necessitates a lower tip speed to avoid interaction of consecutive wakes. An increase in tunnel velocity to 30 m/s is illustrated in

Fig. R3.9 but the resulting wake structure is unacceptable because of the high curvature of the vortex system in the working section.

Figure R3.10 illustrates the optimum continuous running case examined in this study. The parameters are chosen to reduce the high rotational speeds incurred in previous cases and so ease the design criteria. A blade of radius 0.75 metres is positioned at 3.2 metres from the origin of the wind tunnel model co-ordinate system which, interestingly, corresponds to the configuration of the best single rotation case. The tip velocity was again set at 50 m/s with a working section velocity of 20 m/s. The separation between tip vortices is approximately equal to the length of the working section and is sufficient to measure the vortex trajectory without significant influence from preceding vortical wake structures.

3.6 Discussion

The results indicate that the wake geometry is primarily determined by the wind tunnel velocity, the blade rotational speed, and the position of the hub axis. The relative magnitudes of the tunnel velocity and the rotational speed determine the extent to which the wake is skewed, and the hub position dictates the wake curvature and elongation. For the latter, it is important for the blade to be positioned close to the working section to minimise vortex dissipation and to ensure the generation of a well structured vortex with a high local convective velocity. These three parameters are critical irrespective of whether the blade is in continuous running configuration or following an acceleration/deceleration profile over a specified azimuth range.

There are considerable differences between the single rotation (acceleration/ deceleration profile) and the continual running cases. The single rotation configuration is characterised by a continually varying tip velocity profile representing the constant acceleration and deceleration of the rotating blade. This, in the majority of cases investigated, is contained within one revolution. In the numerical model, the motion of the blade is represented by three distinct velocity variations. Initially, there is an acceleration from rest up to a specified tip velocity with the blade pitching up. The blade is then either accelerated again across the entrance to the working section, or held at a constant tip velocity before

deceleration back to rest. The critical phase of the motion is when the blade crosses the working section. Here, the pitch profile is varied to produce a near constant tip vortex strength. If the blade travels at a constant velocity, the incidence of the blade should be approximately constant; but if the blade is accelerated, the blade must be pitched down to balance the higher normal velocities experienced by the blade.

The continuous running configuration, on the other hand, does not require the complicated motion profiles of the single rotation cases. In fact, the blade operates at constant rotational speed and only a pitch variation has to be specified. The pitching motion of the blade is, however, determined with reference to the same objective as the single rotation cases i.e. the generation of a constant strength tip vortex. With the blade traversing the working section, the magnitude of the normal component on the blade from the tunnel is small compared to that of the rotating blade. Hence, it is appropriate to conclude that with an almost constant tip velocity profile in this region, a constant pitch incidence would be acceptable to attain (approximately) a constant tip vortex strength.

From the two configurations investigated, the results indicate that the best case configuration for the generation of a lateral vortex occurs in the acceleration/deceleration case. This corresponds to a single rotation consisting of a rapid acceleration up to a tip speed of 50 m/s, followed by an acceleration phase across the working section up to 90 m/s and finally a rapid deceleration back to rest (Fig. R3.5). In this case, the blade radius is 0.75 metres and the hub is located 3.2 metres from the wind tunnel model origin. To enable the generation of a constant tip vortex strength, the pitch motion of the blade consists of a ramp-up to 5 degrees during the initial acceleration phase, followed by a ramp down to 2.75 degrees to balance the higher normal velocities, before the blade is returned to zero incidence during the deceleration phase.

By restricting the motion of the blade to one revolution, extremely high blade accelerations occur. Consequently, any mechanism to actuate the rotor must be able to impose very high torque to attain the prescribed accelerations. One possible way of ameliorating this requirement could be to extend the range of motion over two or more revolutions to reduce the high loads during the initial acceleration and final deceleration phases. Extending these phases does not adversely affect the wake structure as long as the blade is

held at zero incidence during the extended range of motion. The severe accelerations could also be reduced by either increasing the blade radius or reducing the wind tunnel velocity (which enables a reduction in rotational speeds). The blade radius, however, is restricted by the contraction geometry; and a reduction in tunnel velocity is not advisable due to the need for the vortex to have a high convective velocity. Unfortunately, there is no practical solution to reduce the extremely high loads in the critical phase when the blade is accelerating across the entrance to the working section.

In the continuous running cases, the wake geometry is not significantly different to that produced in the corresponding single rotation acceleration/deceleration cases when the tip velocity is held constant across the working section (Figs. R3.6 & R3.7). However, since the blade now operates with a constant tip velocity around the azimuth, consideration focuses on the separation between the consecutive wake structures generated by each revolution rather than to what extent the wake geometry is skewed. This separation distance is dependent on the relationship between wind tunnel velocity and blade tip velocity. These, together with the rotor hub position, also determine the geometric features of the wake.

The design criteria for the rotating blade are considerably simpler for the continual running case. Since there are no stringent limitations with respect to blade travel, the blade could be run up to speed over a number of revolutions then left to wind-down after measurement. This would result in a considerable reduction in the loads required to rotate the blade.

There is no significant difference between the physical dimensions and position of the rotating blade in the best case continual running and single rotation cases. The difference between the two arises from the type of actuation that would be required to produce the torque for either the short period variable acceleration motion or the long duration constant velocity motion. It is interesting to note that the tip speed of 50 m/s and radius of 0.75 metres corresponds to approximately 10.6 revolutions per second, which is marginally higher than the 10 revolutions per second of the current Glasgow University BVI facility. That facility is driven by a geared down servo-motor and has a larger blade with a higher inertia than the proposed rig. It should, therefore, be possible to utilise the existing motor or one similar as the actuation for the proposed facility if the continuous

running mode is adopted. Initial estimates would indicate that for the acceleration/deceleration configuration a hydraulic system (which would be prohibitively expensive) would be required to produce the prescribed motion profile over two revolutions. Since the geometry of the vortex structure is not significantly worse in the continual running configuration it would be difficult to justify the added expense that would be required to implement the acceleration/deceleration case.

The pitching motion of the blade would also be more easily achieved with the blade in the continuous running configuration. A prescribed incidence variation could be obtained using a simple swash-plate mechanism. This would provide the periodic wake generation depicted in the results. Another option may be to incorporate a motor within the hub. Whilst this would provide ease of control and adaptability to different pitch profiles, it would inevitably be more difficult to implement and incur higher costs. This would be unavoidable if the short period acceleration/deceleration mode was implemented as the optimum prescribed pitch profile is non-periodic.

Practical consideration must also be given to the proximity of the blade tip to the tunnel wall during the rotation of the blade. The numerical model takes no account of the viscous effects that would be experienced in this region. This is not a feature when the blade crosses the working section, but must be considered when the blade initially pitches up to generate the wake. Viscous interaction with the wall may result in vortex dissipation and produce unwanted phenomena in the convecting vortex structure. If this does occur then alteration of the radius of the blade would probably be required.

The panel method and the wake model are loosely coupled. The induced velocities from the wake are not taken into account when calculating the source strengths of the panels. This was done purely to save computational time. The numerical model was satisfactory for the present design application and, based on the results, it would not be worthwhile increasing the complexity . Strongly linking the two models (by calculating the induced velocities from the wake at each panel collocation point) would significantly increase the computational time and so limit the effectiveness of the parametric study. This is purely due to the boundary conditions now becoming time dependant which would result in new source strengths having to be calculated at each time step.

CHAPTER 4

Hot-Wire Anemometry

4.1 Introduction

In the field of vortex measurement, a number of different techniques have been successfully adopted. These techniques can, generally, be split up into the measurement of velocity and vorticity (which can be calculated from velocity measurements). In this investigation, we are primarily interested in the mean flow magnitude and direction.

Velocity measurements are, probably, the most important for the fluid dynamicist. They were first performed using pressure probes. Hot-wire anemometers added the ability to follow high frequency oscillations and with the advent of Laser Doppler Velocimetry (LDV), non-intrusive velocity measurements became possible. These three methods, however, are all characterised as single point measurement techniques. Particle Image Velocimetry (PIV) benefited from the development of LDV and addressed the need for whole field measurements.

Hot-Wire Anemometry (HWA) provides similar information to a LDV system at a fraction of the cost. Hot-wires have an extremely high frequency response making then ideal for measurement in turbulent flow. The main advantages of conventional HWA in comparison with LDV are extensively detailed by Bruun (1995). The disadvantages of HWA are primarily due to the delicate nature of the sensor, which is prone to breakage and sensitive to contamination; the difficulty with measurements in highly reversing flows and high turbulence flows (Champagne et al. (1967), Bruun (1972), Cutler & Bradshaw (1991)); and the influence of the presence of the probe on the measurements. Hot-wire anemometry has proved very successful in the measurement of vortices from rotary wings (Baron et al. (1987)) and fixed wings (Chigier & Corsiglia (1971, 1972), Corsiglia et al. (1973)).

In this Chapter, a detailed description of the fundamental theory of hot-wire anemometry and its application in the two experimental configurations documented in Chapters 5 and 6 is presented. The data acquisition system and traverse system employed are discussed, as well as calibration and measurement using X-wire probes.

4.2 Fundamentals of Hot-Wire Anemometry

The hot-wire anemometer has been used for many years as a research tool in fluid mechanics. In spite of the availability of non-intrusive velocity measurement systems (i.e. multi-component laser doppler velocimeters (LDV)), it is still (and will probably remain) widely applied largely due to improvements in electronic technology and to increased interest in detailed description of turbulent flow fields. Furthermore, the hot-wire anemometer is still the only instrument delivering at the output a truly analogue representation of the velocity with high frequency fluctuations. The hot-wire anemometer consists of a sensor, a small electrically heated wire exposed to the fluid flow, and electronic equipment, which performs the transformation of the sensor output to a useful electrical signal. The electronic circuitry forms an integral part of the anemometric system and has a direct influence on the probe characteristics.

The sensor itself is very small and typical dimensions of the heated wire are 5 μm in diameter and 1 to 3 mm in length, thus giving a very small measurement volume. The basic principle of operation of any hot-wire system is the heat transfer from the heated wire to the cold surrounding fluid. The heat transfer is a function of fluid velocity thus, a relationship between the fluid velocity and the electrical output from the sensor can be established.

The purpose of the electronic circuit is to provide a controlled amount of electrical current to the wire. In the constant temperature method (which is by far the most used type of operation) the electrical current is varied so as to keep the temperature of the sensor constant when the amount of heat transfer (convective cooling) varies.

The principle of this technique is based on the convective heat-transfer from an electrically heated element to the surrounding fluid. The amount of heat transfer depends on the temperature difference and the geometry of the sensor(s) as well as the flow velocity and other physical properties of the fluid. Assuming that only one of the fluid parameters varies during a test (e.g. velocity or temperature), the heat transfer from the sensing element can be interpreted as a direct measure of the parameter in question. Should more than one parameter change there are techniques for differentiating between the effect of each one. However, in the ensuing discussion, only variations of the flow velocity are of interest, whereas changes in other parameters of the flow are assumed to have a negligible effect (e.g. density or viscosity variations) or are explicitly accounted for (e.g. temperature variations).

The analysis of the forced convective heat transfer from a heated body to the surrounding fluid is highly complex. To make the solution tractable, a variety of assumptions have to be made depending on the prevailing conditions. By keeping the temperature of the sensor constant, the voltage obtained across the terminals of the sensor varies as a function of the velocity. Due to the pioneering work of King the convective heat transfer for an infinitely long wire element can be expressed in the form,

$$Nu = A + B\,\mathrm{Re}^{1/2}$$

$$Nu = \frac{hd}{k}$$

which can be shown to reduce to,

$$\frac{I^2 R_{W,\infty}}{R_{W,\infty} - R_a} = A + BU^{0.5} \tag{1}$$

Brunn (1995) documented the derivation of the above for a finite length hot-wire sensor which has a temperature distribution along the heated wire (due to end losses from the conductive heat transfer towards the prongs on which the sensor is located). It was documented that the heat transfer relationship for a finite length wire is often achieved simply by modifying the above to,

$$\frac{I^2 R_W}{R_W - R_a} = A + BU^n$$

which can be expressed as,

$$\frac{E_W^2}{R_W} = (A + BU^n)(T_W - T_a) \tag{2}$$

Due to the resistance of the heated wire R_W, probe lead and cables R_L, and wheatstone bridge resistor R_1 remaining constant, the wire voltage is normally replaced by the bridge voltage via the relationship (Bruun, Section 2.1.2.4),

$$E = \frac{R_1 + R_L + R_W}{R_W} E_W$$

Hence, King's Law for a finite wire is commonly expressed as,

$$E^2 = A + BU^n \tag{3}$$

and the values of A,B and n are usually determined by calibration. This equation assumes that the ambient temperature does not vary i.e. $T_W - T_a$ = constant (which is incorporated into the constants A and B in equation 3). The arbitrary constants A and B for equations 1,2 and 3 are not the same.

All the theory detailed here is covered, in great detail, in the texts by Bruun (1995) and Lomas (1986). These texts provide extensive information on all aspects of the theory, use and application of hot-wires. A simple introduction to hot-wire anemometry is provided by

Comte-Bellot (1976). Here, a brief discussion of the IFA300 Constant Temperature Anemometer system, calibration and measurement using single and x-wire probes is presented.

4.2.1 IFA 300 Constant Temperature Anemometer System

The system (IFA-300) and software (Thermal Pro) for calibration, measurement and analysis was developed by TSI Incorporated. This system is the latest electronic advance in thermal anemometry and was purchased by the Department of Aerospace Engineering for the research detailed in this thesis. The IFA300 is depicted in Figure 4.1 for the case of two single sensor hot-wire probes. The same set-up would be used for calibration and measurement using a single x-sensor probe.

Each IFA300 unit contains one microprocessor system board. This board controls all functions and settings of the anemometer and signal conditioner via an address and data bus. The RS-232-C interface is used to send commands from the computer to the microprocessor. The temperature is determined from a thermocouple circuit on the microprocessor board. This enables the board to send temperature data through the RS-232-C interface to the personal computer.

There are three channels on this particular anemometer but one IFA300 system can take up to eight independent channels. Two boxes may be linked together and so all the 16 BNC channels on the BNC interface board to the A/D converter can be used. Each channel contains a single (wheatstone) bridge circuit and signal conditioner. The bridge circuit includes (what TSI call) SmartTune^{TM} technology which automatically optimises the frequency response and prevents oscillations. This facility means the bridge does not require tuning for frequency response and is independent of type of sensor or length of cable. The frequency response of a hot-wire probe, operated in the constant temperature mode, is discussed by Bruun (1995) .

The back panel includes an input BNC connector for each channel (from each sensor) and a single output voltage after signal conditioning. The bridge voltage is signal conditioned

to best use the resolution of the A/D converter. This is done by applying a gain and offset to each channel to enable the output voltage to fill the -5V to +5V input of the A/D converter. Low pass filters also make up the signal conditioning and allow the removal of high frequency signals which are out of the range of interest and to eliminate aliasing.

The RS-232-C control of the IFA300 and the acquisition of data through the internal A/D converter board, are accomplished through the TSI supplied Thermal Pro™ software. This software was written using National Instruments LabWindows/CVI programming environment. Through the Thermal Pro software, the user can calibrate probes, acquire data and analyse the collected data. The manual provides the necessary information required to operate the system but does not document the method used for analysis. These methods are provided here (in Section 4.4) for completeness and for the benefit of any future user of the system.

4.2.2 Calibration

The two experiments presented in the next two chapters use X-wire probes. As with all measurement systems, an important part of the experimental procedure is the calibration. Hot-wire probes are, unfortunately, among the more difficult measurement devices to calibrate partially due to the non-linear behaviour of the heated wire when the (cooling) velocity is varied.

The velocity calibration of a hot-wire probe usually consists of a series of measurements of the velocity and the anemometer bridge voltage. To obtain sufficient accuracy it is common to carry out 15-30 readings equally spaced over the selected velocity range. The raw calibration data must then be smoothed over the entire velocity range of interest either through an interpolated look-up table method or a fitted analytical function. The most commonly used calibration methods are related to analytical expressions (King's Law, Polynomial curve fit) for the relationship between the velocity and voltage.

A discussion of the relative merits of the different calibration relations is detailed in section 4.4 by Bruun. There are polynomial curve fits, spline fits, extended power laws, and the original power law by King which can be applied to relate the effective velocity to

bridge voltage. Here, the discussion is limited to King's Law,

$$E^2 = A + BV_e^n$$

and a polynomial curve fit,

$$V_e = K + AE + BE^2 + CE^3 + DE^4$$

The polynomial curve fit is used in preference to King's Law to represent the voltage-velocity calibration curve because King's Law is very sensitive to a single error in one velocity calibration point. The polynomial curve fit is less prone to a bad velocity calibration point and gives lower errors in the curve fit at lower calibration velocities.

For cross and triple wire probes the directional sensitivity of the sensors must also be quantified in addition to the velocity calibration. This entails determining the function relationship between the bridge voltage and the velocity magnitude and direction. It is generally accepted that a hot-wire sensor responds uniquely to the velocity provided that it is specified in a wire-fixed co-ordinate system. The velocity vector V may be specified either in terms of its magnitude, yaw angle and pitch angle by,

$$E = F\left(\overline{V}, \alpha, \beta\right)$$

or in terms of the corresponding three velocity components normal, tangential and bi-normal to the sensor (illustrated in Figure 4.2) by,

$$E = F\left(U_N, U_T, U_B\right)$$

The most common method of representing these functions, which defines the concept of effective (cooling) velocity, was proposed by Jorgensen (1971) and is referred to as Jorgensen's equation. Jorgensen proposed the following equation for the effective velocity which can be expressed as,

$$V_e^2 = V_\infty^2\left[\cos^2\alpha + k^2\sin^2\alpha + h^2\cos^2\beta\right]$$

where k and h are often referred to as the sensor's yaw and pitch coefficients (sensitivity coefficients) or yaw and pitch factors. This equation is the most accepted relationship used to quantify the directional nature of heat transfer from a heated cylindrical sensor.

From Fig. 4.1, for a single normal probe, this can be simply rewritten in terms of velocity components in the wire co-ordinate system as,

$$V_e^2 = U_N^2 + k^2 U_T^2 + h^2 U_B^2$$

The simplest relationship between effective velocity is for a single normal wire where the velocity is perpendicular to the wire. In this case the effective velocity equals the freestream velocity such that,

$$V_e = \hat{V}$$

and for a single inclined wire an approximation, which was used in the past, is,

$$V_e = \hat{V}\cos\alpha$$

This is illustrated in Fig. 4.3 for a single sensor. The above equation is referred to as the Cosine law but for inclined wires this is not particularly accurate, due to additional cooling from the component of velocity parallel to the wire sensor, and from the component of velocity bi-normal to the sensor.

Calibration is required to establish the relationship between output bridge voltage and the effective velocity (A,B and n in the Kings law curve fit or the coefficients in the polynomial curve fit) and to quantify the directional sensitivity of the probe (determine k). It is usual to produce a graph of the calibration data to assess the validity of the curve fit.

For a single sensor probe, the calibration provides the voltage versus the effective velocity relationship in the form of an equation ($V_e vs. E$). For an x-wire probe, in addition to the two equations obtained for output voltage versus effective velocity (one for each sensor of the x-wire probe), the directional sensitivity of each of the sensors is provided as a function of velocity (k, Yaw coefficient as a function of velocity). For triple wire probes, there are three voltage vs. effective velocity curves in addition to the yaw (k) and pitch (β) sensitivities for each sensor.

Here, k is a scalar which characterises the sensor and is typically taken as a constant. This non-dimensional k factor is a measure of sensor sensitivity to parallel cooling. When the flow is parallel to a sensor, cooling is much less effective than when the sensor is

perpendicular to the flow. This results in k being much less than 1. In the idealised case, commonly assumed where only the normal component is made responsible for the sensor cooling, the k factor is taken as zero which reduces Jorgensen's equation to the cosine law. However, experiments have shown that for standard hot-wire probes k has values of the order of 0.2. Smaller k values are due to greater length to diameter ratios. Therefore, the cosine law assumes a sensor of infinite length and negligible cooling caused by the tangential component of velocity.

Here, the method detailed and used for single and x-probes is based on the concept of effective velocity. However, another method documented by Johnson & Eckelmann (1984), Lueptow et al. (1988) and Browne et al. (1989) uses the concept of a look-up table for the calibration and measurement with x-wire probes. This method is extensively documented in Bruun (1995). The concept relies on the unique relationship between the two x-probe sensor voltages E_1, E_2 and the velocity magnitude $\overline{V}$ and flow angle α. The table of calibration points is used directly with experimental measurements. With two measured voltage signals, a point can be plotted on the look-up table and the velocity magnitude and direction determined. For points which do not directly coincide with calibration points, an interpolation scheme is used to interpret the voltage data. The main difference between the various implementations of the look-up table method, primarily stem from which type of interpolation routine is used (between the calibration points) to interpret measured voltage data.

Unfortunately, to complete a look-up table, the flow angle is usually varied at every velocity. Thus, if 17 calibration velocities are carried out for 11 flow angles this gives a table with 187 calibration points. This compares with one velocity calibration (17 points) and one yaw angle (flow angle) calibration (11 points) for the effective velocity method giving a total of 28 calibration points needed. It is obvious that the effective velocity method requires considerably less time and effort due to the considerably fewer calibration points required. Also, the effective velocity method is based on the direction sensitivities of each sensor independently and so is applicable for normal and inclined single sensors, x-wire probes and triple wire probes whilst the look-up table method is only of use with x-wire probes.

4.2.2.1 X-Wire Probes

X-Probes are typically used in fluid flow studies for simultaneous measurement of two components of velocity (parallel and normal to the probe stem in the plane of the two wires). Flow velocity vectors that are known to fall within a 30 degree cone from the centre line of the probe can be uniquely quantified by analysis of each of the voltages from the two corresponding channels of thermal anemometers (The TSI IFA 300 in this case). X-probe analysis depends on the use of calibration data that characterises the response of the thermal sensors to fluid flow variations. To clearly understand the analytic procedure used in x-probe data reduction it helps to first be aware of the information that is collected in sensor calibration. A constant-temperature thermal anemometer sensor cannot be used in determining the velocity magnitude and direction until the heated sensor's response to variations in fluid velocity magnitude and direction have been quantified.

In an X-probe calibration, velocity data is taken at a number of specified velocities with the flow at 45 degrees to each sensor and in the plane of the two sensors (i.e. parallel to the probe stem). Yaw data is then taken at a single, as in this case, or a number of specified velocities (up to eight) by rotating the probe about and in the plane of the sensors. Yaw calibration typically records the bridge voltage of a sensor at up to eleven yaw angles in the plane of the sensor and the primary flow direction. The central yaw calibration point (0°) is usually the point where the probe stem is parallel to the primary flow direction with five points on either side of this central point (in the yaw plane). The normal inclination angle for an x-wire probe is 45 degrees and the yaw angles range from 15 to 75 degrees in 6 degree intervals. Since the two sensors are in the same plane, the data for the two sensors can be acquired simultaneously. For example, when the probe is orientated so that the first sensor has its minimum yaw angle (the inclined sensor is tending towards perpendicular to the flow), the second sensor has its maximum yaw angle (where the wire is tending towards being parallel to the flow).

This approach does not directly give the data needed to develop a correlation between cooling velocity and the output of the anemometer. This is because the sensors are not normal to the flow (i.e. they are at 45 degrees to the flow). The flow velocity is equal to

the cooling velocity only when the flow is normal to the sensors as in the case of normal single probes.

To interpret the velocity calibration data for each sensor(calculate the effective velocity and develop the fourth order polynomial curve fit with anemometer voltage), the results of the yaw calibration are needed (k coefficient in Jorgensen's equation). Unfortunately, the interpretation of the yaw calibration data is itself dependent on the speed calibration results. Therefore, to reduce the calibration data into the constants K,A,B,C,D and k an iterative approach is used.

The algorithm implemented in the software assumes three initial values of k. From these k's, sets of effective velocities are calculated from the calibration data via the polynomial curve fit,

$$V_e = K + AE + BE^2 + CE^3 + DE^4$$

and, assuming the calibration velocity is in the plane of the wires, Jorgensen's equation, expressed as,

$$V_e^2 = U_N^2 + k^2 U_T^2$$

The residual of the difference of the two above equations is summed over all the calibration points. The resulting residual sums and their corresponding k values are fitted to a parabola. The minimum of the parabola determines the next best guess for k. The worst of the original three k values is then discarded and the process is repeated until k converges to within an acceptable tolerance. The above information was obtained in discussion with TSI due to the limited information in the manual provided.

The result of the calibration is a screen which depicts the curve fit of the calibration data and the yaw coefficients of each sensor. The curve fit is depicted in Figure 4.7. The polynomial curve fit is for the effective velocity and the points represent the predicted effective velocity calculated from the specified freestream calibration velocity via,

$$V_e^2 = V_\infty^2 \left[\cos^2 \alpha + k^2 \sin^2 \alpha\right]$$

where α is the sensor inclination of 45 degrees and k is the calculated yaw coefficient from

the analytical method discussed previously.

The error represents the difference between the predicted effective velocity and the calculated polynomial curve fit. The predicted effective velocity is the velocity that we expect a single sensor to indicate given the actual velocity , the slant angle and the yaw coefficient. The calculated effective velocity is calculated from the output voltage and the polynomial equation for the curve fit.

4.2.2.2 Design of Calibration Facility

Before any of the individual experiments were conducted, it was necessary to design and construct a calibration facility for single and X-wire probes. Single wire probes are the simplest and quickest to calibrate primarily due to the fact that the onset velocity specified in the calibration facility is equal to the effective velocity. This means that a direct polynomial curve fit can be applied to the original calibration velocities and the single sensor bridge voltage.

To calibrate a probe, some means of positioning the probe in a known flow that can be varied from zero to the maximum required velocity, must be available. These flow facilities can range from the expensive calibration equipment provided by TSI and DANTEC to the actual wind tunnel in which the experimental investigations are to take place. Regardless of the method used, it is necessary to accurately measure the reference flow velocity.

Using the given information on X-wire probes, a simple support was constructed for the calibration of single and cross-wire probes. This probe support was designed to rotate the probe around a point corresponding to the intersection of the two sensors, in the plane of the sensors. A support frame was built onto the vertical tunnel to position the probe at the same height as the pitot probe, which was already located (at a fixed height) in the tunnel. A protractor was aligned to the vertical flow direction where the probe support shaft passed through the external frame. A locking mechanism was also added to the external frame to hold the probe at the appropriate yaw angle. This vertical alignment corresponds to 0 degrees and so the yaw angle can be easily determined up to a maximum of ± 30

degrees. The calibration facility, with support frame, probe support and pitot probe, is shown in Figure 4.6. The vertical open jet wind tunnel can attain speeds up to 42 m/s. This is well above the maximum operating velocity of the 1.15m x 0.8m wind tunnel. However, for tests conducted in the 2.1m x 1.6m wind tunnel the maximum operating speed is well in excess of 42 m/s. The velocity used in the tests documented in Chapter 5 is 47 m/s. A discussion of carrying out measurements in a flow outwith the calibration range is provided in Chapter 5.

The reference velocity was obtained by means of a pitot probe placed in the flow. The probe was located close to the hot-wire probe and it was possible that this may affect the calibration velocity. Simple checks were made by gradually introducing the pitot probe into the flow and monitoring the effect on the hot-wire probe. No significant changes in the x-wire probe were noted. As the calibration tunnel has an open section, the reference static pressure is equal to the atmospheric pressure. Bernoulli's equation is used to determine the air velocity from the differential pressure via,

$$\Delta P = \tfrac{1}{2}\rho V_{\infty}^{2}$$

where ΔP is the difference between the pitot (total) pressure and the corresponding static (atmospheric) pressure and was measured by means of a digital manometer. The calibration facility had two manometers, one which could provide a reading in either m/s or ΔP and the other which could just read ΔP. The simplest calibration method is to use the m/s reading and input that directly into the calibration software. However, a simple table of calibration velocities and their corresponding change in pressure readings was constructed (using Excel) and these pressures were also used to set calibration velocity.

4.2.3 Data Acquisition

Data acquisition is, in principle, simpler than calibration. Once the calibration curves and the coefficients have been determined, it is quite easy to determine the flow characteristics given two acquired voltages. From the acquired voltages, the effective velocities for each wire can be determined from their representative polynomial calibration curves. These effective velocities are then related to the normal and tangential velocities of each sensor. Thus for sensor one,

$$V_{e1}^2 = U_{N1}^2 + k_1^2 U_{T1}^2$$

since the wires are perpendicular to one another,

$$U_{N1} = U_{T2} \quad \text{and} \quad U_{N2} = U_{T1}$$

and so the effective velocity for sensor two can be expressed as,

$$V_{e2}^2 = U_{N2}^2 + k_2^2 U_{T2}^2$$
$$= U_{T1}^2 + k_2^2 U_{N1}^2$$

Thus, there are two equations with two unknowns which can be calculated from,

$$U_{N1}^2 = \frac{V_{e1}^2 - k_1^2 V_{e2}^2}{1 - k_1^2 k_2^2} \qquad U_{T1}^2 = \frac{V_{e2}^2 - k_2^2 V_{e1}^2}{1 - k_1^2 k_2^2}$$

where V_{e1}, V_{e2} are the measured effective velocities and k_1, k_2 the yaw coefficients for sensor 1 and 2 respectively.

The two in-plane flow velocities u, v can now be determined from,

$$u = \frac{U_{N1} + U_{T1}}{\sqrt{2}} \qquad v = \frac{U_{N1} - U_{T1}}{\sqrt{2}}$$

and the velocity magnitude can be expressed by,

$$\overline{V} = \sqrt{u^2 + v^2}$$

Hence, given a pair of cooling velocities from a single measurement of a cross-wire probe, the u and v components and the total magnitude may be determined. Unfortunately the analysis of the data is compromised by the assumption that the two wires are perpendicular. This is not the case in practice. Checks must be carried out after calibration (by acquiring measurement points in the calibration facility) to ensure meaningful data can be acquired.

To determine the third component of velocity the cross-wire probe must be rotated through 90 degrees. To maintain a right-handed co-ordinate system, which is necessary for the software to correctly determine the direction of the flow, the probe must be rotated in the clockwise direction when looking upstream along the probe stem.

The preceding analysis assumes no change in the ambient temperature of the surrounding fluid. This, however, is not the case when conducting measurements in the wind tunnels where changes in flow temperature are common. This is resolved in the analysis software which has automatic temperature compensation. A temperature corrected voltage is used rather than the bridge voltage, which is given by,

$$E = E_b \times \sqrt{\frac{T_s - T_c}{T_s - T_e}}$$

Density correction is also applied between the calibration data and the acquired data via,

$$V_{e(corr)} = \frac{P_c}{P} V_e$$

where the atmospheric pressure during calibration (P_c) and during tests (P) is provided prior to taking calibration or test data.

4.2.4 Probe Repair

One of the most frustrating and time-consuming parts of using the hot-wire technique is the fragility of the sensors employed. These delicate wires can break without notice, are prone to contamination and can be damaged easily with mishandling. The time taken to send the probes back to the manufacturer for repair can significantly delay a test programme and so it was decided to purchase a DANTEC probe repair kit. The significant cost of such equipment was fairly easy to justify as the Department of Aerospace Engineering has a number of single wire probes (20) and x-wire probes (6), which can be repaired by the kit. As stated previously, it is highly unlikely that manual repair will result in two wires exactly perpendicular. Every effort must be made to align the probe at 45 degrees and ensure the wire is horizontal to try and minimise any error which may result.

A stereo microscope was found to be available within the Department. Its magnification was 20x and proved suitable for viewing the probe under repair. The probe repair manual recommended magnification was 40x but the cost of a new stereo microscope was prohibitive.

The problems which can arise during measurement, which necessitate probe repair, are breakage of a sensor or contamination/alteration of the sensor in some way to invalidate the calibration (which could require replacement of sensor). If the probe starts to give low readings, which does occur with extensive use, the sensor should be replaced and the probe re-calibrated. A single sensor takes approximately 30 minutes to repair and 40 minutes to calibrate. It takes about one hour to replace both sensors in an x-wire and another hour is required for calibration.

4.3 Traverse System

The tunnel is equipped with an automated two component traverse which can be mounted vertically on the wall of the tunnel (Fig.5.2), or on a support structure horizontally (Fig.5.3). The traverse is actuated via stepper motors controlled through a data acquisition board by software written under National Instruments Labview™ software. The positional error of the traverse is of the order of 0.5%. The traverse system is depicted in Fig. 5.4. For each test case in Chapter 5, the traverse system was programmed to execute a specified grid sweep. This was conducted twice in each test with the probe rotated the second time to obtain the third component of velocity. In Chapter 6, the traverse was only used to position the probe at a single measurement point.

4.4 Data Analysis and Presentation

The outcome of the measurement process is two digital time-history records for each of the measured velocity components at a specified traverse location. Each individual measurement point has a raw data file of this type. At each measurement point, the data file is analysed to determine the flow conditions or provide a velocity time series representation of the digital records. The output from the time series analysis is normally the mean velocity components (of primary concern here), streamwise turbulence intensity and shear stress. Each time-history will consist of a mean and a fluctuating component which are related by,

$$U(t) = \overline{U} + u(t)$$

$$V(t) = \overline{V} + v(t)$$

For an infinitely long time-history record, the mean value is simply the average of all values which can be expressed as,

$$\overline{U} = \lim_{T\to\infty} \frac{1}{T}\int_0^T U(t)dt$$

When using digital data analysis the continuous signal $U(t)$, $0 \le t \le T$ is replaced by a corresponding digital sample record $U(n)$, $n=1,2,\ldots,N$. The total sample time is T and N is the corresponding number of samples. N and T are related by the sampling rate *(SR)*, which is specified with the number of samples when conducting hot-wire measurements, by the equation,

$$N = SR \times T$$

and the time interval between samples Δt is given by,

$$\Delta t = \frac{1}{SR} = \frac{T}{N}$$

In digital form, the estimate (or measured value) for the mean value of a finite sample record can be expressed as,

$$\overline{U} = \frac{1}{N}\sum_{n=1}^{N} U(n)$$

The streamwise turbulence intensity is usually expressed as,

$$Tu = \frac{\sqrt{\overline{u^2}}}{\overline{U}}$$

but to calculate the turbulence intensity, the variance (second moment about the mean) is required. The variance of a time history record is the mean square value about the mean which can be expressed as,

$$\sigma_u^2 = \lim_{T\to\infty} \frac{1}{T}\int_0^T (U(t)-\overline{U})^2 dt = \lim_{T\to\infty} \frac{1}{T}\int_0^T u(t)^2 dt$$

The square root of this is termed the standard deviation σ_u.

For a digital time-history record, the estimate of the variance can be obtained from,

$$\sigma_u^2 = \overline{u^2} = \frac{1}{N}\left(\sum_{n=1}^{N}(U(n)-\overline{U})^2\right)$$

$$= \frac{1}{N}\sum_{n=1}^{N} U^2(n) - \overline{U}^2$$

From these equations, the standard deviation $\left(\sqrt{\overline{u^2}}\right)$ and, hence, the turbulence intensity can be determined.

The joint amplitude statistics of two simultaneous sample records, which are assumed to have zero means, can be expressed in the form,

$$\overline{uv} = \lim_{T\to\infty} \frac{1}{T}\int_0^T u(t)v(t)dt$$

$$\overline{uv} = \frac{1}{N}\sum_{n=1}^{N} u(n)v(n)$$

and for the case where the means are not zero,

$$\overline{uv} = \frac{1}{N}\left(\sum_{n=1}^{N} u(n)v(n) - N \times \overline{U} \times \overline{V}\right)$$

This quantity is important in turbulent flow studies because it typically represents the shear stress.

The above digital forms of the equations are implemented in the software to conduct an amplitude domain analysis on the time series obtained at each measurement position in an acquired grid (for the work documented in Chapter 5). Since the time series consists of a number of simultaneously measured discrete pairs of values of voltages for each sensor, the individual *U(n)* and *V(n)* can be determined in the manner described in section 4.2.3 in the present Chapter. Only the calculations of the statistics used in the discussion of the results in Chapter 5 have been presented. A complete discussion of the above quantities for the analysis of single and joint time history records is provided in Bruun (Chapter 12).

After acquisition, each individual data file is analysed to determine the flow conditions (mean velocity, turbulence intensity etc.) at each specified grid point. All these data points are then combined into a single ASCII file which contains all the data for one complete traversed grid including the measurement locations. Due to the utilisation of x-wires for three component measurements, there are two files for each grid, one for each cross-flow component. There are, therefore, two measurements of the streamwise component of

velocity and these assist in verification of each acquired grid.

The grid files contain a list of all the parameters and traverse locations which could be measured in a three-dimensional flow field. Hence, when acquiring two components, in the case of x-wires, there are a number of zero columns for the third component of velocity which is not measured and the z (streamwise) traverse co-ordinate (which is not used). These files are then transferred from the Data Acquisition Personal Computer over the local network to a Sun SPARC station in the Dept. of Aerospace Engineering's Computing Laboratory for graphical analysis using PV-WAVE. All files are then reduced in size with the removal of these unnecessary columns and formatted to enable the file to be read into the PV-WAVE software for graphical presentation. The grid points are also rearranged to coincide with the requirements of the individual graphical commands (and the numerical model presented in Chapter 5).

From Chapter 3, it is clear that the passage of a vortex through the working section of the wind tunnel should be periodic if the vortex generator is continuously running. Using the equipment and experimental procedure documented in this chapter, it is obvious that utilising a stationary x-wire probe placed in a flow field similar to that depicted in Fig. 3.10 should result in a periodic (time-dependent) change in the velocity experienced by the probe. Thus, individual (digital) time series records must be looked at, in this case, rather than the amplitude domain analysis discussed previously. This is required in Chapter 6 where the analysis of the periodic flow, as generated by the new experimental facility, is required.

Each measurement location within the tunnel should contain periodic data representative of a transverse vortex passing over an x-wire probe. The phase locked ensemble-averaging technique can be used to extract the periodic signal component from the fluctuating signal. This method is extensively documented in Chapter 11 of Bruun's (1995) text in discussion of conditional sampling techniques. Bruun states that the PLA method can be applied, in principle, to all types of rotating wakes including compressors, turbines, wind turbines, propellers and helicopter rotors. However, most of the extensive reviews documented concentrated on the application of PLA to turbomachinery and there were no references of the application of PLA to helicopter rotors. The only reference to wind-turbines was provided by Clausen & Wood (1988).

Bruun stated that the digital data acquisition can either be carried out continuously or initiated once per revolution. In the continuous mode, the sampling rate must be strongly tied to the period (or rotational frequency) of the blade,

$$SR = \frac{M}{T} = Mf$$

where, M, is the number of points required each revolution, T, the period of the rotor and, f, the rotational frequency. If this is not done the periodic signal will, probably, be averaged out due to individual points in each periodic region of the time series not coinciding. It is extremely difficult to implement this method in the present investigation as there are only a finite number of specified sampling rates available on the IFA300 system. This would require specifying the sampling rate then trying to (very accurately) set the rotational speed of the blade.

However, the method above can be simplified by taking data which is initiated by a once-per-revolution marker pulse or signal from a digital encoder (called 'burst' mode data acquisition in the text by Bruun). This method produces a number (N) of digital time series records all phase-locked to the reference pulse on the shaft and the total sample time can be selected to correspond to one or a number of blade rotations. These time series can then be ensemble averaged to extract the mean periodic component. This ensemble averaging can be expressed, for the streamwise component, as,

$$\overline{U}_E(t) = \frac{1}{N}\sum_{n=1}^{N} U(t,n)$$

The technique is implemented in Chapter 6 and uses a constant trigger point situated on a rotating shaft to acquire a number of individual time series files at specific traverse locations. These files can, then, either be presented individually or ensemble averaged to try and remove the fluctuating component of the signal. It must be pointed out, however, that unless the wake flow events are strongly phase locked, the PLA technique will smooth out significant flow events and the magnitude of the evaluated phase-locked flow quantities may not be an accurate description of the wake flow events. In the event of any problems with the PLA technique, the individual time series can also be analysed to provide a simple means of determining whether a transverse vortex exists (as shown by the numerical model) and so validate this new experimental technique for the generation of a transverse vortex as discussed in Chapter 6.

CHAPTER 5

Twin Vortex Configuration

In Chapter 1, a detailed discussion of helicopter aerodynamics was provided including BVI and helicopter rotor tip profiles. A brief summary of the relevant information is provided here as an introduction to the present investigation into, primarily, twin co-rotating vortices for application in the Glasgow University Blade Vortex Interaction Facility. Single vortex measurements are also presented as well as the previous single vortex investigations conducted by Kokkalis et al. (1988) and Horner et al. (1994).

5.1 Introduction

The association of vortex systems with the production of aerodynamic forces is, for most aeronautical applications, well understood. In some cases, however, such as rotary wing aircraft, the vortex systems are particularly complex and highly unsteady and their interaction with the rotating lifting surfaces creates additional undesirable effects such as noise emission and structural vibration. On a helicopter, Blade-Vortex Interaction (BVI) occurs when the tip vortices trailed from the rotor pass close to, or impact directly with,

any of the blades in the main rotor or tail rotor systems. In some flight conditions BVI can be particularly severe and is manifest as high-frequency impulsive loads on the rotor blades.

Experimental studies have been predominantly wind-tunnel based and have utilised a variety of test geometries to create the BVI phenomenon. Early studies attempted to isolate single interactions in the hope that a clear description of the process would be forthcoming. Unfortunately, these tests were often hampered by problems associated with vortex generation or poor measurement resolution. In recent years, improvements in instrumentation technology have allowed more detailed studies of BVI, both as an isolated phenomenon and also in the full rotor domain to be conducted. Of particular relevance to the present study, detailed in this chapter, is the surface pressure measurement and flow visualisation work of Kokkalis et al.(1988) and, subsequently, Horner et al. (1994). In these tests, a vortex generator was located upstream of a single-bladed rotor in the working section of a low-speed wind tunnel. During the interaction of the vortex with the rotor blade, unsteady surface pressures were measured and Particle Image Velocimetry was used to obtain quantitative flow field information.

As detailed in Chapter 1, one aspect of the present study examines the generation and subsequent behaviour of a vortex pair in a wind tunnel environment (for application to twin BVI experiments). The initial investigation was to design the relevant vortex generators which could represent the Vane Tip flow field (Borcklehurst & Pike (1994)). This entailed:

1. generation of two vortices
2. vortices spaced half chord apart
3. vortices of near equal strength

To this end, a very flexible experimental set-up was required to investigate the behaviour of these vortices as vortex generator parameters were altered. Due to the dearth of information on closely spaced twin vortices (discussed in Chapter 2) a detailed investigation into the associated flow field had to be undertaken.

Hot-wire measurements were conducted downstream of the generators using x-wire probes to document the strength, position and size of the vortices. A numerical model was utilised to provide an accurate means of determining vortex strength, position and size. Finally, the numerical model was successfully extended to consider the rotation of the vortex system. It is shown that the vortices can be modelled accurately using a simple two-dimensional core model and that their rotation can be predicted in a straightforward manner.

In this chapter, the design of the vortex generator, measurement of the associated flow field and the derivation of the numerical model are detailed. Even though this chapter deals primarily with twin co-rotating vortices, other single and counter rotating cases are also documented. The majority of the experimental work was carried out in the 1.15m x 0.8m low speed wind tunnel. Further measurements were also conducted to detail single vortex and twin vortex parameters in the 2.1m x 1.6m low speed wind tunnel. These tests were conducted prior to single and twin vortex BVI investigations (Masson et al. (1997)). Comparison of the acquired single vortex data in the 2.1m x 1.6m with the triple-wire results of Kokkalis and PIV results of Horner is also provided.

While it is not within the scope of this thesis to investigate the detailed flow over the tip, when the tip vortex is being formed, it should be noted that there is a distinct flow field associated with blunt tipped wings. This flow field, associated with the initial formation of the tip vortex over the finite wing, is well documented by Francis & Kennedy (1979) and McInerny et al. (1990). It is highly probable that this flow field is altered in some way by the induced velocity field generated from another blade tip in close proximity (this is the configuration in the present investigation with two blade tips in close proximity).

5.2 Glasgow University's Low Speed Wind Tunnels

A comprehensive investigation of the flow field associated with a twin vortex configuration was conducted in the 1.15m x 0.8m low speed wind tunnel of the Department of Aerospace Engineering, Glasgow University (depicted in Fig. 3.1). This is an atmospheric pressure, closed return facility capable of speeds up to 33 m/s. This gives

a Mach number of 0.1 and a maximum Reynolds Number of $2.3x10^6$ per metre chord. The test section is octagonal with a length of 1.8m.

The tests undertaken prior to single and twin BVI investigations were conducted in the University of Glasgow's 2.1m x 1.6m low speed wind tunnel (depicted in Figure 5.5). This tunnel is of the atmospheric pressure, closed return type with a 2.1m x 1.6m octagonal working section. For short periods of time the wind tunnel may be operated to give a maximum velocity of 61 m/s. For continuous running, however, velocities up to 47 m/s can be obtained. This corresponds to a Mach number of approximately 0.136 and a Reynolds number of $3.2x10^6$ per metre chord. As stated in the introduction, this tunnel was the one in which Kokkalis conducted the initial triple wire vortex measurements and in which Horner documented single vortex strengths utilising PIV.

5.3 Design of Vortex Generators and Support

Previously, Kokkalis (1988) utilised a single vortex generator which generated the vortex at the juncture of upper and lower wings (Fig. 1.18). These wings were of NACA 0015 profile and mounted vertically, from floor to ceiling, along the centre line of the wind tunnel. The vertical orientation of the vortex generators was chosen to minimise the interference of the vortex generator wake with the fluid phenomena measured in the vicinity of the horizontal downstream rotor disk. Each of the aerofoils had a chord of 6 inches (0.1524 m) and a semi-span of 0.75 m. The wing was fabricated using glass-fibre around a solid aluminium spar. The two sections were joined at the quarter-chord position by a steel pin. By moving the relative angle of attack of each aerofoil section with respect to the airflow, the strength of the resulting vortex could be varied. Also, the starting position of the vortex with respect to the interacting rotor blade could be adjusted by moving the juncture vertically up or down. The maximum vortex offset that could thus be achieved was one chord length above or below the interacting blade (centreline). Hot-wire measurements, utilising triple wire probes, were conducted to determine the vortex characteristics before the BVI tests were conducted. This set-up was also used by Horner in his PIV investigations. Both sets of results (from Kokkalis and Horner) are documented in Appendix E.

In the present study, the vortex generators (designed for the 1.15m x 0.8m low speed wind tunnel) consisted of two rectangular cantilever wings of chord 0.1m - one mounted from the floor of the wind tunnel and the other from the roof (Figs. 5.1 & 5.2). The length of each wing, 0.4m, was almost half of the tunnel height at the generator location such that, when the wings were exactly aligned, they formed a near continuous vertical blade. In a manner similar to Kokkalis and Horner, a single vortex could be generated at the junction of the two wings by setting the wings at opposite incidence to each other. Similarly, twin trailed vortices could easily be produced by introducing lateral spacing of the two wings.

The wings were manufactured from wood and the base plates from aluminium. The technical drawing of this vortex generator is show in Fig. B.1. Each blade was secured to its base plate by a locking mechanism which passed through the ¼ c position of its NACA 0015 aerofoil section. The base plates were then surface mounted to the floor and roof of the tunnel. Looking upstream, the vortex generator mounted on the floor of the tunnel was positioned left of the centre-line and the top generator on the right. The base plates allowed each blade to be varied laterally from the centre line of the tunnel by approximately 1.5 chord lengths. A blade incidence variation of $\pm 12^{\circ}$could be achieved in 2° increments.

The single vortex generator, implemented in the 2.1m x 1.6m wind tunnel for the present investigation, was based on the previous one utilised by Kokkalis. Both the single and twin vortex generators implemented in the larger low speed wind tunnel were designed by Masson (1997, to be published at time of writing). The single vortex generator consists of two half wings set at opposite incidence to each other. The variation in vertical position of the intersection of the two blades was automated and the movement was increased to 1.5 chord lengths above and below the centre line of the wind tunnel (to investigate the effect of vortex separation on the BVI). In addition, the generators could be varied laterally to investigate oblique BVI (illustrated in Figs. 1.18 & 1.19). The chord length of the single and twin vortex generators was 6 inches (0.1524m) which was the same as previous BVI investigations.

The twin vortex generator implemented in the 2.1m x 1.6m wind tunnel was based on the design of the twin vortex generator implemented in the 1.15m x 0.8m wind tunnel. The

larger vortex generator, as well as being able to vary the blade incidence and horizontal spacing, also could be varied vertically. This development was included to enable the orientation of the downstream vortices to be varied. With the fixed generators in the 1.15m x 0.8m wind tunnel, with a half chord blade separation, the twin vortices would always have the same orientation at a specific downstream measurement location for a given incidence.

Figures B.3 & B.4 illustrate the general design and photograph of one of the 2.1m x 1.6m vortex generator blades respectively. Each generator consists of a glass fibre half wing complete with aluminium spar to provide sufficient rigidity to withstand the anticipated aerodynamic loads. These loads are transferred via a lead screw, guide rod and Nylatron shroud to the tunnel walls. The knurled disk, lead screw and nut provide the means to adjust the vertical position of the blade in a telescopic arrangement within the Nylatron shroud. A scale was fixed on the outside of the shroud to enable accurate vertical positioning the tip. Horizontal positioning was accomplished via a scale on the base plates with reference at the ½c aerofoil position. The incidence was set by rotation of the vortex generator about the ½c location as opposed to the ¼c on the 1.15m x 0.8m vortex generator. The horizontal and vertical movement of the blade tips is illustrated in Fig. B.5.

5.4 Calibration and Measurement

Measurements of the magnitude and associated direction of the time-dependent velocity vector were obtained using a cross-wire probe connected to a TSI IFA-300 three-channel constant temperature anemometer system. For a single cross-wire, the maximum sampling rate for this system is 400 kHz. The cross-wire probes used in this study were DANTEC 55P61 probes. The sensor wires on these probes are 5μm diameter platinum plated tungsten wires with a length/diameter ratio of 250, which form a measuring volume of approximately 0.8mm in diameter and 0.5mm in height. The wires are orientated perpendicular to each other corresponding to 45 degrees from the freestream direction which gives the best angular resolution. An additional temperature probe was used to correct the anemometer output voltages for any variation in ambient flow temperature.

The calibration of x-wire probes, for the present investigation, is detailed in Chapter 4 and the calibration procedure in Appendix A.

For the 2.1m x 1.6m wind tunnel, however, the test velocity of 47 m/s was above the maximum velocity of the calibration facility (42 m/s). Fortunately, this did not hamper the use of the calibration data for higher velocities. In these cases, the yaw calibration was conducted at the maximum velocity of the calibration facility to try and reduce any errors arising from the yaw coefficient varying with velocity. It must be emphasised that the extension of the polynomial curve fit, above the last calibration point, can result in errors which cannot be quantified. Tests were conducted prior to these single vortex measurements to investigate the extrapolation of the calibration curve. This was done by calibrating a probe up to a velocity of 30 m/s then conducting measurements at 42 m/s. The results obtained were of sufficient accuracy to have confidence in this method.

When conducting measurements at velocities higher than the maximum calibration velocity, care must be taken when setting the signal conditioner offset and gain for each channel (sensor). If the offset and gain are not altered from calibration, the results will be meaningless. Therefore, prior to any measurements, at the correct operating velocity (47 m/s), tests must be conducted to ascertain whether the signal conditioned voltage is within the $\pm$ 5V limit for the A/D converter and that the probe measurements are acceptable. If the sensor signal conditioned voltage is outwith the range (which it usually is), the value of the sensor gain must be reduced to bring the voltage within the A/D limits. The relationship between bridge voltage and signal conditioned voltage is documented in Appendix A with discussion the calibration procedure.

In order to fully determine the lateral and vertical components of velocity in both wind tunnels, the probe had to be rotated around its axis by 90 degrees to adjust the wire plane (horizontal and vertical) against the main flow direction. Thus, two traverse sweeps were necessary to obtain the vertical (u) and lateral (v) components respectively. The streamwise component of velocity was thus acquired twice but this component was strongly affected by the unmeasured velocity component which is perpendicular to the wire plane. This transverse contamination does not adversely effect the other in-plane measured velocity component (Clausen et al. (1989)) which is of primary interest.

5.5 Traverse Grid Sizes

The same traverse system was used in both wind tunnels. The primary difference between tunnels was the mounting arrangement used for the traverse in each working section and the physical size of the grids employed. In both cases the traverse grid origin was located at the centre of the working section (along the centre line). For single vortex cases in the larger wind tunnel, the height of the intersection of the blades was varied vertically and so the origin was located at the appropriate height of the intersection.

In the 1.15m x 0.8m wind tunnel, the automated two-component traverse may be mounted vertically on the wall (Fig. 5.2), or on a support structure horizontally (Figs. 5.3 & 5.4). Due to the change in orientation, the traverse co-ordinates must be transformed from a traverse co-ordinate system into a grid co-ordinate system. Only when the traverse is horizontal with the probe situated above, do the traverse and grid co-ordinates coincide and, therefore, no transformation is required.

The grid size was dependent on the position of the traverse with respect to the walls of the working section. A grid size of 100mm horizontal and 200mm vertical was attainable with the traverse in a vertical orientation. Only 100mm of horizontal travel is available with the traverse in this orientation. The grid spacing was 10mm from the centreline (0mm) up to $\pm$60mm then 20 mm up to $\pm$100mm giving 231 measurement points. Horizontally, the maximum grid size was 160mm horizontally and vertically. Measurements were conducted every 10mm and so 289 points were acquired. These grids are depicted in Fig. B.2.

For the tests conducted in the 2.1m x 1.6m wind tunnel, the traverse was mounted on a 2 inch box section beam which spanned the working section horizontally (depicted in Figs. 5.6 & 5.8). The beam was secured at each end to wooden plates which ran up the sides of the working section walls. This enabled the height of the traverse to be varied to coincide with the variation in height of the intersection of the single vortex generator. The grid size used for the single vortex measurements was 240mm by 240mm. This grid was not uniform with a 10 mm separation from the centre line (0mm) to $\pm$40mm, and thereafter

every 20mm up to ± 120mm. This non-uniform grid was used to try and increase the resolution of the grid in the region of the vortex core and gain an adequate representation of the velocity field further from the vortex core. This grid geometry resulted in a total of 289 measurement points. For the lowest vortex generator position, the traverse had to be inverted (rotated 180 degrees around the centre line of the tunnel) to acquire data (inverted traverse depicted in Figs. 5.6 & 5.7 with single vortex generator). This again meant that the traverse data in the results file had to be transformed into the standard grid co-ordinate system.

For the twin vortex tests, the grid size was 300mm x 300mm (± 150mm from centre line) with a measurement every 20mm. To obtain the usual 17 x 17 grid resolution, additional points were also taken with a horizontal and vertical traverse through the centre line of the tunnel (which corresponds to the origin of the measurement grid). The traverse is depicted in the 'upright' position in Figs. 5.8 & 5.9 in relation to the twin vortex generator.

The downstream location of the traverse was held constant in the 2.1m x 1.6m wind tunnel for both the single and twin vortex tests. This location corresponded to an x-wire probe sensor location of 7.1 chord lengths behind the trailing edge of the vortex generator. This location was chosen because it was coincident with the location of the furthest outboard location of chordwise pressure transducers on the rotating blade with the blade pointing into the flow.

5.6 Test Configurations

All flow field measurements were conducted in a cross-flow plane perpendicular to the freestream direction. The experimental procedure for each individual grid acquisition is documented in Appendix A. In the 1.15m x 0.8m tunnel, a constant freestream velocity of 30 m/s was set for all the test configurations. This gave a Reynolds number of approximately $Re=2.06x10^5$ based on the chord of the vortex generator($0.1m$). On the basis of previous studies, this Reynolds number is above the threshold below which low Reynolds number effects become significant on the NACA 0015 section. In the 2.1m x

1.6m wind tunnel, the constant freestream velocity was set at 47 m/s giving a Reynolds number of approximately $Re=4.9x10^5$ based on the chord of the vortex generator ($0.1524m$). This velocity was specified in all vortex and BVI measurements conducted by Kokkalis and Horner.

The sampling frequency for each channel was set at 2 kHz. The anemometer signals were then automatically low pass filtered at 1 kHz, to counter aliasing, before digitising. The sampling time for each point was 2 seconds which enabled a single grid traverse to be acquired in approximately 2 hours. The sampling rate and time were chosen based on the available computer-memory space and the time required to acquire a large number of measurement points. However, in turbulence measurements, 30kHz are about the highest frequency found at subsonic speeds (Bradshaw (1971)). With the present sampling criteria these higher frequency characteristics will not be captured and hence the turbulence intensity measurements could be in error. This is not crucial for the present investigation, as we are primarily interested in mean velocity components. Refer to Bruun (1995) section 3.5 and Bradshaw (1971) section 6.6 for a complete discussion of digital measurement requirements.

All the test configurations are documented in Tables 5.3-5.9. Initial tests, in the 1.15m x 0.8m tunnel, were conducted with the traverse orientated vertically (Fig. 5.2). This was sufficient for initial testing but proved inadequate for extensive downstream measurements. It was decided to opt for a horizontal orientation with a support structure for the traverse for several important reasons:

1. More downstream positions could be documented (from 0.1c to 1.0c behind the trailing edge) compared to only three downstream locations with the vertical orientation (0.25c, 0.43c, 0.6c).
2. The traverse could be easily and quickly moved between these positions (which was not the case in the vertical orientation)
3. The resolution of the grid could be increased due to less interference in the traverse motion from tunnel walls.

Table 5.3 documents the general investigations conducted in the 1.15m x 0.8m wind tunnel. Initial tests were conducted to investigate the behaviour of the vortex generators in several general configurations. These tests were conducted at two downstream positions corresponding to 2.5 and 6 chord lengths behind the trailing edge of the vortex generators. The vortex generators were also varied to generate different sense vortex rotations in both a single and twin vortex configuration. These ranged from twin co-rotating vortices to different sense single vortices and counter rotating vortices. These tests were also conducted to find the optimum configuration for the generation of vortices of the same sense and equal strength with a separation of ½ chord (50 mm) which is representative of the Vane Tip flow field. A description of the first eight general configurations is included below to expand on the tabulated information given in Table 5.4. Refer to the figure above Table 5.3 for the movement and orientation of the blades in relation to the descriptions.

Case *Description*

1. 0.5c separation between ¼c positions which corresponds to a 76mm T.E. Separation. The respective trailing edges are pointing towards the tunnel walls. Both vortices rotate in a clockwise direction when looking upstream.
2. 0.5c separation between ¼c positions with the blade in an opposite orientation to Case 1 i.e. both vortices rotate in an anti-clockwise direction looking upstream. Both trailing edges point inwards, towards the centre line. This corresponds to a 24mm trailing edge separation.
3. 0.5c separation between ¼c positions - blade Incidence 2 degrees same sense vortices (blade orientation) as configuration 1 i.e. trailing edges towards tunnel walls.
4. No separation between ¼c positions- single vortex with clockwise rotation when looking upstream. This corresponds to the figure above Table 5.3.
5. No separation between ¼c positions. Generator blades in opposite orientation to 4 corresponding to a single vortex with anticlockwise rotation looking upstream.
6. 0.5c separation between trailing edges. The trailing edges point towards tunnel walls (outwards) corresponding to a 24mm separation between ¼c locations and clockwise rotation looking upstream.

7. 0.5c separation between trailing edges. The vortex generators are in opposite orientation to 6 with the trailing edges towards centre line (inwards). This corresponds to a 76mm separation between ¼c locations and an anticlockwise rotation of the vortices.
8. 0.5c separation between trailing edges and ¼c positions. The vortices are of opposite sense with the left vortex generator generating a clockwise rotating vortex looking upstream and the right an anticlockwise vortex. Both blades have their trailing edges pointing towards the left tunnel wall when looking upstream.

Further tests were then implemented at the optimum settings which generated a 0.5c separation of vortex cores - as produced by the Vane Tip. The first study was an investigation of the variation of blade incidence conducted at 4.3 chord lengths downstream of the trailing edge. The incidence of the blade was varied in two degree increments from 2-12 degrees. These test configurations are presented in Table 5.5. One other single vortex case at 10 degrees was conducted to allow comparison with the single vortex cases carried out in the first series of tests.

After this, it was decided to try and map the complete rotation of the twin vortex flow field by conducting extensive downstream measurements. The detailed flow field measurements were conducted with the vortex generators set at 10 degrees incidence with a ½ chord separation between the ¼c locations on the vortex generators. This configuration was the optimum for the generation of the idealised flow field associated with the Vane Tip. Measurements were conducted in the cross flow plane at 0.1c and 0.5c behind the trailing edge of the vortex generators and then at 1-10 chord lengths downstream in 1c (0.1m) increments. The downstream measurement configurations are detailed in Table 5.6. As can be seen, two tests were conducted at 0.1c and 0.5c.. These were repeated due to the highly three dimensional nature of the flow field at these two locations close to the vortex generators.

Finally, in the 1.15m x 0.8m tunnel, an investigation into the effects of vortex generator blade separation was carried out. The test configurations for this investigation are detailed in Table 5.7. Blade separation was varied from 0c to 1c every ¼ c with the downstream measurement location set at 4 and 8 chord lengths from the trailing edge.

These tests were conducted to detail the effect of vortex generator separation with respect to actual vortex separation at the two specified measurement locations. The measurement locations were chosen on the basis of the results of the detailed downstream investigation previously detailed.

The tests conducted in the 2.1m x 1.6m wind tunnel consisted of both single and twin vortex measurements. The single vortex measurements were conducted to investigate a discrepancy that was evident between the initial triple wire measurements conducted by Kokkalis and the PIV data obtained by Horner and to verify that the new single vortex generator was functioning properly. The vortex generator sections were set to incidences of 2.5-12.5 degrees in 2.5 degree increments. These settings were chosen to coincide with the measurements conducted by Kokkalis and Horner. The test configurations for the single vortex measurements are documented in Table 5.8.

The twin vortex measurements conducted in the 2.1m x 1.6m wind tunnel are documented in Table 5.9. Reference should be made to Fig. B.5 for the horizontal and vertical movement of the vortex generators. It must be remembered that the twin vortex generators pivot about the ½c location. This causes difficulty when trying to keep the ¼c separation constant with variation of blade incidence. As the blade incidence is increased the two generators have to be moved horizontally outwards to keep the ¼c separation constant.

5.7 Two-Dimensional Numerical Model

As with all measurements in vortex flows, a consistent method must be used to determine the relative parameters of the flow field. Previous investigations have utilised an analytical vortex model to curve fit the two dimensional tangential velocity component. These models are usually derived from fixed wing studies. This is perfectly satisfactory for single vortex configurations but when dealing with two vortices, which are closely spaced, the tangential component of velocity varies significantly between the cores. The two primary factors for determining the vortex strength, core size and maximum (tangential) velocity, are difficult to predict when dealing with a discretised grid. Measurements may

not provide values for the maximum velocity and so underestimate the vortex strength and overestimate core size.

The immense complexities associated with concentrated vortices have prevented the derivation of a theoretically rigorous vortex model which describes the phenomena in every respect. For this reason several empirical formulae for the tangential velocity have been used by many to study different aspects of concentrated vortices. The best known among these are the Rankine, Scully and Lamb-Oseen models (Chapter 2). In this present study, the Scully model was chosen due to its common use in curve fitting (fixed wing) experimental single vortex data.

As a prerequisite for the numerical model, initial values for the position (x and y co-ordinates), core size (r_c) and vortex strength (Γ) must be specified for the two vortices. These parameters are then altered to obtain a suitable fit for the majority of the horizontal and vertical mean velocity components acquired experimentally. Two sets of experimental data (one for each in plane velocity component) are fitted to one set of numerical data. There were slight differences between the two separately acquired components in some configurations (as can be seen from Fig. 5.3). This was primarily due to vortex meander and probe interference. In some cases, however, this proved insignificant compared with the discrepancies attributable to the highly three-dimensional nature of the flow field. Outside the cores, the two wake structures from the vortex generators were dominant flow features. These errors were localised to specific regions of the grid for the vertical (u)velocity component when measurements were conducted close to (<5c) the generator blades. An adequate curve fit to both sets of data (u,v) could, however, be determined from the horizontal component of velocity (v).

Each of the Scully vortices induces a tangential velocity component on each of the discrete grid points. At these points the tangential velocity from each vortex is decoupled into the appropriate grid horizontal and vertical velocity components which are then superposed. The numerical model grid and experimental grid are of the same dimensions which enabled a direct point for point comparison to be conducted. The calculation of the tangential velocity can be expressed by,

$$u_\theta = \frac{\Gamma}{2\pi r} \cdot \frac{r^2}{r^2 + r_c^2}$$

In this case, to calculate the induced velocity from vortex 1 at a specific grid location, the parameters which are required as input to the numerical model are vortex strength Γ_1, vortex position x_1, y_1 and vortex core size r_{c1}, therefore,

$$u_{\theta 1} = \frac{\Gamma_1}{2\pi r_1} \cdot \frac{r_1^2}{r_1^2 + r_{c1}^2}$$

where r_1 is the radial distance between the specified grid point and the position of vortex 1 expressed by,

$$r_1 = \sqrt{(x_G - x_1)^2 + (y_G - y_1)^2}$$

The angle between r_1 and the horizontal axis is

$$\theta_1 = \tan^{-1}\left(\frac{x_G - x_1}{y_G - y_1}\right)$$

and therefore the horizontal and vertical grid velocity components induced by vortex 1 are,

Horizontal component of velocity $v_1 = u_{\theta 1} \sin(\theta_1)$

Vertical component of velocity $u_1 = u_{\theta 1} \cos(\theta_1)$

The same calculations are carried out for vortex 2 to obtain the horizontal and vertical velocity components induced by vortex 2. The induced velocity components are then summed to give the final total horizontal and vertical velocities at each grid location.

$$v = v_1 + v_2$$

$$u = u_1 + u_2$$

It must be remembered that this derivation is done in a grid co-ordinate system with the x co-ordinate and u velocity in the vertical direction as depicted in Figure B.2. Also, the above equations for the components of velocity represent a means of determining the velocity magnitude. Specific conditions must be set to avoid singularities when using the

trig function tan and also to determine the appropriate sign of the horizontal and vertical velocities before summation for the total velocity at a specific grid point. These signs are dependent on the sign of the initial vortex strength Γ and the relative position of the grid point in relation to the vortex ($x_G - x_1$ and $y_G - y_1$).

These numerical model results can be directly compared to the two measured in-plane velocity component obtained from the experimental data. By analysing the two in-plane components separately, any flow field features and errors in experimental measurements can be easily determined. This technique surface fits two sets of experimental data (grid u and v velocity components) to one set of input parameters from the numerical model. Any major discrepancy in vortex position between the two sets of experimental data is highlighted with this method.

Once the fitting parameters had been obtained for all the experimental data in the cross-flow plane, a quasi three-dimensional adaptation was used to predict the rotation of the vortex system as it travelled downstream. This model utilised a 2nd order Adams-Bashforth multi-step integration based on the two velocity components induced at each vortex location. In this scheme, data from a measurement plane close to the vortex generator (determined from the 2D numerical model) was used as initial conditions for the 3D model. By consideration of the induced flow field it was then possible to apply the technique to predict the orientation of the vortices further downstream. This proved successful with errors primarily arising from the interference effect of the traverse and the time dependant change in vortex size and strength. This quasi 3D model provides an ideal solution to the inviscid flow where the vortex size and strength does not vary with time. Unfortunately, the vortices do not behave as the inviscid analysis predicts and the effects of turbulence and vortex diffusion/dissipation (change in core size) must also be considered.

5.8 Results

The complete set of results, as determined from the numerical model, are presented in Tables 5.10-5.15. These tables document the vortex strength(s), two-dimensional grid co-

ordinates and the vortex core size(s) and are related to the previously documented test configurations. Results are presented for both single and twin vortex data for both the 1.15m x 0.8m and 2.1m x 1.6m wind tunnels. The latter set of single vortex data represents the same configurations as tested by Kokkalis and Horner. Their triple wire and PIV results, for the single vortex configuration, are presented in Appendix E.

Only a few representative figures for individual cases are presented in this thesis. These illustrate the main features of the flow field associated with the vortex generators and the success of the simple 2D and 3D numerical models. Compiled information from a number of measurement grids are also presented in graphical form to illustrate the downstream (time dependent) progression of the twin vortex system.

Figures R5.1-R5.4 illustrate the vector plots, mean cross flow velocity components, axial velocity and turbulence intensity/shear distribution for a representative single vortex configuration, Case 17. This case was conducted at a measurement location of 4.3c aft of the trailing edge with the vortex generators set at an incidence of 10 degrees which generated a clockwise rotating vortex when looking upstream. The (streamwise) turbulence intensities are directly comparable even though they represent two independent tests. The first shear stress distribution is for the horizontal plane and the other the vertical. There should be a third shear stress component for a three-dimensional flow for the cross-flow plane, but this requires the simultaneous measurement of the two cross flow components which cannot be done with the x-wire probes. Only reference to the general distribution of the turbulence intensity and shear stress is made and not to specific values.

Figures R5.5-R5.8 represent the same plots for the representative flow field associated with a twin vortex configuration, Case 42. This case represents the configuration adopted to mimic the Vane Tip vortex flow field. The measurement position was 4c downstream with the blades orientated at 10 degrees incidence with a 0.5c separation between ¼c aerofoil locations. The trailing edges pointed towards the tunnel walls thus generating two clockwise rotating vortices when looking upstream.

Figures R5.9 & R5.10 represent Case 26 and show the in-plane velocity components and the axial velocity components respectively associated with the closest measurement

location to the vortex generators (0.1c behind the trailing edge). In Fig. R5.9, the in-plane velocity components are compared to the numerical model. In Fig. R5.10 the two measured axial velocities are compared. The first axial velocity measurements were conducted with the horizontal orientation of the sensors (measuring in-plane v-velocity component) and the second with the vertical orientation of the sensors. Figures R5.11 & R5.12 correspond to a Case 27 with a 0.5c measurement location.

Figures R5.13 & R5.14 correspond to vector plots of Cases 1 & 9 respectively. They illustrate the general rotation of the twin co-rotating vortex system between downstream measurement positions of 2.5c to 6c. In Figs. R5.15 & R5.16, corresponding to Cases 8 & 16, the downward convection of a twin counter-rotating vortex system is illustrated again between 2.5c and 6c downstream measurement positions.

Figure R5.17 represents a summary of the first six twin vortex configurations conducted. In these cases the locations (x,y co-ordinates) of the vortices, for 2.5c and 6c downstream measurement positions, are plotted for the same generator settings. A prediction of the location of the two vortex positions at 6c, from the quasi 3D numerical model, is included with input parameters obtained from the experimental results at 2.5c. The single vortex tests are omitted because there was very little change in vortex position between 2.5 and 6c and Figs. R5.1-R5.4 give an accurate representation of this configuration.

The graphs depicted in Figs. R5.18-R5.20 illustrate the effect of the variation in generator incidence on the vortex strength, vortex separation and core size respectively. In these cases, the blade 1/4c separation was held constant at 0.5c and measurements conducted at 4.3c downstream of the trailing edge. This corresponds to Cases 18-23 in Tables 5.5 & 5.11.

The graphs depicted in Figs. R5.21-R5.24 illustrate the detailed downstream investigation conducted for the optimum setting for the generation of the idealised flow filed associated with the Vane Tip. The generators were set at an incidence of 10 degrees with a 0.5c separation between 1/4c chord positions. Figure R5.24 compares the vortex positions obtained from the experimental data (via the 2D numerical model)with the quasi three-

dimensional numerical model with input parameters taken from experimental data at 2c downstream of the trailing edge.

Figure R5.25 represents a graph of the variation in generator ¼c separation to vortex cores separation at 4c and 8c downstream measurement locations. Figs. R5.26-R2.28 illustrate the comparison between the 8c experimental locations and the 8c predicted locations from the 3D numerical model with input parameters from the 4c experimental data. The single vortex case is omitted and also the 0.25c blade separation due to vortex merging which has occurred by the 8c measurement position. The 3D numerical model cannot predict this behaviour.

Figures R5.29-R5.30 depict a comparison of two experimental configuration with the same generator settings and downstream measurement locations. The comparison is between Cases 31 & 42 and shows a good level of agreement between two different sets of experimental measurements. There was approximately a five month interval between these cases.

The vorticity calculations (documented previously) were only performed for the variation in downstream measurement positions (Figs. R5.31-R5.42) and the variation in blade separation (Figs. R5.43-R5.52) due to the constant grid spacing which was used in these investigations. Two other vorticity figures (R5.53 & R5.54) are presented to illustrate twin counter-rotating vortices. The calculated experimental streamwise vorticity values were directly compared to the numerical model streamwise vorticity calculations which could be determined from the relevant cross-plane (grid) velocity records. The calculation procedure was the same for both numerical model and experimental results and was documented previously. The vorticity results depicted in the figures are in dimensional form (sec^{-1}) and can be made non-dimensional by multiplying by wing half-span(0.4m) and division by tunnel freestream velocity (30m/s).

Figures R5.55 and R5.56 are representative of a single vortex case conducted in the 2.1m x 1.6m wind tunnel. These figures, which show velocity vector plots and individual components of velocity respectively, represent Case 1 in Tables 5.8 & 5.14 and depict the comparison of the 2D numerical model with the experimental data. This case has the

vortex generator intersection positioned at the centre line of the tunnel with an incidence of 12.5 degrees. This case is directly comparable to the data obtained by Kokkalis (Fig. E.4) and Horner (Fig. E.6). All the other single vortex cases show the same general velocity distributions and give the same excellent correlation between the 2D numerical model and experimental data. These configurations are only discussed in reference to the determined vortex strengths and core sizes. The 7.1c measurement plane is significantly downstream to convect the wake outwith the measurement plane and so is undetectable. At lower incidences the wake does become apparent in turbulence intensity plots due to the lower induced velocities which convect the wake across the measurement plane. Similar distributions for the turbulence intensity and shear distributions were obtained for the 2.1m x 1.6m single vortex cases when compared to the 1.15m x 0.8m single vortex cases. Generally, these consisted of an increase in turbulence intensity in the wake and core regions and shear stresses in the cores region only (illustrated in Fig. R5.4).

Figure R5.57 (Case 8) has the same generator configuration as Case 1 but the traverse has been inverted (Fig. 5.6). This was done to investigate the obvious offset in the location of the vortex above the centre line as seen in Fig. R5.55. By completely inverting the traverse and keeping the generator in the same orientation the interference effect should now be in the opposite direction. The interference effect in Case 1 resulted in an upward movement of the vortex and correspondingly in Case 8 there is a corresponding downward movement due to the re-orientation of the traverse support. From this, it can be concluded that if the traverse was not present the vortex would approximately convect along the centreline of the tunnel.

The twin vortex results obtained for the 2.1m x 1.6m showed the same representative velocity distributions as depicted previously in the 1.15m x 0.8m wind tunnel, the only difference being the increase in the relative magnitudes of the velocities. The complete twin vortex results are depicted in Table 5.15. Figure R5.58 illustrates the variation in vortex separation with blade incidence. In Fig. R5.59, the positions of the vortices are chown for the different incidence cases.

Figure R5.60 illustrates the change in vortex strength with a variation in generator incidence. The graph depicts both the single and twin vortex strengths. The twin vortices

were of equal strength and so there is only one line corresponding to both vortices. The variation in vortex strength with incidence is linear for both the single vortex and twin vortex cases. In Fig. R5.61, the variation in core size with respect to variation in incidence is plotted for both the single and twin vortex generators. As can be seen, the core radius is virtually invariant with incidence for both the single (0.023m) and twin vortex (0.018m) cases.

Figure R5.62 shows the comparison of the present vortex strength measurements with the data obtained by Kokkalis and Horner. The vortex strengths are plotted with respect to a change in incidence and very good correlation is obtained between the present study and the Kokkalis data presented in Figs. D.1 & D.2 up to 7.5 degrees. However, there are significant differences at 10 and 12.5 degrees. The line represents the linear fit to the data depicted in Fig. R5.60. In Fig. R5.63, comparison of the core size is presented for the present study and the data obtained by Kokkalis.

5.9 Discussion

Comparisons of the experimental data with the numerical model are provided in the vector plots (Figs. R5.1,R5.5,R5.13-R5.18), and the velocity surface plots (Figs. R5.2,R5.6,R5.9 & R5.11) for the 1.15m x 0.8m tunnel. Figure R5.5 depicts the flow field associated with the optimum configuration to produce a similar flow to that generated by the Vane Tip. In this case, each vortex generator was set at an incidence of 10 degrees with a 0.5c separation between the ¼ c locations of the aerofoils. The vector plots are shown looking upstream and clearly illustrate the level of correlation between the experiment and numerical model. The vortex parameters were obtained from the numerical model. These correspond, for position 1 in Fig. R5.5 (where the vortex originates from the lower vortex generator), to a strength of 0.95 m^2s^{-1}, vertical position x=0.03m and horizontal position y=-0.01m and, for position 2, a strength of $1.0m^2s^{-1}$ at x=-0.017m, y=0.012m. Both vortices have a core radius of 0.01m.

The axial velocity flow field is dominated by the development of the velocity deficit resulting from the generator boundary layers close to the blades and dissipates with

downstream position (Figs. R5.3,R5.7,R5.10,R5.12). The increase in the axial velocity in the core is characteristic of transverse contamination. This effect is due to the increasing component of velocity perpendicular to the sensor plane, which is not measured, increasing the cooling on the sensor. This corresponds to an increased effective velocity and so results in the increased axial velocity. The only discussion found on transverse contamination was by Clausen et al. (1989) and stated that the velocity components orthogonal to the probe axis (the cross-flow velocity components of interest here) were hardly altered by this effect. The general distribution of axial velocity is consistent in the single and twin vortex cases for both tunnels. Also, the increase in turbulence intensity in the wake and core are general characteristics which are common among all cases. The localisation of the two shear stress components to the core region is also a common feature among all configurations.

As can be seen from Fig. R5.7, there is a lack of geometric repeatability with respect to the highest axial velocities. However, in Fig. R5.8 the points representing the highest turbulence intensity readings are very similar. Vortex 1 at X=-20mm, Y=10mm and vortex 2 at X=30mm, Y=-10mm. It is possible that changes in the atmospheric conditions have affected the axial velocity readings during acquisition. The tunnel is prone to a significant temperature increase when running which does alter the test conditions throughout the 2 hour acquisition time. Another possibility is that the two vortices are not stable – they may oscillate. This, however, cannot be proven with the present data.

With a single finite wing, it is expected that the vortex will roll up inboard of the tip. However, in the twin vortex configuration documented here, the second vortex induces a velocity which acts against this inboard motion. When the trailing edges of the blades are oriented towards the centre line (reversing the sense of rotation) the induced velocities are in the same direction as the inboard roll-up.

When consideration is given to the movement of the wake from the vortex generators, a configuration with the trailing edges oriented towards the tunnel walls results in the wake being convected away from the centre of the tunnel. Correspondingly, the wake is convected toward the centre of the tunnel and the other vortex when the blades are oriented towards the centre-line. For BVI investigations it is inadvisable to have the wake

structure convecting across the interacting plane as this may have a significant effect on the BVI event.

As can be seen from the figures, there is a significant variation in the u velocity magnitudes (Figs. R5.9,R5.11). This discrepancy is evident for two localised regions in the complete grid (Y=-80 to 80mm) and is due to the momentum deficit in the wake behind each generator. The region does grow, due to the reduction in velocity when moving away from the core. All the regions of positive x and positive y co-ordinates corresponding to a location on the right and above the centre line. This is the region of the upper vortex generator. A corresponding effect is noted in the measurement plane for the lower generator.

The v-component is not as adversely affected by the generator wake and so the strengths of the vortices, in this case, were determined from the v-components. In Fig. R5.9, at 0.1c aft of the trailing edge, the wake affects both components of velocity. At 0.5c aft of the trailing edge, Fig. R5.10, the wake affect is not apparent in the v-velocity surface plot but is still highly visible in the u-velocity component. The general distribution of velocity through the vortex cores, and in the irrotational region outwith the cores, is very good. The interference problem with the wake reduces with increasing distance from the generator due to viscous diffusion and convection out of the measurement plane from the induced vortex velocities.

It should be noted that when surface fitting the two components, initially the vortex strength is varied to obtain the correct irrotational velocity magnitudes and then the core size is varied to alter the velocity gradients for each core. The curve fit is highly sensitive to the vortex position (x,y co-ordinate specification) but not to vortex strength.

In Fig. R5.18, the vortex strengths produced by each blade of the generator are plotted against blade incidence setting. As may be expected from the Kutta-Joukowsky theorem, the strength was found to vary linearly with incidence at moderate incidence settings. There was, however, a consistent difference between the strength of the vortices trailed from each blade of the generator. This was apparently due to flow angularity in the test section of the wind tunnel.

Figure R5.19 depicts the variation in vortex core separation with respect to blade incidence. The graph shows an almost linear relationship with the vortices moving closer together as the incidence is increased. This relationship initially appears surprising since the increase in blade incidence also corresponds to an increase in trailing edge separation. For example, a blade incidence of 2 degrees corresponds to a separation of 0.552c between trailing edges and a blade incidence of 10 degrees a separation of 0.76c. Obviously, the initial development of the twin vortex system cannot be considered purely on the basis of the generator geometry. Consideration must also be given to the fluid dynamic behaviour at the two wing tips.

As the blade incidence is increased, there is a corresponding increase in mass flow over the blade tips. On a single finite wing, this has the effect of moving the vortex roll-up location in-board and slightly raising the height of the core above the trailing edge. In the present case, the situation is complicated by the inevitable confluence of the two wing-tip flows. It has been established that one consequence of this is a reduction in the inboard movement of the tip vortices due to the induced effect of one tip vortex on the other. Given this behaviour, momentum considerations would suggest that this should be accompanied by an increase in the distance between the vortex and the suction side of the trailing edge in the direction normal to the chord line. Further, it would be expected that this distance would progressively increase with blade incidence in a manner which is consistent with the results of Fig. R5.19. Also, there is an initial inward convection of the vortices between 0.1 and 2 chord lengths downstream of the trailing edge which is illustrated in Fig. R5.24. This was detailed for one incidence case only, where the blades were at 10 degrees incidence with a separation of 0.5c. It is possible that this inward convection is related to vortex strength and hence incidence. If the incidence is reduced there should be a reduction in the inward convection and so an increase in vortex separation as shown in Fig. R5.19.

In Fig. R5.20, the variation in core size with incidence is presented. It may be observed that, over the incidence range considered in this study, the core size was found to be insensitive to the blade incidence setting. This result is interesting, when taken together with Fig. R5.21 which documents the growth of the core radius with downstream position. Clearly the rate of growth is approximately linear with a core radius of 0.004m (0.04c) at

0.1 chords behind the trailing edge growing to 0.017m (0.17c) at 10 chord lengths downstream. It is interesting to note that these two results suggest that regardless of blade setting, the growth of the vortex cores will be linear and the size of the core will be consistent with Fig. R5.21. It is inevitable that the test Reynolds number will influence the core size and its rate of growth. Nevertheless, the result presented above has implications for wind tunnel based BVI tests which aim to reproduce core sizes of equivalent non-dimensional scale to those anticipated at full scale. Clearly, the distance between the point of generation and the interaction location must be chosen carefully. The linear variation in vortex strength with incidence and the invariant nature of the core size is discussed later with comparison of the single vortex data acquired in the 2.1m x 1.6m tunnel.

In Fig. R5.22, the variation in vortex separation distance with downstream measurement position is shown. There is an initial reduction of the core spacing from just over 0.06m to approximately 0.05m within 2 chord lengths. Further downstream the core separation varies slightly and this can be attributed to the interference effect of the horizontally mounted traverse. This interference effect causes the vortex, which is convected downwards (towards the traverse), to be forced toward the other vortex and so reduce the spacing. This occurs when the vortices are vertically oriented to one another between 5c and 6c downstream. Subsequently, as the vortices convect horizontally away from each other the spacing increases before returning to the general downward trend of the curve. Nevertheless, this apparent reduction in the separation distance is very slow and the vortices maintain their approximate ½ chord spacing throughout the graph.

Figure R5.23 illustrates the growth in vortex strength with downstream position. Here, there is an initial growth in vortex strength up to approximately 4c. This corresponds to the growth in core size downstream illustrated in Fig. R5.21. This behaviour is due to the vorticity from the wake rolling up into the vortex. After 4c, however, the cores are fully rolled up and the core strength remains constant whilst the core radius continues to increase. This is associated with a redistribution of vorticity within the core, through diffusion, resulting in an enlargement of the core radius.

As may be observed in Fig. R5.25, the variation of vortex separation with generator blade spacing is approximately linear when measured at 4 chord lengths downstream. However,

at 8 chord lengths, there is a dramatic change in vortex separation distance for 0.25c blade separation case. The behaviour illustrated for the 0.25c blade separation case is indicative of vortex merging. Rossow (1977,1987) documented that vortex merging is dependent primarily on vortex core diameter and vortex separation distance. When the ratio of separation distance to vortex core diameter is approximately 1.9 the two cores will merge downstream to form one vortex.

Based on the core radius documented in Fig. R5.21 for 4c, the ratio of core separation (0.025m) to core diameter (0.018m) is approximately 1.4 and the vortices, at this location, should be in the process of merging as this value is below the threshold for vortex merging to begin. At 8 chord lengths downstream the vortices are virtually completely merged and so the rapid formation of the single vortex agrees with the Rossow condition.

There is a slight discrepancy between the vortex separation depicted in Figs. R5.22 and R5.25 for 8 chord lengths downstream, 0.5c blade separation. The discrepancy results from the difference in individual vortex positions, which is less than 2mm. These two investigations were conducted independently. In Fig. R5.22, the blades were set at the required incidence and spacing and not altered when the downstream investigation was conducted. However, in the blade separation investigation (Fig. R5.25) the blades were altered significantly between individual measurements which may account for this slight discrepancy.

In Figs. R5.26-R5.28, a comparison of the 8c experimental locations and the 8c predicted locations are provided for ¼c blade separations of 0.5, 0.75 and 1.0c respectively. The predicted values were determined from the 3D numerical model with input parameters obtained from the 4c experimental data (which are also depicted). Once again, the three dimensional model provides a good approximation of the location of the vortices. The quasi-3D numerical model could not be used to predict the vortex locations in the 0.25c blade separation case to the vortices merging at the 8c downstream measurement position.

In Fig. R5.24, the spacial evolution of each vortex is plotted with respect to the centre line of the tunnel (looking upstream). The figure illustrates a significant initial inward convection of the two vortices with a slight rotation before the vortex assumes the typical

full rotational behaviour expected. This inboard convection is consistent with the reduction in core separation with increasing blade incidence discussed in relation to Fig. R5.19. Also illustrated in this figure, is a comparison between the experimental vortex trajectory and that predicted from the quasi three-dimensional numerical model. The initial inputs to the model were the vortex strength, position and size determined from experiment at two chord lengths downstream. This is the first position which is outwith the initial inward convection region.

At two chord lengths the vortex has not completely rolled up and so the vortex strength is slightly underestimated. This reduced strength of the vortices was investigated by using input parameters at 3 and 4 chord lengths downstream for comparison with the case presented. No appreciable difference was noted. As can be seen from the figure, vortex 1 follows the theoretical trajectory very well and the predicted locations up to 7 chord lengths are satisfactory. However, the cross-flow velocities recorded at nine and ten chord lengths downstream were low and the vortex cores were particularly diffuse. This made accurate determination of the x-axis (horizontal) core locations very difficult.

The trajectory of vortex 2 is, unfortunately, significantly different from that predicted by the numerical model. In these experiments, the traverse was oriented horizontally and rested below the centre line of the wind tunnel. It is believed that vortex 2 was influenced by a vertical velocity component created by the blockage of the traverse which, on the right of Fig. R5.24, acted against the induced velocity from vortex 1 and correspondingly acted with the induced velocity on the left. This is the most stringent test of the quasi three-dimensional numerical model and despite the interference effect of the traverse the position of the vortices is well predicted.

Figures R5.29 & R5.30 provide a comparison of similar cases which were conducted during different investigations (Cases 31 & 42). They clearly show that the approximate locations between these cases are good, with errors arising primarily from the curve fit of the experimental data and slight differences in blade geometry between the different investigations.

Figures R5.31-R5.54 illustrate the vorticity plots for the investigations of the downstream measurement positions and the blade separation. It was found that after excluding all

vorticity below a value of 50 sec^{-1} (non-dimensional value of $\frac{2}{3}$), and applying the same scaling factors to all the figures, a low vorticity redistribution path emerged which apparently is the highway along which vorticity is transported. Maximum calculated values of vorticity were in the core region with the peak values located at the centre of the vortex. This is also depicted in the cross flow velocity component and evident in the turbulence intensity distributions with an increase in both the wake region and the vortex core. However, the vorticity plots are significantly better at depicting the spacial evolution of the flow field and so the majority of these plots are included in this thesis. The plots also depict a comparison of the calculated vorticity for the two-dimensional numerical model data and the acquired experimental data. The surface plots are included to illustrate the reduction in peak vorticity resulting from a redistribution due to the increasing core size. The contour plots depict the vorticity confined to the wake (which is not easily determined in the surface plots) and illustrates the wakes convection across the measurement plane under the induced velocities of the vortices. Once again, excellent correlation between the numerical model and the experimental data is evident. The two final vorticity figures represent the counter rotating vortex cases. Figure R5.53 represents an upward convection of the two vortices under their mutual induction and Fig. R5.54 represents the opposite case (opposite sense vortices to Fig. R5.53) with a downward convection.

The single vortex velocity measurements conducted by Kokkalis were taken by means of a triple hot-fibre probe traversing 0.8c (0.12m) either side of the vortex centre. The data presented in Appendix E consists of the calculated tangential velocity and the estimated vortex strength and core size. The variation of the normalised tangential velocity profile across the vortex core, for the various angles of incidence, is shown in Figures E.4-E.8. The estimate of the vortex characteristics were determined by means of a Scully model. However, for the calculation of these characteristics, a transformation was applied to the measured velocities in a Cartesian frame, to a cylindrical one for direct comparison with the tangential velocities determined by the Scully model. This differs from the approach adopted in the present investigation which employs a transformation of the Scully model (tangential velocity) into Cartesian co-ordinates. A representative curve fit is depicted in Fig. E.4 for a generator incidence of 12.5 degrees (corresponding to δ=25°).

The vortex strengths for the various differential angles of incidence were evaluated by assuming axial symmetry of the vortex and that the tangential velocity profile was represented by Scully's model. The resultant variation in vortex strength with incidence is shown in Fig. E.2 which also details the variation in non-dimensional vortex core diameter with incidence. The core radius was defined as the position where the tangential velocity reached a maximum.

In Fig. E.2, it is evident that the vortex strength did not vary linearly with incidence. Also, the core radius decreased as the generator incidence was increased. Both of these trends are in contrast to those observed with vortices generated from a single semi-span wings as well as those expected from theory. As the angle of incidence is increased the increase in the lift generated is expected to result in an increased vortex strength. McCormick et al. (1968) states that the circulation of the core radius is a constant fraction of the vortex strength and that the normalised tangential velocity is linearly proportional to the lift coefficient. In the experimental investigation of Orloff et al. (1973) and Chigier et al. (1971) it was found that the maximum tangential velocity increased linearly with respect to the angle of incidence with no significant change in the core radius.

Figure E.3 presents the maximum values of the normalised tangential profile as documented by Kokkalis. This figure is somewhat redundant given the previous information (vortex strength and core size). If the core radius were invariant with incidence and there was a linear relationship between vortex strength and incidence (as shown in the 1.15m x 0.8m wind tunnel tests), the corresponding relationship between peak tangential velocity would also vary linearly. Also, when conducting vortex measurements at discrete points in the flow, the peak tangential velocity may not be measured (see beginning of Section 5.7). Kokkalis states that the non-linear variation in the maximum tangential velocity may be attributed to the increased interference from one aerofoil section of the vortex generator on the other particularly as the incidence decreases.

Figures R5.62 & R5.63 show the comparison of the present data with that obtained by Kokkalis and Horner. The present data and the Kokkalis data have virtually the same vortex strengths up to 7.5 degrees. At 10 and 12.5 degrees, the values determined by

Kokkalis for the vortex strengths are higher than the present linear approximation and it is believed that these two measurements are in error. These errors would explain the non-linear behaviour documented above. In Fig. R5.63, the core sizes are plotted for the present data and the Kokkalis data. The core sizes are similar but the present data indicates that the core size is invariant with incidence. This does not corroborate the general decrease in core size with increased incidence as seen in the Kokkalis data. There is extensive data from the twin vortex tests (in both tunnels) which also show linear variations in vortex strength with incidence and an invariant core size with incidence which suggests that the present measurements are more reliable than the study conducted by Kokkalis. It is evident that the characteristics stated in the present studies in both wind tunnels agree with the previously documented findings (of McCormick et al.(1968), Orloff et al.(1973) and Chigier et al.(1971)).

There are considerable questions to be asked when interpreting the Kokkalis data. The measurements were taken with no documented reference e.g. tunnel wall or centre line. The traverse and support used were also not documented. The positions of specific measurement locations were not detailed (but they can be calculated from Fig. E.4). A documented grid size of 5 vertical and 31 horizontal locations was used but the location of the origin in respect to the vortex generator intersection is unknown. The procedure for the calibration of triple wire probes was omitted but it appears that calibration information, for the DANTEC 55P91 probes, was supplied by the manufacturer.

Horner re-interpreted the original triple wire data supplied by Kokkalis and calculated that a significant reduction in the circulation strengths of the single vortex at each incidence was warranted. Horner stated that the strengths should be 0.6, 1.1, 1.7, 2.6 and 3.4 m^2/s respectively. This is depicted in Fig. R5.62 in comparison with the present data and Kokkalis's data. No reason was given to why the vortex strengths were changed. Horner also measured the vortex using PIV. These data are plotted in the form of a velocity map depicted in Fig. E.5. The tail of each vector represents the measurement location and the length and directional orientation are representative of the velocity magnitude and direction respectively. The scale is in millimetres with an arbitrary origin at the top left negative edge.

The isolated interaction vortex velocity distribution is shown in Fig. E.6 which corresponds to the velocity vector data depicted in Fig. E.5. Only one core size (25mm) was documented by Horner for an incidence of 12.5 degrees which was determined from Fig. E.6. On consideration of this figure, the core size could be anywhere from 20mm to 26mm which represents the two lines in Fig. E.6. The results obtained in this study (Fig. R5.61) show the core size to be approximately 0.023m and invariant with incidence. This corresponds almost exactly to the centre of the region bounded by the two vertical lines in Fig E.6. Therefore, a better approximation for the core size of Horner's data would by 23mm instead of 25mm. In Fig. 5.63, this value agrees with the present data rather than the Kokkalis data.

Outside the core, the tangential velocity is seen to decrease. Figure E.7 represents a subset of these data and shows the velocity distributions taken from those points in Fig. E.5 that lie within 10mm of a line emanating from the vortex centre to the right. This simulates a horizontal traverse of the vortex velocity field from the vortex centre. The line overlaid on the point data, represents that which is expected for an ideal potential vortex (Biot-Savart law) with a circulation of 3.4 m^2/s, Horner's documented vortex strength. As can be seen the strength of the potential vortex underestimates the PIV data.

It appears that Horner assumed that since the line (potential representation from Biot-Savart Law for a strength of 3.4 m^2/s) passed through the maximum tangential velocity location, the vortex strength was correct. This is, unfortunately, not the case and, the potential vortex model should have been curve fitted to the mean value of the tangential velocity data depicted in Fig. E6. If the core is taken as 23mm and the peak tangential velocity is estimated at approximately 20 m/s then, from the Scully model, the vortex strength can be calculated as 5.78 m^2/s. Based on this vortex strength and core size the induced velocity, at a radial location of 100mm from the vortex centre, is 8.73 m/s which is significantly better than the 5m/s represented in Fig. E.7. If this core model, with a vortex strength of 5.78m^2/s, was plotted onto the tangential velocity data in Figure E.6 the line would approximately lie on the mean line of the tangential data. This gives a higher vortex strength, which also corroborates the values (at lower incidence) determined by Kokkalis. The relative magnitudes of the Horner data and the velocity data depicted in Fig. R5.56 are in agreement with a maximum of approximately 20 m/s. Also, for the

above discussion of the curve fit of the PIV data, the determined vortex strength on 5.78 m^2/s is almost exactly the same as the vortex strength determined for the present data, $5.8m^2/s$ (from Fig. R5.56). A comparison of the Scully model and Biot-Savart law with a vortex strength of $5.8m^2/s$ (from re-interpreting the PIV data (Fig. E.6)) and Horner's curve fits representing a vortex strength of $3.4m^2/s$ and $5m^2/s$ is presented in Fig.E.8.

There are significant difficulties in discussion of the twin vortex measurements conducted in the 2.1m x 1.6m wind tunnel. Since there is no information regarding the formation and development of the vortex system from the generators due to the single measurement location, the results only discuss the relevant positions of the vortices and not which generator they originated from (as with the 1.15m x 0.8m results).

There are, unfortunately, also problems with the acquired data. The interference effect of the traverse proved more significant in these cases than the single vortex cases. As can be seen in Table 5.15, there are discrepancies between the positions of the vortices as determined from the horizontal and vertical velocity components (Cases 18 & 20) due to the interference from the traverse support which seems to have an inconsistent effect in these cases. The results for the vortex strengths and core sizes are good and consistent with the incidence variation depicted in Figs. R5.60 & R5.61 but the vortex locations are in considerable error. This positional error cannot be documented or quantified as in the single vortex case due to the different locations of the vortices for each of the configurations. A further study, with a different traverse structure, would be required to address these problems.

Cases 15 & 16 are however still interesting despite these problems. In the previous 1.15m x 0.8m investigation with a 0.25c separation between the ¼c locations of the generators, the two vortices have virtually merged at 8c downstream (Fig. R5.25). In Case 15 vortex merging is also nearly complete at 7.1c downstream, however, the blades are separated vertically by 0.25c instead of horizontally. The generation of the vortices may, possibly, be altered compared to the horizontal separation case due to the different induced velocities which would be experienced. Case 16 shows the 0.25c horizontal separation and the vortices are still distinct. This is not surprising due to the considerable difference in the Reynolds number in the 2.1m x 1.6m tunnel. The downstream progression of the vortex (rate of core expansion) may differ and be dependent on the

Reynolds number. However, it can be stated with a fair degree of confidence that the vortices will merge fairly soon after the 7.1c position. This is purely due to consideration of the core separation and diameter at this position.

It is also interesting to note that in Fig. R5.61 the non-dimensional core size with respect to the chord (c=0.1524m) is 0.117 - at 7.1c downstream of the trailing edge and a freestream velocity of 47 m/s. However, in the 1.15m x 0.8m tunnel (Fig. R5.21) the non-dimensional core size is 0.14 with respect to a chord length of 0.1m - at the same downstream position but at a freestream velocity of 30 m/s. These two non-dimensional core sizes are clearly not the same indicating that a simple relationship between chord length and core size is not valid for this twin vortex configuration. A link between Reynolds number and core size may be more valid but this cannot be proven with the available data. Not enough data was acquired to correlate the single vortex measurements in the two wind tunnels.

In Fig. R5.58 the variation in vortex separation with respect to blade incidence is not as would be expected when compared to previous 1.15m x 0.8m tests (Fig. R5.19). Even though the downstream positions are different, 7.1c as opposed to 4.3c, it would be expected that the general trend should be the same. Figure R5.59 shows the locations of the two vortices at 7.1c downstream and it can be seen that at the lower incidences the vortices are oriented more to the vertical. With the interference effect, the vortices are forced together and so the vortex separation is reduced. It is believed that the trend depicted in Fig. R5.19 should also apply here, if the interference effects were not present. Once again, the only way to investigate these problems is to conduct these tests again implementing a different traverse support. A more detailed study with a different traverse support should be carried out to investigate these problems and determine more accurate locations for the vortices.

These twin vortex measurements, however, do document the existence of two distinctive co-rotating vortices at the downstream position corresponding to the measurement position on the rotating blade. These vortices are separated by approximately half a chord and have equal vortex strengths (each half the strength conpared to the original single vortex). Thus, both twin vortex generators have proved successful in the generation of the idealised flow field associated with the Vane Tip.

CHAPTER 6

Transverse Vortex Configuration

6.1 Introduction

Ellin (1993) stated that the furtherance of the understanding of main rotor/tail rotor interactions would benefit from an experimental investigation of blade vortex interaction with the vortex perpendicular to the blade surface. To this end, a means of generating a transverse vortex, in a controlled environment, was required. This present chapter documents the experimental feasibility study into the generation of transverse vortices for perpendicular BVI. A detailed discussion of main rotor tip vortex/tail rotor interaction is provided in Section 1.2.2.4 of Chapter 1.

To gain some insight into the sizing of the drive and mechanical set-up for the rotor blade, a numerical model of the wake produced by the vortex generator was developed (documented in Chapter 3). This model provided vital information for the design of the transverse vortex experimental facility. Once the vortex generator was constructed,

measurements were taken, using x-wire probes, to determine the existence of a tip vortex and its periodic nature. The measurements were taken using cross-wire probes and a TSI Model IFA 300 Constant Temperature Anemometer (CTA) as detailed in Chapter 4. The traverse, traverse support and data acquisition system were the same as utilised in Chapter 5.

The transverse vortex generator facility consisted of a single, variable pitch, rotating blade with a NACA 0015 cross section. It was positioned in the contraction (illustrated in Figs. 3.2 & 6.2) of the Department of Aerospace Engineering's 1.15m x 0.8m low speed wind tunnel at the University of Glasgow. As the blade rotated and pitched up, a vortical wake was generated containing a strong trailed tip vortex. The wake then convected downstream through the remainder of the contraction and into the working section. This arrangement should allow (in future) an instrumented, vertically oriented, blade to be placed in the wind tunnel working section to examine perpendicular blade-vortex interactions (Fig. 1.21).

In this Chapter, the design, construction and operation of the experimental facility is documented along with the preliminary results which prove its success in the generation of the required transverse tip vortex. The assembly/disassembly of the transverse vortex generator is also detailed. The experimental procedure is detailed in Appendix A for any future user of this facility.

It is important to note that the primary objective of this study is to assess the feasibility of a specified technique for generating a transverse trailed tip vortex. The success of the facility will be based on the measurement of a periodic vortex structure in the working section of the tunnel to prove that this vortex generating technique is viable. If this vortex structure is present then future adaptation of the facility, to alter the vortex strength and size, would be easily accomplished by alteration of chord length, blade incidence and rotational speed. If the feasibility study proves successful, a larger facility may be constructed and BVI studies will be initiated.

6.2 Design of Mechanical Assembly

The general guidelines for the design of the experimental facility were as follows:

1. It should produce repeatable and reliable results.
2. Relatively easy to use.
3. Keep alteration of the wind tunnel to a minimum.
4. Simple to assemble/disassemble thus minimising down-time in the tunnel.

These design requirements were not simple to implement and after the initial design work was finished considerable alteration was required to satisfy, primarily, 3 and 4 in the above.

The design of the mechanical assembly was very loosely based on the previous Blade Vortex Interaction facility documented by Kokkalis. However, due to the complexity of the proposed facility (with variable pitch) a completely new approach to the detailed design was required. The rotational speed of the previous BVI rig was, however, similar to the present transverse vortex rig (documented in Chapter 3) and the fundamental dimensions for the rotating shaft and bearing housings are common between facilities.

The numerical model, documented in Chapter 3, proved crucial in determining the operating parameters of the new facility. From the discussion presented in Chapter 3, it was decided that the continuous running configuration would result in a more simple design and a more cost effective means of producing the desired transverse vortex. The physical parameters which determined the design of the experimental facility were,

1. Rotating Shaft location - approximately 3.2m from the origin utilised in the numerical model (corresponds to approximately the start of the settling chamber.
2. Rotational speed - maximum 600 rpm (10 Hz).
3. Pitch profile.
4. Length of rotating blade - based on rotating shaft location

In this section the design, manufacture and assembly of the mechanical components relating to the experimental set-up are considered. A brief description of the wind tunnel in which the experiments were conducted is also presented. Details of the design of the rotor rig model are given, as well as a description of the support structure which transferred loads from the rotor rig to the framework erected around the wind tunnel. It must be pointed out that the design of the hub, pitch mechanism and rotating blade were done in unison even though they are detailed separately in this section.

6.2.1 Wind Tunnel

The operating parameters of the 1.15m x 0.8m wind tunnel are documented in Chapter 5. However, in this investigation, due to the location of the vortex generator, considerable attention focused on the contraction of this tunnel. The position of the vortex generator, as determined by the numerical model, proved very fortunate. This was due to the presence of a heating pipe which ran along the outside of the settling chamber wall (illustrated in Fig. 6.12). Due to this interference problem, the blade could not be positioned any further upstream into the settling chamber. However, the final location of the rotating shaft was 3.15m from the origin used in the numerical model (documented in Chapter 3).

As discussed previously, minimum alteration of the wind tunnel contraction was required. This entailed the installation of two replaceable panels on the upper and lower contraction walls. These were removed when the rotating shaft was placed in the contraction and replaced by a second set of panels which were shaped to allow the vortex generator to pass through. These alterations resulted in very little modification to the original contraction.

6.2.2 Design of Rotor

The geometric size of the rotor was determined from both physical and aerodynamic considerations. The final design was chosen because of its symmetric design, ease of construction and installation. Since the rotor had a single blade, its shape and dimensions

were primarily determined from the space available in the contraction (which determines the blade length) and the requirement to achieve a sufficient chord Reynolds number on the outer sections of the blade. The result was a blade which had a NACA 0015 profile, a chord-length of 0.1m and an aspect ratio of 6.6 based on the final length of the rotating blade (omitting clearance for hub).

Next, the blade's structural design requirements were considered in some detail. The most important of these were that the blade structure should,

1. Withstand the maximum dynamic loading due to high rotational speeds (with adequate safety margin).
2. Withstand the varying lift and drag forces - due to pitching aerofoil and non-uniform velocity components in the contraction.
3. Offer a high degree of stiffness in torsion and bending modes- it is important that the blade does not flap up as this will affect vortex trajectory.
4. Be light enough to eliminate the need for a counter balance which would increase blockage.

At the preliminary design stage, a number of materials and constructional configurations that could fulfil the above requirements were considered. Although material costs had to be kept to a minimum, constructional simplicity, manufacturing and assembly time were also of importance. Of prime concern was the safety of any personnel in the tunnel at the time of testing. The worst case scenario would be the blade detaching from the hub at maximum rotational speed.

The configuration adopted was that of a rigid blade with no flap and lag hinges. This is identical to the numerical model of the rotating blade. A flap hinge would have alleviated the root stresses and moments transferred to the hub by allowing out of plane motion. However, the vertical location of the tip could possibly have varied causing the position of the generated tip vortex to be uncertain. Also, if a flap hinge had been employed the motion of the blade would have introduced aerodynamic and inertial forces in the plane of

the rotor and so, a corresponding lag hinge would probably have been required (as is the case with helicopters rotors). These hinges would have increased the complexity of the apparatus significantly and therefore the cost. Adaptation of the numerical model may have to have been made for comparative purposes. In the rigid blade design, the aerodynamic forces generated on the blade were transferred through the hub and shaft to the external support structure.

The rotating blade was manufactured in three parts - the main body of the blade, a pitch barrel and a connecting rod. The main body of the blade was manufactured from wood with the grain running spanwise. The pitch barrel and rod were manufactured out of steel. All these components, when assembled, rotated in unison about the same axis (which corresponded to the ¼ chord location on the main body of the blade). These components are depicted in Fig. D.2 with the attached pitch arm. The steel rod was glued and pinned into the main body of the blade then screwed into the main pitch barrel and pinned (at a location close to the hub). Thus, one complete structure was formed which was secured to the hub via four radial bearings. The wooden blade was initially manufactured to a length of 0.8m.

After final assembly, in the wind tunnel contraction, the rotating blade was cut to the maximum possible which would allow an appropriate clearance distance between the tip and the contraction wall. This resulted in a blade with a tip radius of 0.75m from the hub centre (0.66m total blade length) with a clearance of 1 inch between rotor tip and tunnel wall. This coincides with the recommendations determined from the numerical model.

With hindsight the blade should not have been pinned at this location (close to the hub) as this weakened the steel rod which connects the blade to the pitch barrel. Fatigue was evident at the pinned location and this resulted in the mechanical failure of the rotating rig. The failure occurred at the end of the manual triggering tests and so the external triggering tests could not be conducted (due to time limitations). Six to eight weeks would be required to replace the pitch barrel and blade and conduct the remaining tests (for a person familiar with the equipment). The majority of this time would be taken up with the manufacture of a new pitch barrel. No change would be necessary to the design of the

blade, steel shaft and pitch barrel but, if the blade were to be pinned it should be internally at a location as near to the rotating axis as possible.

6.2.3 Design of Hub

The first sketches and drawings, in the preliminary design phase, centred on the hub. This was due to the complex nature of the motion required of the rotating blade. The mechanism to actuate the blade had to be simple, relatively compact, and able to withstand the rotational/aerodynamic loads. Due to the limited space available in the contraction of the 1.15m x 0.8m tunnel, the hub and pitch assembly had to be as compact as possible (in a larger tunnel the space constraint would not be as severe). To this end, the size of the hub was determined from the size of the rotating shaft flanges which connect onto the hub. This resulted in a hub initially manufactured as a square with dimensions 180 x 180mm. After initial assembly, and preliminary running of the facility, the hub was machined into a circular profile.

The hub was designed around the pitch barrel, documented previously, and the locations of the bolts which secure the upper and lower shaft flanges and hub together. Two bearings were situated on either side of the rotating axis. These were secured to the hub by two aluminium collars which were attached to the lower half of the hub with grub screws. These collars had an inside radius of 14mm which resulted in a 4mm clearance between the collars and the main pitch barrel. The pitch arm was screwed into the central section of the pitch barrel (with a diameter of 40mm) and exited the hub at 90 degrees to the rotating blade (and pitch barrel).

Due to the mechanical nature of the pitch mechanism, a method to keep the roller on the cam had to be incorporated internally into the hub. This was achieved by placing a simple spring above the pitch arm to force it down. The initial drawing depicted in Fig. D.1 illustrates the spring housing. This was altered slightly, during manufacture, by drilling a hole vertically down, through the recess for the upper flange, into the bearing housing. This enabled the spring to be replaced without splitting the hub. The spring then rests

against the upper flange face. Without the spring, the roller would not follow the prescribed pitch motion determined by the cam.

6.4.4 Design of Pitch Mechanism

The pitch mechanism was loosely based on that implemented in a helicopter. The idea for the present pitching mechanism came from Fig. 6.1 which shows the idealised (helicopter) mechanism for producing cyclic pitch. In this figure, the pitch arm is depicted with a 90 degree bend which connects the blade to the swashplate. In the present design this component was split into two elements comprising the pitch arm (horizontal) and the pitch link (vertical). These two components were connected together with the aid of a small needle bearing and a short clevis. The articulated nature of this mechanism allowed the pitch link to remain vertical throughout a complete rotation and so reduced the size of the static cam on which the pitch link rests. The pitch arm is depicted in Fig. D.2 connected to the pitch barrel. The pitch link is depicted in Fig. D.3. A series of photographs (Figs. 6.6 - 6.8) show the connected pitch arm and link (also shown in Fig. D.1 (Sectional Elevation on A-A)).

It was necessary to limit the radial movement of the roller attached to the pitch link. This was done via a constraining arm which was attached to the lower rotating shaft. In Fig. D.4, the technical drawing of the constraining arm is illustrated and a photograph of this component is depicted in Fig. 6.3 (with the complete pitch mechanism). The assembly of the pitch mechanism is illustrated in Fig. D.5 and the complete pitch mechanism (omitting the cam on which the roller rests) is depicted in Fig. D.6. There is an error in this drawing relating to the incidence of the aerofoil. With the pitch arm and constraining arm horizontal the blade should be at an incidence of 10 degrees (rather than the 0 degrees depicted in the drawing). As the roller moves down the blade incidence should decrease to zero degrees.

The roller was designed to rest on a cam, hence, the profile of the static external cam was designed along with the pitch mechanism. The profile required on the cam was slightly altered from that determined by the numerical model. This was purely to simplify the

manufacture of the cam. The pitch profile was split into four 90 degree phases. The first, at zero degrees blade incidence, occurred when the blade was pointing into the settling chamber (45 degrees azimuthal travel on either side of the centre line). In this phase, the roller was at its lowest position. In the next 90 degree phase of motion, the blade was pitched up to 10 degrees. In this phase, the constraining arm and pitch arm return to the horizontal and the spring internally housed in the hub is compressed. After this, the blade crossed the working section at a constant incidence of 10 degrees (azimuthal position 45 degrees either side of the centre line). In the final 90 degree phase, the blade returned to zero degrees (with the pitch arm and constraining arm returning to an inclination of 10 degrees to the horizontal). In this phase, the spring forced the roller to remain in contact with the cam. Due to the roller being 90 degrees ahead of the rotating blade, the cam was necessarily 90 degrees out of phase with the blade.

This pitch profile does differ from that obtained using the numerical model (refer to Chapter 3). However, the main characteristics (which were determined in Chapter 3) are still inherent in this simplified pitch profile. The blade is still at zero degrees incidence on the upstream part of the rotation (to counter any wake/wake interactions which may occur during each rotation) and the incidence is constant as the blade crosses the entrance to the working section (to generate a well defined vortex). The pitch up and down phases are less extreme with the simplified pitch profile utilised in the experimental facility which is beneficial in reducing the shed vorticity in these regions. In general, the change in pitch profile will not produce a significant effect in the generation and convection of the tip vortex. Therefore, a similar vortex structure, as depicted in the present numerical model results, will still convect through the working section.

6.2.5 Rotor Support Structure

Once the design of the rotating blade, hub and pitch mechanism were complete (and manufacture was in progress) attention turned to the external support for the rotating assembly. When design of the BVI rig in the 2.1m x 1.6m wind tunnel was taking place, the rotor support was fairly easy to construct. This was mainly due to the already existing

steel box section framework of the tunnel on which the rotor support could be placed (this could be of benefit if the present facility method of generating a transverse vortex was implemented in this tunnel). In the smaller wind tunnel, however, there was no external supports on which to work from. A considerable lack of space above and below the tunnel had to be taken into account in the design along with the presence of an external heating pipe which ran along the exterior tunnel wall. These were the primary factors which determined the location of the vortex generator and the motor support.

The complete rotating blade support structure is depicted in Fig. D.7. A photograph of the lower support structure is given in Fig. 6.9 and the upper roller bearing housing in Fig. 6.10 and 6.11. The interference which was noted with the heating pipe is also shown in Fig.6.12.

There was an external cam on the lower rotating shaft on which the roller of the pitch mechanism rested (depicted in Figs. 6.2 & 6.3). This cam was manufactured in two sections and was mounted on its own support structure which was, in turn, attached to the main rotor support. This cam support was positioned over the lower bearing housing (Fig. D.7). For assembly, it was necessary to allow the flange, on the lower rotating shaft, to pass through the base plate of the cam support. In addition, the cam was required to have a diameter large enough to coincide with the location of the roller on the pitch link. To achieve this, the cam was manufactured from a ½ inch thick high tensile steel tube with an outside diameter of 7 inches. A close-up photograph of the roller and cam is depicted in Fig. 6.3.

The cam profile was machined with respect to a reference length, which corresponded to the vertical distance between the base plate of the cam support and the roller on the pitch link when the blade incidence was 10 degrees. This was the highest point on the cam (68.5cm) when the pitch arm and constraining arm were both horizontal. The height of the cam reduces to 66.75cm when the blade is at zero degrees. In Fig. D.9, the right half of the cam is 66.75 cm in length from the base of the cam support when looking upstream.

6.2.6 Design of Motor Support

The motor was positioned below the wind tunnel, primarily due to space constraints, on a separate support structure. A suitable motor rated at 0.5hp was available although there was no paperwork with it and the identification plate (which should have been on the motor) was also missing. The motor controller enabled the minimum and maximum rotational speeds to be set and the torque to be varied.

The motor was connected to the rotating shaft via a high torque belt drive with 1:1 gearing and the motor support was bolted to the floor of the building (as was the rotor support). The position of the motor with respect to the main rotor support structure is depicted in Fig. D.7 and, the lower assembly, in Figs. D.8 & 6.9.

6.2.7 Assembly of the Vortex Generator

The hub was linked to the external structure via 5 individual components. The first was the upper shaft, which was located in a roller bearing mounted above the tunnel. This upper shaft can be locked in the vertical position via two securing brackets during alignment. The lower rotating shaft, with the hub on top, was then placed onto the drive shaft, which was connected to the motor via the drive belt. These two components were then raised up to meet the upper shaft and a 2-inch spacer placed between the lower shaft and drive shaft. Six high tensile steel bolts secured the lower shaft, spacer and drive shafts together and five high tensile steel bolts secured the hub, upper and lower shafts together (see Fig. D.9). The constraining arm of the pitch mechanism was located through a hole in the lower shaft and secured to the pitch link.

The external cam was then placed around the lower rotating shaft and secured to its base plate via six bolts that screwed directly into the base plate. The two halves of the cam were then joined along their vertical edges by six bolts. Finally two wooden panels were placed around the upper rotating shaft and the lower camshaft to complete the contraction wall. The complete installation takes approximately 1½ hours to complete and about an hour to disassemble. The speed of assembly/disassembly has proved advantageous.

As can be seen in Fig. 6.2, when the facility was first assembled the hub was square. This initial assembly was done to validate the operation of the rotating facility. Initial tests were also conducted at this time to verify the existence of a tip transverse vortex. However, when the probe was positioned along the centre line, the tip vortex was difficult to detect. This resulted in the hub being machined into a circular profile with fairings added around the upper shaft and lower cam to try and reduce any interference effects. These fairings were one metre in length and shaped like a symmetric aerofoil with the rotating shaft positioned at the maximum thickness location. These changes were successful in improving the signal associated with the transverse tip vortex in this region.

6.3 External Trigger

The experimental facility had two sensors situated on the upper transverse beams of the support structure (illustrated in Fig. D.7). The first optical sensor provided a measurement of the rpm of the rotating blade to enable the rotational speed of the blade to be set. The second sensor provided an external trigger for the hot-wire system via a 16 channel BNC input board for the internal A/D Converter (see Fig. 4.1). This board had one connection for the trigger and another for the trigger reset. These were both configured as TTL normally high signals and were activated by shorting to ground (i.e. bringing them to TTL low). This means the acquisition and reset were triggered by a falling edge. An electronic circuit was designed to convert the signal from the reflective opto switch (RS stock number 307-913) to a TTL high/low signal which was supplied to the BNC interface board. The electronic circuit could then be activated by the optical trigger (from the rotating shaft) or by a manual trigger button. Another manual button was provided for the trigger reset on the BNC interface board. The procedure for acquiring data with either of the external triggers (manual external trigger or optical trigger on the rotating blade) is discussed in the experimental procedure detailed in Appendix A.

The external trigger was designed to primarily investigate the curvature of the wake structure and, thus, compare with the numerical model. Also, it was decided that phase locked averaging of the results using the external trigger may be beneficial. These investigations, unfortunately, could not be carried out during the present study in the time

available. However, all the experiment equipment is available and, hopefully, these tests will be conducted in the near future.

6.4 Test Configurations

The complete list of the tests conducted are documented in Tables 6.1-6.5. The main variables in these tests were primarily the working section velocity and rotational speed. The measurement position, sampling time and sampling frequency could also be varied, however, a constant sampling frequency of 5000 Hz and a sampling time of 0.8 seconds was used for the majority of tests. These settings gave the best representation of the periodic signal using the manual trigger. All tests were conducted with the x-wire probe situated at, approximately, 1.65 m downstream of the rotating axis. This corresponds to the 2c position on the horizontal traverse support as used in the previous twin vortex investigation (Chapter 5).

Table 6.1 details the initial tests which were conducted at the two extremes of the operating range to investigate the actual existence of a periodic signal representative of a transverse vortex. Tests 1 and 2 were conducted at low working section velocity and rotational speed settings (10 m/s and 400 rpm respectively) and tests 3 and 4 at high wind tunnel and rotational speed settings (20 m/s and 520rpm (test3), 600 rpm(test4)). All measurements were conducted at a location of y=150mm which represents a horizontal position to the right of the centre line (when looking upstream into the settling chamber). The vertical position was set by acquiring data in the display mode (which does not store any data on disk). A quick vertical traverse was made from x=50mm to -50 mm (downward through the centre line) in 10 mm increments to locate the vortex and, hence, decide on a fixed vertical position (x=-30mm which corresponds to a position below the centre line) for the main tests.

The next set of tests were conducted at a constant working section velocity of 10 m/s (Table 6.3). In tests 5-9, the relationship between the rotational speed setting and the periodic nature of the convecting vortex was investigated. In tests 10-14, the horizontal measurement location was varied to investigate the influence, in any, of the wake from the

generation assembly. These tests were conducted at 5 horizontal measurement locations (150, 75, 0, -75, -150 mm) at a constant rotational speed of 500 rpm. This produced a stronger periodic signal compared with lower rpm settings.

The tests documented in Tables 6.4 & 6.5 repeated the above investigations but for working section velocities of 20 and 15 m/s respectively. All other parameters - rotational speed, sampling time and measurement positions - were the same as in Table 6.3.
All the tests documented here used a manual trigger to obtain a time history containing the signature of several vortex systems. These were sufficient to both identify and document the characteristics of the periodic vortex passage.

6.5 Results and Discussion

The results are presented in the form of time series for the streamwise (u) and the vertical (v) velocity components. The figure below illustrates the orientation of the probe and a convecting vortex when looking horizontally through the working section. The associated sign convention is used for the determination of the velocity components - u streamwise velocity, v vertical velocity (this sign convention is different from that employed for the traverse co-ordinates as discussed previously).

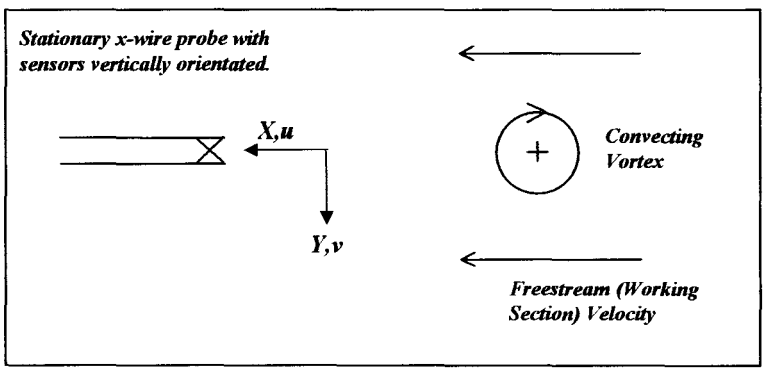

In Fig. R6.1, the time series for case 1 is presented. The streamwise and vertical velocity components are illustrated. As can be seen, there is a strong periodic signal in both time series, with three vortices evident in the 0.4 second sample time. The period between each vortex is approximately 0.15 seconds which corresponds exactly to the prescribed rotational speed of 400 rpm. This corresponds to a vortex spacing of 1.5m. The first two

vortices have a sharp rise in the streamwise velocity component with the peak corresponding to the change over from -ve to +ve velocity in the vertical velocity component (taken as the vortex location in the time series). As can be seen from the above diagram, if the vortex were to pass above the probe, the superposition of the freestream velocity with the induced velocity from the convecting vortex would result in a sharp increase in streamwise velocity as the vortex passes the measurement location. This is the case for the first and second vortices in the time series. If the vortex were to pass the probe at exactly one core radius above the probe a maximum in streamwise velocity would result from the maximum induced velocity superposed with the freestream velocity. If the vortex were to move downward into the core the streamwise velocity would decrease rapidly (if a finite core size were assumed). As the vortex location moved through the vortex centre the streamwise velocity component would reverse to become a decrease in velocity. Then, at one core radii below the probe a minimum in streamwise velocity would result. Outwith the core the velocity would either increase slowly and tend toward the freestream value - with a vortex positioned at ever increasing distances below the probe, or, decrease slowly to the freestream value - with a vortex positioned at ever increasing distances above the probe. With respect to the third vortex in Fig. R6.1, it appears to pass below the probe but within the core radius. However, the magnitude of the vertical velocity is smaller than the previous cases indicating that the vortex has, probably, been influenced by turbulence.

In Figs. R6.2-R6.4, an expanded view of the individual vortices in the time series depicted in Fig. R6.1 are presented. Here, an estimate of the locations of the minimum and maximum velocities are made to try and estimate the core diameters. As can be seen, the three vortices give different estimates of the core size. This is most likely caused by the miss distance between the vortex and the probe. As can been seen, the third vortex has the smallest core size which again indicates that the vortex is close to the probe position.
In Fig. R6.5 (test case 2), the sampling time has been increased to 0.8 seconds and all other parameters have been held constant (from Fig. R6.1). Here, the strong periodic signal is very evident and all the vortices are above the probe measurement location. There is a difference between the peak values of streamwise velocity and this is related to the distance between the vortex centre and the probe.

In Fig. R6.6, the freestream velocity has been increased to 20 m/s which represents the maximum designed operating velocity. The rotational speed of the blade has also been set at a value of 520 rpm. Again, the period between convecting vortices (0.115 secs) agrees with the rotational speed of the blade. This figure depicts three convecting vortices, which are numbered and pass below the probe, but, also what looks like a second, weak, periodic signal. This signal is characteristic of a vortex of the opposite sign to the strong transverse tip vortex. As can be seen from Fig. R3.10 (numerical model configuration at approximately the same operating conditions but with a geometric incidence of 5 degrees) there is a strong root vortex which exists to the right of the centre line. This corresponds to the same location as the measurement probe and so this second periodic signal could be a rolled up root vortex. However, this could also be due to a coalescing of the shed vorticity which may, possibly, give a similar result. More detailed tests would be required to fully investigate the operating conditions which generate this secondary periodic signal and the measurement locations where it is evident. However, it is apparent that this weak signal is severely affected by turbulence as can be seen in case *B*.

In Figs. R6.7-R6.9, the three primary transverse vortices from Fig. R6.6 are expanded and the vortex core sizes calculated. There is good agreement between the first and third vortices but the second gives a vortex diameter twice that of the other two. This is possibly due to a greater distance between the probe and this vortex indicating that the vortices are convecting at slightly different vertical locations through the tunnel. The larger core size, lower vertical velocity components and higher minimum streamwise velocity are all characteristic of the probe resting above the vortex outwith the core.

In Fig. R6.10, the velocity is again 20 m/s but the rotational speed is at the optimum 600 rpm to generate a uniform transverse vortex. The period of the vortices is 0.105 seconds which giving a rotational frequency slightly lower than the value set on the rpm counter. Again, there appears to be a periodic signal associated with a root vortex (*B*). However, there also seems to be another signal *A* which, it is assumed, is due to turbulence. The turbulence intensity at 20 m/s is considerably higher (4.9%) than at 10 or 15 m/s (2%).

Figures R6.11-R6.14 illustrate the effect of rotational frequency at a constant freestream velocity of 10 m/s. All these (and subsequent) tests were conducted with a sample time of

0.8 secs which gives the best representation of the periodic signal from low to high rpm. Figure R6.11 illustrates the lowest possible rotational speed to generate a tip vortex. The period of vortex convection is 0.2 seconds (which agrees with the 300 rpm setting) and, as can be seen, the second vortex convects above the probe with all the others below. The other three figures (R6.12-R6.14) represent higher rpm (375,500 and 600 rpm) values. At the lowest rpm setting (300 rpm) the vortices convect on either side of the probe. However, at the higher rpm settings all the vortices convect below the probe and the signal (associated with each individual vortex) appears to be more consistent. There seems to be an apparent trend with the transverse vortex signal being less prone to wander as the rpm is increased.

Figures R6.15 & R6.16 also illustrate the effect of rotational frequency but, this time, at a freestream velocity of 20 m/s. Below 500 rpm the periodic signal is not evident due to the relatively weak vortex signal being swamped by the higher turbulence intensity discussed above. A strong periodic signal is, however, evident when the rotational speed is set at 500 rpm or above (as depicted in these figures). Once again, it appears that there is less wander of the vortex with higher rpm.

Figures R6.17 to R6.20 depict the times series for the variation in rotational speed with a working section velocity of 15 m/s. Once again the time between each convecting transverse vortex can be strongly linked to the rotational frequency of the rotating shaft. However, due to the lower turbulence intensity, in this case, the periodic signal is evident throughout the 300-600 rpm rotational speed range. From previous numerical model investigations (Fig. 3.5), the reduction in working section velocity from 20 to 15 m/s improves the curvature of the tip vortex. Even though this case was conducted in the single rotation configuration, it was proved that the wake geometry varied little between the continuous running and single rotation cases as long as the individual wakes did not overlap. If an instrumented vertical blade were to be placed in the working section of this tunnel, it should positioned at the same location as the measurement probe in this investigation. Investigations should, also, start with a working section velocity of 15 m/s as this produces the optimum wake structure (from the numerical model) and a strong periodic signal throughout the rotational speed range.

In Figs. R6.21-R6.23, the time series for each working section velocity is depicted with the blade stationary. These figures are presented with the corresponding turbulence intensity (which were calculated from each digital time series) and are included for comparison with the periodic time series. The calculation of turbulence intensity for the periodic time series are meaningless.

All the results presented are from the investigations of the variation in rotational frequency of the vortex generator. The horizontal traverse measurements (which have not been presented), conducted at 500 rpm for working section velocities of 10, 15 and 20 m./s, differed little from the measurements conducted at y=150mm. Since there is, apparently, no difference between measurements at these different the horizontal locations, there is little interference from the vortex generator.

The new vortex generator facility has proved extremely successful in the generation of a transverse vortex which convects through the working section of a low speed wind tunnel. This facility can now be used for the experimental investigation into Blade Vortex Interaction with the vortex orthogonal to the plane of the aerofoil. The experimental technique can now be extended to a larger wind tunnel.

The implementation in a larger facility should prove advantageous over the present facility for a number of reasons. There is a possibility that the large fairings in the present facility influence the time series due to the non-uniform flow that exists on either side of the symmetric aerofoil. This may change the incidence and shed vorticity may be generated. This however, does not appear to alter the strong periodic signal which is of paramount importance in this investigation and, therefore, was deemed not significant. The design of a similar facility in a larger wind tunnel should not suffer from this problem. The general parameters such as shaft diameter should vary little between the two facilities and there will be a considerable increase in the physical size of the contraction in a larger facility.

CHAPTER 7

Conclusions and Recommendations

The conclusions and recommendations for the twin longitudinal vortex configuration (Chapter 5) are documented in Section 7.1. In Section 7.2, the conclusions for the numerical model of the transverse vortex (Chapter 3) and the experimental facility (Chapter 6) are presented along with combined recommendations (Section 7.2.3) for their future use.

7.1 Twin Vortex Configuration

A study of the flow field created by a twin vortex generator has been conducted. It has been demonstrated that the cross-flow created by the resulting vortex system can be adequately represented by a simple vortex core model. On the basis of this model, the strength, growth, lateral spacing and rotation of the vortex system were studied. It was found that the core size of the twin vortices grew almost linearly with downstream

distance while the strength remained constant. The spacing between the two cores remained almost constant with only a slight decrease as the downstream distance increased. Finally, the rotation of the vortex system was modelled by a straight forward consideration of the induced velocity field. Generally, good agreement with experiment was obtained despite the influence of interference effects on the experimental data.

The conclusions for the complete tests conducted in the 1.15m x 0.8m tunnel and the 2.1m x 1.6m tunnel are,

1) The two dimensional numerical model proved extremely successful in the determination of the single and twin vortex parameters, vortex core size, strength and position, for both the single vortex cases and the twin co and counter rotating vortex cases.

2) There was a linear relationship between the vortex strength and the incidence for both single vortex and twin vortex cases.

3) An invariant core size with incidence was noted for both single vortex and twin vortex test cases.

4) A linear expansion of the core from 0.1 to 10 chord lengths downstream of the trailing edge was noted.

5) The vortex strength initially increased up to 4 chord lengths downstream and thereafter the vortices were of constant strength.

6) The calculation of the vorticity from the velocity components highlighted the convecting wake structure with downstream movement and a redistribution of the vorticity in the core as it expands.

7) The quasi-three dimensional model adequately predicted the downstream locations of the twin vortices. However, the lower vortex was prone to interference from the traverse which was the primary source of errors. This model also adequately predicted the behaviour of the counter rotating vortex pair and the reduced rotation as would be

expected when the vortex separation distance is increased. The model, however, could not predict vortex merging.

8) Single vortex measurement in the 2.1m x 1.6m resolved the discrepancy between the previous triple wire measurement of Kokkalis and the PIV data of Horner.

9) The single vortex measurements were prone to interference from the traverse support and this was verified by inverting the traverse.

10) Twin vortex measurement were conducted in the 2.1m x 1.6m wind tunnel but the interference proved so significant that severe doubt must be placed on the results of the vortex location.

As a recommendation, a more detailed investigation into the 0.25c separation between the ¼ c locations of the aerofoils should be conducted to fully investigate the fundamental phenomenon of vortex merging. With the resurgence of interest in the Sub Wing tip, which relies on twin vortices prior to Blade Vortex Interaction, this could prove a worthwhile exercise.

7.2 Transverse Vortex Configuration

7.2.1 Numerical Model of Transverse Vortex

A numerical model has been used in the conceptual design of a new blade vortex interaction facility. The model showed the convecting wake geometry was dependant on the wind tunnel velocity, the tip velocity profile and the pitching motion of the rotating blade. Two independent cases for the motion of the blade were investigated, a single rotation acceleration/deceleration motion of the blade and a continuous running motion with constant tip velocity. The single rotation case, with an acceleration across the entrance to the working section, produced the optimum wake geometry for the generation of a transverse vortex but was impractical to implement due to the excessively high torque

loads required to accelerate and decelerate the blade. The continuous running configuration produces a wake geometry which is not significantly worse than the single rotation case but has the advantage of being considerably easier to implement.
The general operating parameters which were concluded from the numerical model were,

1. Rotating Shaft location - approximately 3.2m from settling chamber origin.
2. Rotational speed - maximum 600 rpm (10 Hz).
3. Pitch profile (see Table 3.2).
4. Length of rotating blade based on rotating shaft location but around 0.75m with the blade positioned at 3.2m from the tunnel model origin.

7.2.2 Transverse Vortex Experimental Facility

The present experimental facility has proved to be highly successful in the generation of the required transverse vortex. The main conclusions from the tests conducted were,

1) At 10 and 15 m/s there is a strong periodic signal in both the streamwise and vertical velocity components representative of a transverse vortex. This is evident at all the horizontal measurement locations investigated.

2) At 20 m/s a strong periodic signal is noted but only at a rotational speed of around 500 rpm or greater.

3) Secondary periodic structures were noted which seem to highlight a second weak vortex of opposite sign to the strong trailing tip vortex. This could result from the trailing root vortex or a coalescing of the shed vorticity.

4) The vortex trajectory seems less likely to meander with higher rpm settings.

With the proposed design of a new larger facility (based on this feasibility study) the numerical model should be used to conduct a similar design exercise. This would entail simply replacing the existing specification of tunnel geometry (and subsequently panel

geometry) with the new geometry of a larger facility and conducting another parametric analysis.

The strong highly periodic signal, which characterises the convecting transverse vortex, should prove sufficient for a preliminary examination of Blade Vortex Interaction (with the vortex orthogonal to the plane of the blade) in the present facility.

7.2.3 Recommendations for Future Work

The optimum working section velocity for conducting any experimental investigations, in the present facility, with an instrumented blade is 15 m/s. This was the speed which produced an adequate separation between transverse vortices and a corresponding periodic signal throughout the rpm range investigated (300-600 rpm). This was purely due to the reduced turbulence intensity which is evident at 15 m/s when compared to 20 m/s. Ideally, the blade should also be positioned at the x-wire measurement location used in this investigation.

If possible, measurements should be conducted at different downstream measurement locations to investigate the development of the vortex structure as it progresses through the wind tunnel working section. This should be compared, in detail, to the numerical model predictions. Comparison of the test configurations and the numerical model should also be made to investigate the position and strength of the trailing root vortex which may, ass discussed above, be the source of some disturbance in the measured data. This effect seems to be dependant on the operating conditions of the facility and measurement location. If the root vortex is the cause of this secondary signal it should only be evident within a specific horizontal measurement range (situated either side of the centre line). Outwith this region there should be no evidence of the signal. However, in Figs. R3.5 & R3.6 there is evidence of a coalescing of shed vorticity in the inboard region of the wake which would also be of opposite sign to the strong trailing tip vortex. This is on the right hand side of the tunnel and could also be a possible explanation for this secondary signal. More measurements are required if the cause of this secondary signal is to be isolated.

Prior to any attempt to ensemble average a large number of files, a simple investigation, using the external opto switch trigger on the rotating shaft, should be conducted. Tests should be carried out with the operating parameters and measurement location constant. With simple comparison of the individual time series (10 time series should be adequate) it should be immediately apparent whether the vortices are in the same location in the time series. If they are, phase locked averaging should prove successful, if not the periodic signal will be averaged out.

If, as appears to be so from the high rpm case, the application of phase locked averaging proves successful, it will be possible to determine the mean characteristics of the vortex. To apply this technique, the external triggering mechanism incorporated in the present facility will need to be employed. This trigger should also be used to investigate the curvature of the tip vortex. This is depicted in the numerical model results and a change in the location of the vortex in the time series should be noted with variation in the horizontal measurement location. This would provide a fuller validation of the numerical model for future design of the larger facility.

Bibliography

Abbott I.H., von Doenhoff A.E., "Theory of Wing Sections", *Dover Publications, 1959.*

Acheson D.J., "Elementary Fluid Dynamics", *Oxford University Press, 1990.*

AGARD-CP-494, "Vortex Flow Aerodynamics", 1990.

AGARD-R-781, Aerodynamics of Rotorcraft, 1990.

AGARD-CP-584, "The Characterisation and Modification of Wakes from Lifting Vehicles in Fluids", 1996

Anderson J.D., "Fundamentals of Aerodynamics", *McGraw-Hill, 1991.*

Batchelor G.K., "An Introduction to Fluid Mechanics", *Cambridge University Press, 1967.*

Borse G.J., "FORTRAN 77 and Numerical Methods for Engineers", *PWS-KENT Publishing Company, 1991.*

Bradshaw P., "An Introduction to Turbulence and its Measurement", *Pergamon Press, 1971.*

Bramwell A.R.S., "Helicopter Dynamics", *Edward Arnold, 1976.*

Bruun H.H., "Hot-Wire Anemometry : Principles and Signal Analysis", *Oxford Science Publications, 1995.*

Johnson W., "Helicopter Theory", *Princeton University Press, 1980.*

Katz J., Plotkin A., "Low Speed Aerodynamics : From Wing Theory to Panel Methods", *McGraw-Hill, 1991.*

Kuethe A.M.,Chow C., "Foundations of Aerodynamics", *John Wiley & Sons, 1986.*

Lamb H., "Hydrodynamics", *Cambridge University Press, 1932.*

Lewis R.I., "Vortex Element Methods for Fluid Dynamic Analysis of Engineering Systems", *Cambridge University Press, 1991.*

Lomas C.G., "Fundamentals of Hot-Wire Anemometry", *Cambridge University Press, 1986.*

Milne-Thompson L.M., "Theoretical Aerodynamics", *Dover Publications, 1973.*

NASA-SP-409, "Symposium on Wake Vortex Minimisation", 1977.

Olsen J.H., Goldburg A., Rogers M., "Aircraft Wake Turbulence and its Detection", *Plenum Press, 1971.*

Prandtl L., Tietjens O.G., "Fundamentals of Hydro- and Aeromechanics", *McGraw-Hill, 1934.*

Prouty R.W., "Helicopter Aerodynamics", *PJS Publications, 1985.*

Rae W.H., Pope A., "Low-Speed Wind Tunnel Testing", *John Wiley & Sons, 1984.*

Rom J., "High Angle of Attack Aerodynamics:Subsonic, Transonic and Supersonic Flows", *Springer-Verlag, 1992.*

Saffman P.G., "Vortex Dynamics", *Cambridge University Press, 1995.*

Seddon J., "Basic Helicopter Aerodynamics", *BSP Professional Books, 1990.*

Stepniewski W.Z., Keys C.N., "Rotary-Wing Aerodynamics", *Dover Publications, 1984.*

References

Acrivlellis M., "Determination of the Magnitudes and Signs of Flow Parameters by Hot-Wire Anemometry", *Rev. Sci. Instrum. 60, 1275-85, July 1989.*

Ashby D.L., Sandlin D.L., "Application of a Low Order Panel Method to Complex Three-Dimensional Internal Flow Problems", *NASA CR-179656, Dec. 1985.*

Baker G.R., Barker S.J., Bofah K.K., Saffman P.G., "Laser Anemometer Measurements of Trailing Vortices in Water", *J. Fluid Mech. 65, 325-336, 1974.*

Baron A., De Ponte S., Mignemi B., "Three Component Hot-Wire Measurements in the Wake of a Rotor Model", *Vertica 11, 513-23, 1987.*

Batchelor G.K., "Axial Flow in Trailing Line Vortices", *J. Fluid Mech. 20, 645-658, 1964.*

Beard J., "Danger in the Wake of a Aeroplane", *New Scientist, 16th Nov. 1991.*

Bearman P.W., "Corrections for the Effect of Ambient Temperature Drift on Hot-Wire Measurements in Incompressible Flow", *DISA Info. 11, May 1971.*

Betz A., "Behaviour Of Vortex System", *NACA TM-713, June 1933.*

Booth E.R., Yu J.C., "Teo Dimensional Blade-Vortex Interaction Flow Visualisation Investigation", *AIAA Paper 84-2307, Oct. 1984.*

Booth E.R., "Surface Pressure Measurement During Low Speed Two-Dimensional Blade-Vortex Interaction", *AIAA Paper 86-1856, July 1986.*

Booth E.R., Yu J.C., "New Technique for Experimental Generation of Two-Dimensional Blade-Vortex Interaction at Low Reynolds Number", *NASA TP-2551, March 1986.*

Bristow D.R., "Development of Panel Methods for Subsonic Analysis and Design", *NASA CR-3234, Feb. 1980.*

Brocklehurst A., Pike A.C., "Reduction of B.V.I. Noise Using a Vane Tip", *A.H.S. Aeromechanics Specialists Conf., San Francisco, Jan. 1994.*

Brown C.E., "Aerodynamics of Wake Vortices", *AIAA J. 11, 531-36, 1973.*

Browne L.E., Ashby D.L., "Study of the Integration of Wind Tunnel and Computational Methods for Aerodynamic Configurations", *NASA TM-102196, Oct. 1989*

Browne L.E., Katz J., "Application of Panel Methods to Wind Tunnel Wall Interference Corrections", *AIAA Paper 90-0007, Jan. 1990.*

Browne L.W.B., Antonia R.A., Chua L.P., "Calibration of X-Probes for Turbulent Flow Measurements", *Exp. Fluids 7, 201-8, 1989.*

Bruin A.C.de, Hegen S.H., Rohne P.B., Spalart P.R., "Flow Field Survey in Trailing Vortex System Behind a Civil Aircraft Model at High Lift", *AGARD CP-584, Nov. 1996.*

Bruun H.H., "Hot-Wire Data Corrections in Low and in High Turbulence Intensity Flows", *J. Phys. E: Sci. Instrum. 5, 812-18, 1972.*

Bruun H.H., "Interpretation of Hot-Wire Probe Signals in Subsonic Airflows", *J. Phys. E: Sci. Instrum. 12, 1116-28, 1979.*

Bruun H.H., Tropea C., "The Calibration of Inclined Hot-Wire Probes", *J. Phys. E: Sci. Instrum. 18, 405-413, 1985.*

Bruun H.H., Nabhani N., Fardad A.A., "A Comparative Study of Signal Analysis Procedures for X Hot-Wire Probes and Multi-Position Single Yawed Probes", *Proc. 2nd World Conf. on Exp. Heat Trans. Fluid Mech. & Thermo., Dubrovnik Yugoslavia, 443-451, 1991.*

Burgers J.M., "A Mathematical Model Illustrating the Theory of Turbulence", *Adv. Appl. Mech. 1,171-99, 1948.*

Bushnell D.M., "The 32nd Lanchester Lecture : Longitudinal Vortex Control - Techniques and Applications", *Aero. J. 96, 293-305, 1992.*

Caradonna F.X., Lautenschlager J.L., Silva M.J., "An Experimental Study of Rotor-Vortex Interaction", *AIAA Paper 88-0045, Jan. 1988.*

Caradonna F.X., Strawn R.C., Bridgeman J.O., "An Experimental and Computational Study of Rotor-Vortex Interactions", *Vertica 12, 315-327, 1988.*

Caradonna F.X., "The Application of CFD to Rotary Wing Flow Problems", *AGARD-R-781, Aerodynamics of Rotorcraft, 1990.*

Caradonna F.X., "Recent Methods for the prediction of Rotor-Wake Problems", *Int. Colloquium on Vortex Flow Aeronautics, Aachen, 12-14th Oct. 1994.*

Champagne F.H., Sleicher C.A., Wehrmann O.H., "Turbulence Measurements with Inclined Hot-Wires", *J. Fluid Mech. 28, 153-75, 1967.*

Chigier N.A., Corsiglia V.R., "Tip Vortices - Velocity Distributions", *NASA TM X-62087, Sept. 1971.*

Chigier N.A., Corsiglia V.R., "Wind-Tunnel Studies of Wing Wake Turbulence", *J. Aircraft 9, 820-825, 1972.*

Christiansen J.P., "Numerical Simulation of Hydrodynamics by the Method of Point Vortices", *J.Comp. Phys. 13, 363-79, 1973.*

Christiansen J.P., Zabusky N.J., "Instability, Coalescence and Fission of Finite-Area Vortex Structures", *J. Fluid Mech. 61, 219-243, 1973.*

Clark D.R., Leiper A.C., "The Free Wake Analysis - A Method for the Prediction of Helicopter Hovering Performance", *J. American Helicopter Soc. 15, 3-11, Jan. 1970.*

Clark R.W., "A New Matrix Solution for Three-Dimensional Panel Methods", *AIAA Paper 85-0176, Jan 1985.*

Clausen P.D.,Wood D.H., "The Correction of X-Probe Results for Transverse Contamination",*J. Fluids Eng. 111, 226-9,June 1989.*

Clausen P.D., Piddington D.M., Wood D.H., "An Experimental Investigation of Blade Element Theory for Wind Turbines - Part 1. Mean Flow Results", *J. Wind Eng. Ind. Aero. 25, 189-206, 1987.*

Clausen P.D., Piddington D.M., Wood D.H., "An Experimental Investigation of Blade Element Theory for Wind Turbines - Part 2. Phase-Locked Averaged Results", *J. Wind Eng. Ind. Aero. 31, 305-22, 1988.*

Cliffone D.L., Orloff K.L., "Far-Field Wake-Vortex Characteristics of Wings", *AIAA J. 12, 1154-5, 1974.(Also J. Aircraft 12, 464-70, 1975).*

Comte-Bellot G., "Hot-Wire Anemometry", *Ann. Rev. Fluid Mech. 8, 109-231, 1976.*

Corsiglia V.R., Schwind R.G., Chigier N.A., "Rapid Scanning, Three-Dimensional Hot-Wire Anemometer Surveys of Wing-Tip Vortices", *J. Aircraft 10, 752-7, 1973.*

Coton F.N., De la Iglesia F., Galbraith R.A.McD., Horner M.B., "A Three-Dimensional Model of Low Speed Blade-Vortex Interaction", *20th European Rotorcraft Forum, Amsterdam, The Netherlands, Oct 1994.*

Crow S.C., "Stability Theory for a Pair of Trailing Vortices", *AIAA J. 8, 2172-79, 1970.*

Cutler A.D., Bradshaw P., "A Crossed Hot-Wire Technique for Complex Turbulent Flows", *Exp. Fluids 12, 17-22, 1991.*

Dacles-Mariani J., Zilliac G.G., Chow J.S., Bradshaw P., "Numerical/Experimental Study of a Wingtip Vortex in the Near Field", *AIAA J. 33, p1561-8, Sept. 1995.*

Davis S.S., Chamg I.C., "The Critical Role of Computational Fluid Dynamics in Rotary Wing Aerodynamics", *Vertica 11, 43-63, 1987.*

De la Iglesia F., "Development of a Fully Unsteady Blade-Vortex Interaction Model", *University of Glasgow, Dept. of Aerospace Eng. Report, 1993.*

Donaldson C. duP., Bilanin A.J., "Vortex Wakes of Conventional Aircraft", *AGARD-AG-204, May 1975.*

Dosanjh D.S.,Gasparek E.P., Eskinazi S., "Decay of a Trailing Vortex", *Aero. Quarterly 13, 167-188, May 1962.*

Ellin A.D.S., "An In-Flight Investigation of Lynx AH Mk5 Main Rotor/Tail Rotor Interactions", *19th European Rotorcraft Forum, Cernobbio, Italy, Sept. 1993.*

Ellin A.D.S., "An In-Flight Experimental Investigation of Helicopter Main Rotor/Tail Rotor Interactions", *PhD Dissertation, University of Glasgow, Dept. of Aerospace Eng., 1993.*

Erickson L.L., Madson M.D., Woo A.C., "Application of the TRAN AIR Full-Potential Code to the F-16A", *J.Aircraft 24, 540-5, Aug. 1987.*

Farassat F., Brentner K.S., "The Uses and Abuses of the Acoustic Analogy in Helicopter Rotor Noise Prediction", *J. American Helicopter Soc. 32, 29-36, June 1987.*

Favier D., Maresca C., Castex A., Barbi C., "Vortex Influence on Oscillating Airfoils at High Angle of Attack", *J.Aircraft 24, 424-32, 1987.*

Favier D., Nsi Mba M., Barbi C., Maresca C., "A Free Wake Analysis for Hovering Rotors and Advancing Propellers", *Vertica 11, 493-511, 1987.*

Felker F.F., Quackenbush T.R., Bliss D.B., Light J.S., "Comparisons of Predicted and Measured Rotor Performance in Hover Using a New Free Wake Analysis", *Vertica 14, 361-383, 1990.*

Francis M.S., Kennedy D.A., "Formation of a Trailing Vortex", *J. Aircraft 16, 148-54, March 1979.*

Gessow A., "An assessment of Current Helicopter Theory in Terms of Early Developments", *5th Nikolsky Lecture, 41st Annual Forum of the American Helicopter Soc., May 1985.*

Govindaraju S.P., Saffman P.G., "Flow in a Turbulent Line Vortex", *Phys. Fluids 14, 2074-80, 1971.*

Graber A., Rosen A., "A Parametric Investigation of a Free Wake Analysis of Hovering Rotors", *Vertica 12, 179-96, 1988.*

Graham W.R., "Experimental Assessment of the Extended Betz Method for Wake Vortex Prediction", *AGARD CP-584, Nov. 1996.*

Gray R.B., "Vortex Modelling for Rotor Aerodynamics - The 1991 Alexander A. Nikolsky Lecture", *J. American Helicopter Soc. 37, 3-14, Jan. 1992.*

Hall M.G., "The structure of Concentrated Vortex Cores", *Prog. Aero. Sci., Vol. 7, 53-110, 1966.*

Hall M.G., "Vortex Breakdown", *Ann. Rev. Fluid Mech. 4, 195-217, 1972.*

Ham N.D., "Some Preliminary Results from an Investigation of Blade-Vortex Interaction", *J. American Helicopter Soc. 19, 45-48, June 1974.*

Ham N.D., "Some Conclusions from an Investigation of Blade-Vortex Interaction", *J. American Helicopter Soc. 20, 26-31, Oct. 1975.*

Hansford R.E., "Rotor Load Correlation with the British Experimental Rotor Program Blade", *J. American Helicopter Soc. 32, 43-53, July 1987.*

Hardin C., Lamkin S.L., "Concepts for Reduction of Blade/Vortex Interaction Noise", *J. Aircraft 24, 120-25, 1987.*

Hess J.L., "Panel Methods in Computational Fluid Dynamics", *Ann. Rev. Fluid Mech. 22, 255-74, 1990.*

Hess J.L., Smith A.M.O., "Calculation of Non-lifting Potential Flow About Arbitrary Three-Dimensional Bodies", *J. Ship Res. 8, 22-42, 1964.*

Hess J.L., Smith A.M.O., "Calculation of Potential Flow About Arbitrary Bodies", *Prog. Aero. Sci. 8, 1-138, 1967.*

Hirota M., Hideomi F., Hajime Y., "Influences of Velocity Gradient on Hot-Wire Anemometry with an X-Wire Probe", *J. Phys. E: Sci. Instrum. 21, 1077-84, 1988.*

Hoad D.R., "Helicopter Model Scale Results of Blade-Vortex Interaction Impulsive Noise as Affected by Tip Modification", *36th Ann. Forum of the Americam Helicopter Society, May 1980.*

Hoeijmakers H.W.M., "Panel Methods for Aerodynamic Analysis and Design", *AGARD-R-783, Special Course on Engineering Methods in Aerodynamic Analysis and Design of Aircraft, Jan. 1992.*

Hoffmann E.R., Joubert P.N., "Turbulent Line Vortices", *J. Fluid Mech. 16, 395-411, 1963.*

Horner M.B., Saliveros E., Galbraith R.A.McD., "An Experimental Investigation of the Oblique Blade-Vortex Interaction", *17th European Rotorcraft Forum, Berlin, Germany, Sept. 1991.*

Horner M.B., Stewart J.N., Galbraith R.A.McD., Grant I., Coton F.N., Smith G.H., "Preliminary Results from a Particle Image Velocimetry Study of Blade-Vortex Interaction", *19th European Rotorcraft Forum, Cernobbio, Italy, Sept. 1993.*

Horner M.B., Stewart J.N., Galbraith R.A.McD., Grant I., Coton F.N., Smith G.H., "An Examination of Blade Vortex Interaction Utilising Pressure Measurements And Particle Image Velocimetry", *University of Glasgow, Dept. of Aerospace Eng. Internal Rep. 9427, 1994.*

Horner M.B., Stewart J.N., Galbraith R.A.McD., Grant I., Coton F.N., "An Examination of Vortex Deformation during Blade-Vortex Interaction Utilising Particle Image Velocimetry", *19th Congress of the International Council of the Aero. Sciences, Anaheim, California, Sept 1994.*

Horner M.B., Stewart J.N., Galbraith R.A.McD., Grant I., Coton F.N., Smith G.H., "Preliminary Results from a Particle Image Velocimetry Study of Blade Vortex Interaction", *Aero. J., 91-8, March 1995.*

Hopkins H., " Fastest Blades in the World", *Flight International, 24-27, Dec. 1986. (Also Flight International, 35, Aug. 1985)*

Huenecke K., "Structure of a Transport Aircraft-Type Near Field Wake", *AGARD CP-584, Nov. 1996.*

Iversen J.D., "Correlation of Turbulent Trailing Vortex Decay Data", *J. Aircraft 13, 338-42, 1976.*

Jenkins J.L., "Rotorcraft Design Technology Trends at Bell Helicopter Textron", *23rdEuropean Rotorcraft Forum, Dresden, Germany, Sept. 1997.*

John J., Schobeiri T., "A Simple and Accurate Method of Calibrating X-Probes", *J. Fluids Eng. 115, 148-152, March 1993.*

Johnson F.D., Eckelmann H., "A Variable Angle Method of Calibration for X-Probes Applied to Wall-Bounded Turbulent Shear Flow", *Exp. Fluids 2, 121-30, 1984.*

Johnson F.T., "A General Panel Method for the Analysis and Design of Arbitrary Configurations in Incompressible Flows", *NASA CR-3079, May 1980.*

Johnson W., " Development of a Comprehensive Analysis for Rotorcraft-I.Rotor Model and Wake Analysis",*Vertica 5, 99-129,1981.*

Johnson W., "Airloads and Wake Models for a Comprehensive Helicopter Analysis", *Vertica 14, 255-300, 1990.*

Jordan P.F., "Structure of Betz Vortex Cores", *J. Aircraft 10, 691-3, 1973.*

Jorgensen F.E., "Directional Sensitivity of Wire and Fiber Film", *DISA Info. 11, May 1971.*

Katz J., Maskew B., "Unsteady Low-Speed Aerodynamic Model for Complete Aircraft Configurations",*J. Aircraft 25, 302-10, 1988.*

Kokkalis A., "An Experimental Investigation of Parallel Blade-Vortex Interaction for a NACA0015 Airfoil", *PhD Dissertation, University of Glasgow, Dept. of Aerospace Eng., 1988.*

Kufeld R.M., Bousman W.G., "UH-60A Helicopter Rotor Airloads Measured in Flight", *Aero J. , 217-27, May 1997.*

Lakshminarayana B., "Three Sensor Hot-Wire/Film Technique for Three-Dimensional Mean and Turbulence Flow Field Measurement", *TSI Quart., Vol. 8, Issue 1, 1982.*

Lakshminarayana B., Davino R., "Sensitivity of three Sensor Hot-Wire Probe to Yaw and Pitch Variation", *J. Fluids Eng. 110, 120-122, June 1988.*

Landgrebe A.J., "An Analytical Method for Predicting Rotor Wake Geometry", *J. American Helicopter Soc. 14, 20-32, Oct. 1969.*

Landgrebe A.J., Moffitt R.C., Clark D.R., "Aerodynamic Technology for Advanced Rotorcraft-Parts I & II", *J. American Helicopter Soc. 22, (I) 21-27, April 1977, (II) 2-9, July 1977.*

Lauder B.E., "Modelling the Formation and Dispersal of Streamwise Vortices in Turbulent Flow", *35th Lanchester Lecture, Aero. J., 419-31, Dec. 1995.*

Leibovich S., "The Structure of Vortex Breakdown", *Ann. Rev. Fluid Mech. 10, 221-46, 1978.*

Leishman J.G., Baker A., Coyne A., "Measurements of Rotor Tip Vortices Using Three-Component Laser Doppler Velocimetry", *J. American Helicopter Soc. 41, 342-353, Oct. 1996*

Leishman J.G., Bagai A., "Free-Wake Analysis of Twin-Rotor Systems", *20th European Rotorcraft Forum, Amsterdam, The Netherlands, Oct. 1994.*

Lekakis I.C., Adrian R.J., Jones B.G., "Measurement of Velocity Vectors with Orthogonal and Non-Orthogonal Triple-Sensor Probes", *Exp. Fluids 7, 228-40, 1989.*

Leonard A., "Vortex Methods for Flow Simulation - A Review", *J. Comp. Phys. 37, 289-335, 1980.*

Leonard A., "Computing Three-Dimensional Incompressible Flows with Vortex Elements",*Ann. Rev. Fluid Mech. 17, 523-59, 1985.*

Leverton J.W., Pollard J.S., Wills C.D., "Main Rotor Wake/Tail Rotor Interaction", *Vertica 1, 213-221, 1977.*

Lezius D.K., "Study of the Far Wake Vortex Field Generated by a Rectangular Airfoil in a Water Tank", *NASA TM X-62274, May 1973.*

Logan A.H., "Vortex Velocity Distributions at Large Downstream Distances",*J. Aircraft 8, 930-932, 1971.*

Lowson M.V., "Progress Towards Quieter Civil Helicopters", *Aero. J. , 209-23, June/July 1992.*

Lowson M.V., Balmford D.E.H., "Future Advanced Technology Rotorcraft", *Aero. J. , 39-49, Feb. 1980.*

Lueptow R.M., Breuer K.S., Haritonidis J.H., "Computer-Aided Calibration of X-Probes Using a Look-Up Table", *Exp. Fluids 6, 115-8, 1988.*

Lyrintzis A.S., Koutsavdis E.K., Strawn R.C., "A Comparison of Computational Aeroacoustic Prediction Methods", *J. American Helicopter Soc. 42, 54-57, Jan. 1997.*

Margason R.J., Kjelgaard S.O., Sellers W.L., Morris C.E.K., Walkley K.B., Shields E.W., "Subsonic Panel Methods - A Comparison of Several Production Codes", *AIAA Paper 85-0280, Jan. 1985.*

Martin D.M., Fortin P.E., "VSAERO Analysis of Tip Planforms for the Free-Tip Rotor", *NASA CR-177487, June 1988.*

Maskew B., "Prediction of Subsonic Aerodynamic Characteristics: A Case for Low-Order Panel Methods", *J. Aircraft 19, 157-163, 1982.(Also AIAA paper 81-052, Jan 1981)*

Maskew B., "Program VSAERO, A Computer Program for Calculating the Non-Linear Aerodynamic Characteristics of Arbitrary Configurations", *NASA CR-166476, Dec. 1982.*

Maskew B., "Program VSAERO Theory Document: A Computer Program for Calculating Non-Linear Aerodynamic Characteristics of Arbitrary Configurations", *NASA CR-4023, Sept. 1987.*

Masson C.A., Green R.B., Galbraith R,A,McD., Coton F.N., "An Experimental Investigation of a Loaded Blade Interacting with Single and Twin Vortices", *Technical Specialists Meeting for Rotorcraft Acoustics & Aerodynamics, Williamsburg, USA, 1997.*

McCormick B.W., Tangler J.L., Sherrieb H.E., "Structure of Trailing Vortices", *J. Aircraft 5, 260-267, 1968.*

McCroskey W.J., "Some Rotorcraft Applications of Computational Fluid Dynamics", *NASA TM-100066, March 1988.*

McInerny S.A., Meecham W.C., Soderman P.T., "Pressure Fluctuations in the Tip Region of a Blunt Tipper Airfoil", *AIAA J.28,6-13, Jan. 1990.*

Miller R.H., "Rotor Hovering Performance Using the Method of Fast Free Wake Analysis", *J. Aircraft 20, 257-61, 1983.*

Mokry M., Digney J.R., Poole R.J.D., "Doublet-Panel Method for Half-Model Wind Tunnel Corrections", *J. Aircraft 24, 322-27, 1987.*

Moore D.W., Saffman P.G., "Axial Flow in Laminar Trailing Vortices", *Proc. R. Soc. Lond. A.333, 491-508, 1973.*

Moore D.W., "Vortex Motion", *Imperial College of Science and Technology, Inaugural Lecture, Jan 1976.*

Morino L., Kaprielian Z., Sipcic S.R., "Free Wake Analysis of Helicopter Rotors", *Vertica 9, 127-40, 1985.*

Morton B.R., " The Generation and Decay of Vorticity", *Geophys. Astrophys. Fluid Dynamics Vol. 28, 277-308, 1984.*

Mracek C.P., Kim M.J., Mook D.T., "Three-Dimensional Potential Flows by a Vorticity-Panel Method", *Comp. Fluids. 21, 31-42, 1992.*

Muller R.H.G., "Special Vortices at a Helicopter Rotor Blade", *J. American Helicopter Soc. 35, 16-22, Oct. 1990.*

Muller R.H.G., "Winglets on Rotor Blades in Forward Flight - A Theoretical and Experimental Investigation", *Vertica 14, 31-46, 1990.*

Muller R.H.G., Staufenbiel R., "The Influence of Winglets on Rotor Aerodynamics", *Vertica 11, 601-18, 1987.*

Muller U.R., "On the Accuracy of Turbulence Measurements with Inclined Hot-Wires", *J. Fluid Mech. 119, 155-72, 1982.*

Muller U.R., "Comparison of Turbulence Measurements with Single, X and Triple Hot-Wire Probes", *Exp. Fluids 13, 208-216, 1992.*

Mullins J., "Trails of Destruction", *New Scientist, 16th Nov. 1996.*

Narinder K.T., Chevray R., "Cross-Wire Anemometry in High Intensity Turbulence", *J. Fluid Mech. 71, 785-800, 1975.*

Nathman J.K., Frank J.H., " Application of VSAERO to Internal Flows", AIAA Paper 87-2415, Aug. 1987.

Newman B.G., "Flow in a Viscous Trailing Vortex", *Aero. Quarterly 10, 149-162, May 1959.*

Orloff K.L., Grant G.R., "The application of a scanning Laser Doppler Velocimeter to Trailing Vortex Definition", *AIAA Paper 73-680, July 1973.*

Owen P.R., "The Decay of a Turbulent Trailing Vortex", *Aero. Quarterly 21, 69-78, Feb. 1970. (Also ARC 25818,1964).*

Padakannaya R., "Experimental Study of Rotor Unsteady Airloads due to Blade-Vortex Interaction", *NASA CR-1909, Nov. 1971.*

Padakannaya R., "The Vortex Lattice Method for the Rotor-Vortex Interaction Problem", *NASA CR-2421, July 1974.*

Perry F.J., "Aerodynamics of the World Speed Record", *43rd Annual Forum of the American Helicopter Soc., St. Louis, May 1987.*

Phillippe J.J., Roesch P., Dequin A.M., Cler A., "A Survey of Recent Advances in Helicopter Aerodynamics", *AGARD Lecture Series No. 139 on Helicopter Aeromechanics, May 1985.*

Poling D.R., Dadone L., Telionis D.P., "Blade-Vortex Interaction", *AIAA Paper 87-0497, Jan. 1987.*

Preisser J.S., Brooks T.F., Martin R.M., "Recent Studies of Rotorcraft Blade-Vortex Interaction Noise", *J. Aircraft 31, 1009-15, 1994.*

Quackenbush T.R., Bliss D.B., "Free Wake Flow Field Calculations for Rotorcraft Interactional Aerodynamics", *Vertica 14, 313-27, 1990.*

Quackenbush T.R., Wachspress D.A., Botschitsch A.H., "Rotor Aerodynamic Loads Computation Using a Constant Vorticity Contour Free Wake Model", *J.Aircraft 32, 911-20, 1995.*

Ramachandran K., "The Free-Wake Prediction of Rotor Hover Performance using a Vortex Embedding Method", *AIAA Paper 89-0638, Jan. 1989.*

Rand O., Rosen A., "A Lifting Line Theory for Curved Helicopter Blades in Hovering and Axial Flight", *J. American Helicopter Soc. 29, 3-10, July 1984.*

Rand O., Rosen A., "An Unsteady Prescribed Wake Model for a Helicopter Rotor in Forward Flight", *J. American Helicopter Soc. 29, 11-21, Oct. 1985.*

Roberts K.V., Christiansen J.P., "Topics in Computational Fluid Mechanics", *Comp. Phys. Comm. 3, 14-32, 1972.*

Roggero F., Larguier R., "Aerodynamic Calculation of Complex Three-Dimensional Configurations", *J. Aircraft 30, 561-70, 1993.*

Rosen A., Graber A., "Free Wake Model of Hovering Rotors having Straight or Curved Blades", *J. American Helicopter Soc. 33, 11-19, July 1988.*

Rossow V.J., "On the Inviscid Rolled-Up Structure of Lift-Generated Vortices", *NASA TM X-62224, Jan 1973.*

Rossow V.J., "Theoretical Study of Lift-Generated Vortex Wakes Designed to Avoid Rollup", *AIAA J. 13, 476-84, 1975.*

Rossow V.J., "Convective Merging of Vortex Cores in Lift-Generated Wakes", *J. Aircraft 14, 283-290, 1977.*

Rossow V.J., "Prospects for Destructive Self-Induced Interactions in a Vortex Pair", *J. Aircraft 24, 433-40, 1987.*

Sadler S.G., "A Method for Predicting Helicopter Wake Geometry, Wake-Induced Flow and Wake Effects on Blade Airloads", *27th Annual Forum of the American Helicopter Soc., May 1971.*

Saffman P.G., "Structure of Turbulent Line Vortices", *Phys. Fluids 16, 1181-88, 1973.*

Saffman P.G., "The Structure and Decay of Trailing Vortices", *Archives of Mechanics 26, 423-439, 1974.*

Saffman P.G., Szeto R., "Equilibrium shapes of a pair of equal uniform vortices", *Phys. Fluids 23, 2339-42, 1980.*

Saffman P.G., "Dynamics of Vorticity", *J.Fluid Mech. 106, 49-58, 1981.*

Sarpkaya T., Daly J.J., "Effect of Ambient Turbulence on Trailing Vortices", *J. Aircraft 24, 399-404, 1987.*

Sarpkaya T., "Computational Methods With Vortices - The 1988 Freeman Scholar Lecture", *J. Fluids Eng. 111, 5-52, March 1989.*

Schmitz F.H., Yu Y.H., "Helicopter Impulsive Noise: Theoretical and Experimental Status", *NASA TM-84390, 1983.*

Schultz K.-J. et. al., "A Parametric Windtunnel Tests on Rotorcraft Aerodynamics and Aeroacoustics- Tests Procedures and Representative Results", *Aero. J.,143-54, April 1997.*

Scott M.T., Sigl D., Strawn R.C., " Computational and Experimental Evaluation of Helicopter Rotor Tips for High-Speed Flight", *J. Aircraft 28,403-409, June 1991.*

Scully M.P., "Computation of Helicopter Rotor Wake Geometry and its Influence on Rotor Harmonic Airloads", *ASRL TR-178-1, M.I.T., March 1975.*

Seath D.D., "Vortex-Airfoil Interaction Tests", *2nd Atmos. Flight Mech. Conf., Palo Alto, California, Sept. 1972.*

Seath D.D., Kin J.-M., Wilson D.R., "An Investigation of the Parallel Blade-Vortex Interaction in a Low Speed Wind Tunnel", *AIAA Paper 87-1345, June 1987.*

Sheridan P.F., Smith R.P., "Interactional Aerodynamics - A New Challenge to Helicopter Technology", *35th American Helicopter Society Forum, Paper 79-59, May 1979.*

Smith J.H.B., "Vortex Flows in Aerodynamics", *Ann. Rev. Fluid Mech. 18, 221-42, 1986.*

Splettstoesser W.R et. al.., "Key Results from a Higher Harmonic Control Aeroacoustic Rotor Test (HART)", *J. American Helicopter Soc. 42 , 58-78, Jan. 1997.*

Spreiter J.R., Sacks A.H., "The Rolling Up of the Trailing Vortex Sheet and Its Effect on the Downwash Behind Wings", *J. Aero. Sci. 18,21-32, Jan. 1951.*

Squire H.B., "The Growth of a Vortex in Turbulent Flow", *Aero. Quarterly 16, 302-306, Aug. 1965. (Also ARC 16666, 1954).*

Srinivas V., Chopra I., Haas D., McCool K., "Prediction of Yaw Control Effectiveness and Tail Rotor Loads", *19th European Rotorcraft Forum, Cernobbio (Como), Italy, Sept. 1993.*

Staufenbiel R.W., "Structure of Lift-Generated Rolled-Up Vortices", *J. Aircraft 21, 737-44, 1984.*

Straus J., Renzoni P., Mayle R.E., "Airfoil Pressure Measurements During a Blade-Vortex Interaction and a Comparison with Theory", *AIAA Paper 88-0669, Jan. 1988. (Also AIAA J. 28,222-8,Feb. 1990)*

Strenfeld H., "Recent Developments in Helicopter Noise", *Aero. J. , 306-13, August 1979.*

Stroub R.H., Young L.A., Keys C.N., Cawthorne M.H., "Free-Tip Rotor Wind Tunnel Test Results", *J. American Helicopter Soc. 31, 19-26, July 1986.*

Surendraiah M., "An Experimental Study of Rotor Blade-Vortex Interaction", *M.S. Thesis, The Pennsylvania State University, Dec. 1969.*

Tangler J.L., "The Design and Testing of a Tip to Reduce Blade Slap", *31st Annual Forum of the American Helicopter Soc., May 1975.*

Tangler J.L., "Experimental Investigation of the Subwing Tip and its Vortex Structure", *NASA CR-3058, 1978.*

Tavoularis S., "Simple Corrections for the Temperature Sensitivity of Hot-Wires", *Rev. Sci. Instrum. 54, 741-43, June 1983.*

Tinoco E.N., Ball D.N., Rice F.A., "PAN AIR Analysis of a Transport High-Lift Configuration", *J. Aircraft 24, 181-87, 1987.*

Tyler D.J., Vincent A.H., "Future Rotorcraft Technology Developments", *Aero. J., 451-60, Dec. 1996.*

Van der Wall B.G., "CP-ROT, First Results from Pressure Instrumented BO-105 Hingeless Model Rotor Tests", *19th European Rotorcraft Forum, Cernobbio, Italy, Sept. 1993.*

Vatistas G.H., Kozel V., Mih W.C., "A Simpler Model for Concentrated Vortices", *Exp. Fluids 11, 73-6, 1991.*

Vatistas G.H., Lin S., Li P.M., "A Simpler Profile for the Tangential Velocity in Vortex Chambers", *Exp. Fluids 6, 135-7, 1988.*

Verstynen H.A., Dunham R.E., "A Flight Investigation of the Trailing Vortices Generated by a Jumbo Jet Transport", *NASA TN D-7172, April 1973.*

Vuillet A., "Rotor and Blade Aerodynamic Design", *AGARD-R-781, Aerodynamics of Rotorcraft, 1990.*

Wanstall B., "BERP Blades: Key to the 200-Knot Helicopter", *Interavia, 322-4, March 1986.*

Widnall S.E., Wolf T.L., "Effect of Tip Structure on Helicopter Noise Due to Blade-Vortex Interaction", *J. Aircraft 17, 705-11, 1980. (application of Betz Vortex Model)*

Widnall S.E., "The Structure and Dynamics of Vortex Filaments", *Ann. Rev. Fluid Mech. 7, 141-65, 1975.*

Wieser W., Kohler G., "Tail Rotor Performance in the Presence of Main Rotor, Ground and Winds", *J. American Helicopter Soc. 19, 2-9, July 1974.*

Williams G.M., "Viscous Modelling of Wing-Generated Trailing Vortices", *Aero. Quart. 25, 143-54, 1974.*

Youngren H.H., Bouchard E.E., Coppersmith R.M., Miranda L.R., "Comparison of Panel Formulations and its Influence on the Development of QUADPAN, an Advanced Low Order Method", *AIAA Paper 83-1827, July 1983.*

FIGURES

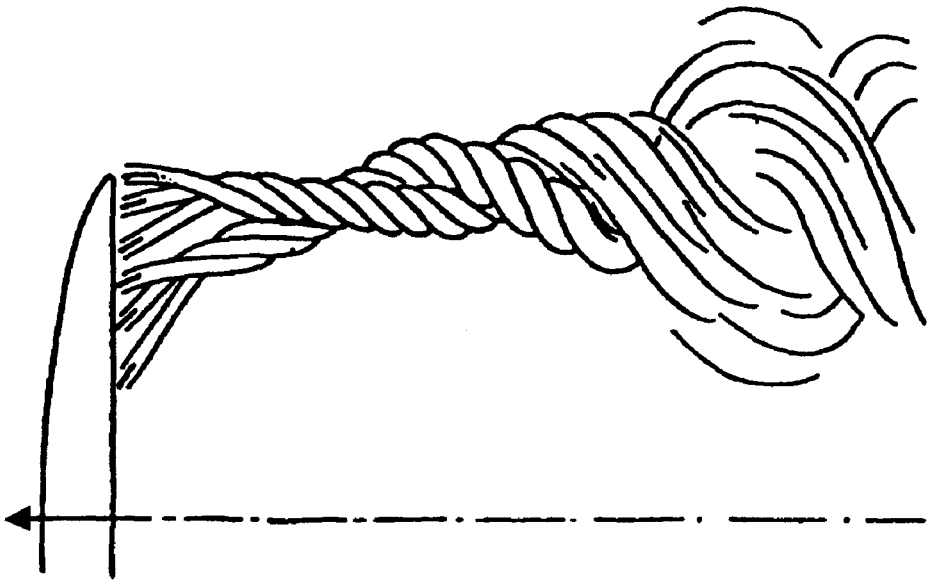

Figure 1.1- Trailing vortices and their tendency to intercoil (Lanchester (1907) taken from Lauder (1995)).

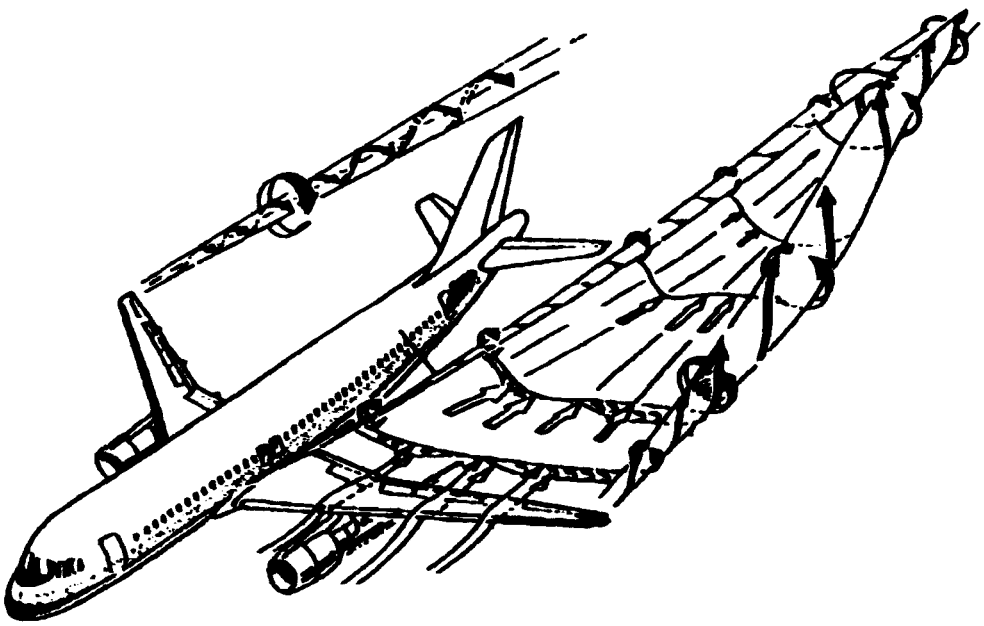

Figure 1.2- Illustration of the flow field associated with a commercial fixed wing aircraft (Hueneche (1996)).

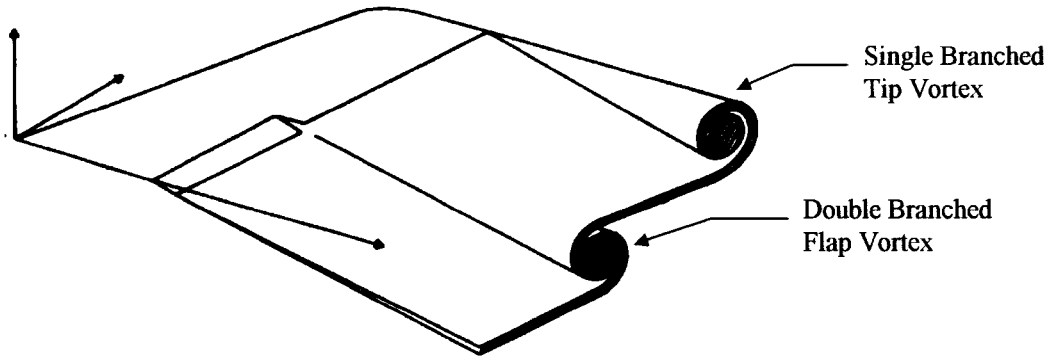

Figure 1.3- Idealisation of flap-down (landing configuration) vortex generation.
(taken from AGARD CP-494)

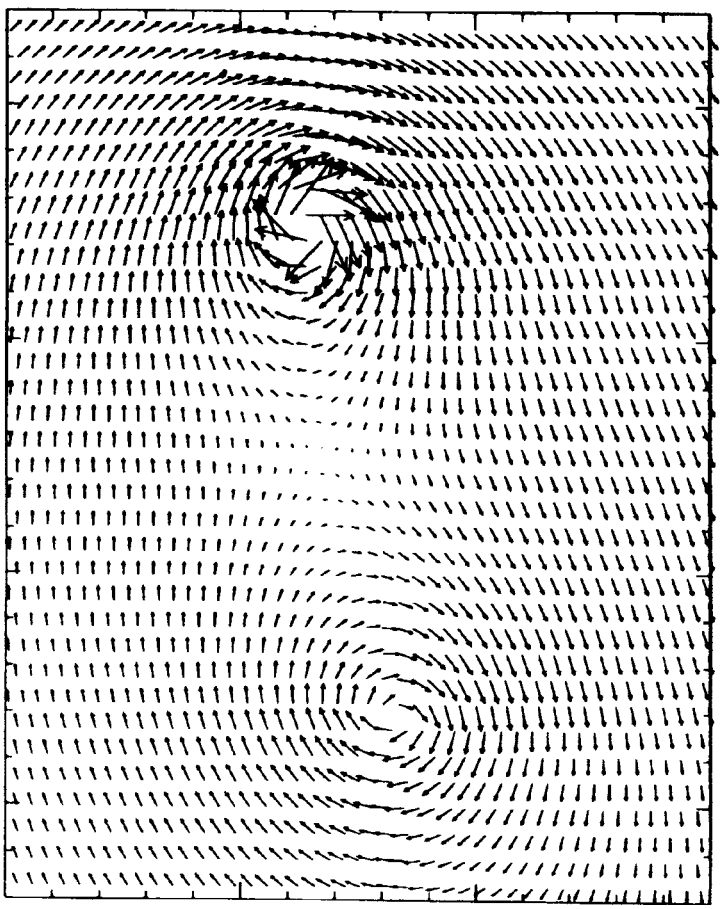

Figure 1.4- Flow field measurements behind a finite wing with flaps deployed
(Bruin et al. (1996)).

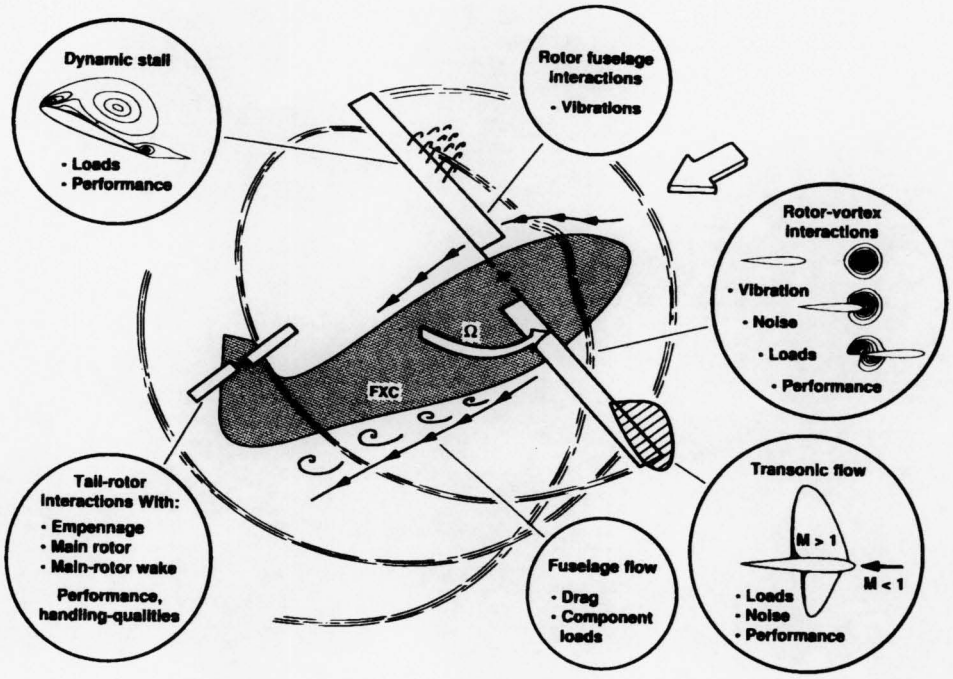

Figure 1.5- Illustration depicting the complex flow field associated with helicopters (Caradonna (1990)).

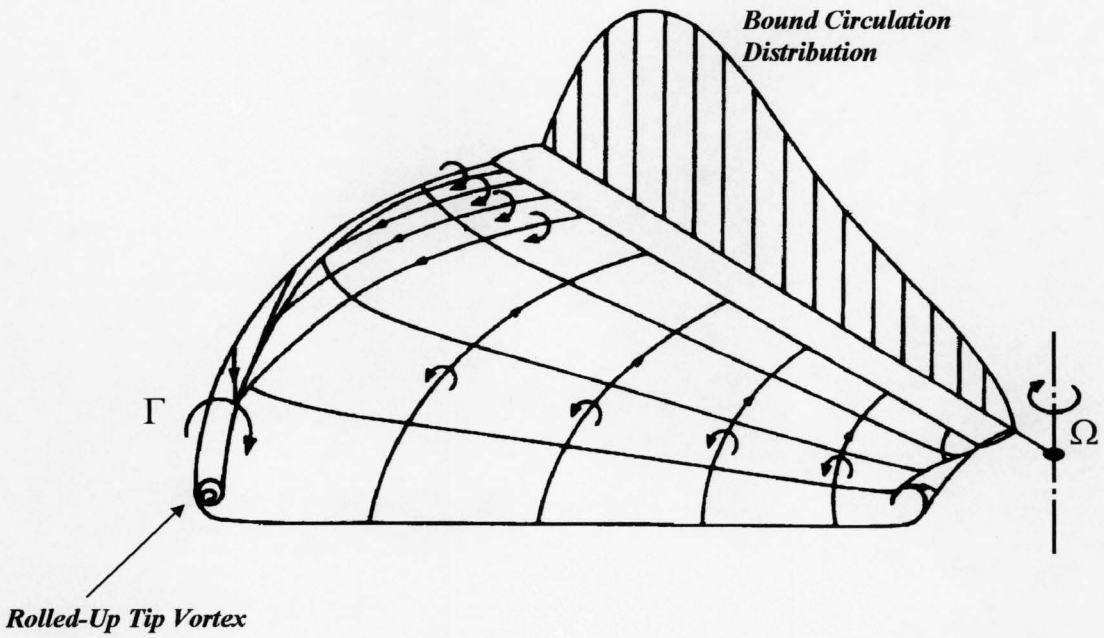

Figure 1.6- Illustration of the roll-up of the wake vortex sheet (as generated by a rotating blade) to form the tip vortex.

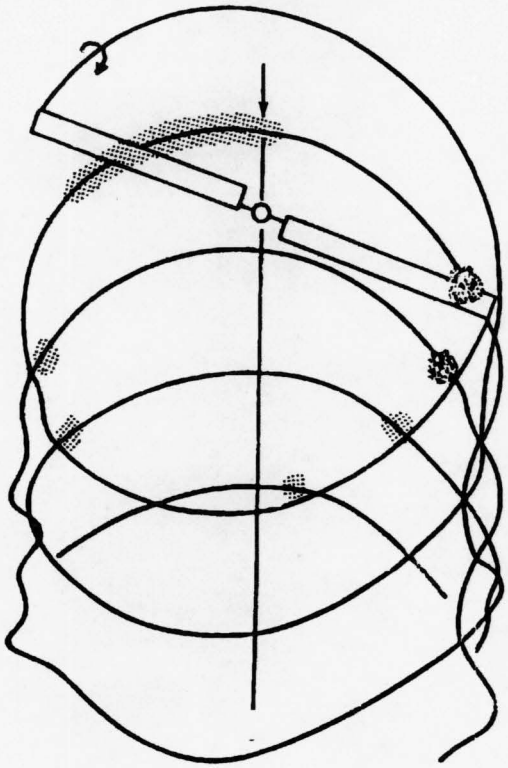

Figure 1.7- Regions of main rotor Blade-Vortex Interactions (dependent on flight conditions).

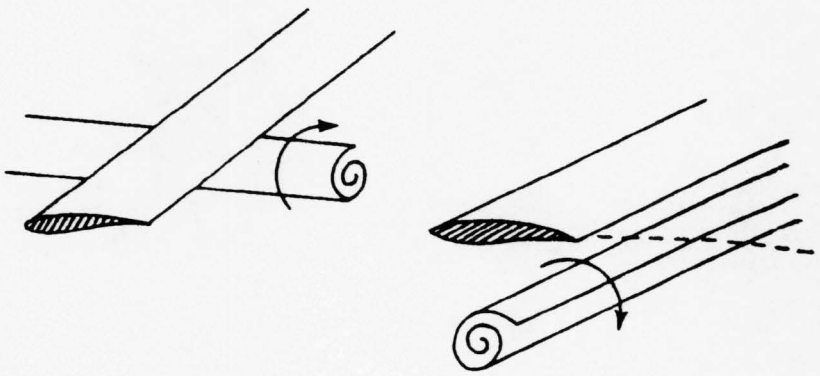

Figure 1.8- Sketches of how vortex and blade geometry can vary in different BVI regions.

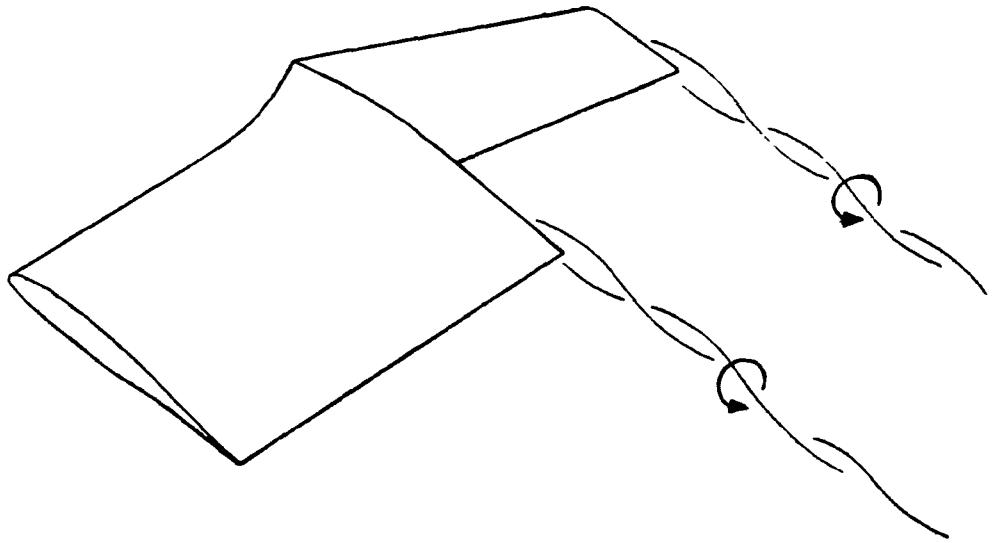

Figure 1.9- Illustration of vortex system associated with the Westland Helicopters Vane Tip (Borcklehurst & Pike (1994)).

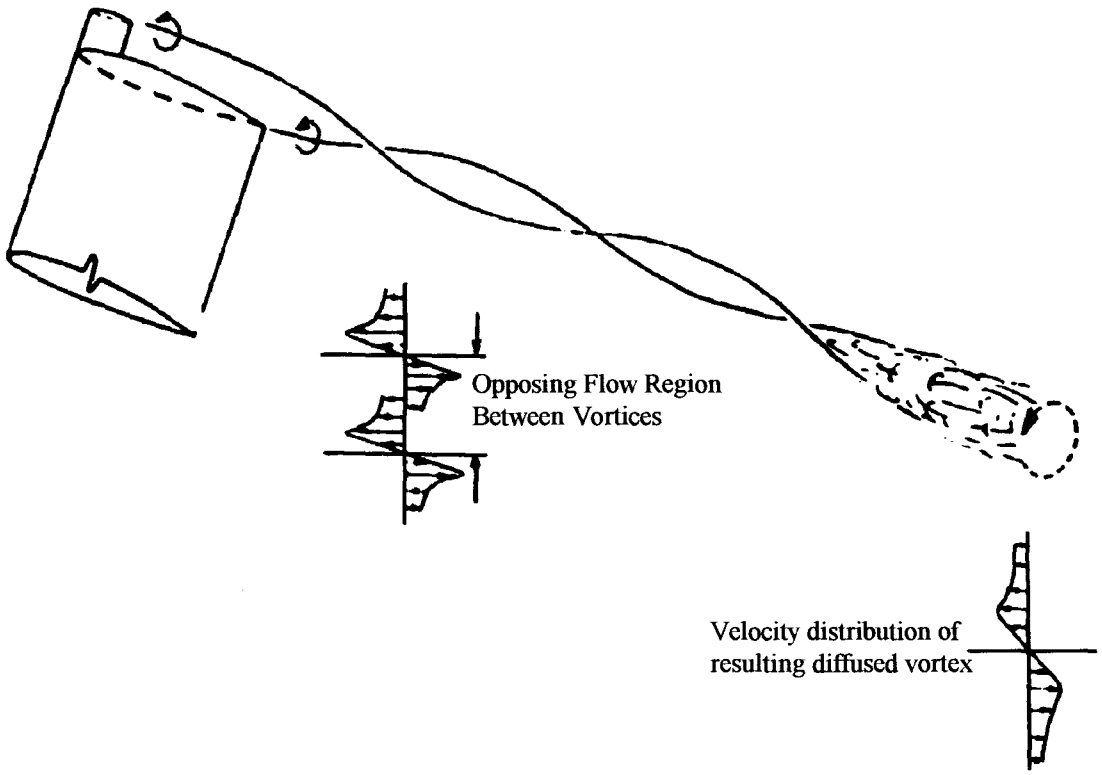

Figure 1.10- Illustration of the vortex system generated by the 'Sub Wing' as proposed by Tangler (1978).

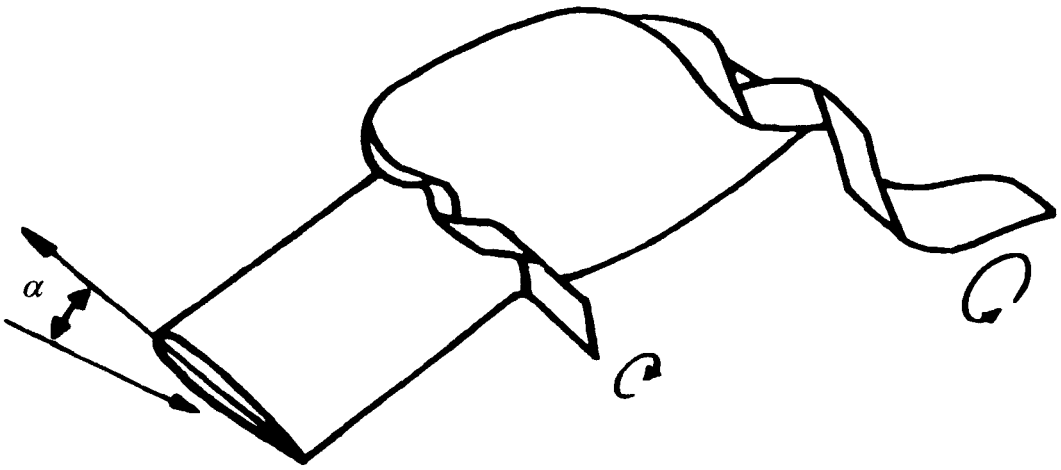

Figure 1.11- Illustration of the vortex system associated with the Westland Helicopters BERP Tip at high incidence (Scott et al.(1991)).

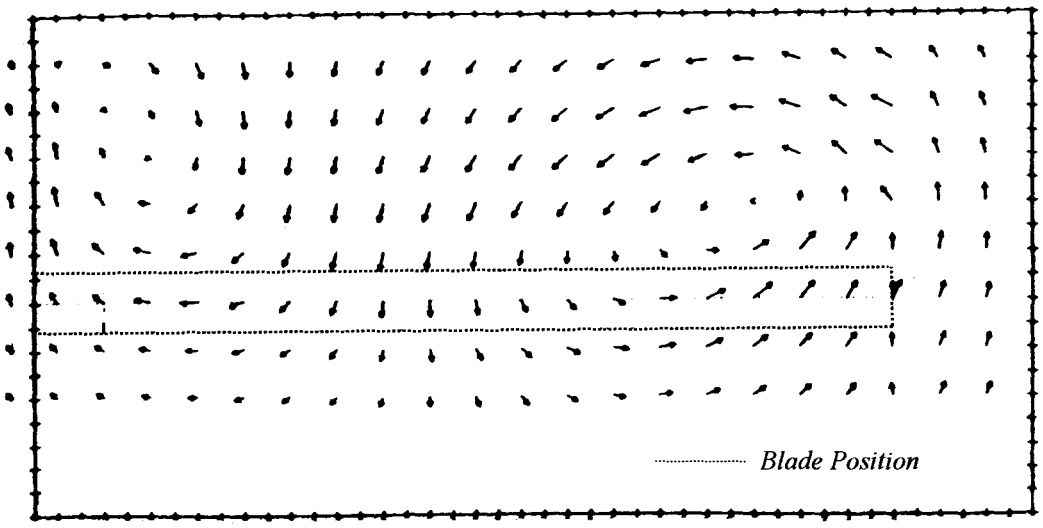

1 inch increments

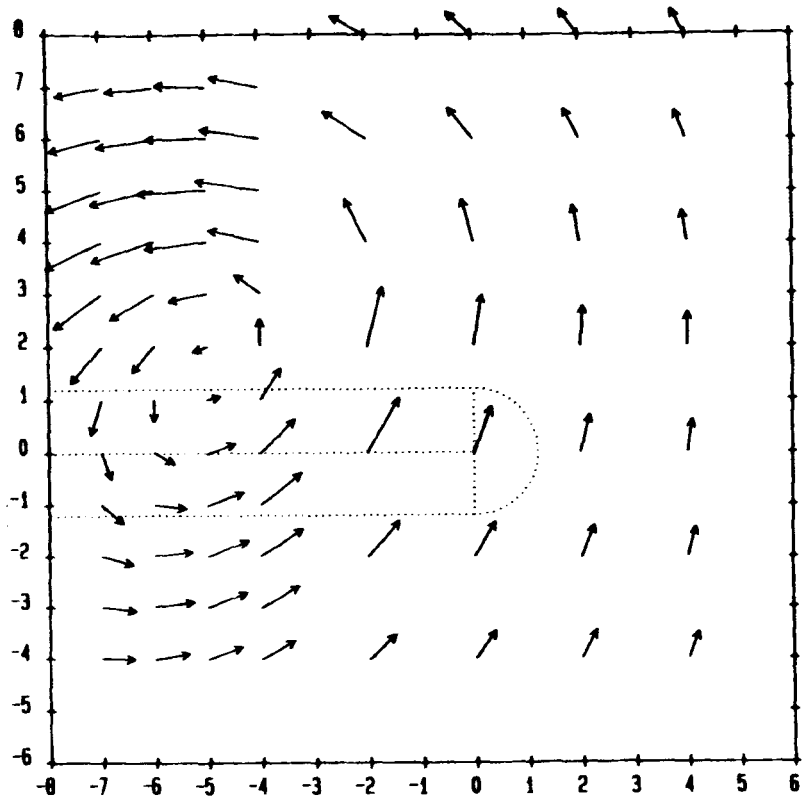

Figure 1.12- Hot-Wire measurements behind the BERP tip at high incidence (conducted by Scott et al. (1991)).

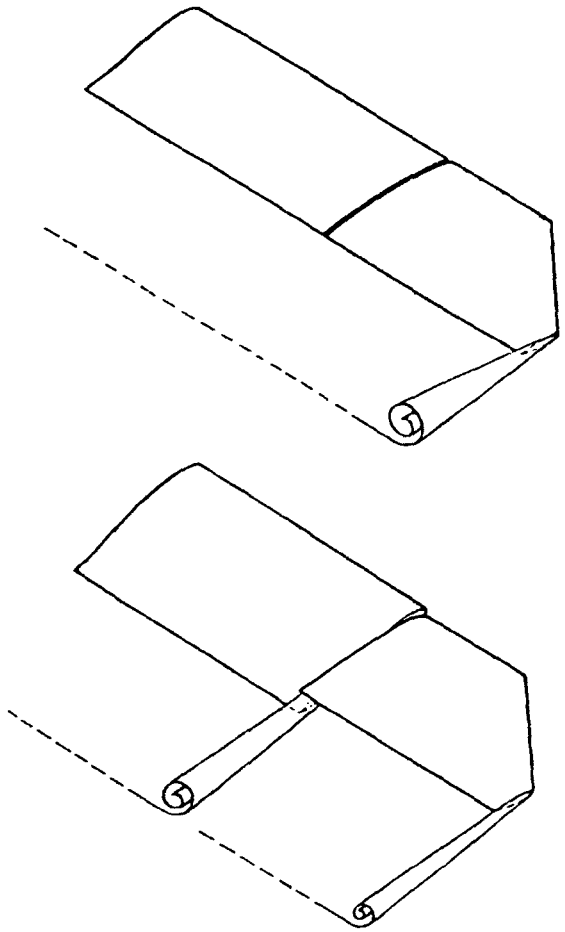

Figure 1.13- Illustration of two possible vortex systems associated with the Free-Tip concept (Martin & Fortin (1988)).

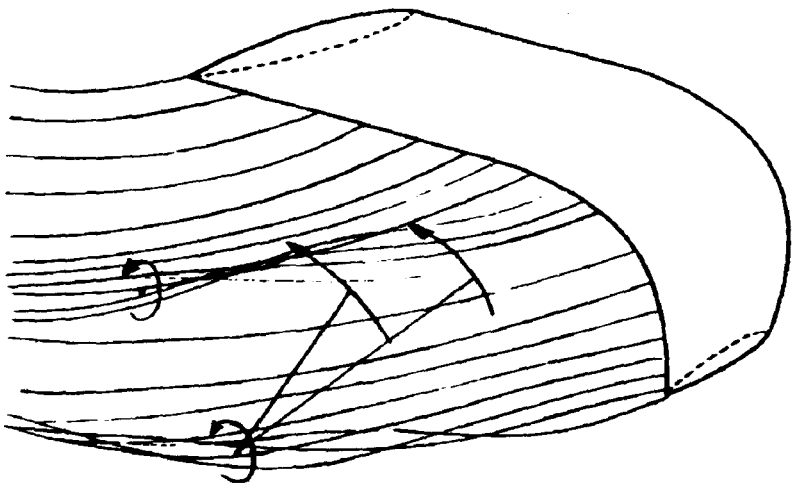

Figure 1.14- Illustration of vortex system associated with the Muller (1990) winglet.

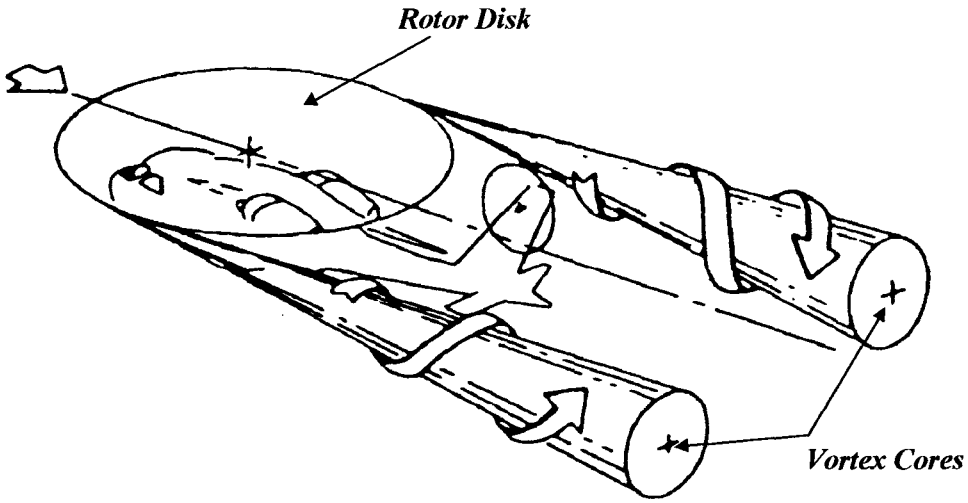

Figure 1.15- Sketch showing how the wake behind a helicopter in forward flight can resemble that of a fixed wing aircraft (Ellin (1993)).

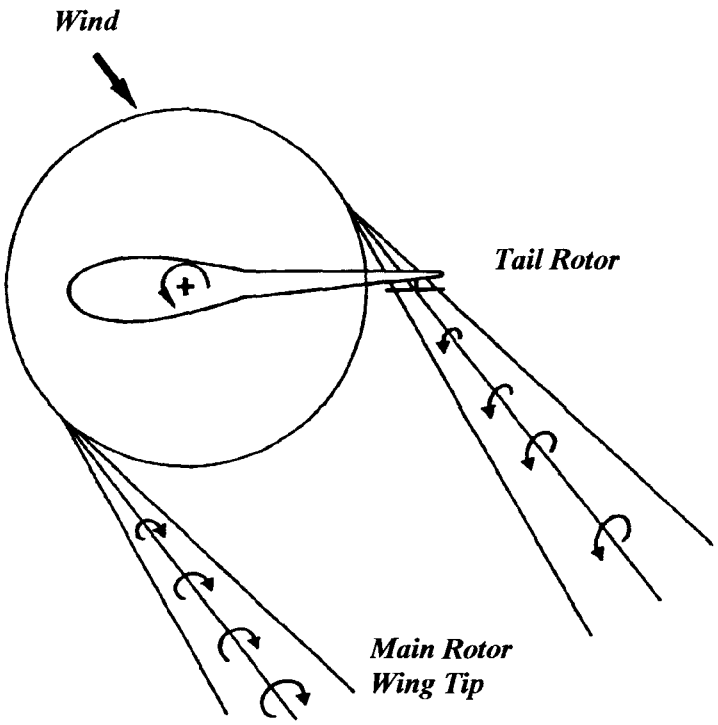

Figure 1.16- Illustration of main rotor tip vortex/tail rotor interaction in quartering flight (Vuillet (1990)).

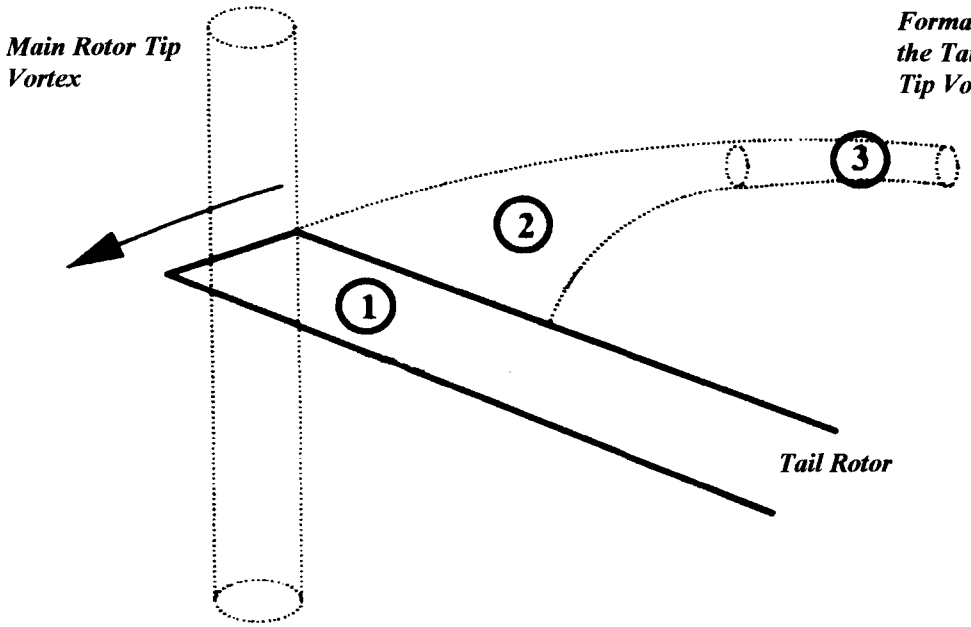

Figure 1.17- Illustration of Tail rotor BVI depicting three main interaction regions with blade(1), during roll-up(2), and with trailing tail rotor tip vortex(3) (Ellin(1993)).

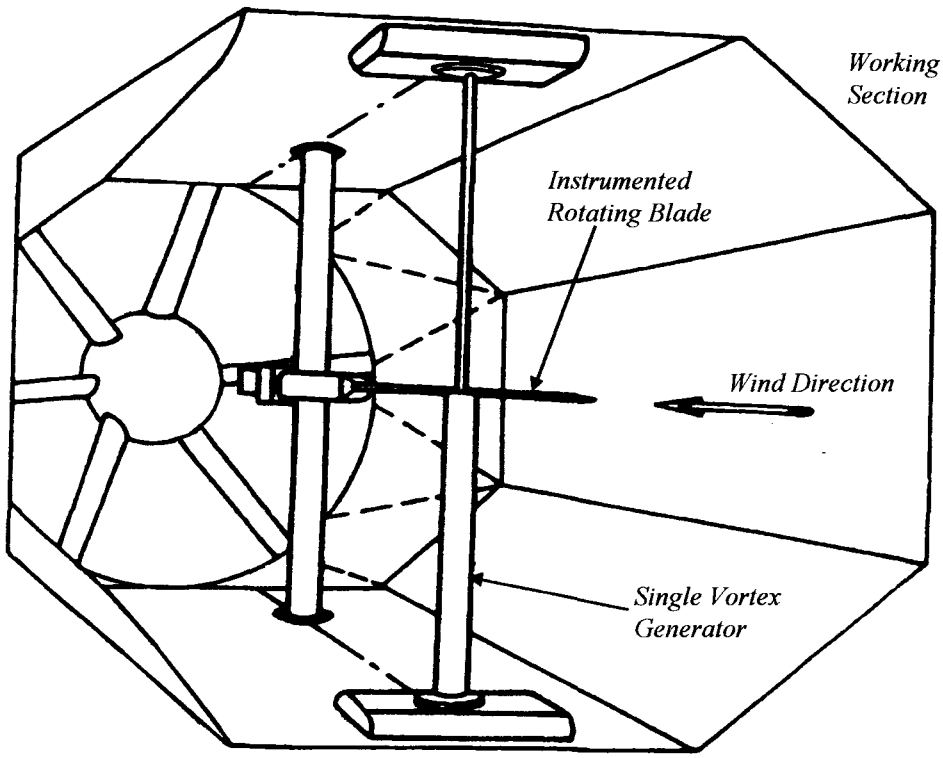

Figure 1.18- Illustration of Glasgow University's BVI Facility.

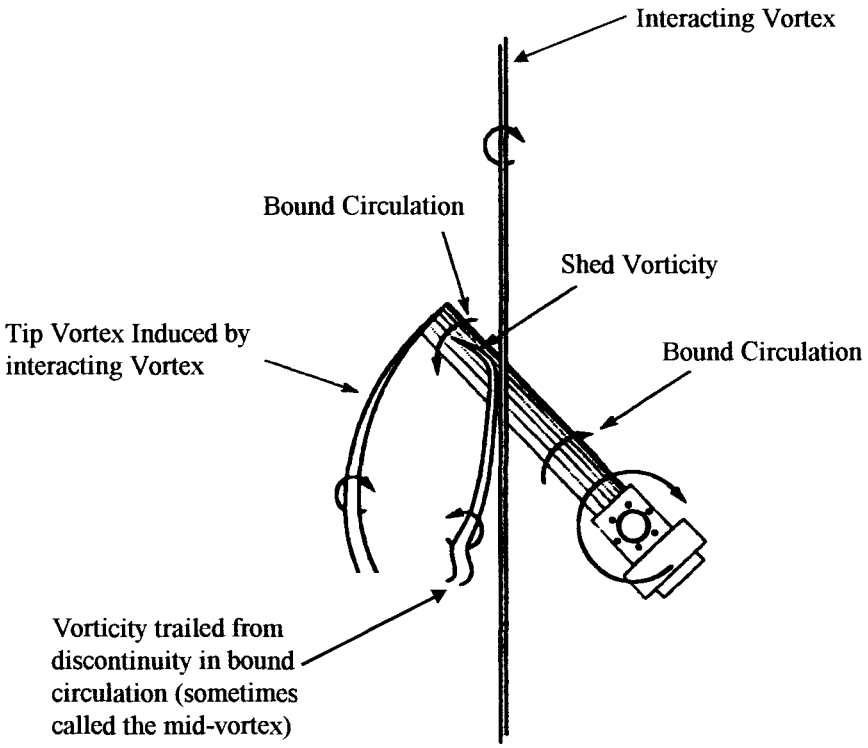

Figure 1.19- Illustration of oblique BVI on an unloaded blade (Horner (1994)).

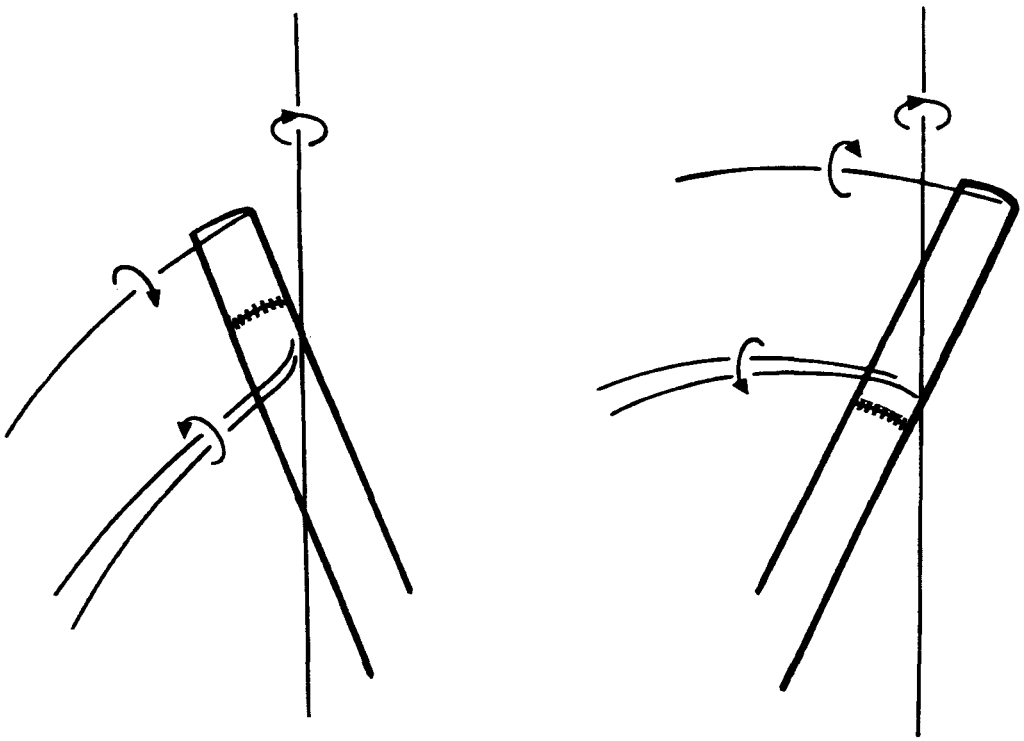

Figure 1.20- Illustration of different vortices generated on an unloaded rotor blade by an interacting vortex in different quadrants (Horner (1994)).

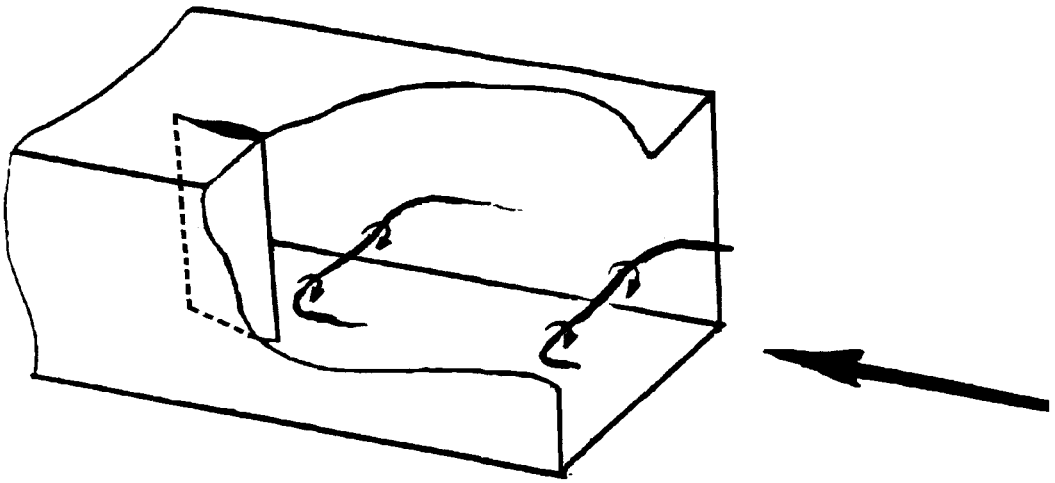

Figure 1.21- Sketch of transverse vortex interacting with a downstream model.

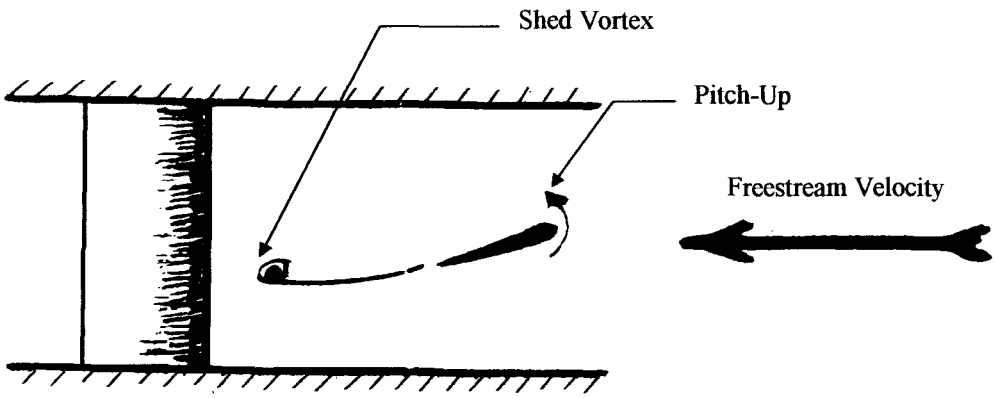

Figure 1.22- Sketch of a transverse vortex generated by a pitching aerofoil.

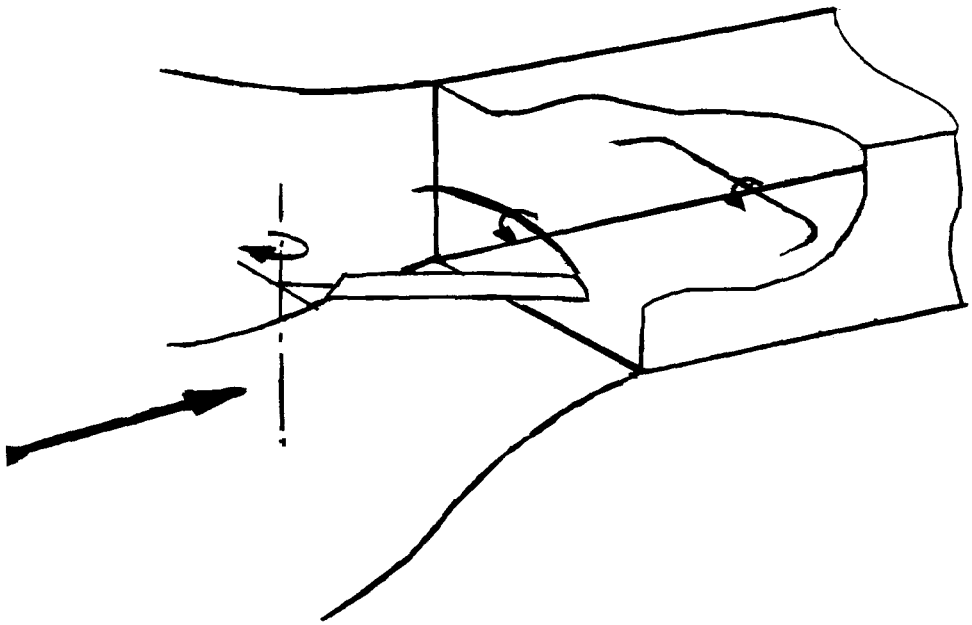

Figure 1.23- Sketch of the proposed method of generating a transverse vortex.

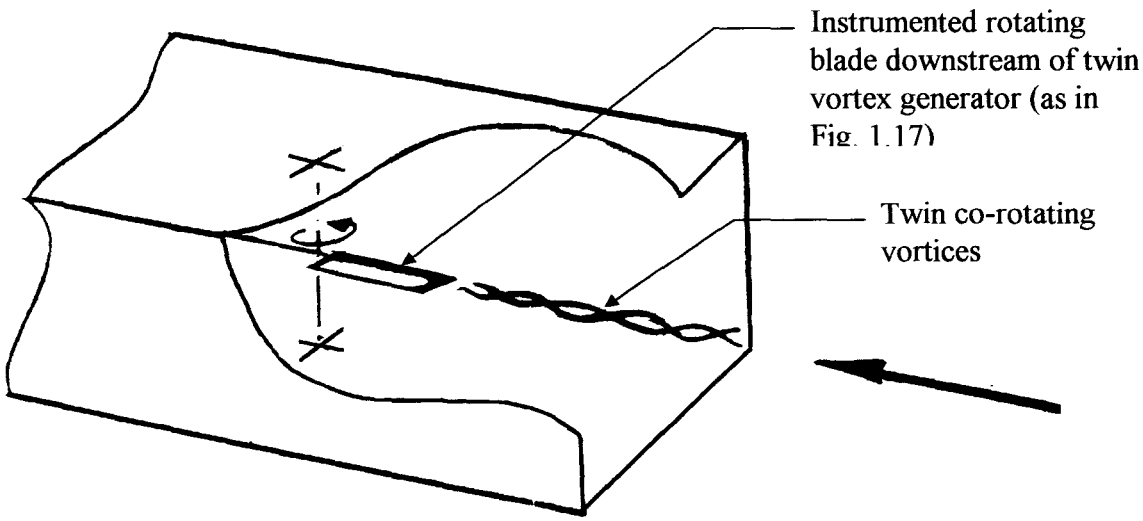

Figure 1.24- Sketch of a rotating blade interacting with twin vortex system.

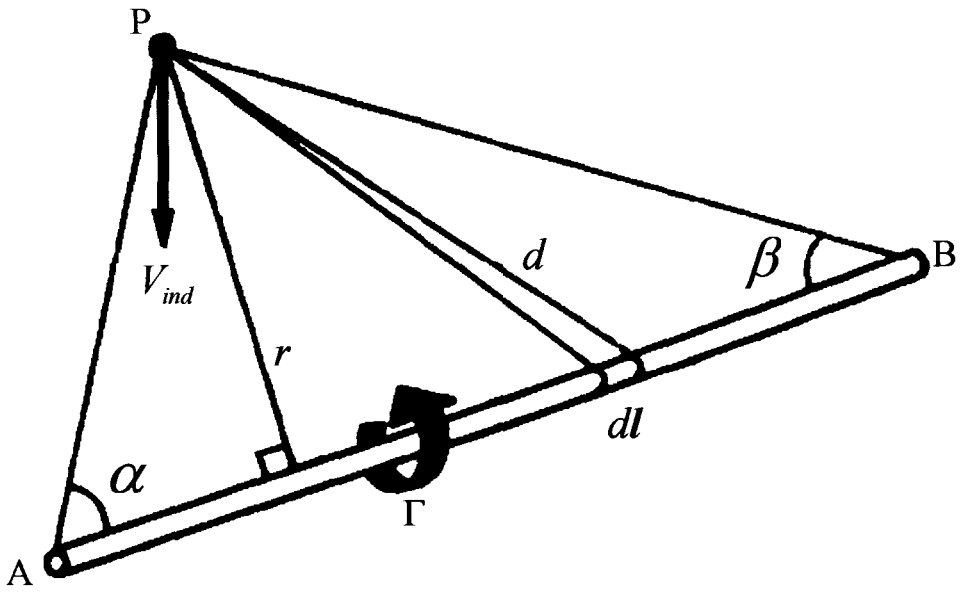

Figure 2.1- Illustration of induced velocity from a vortex filament (Biot-Savart Law).

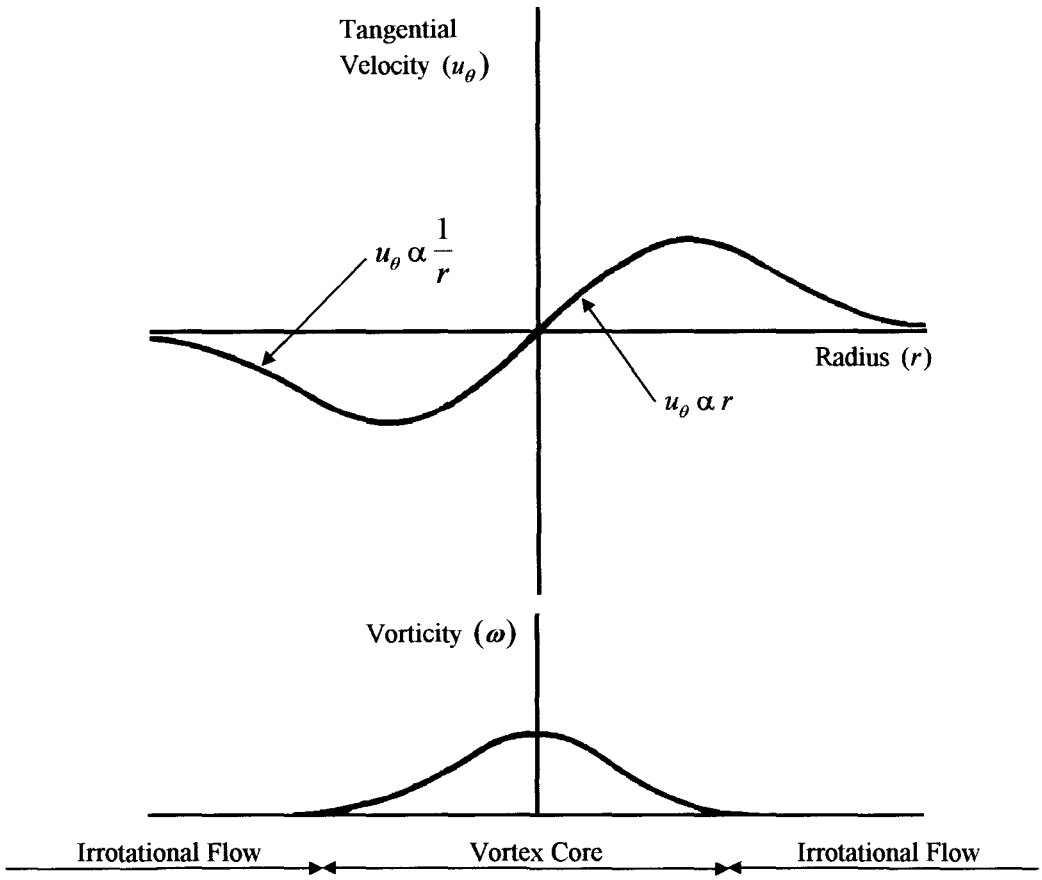

Figure 2.2- Velocity and vorticity distributions for a simple line vortex (Bradshaw (1971)).

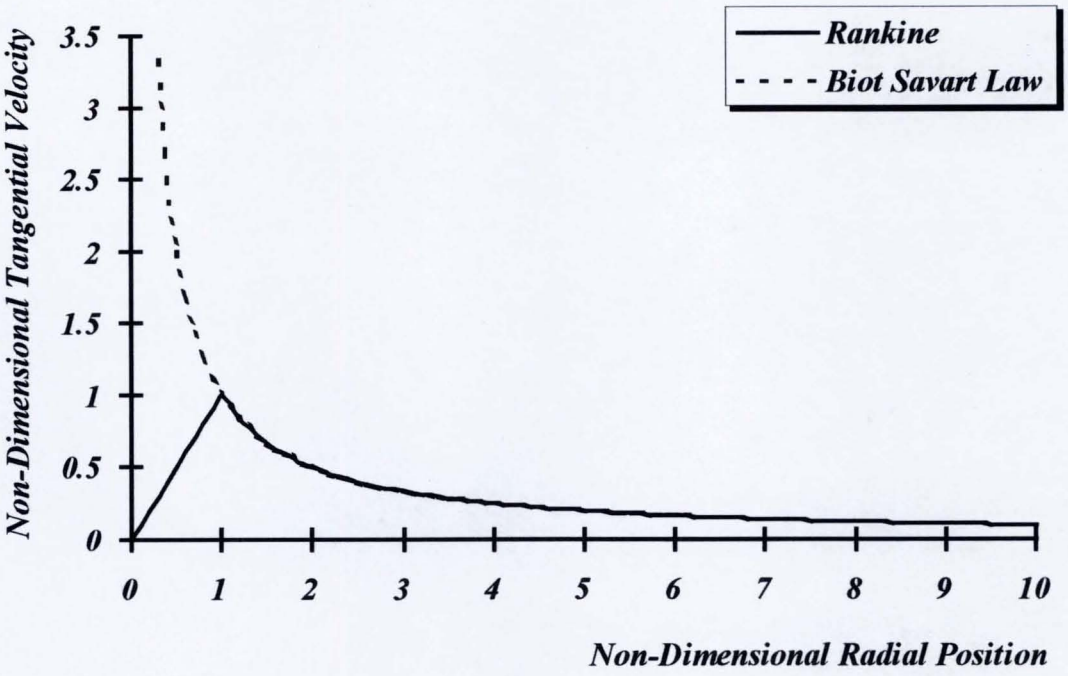

Figure 2.3- Comparison of the Biot-Savart Law and Rankine vortex model.

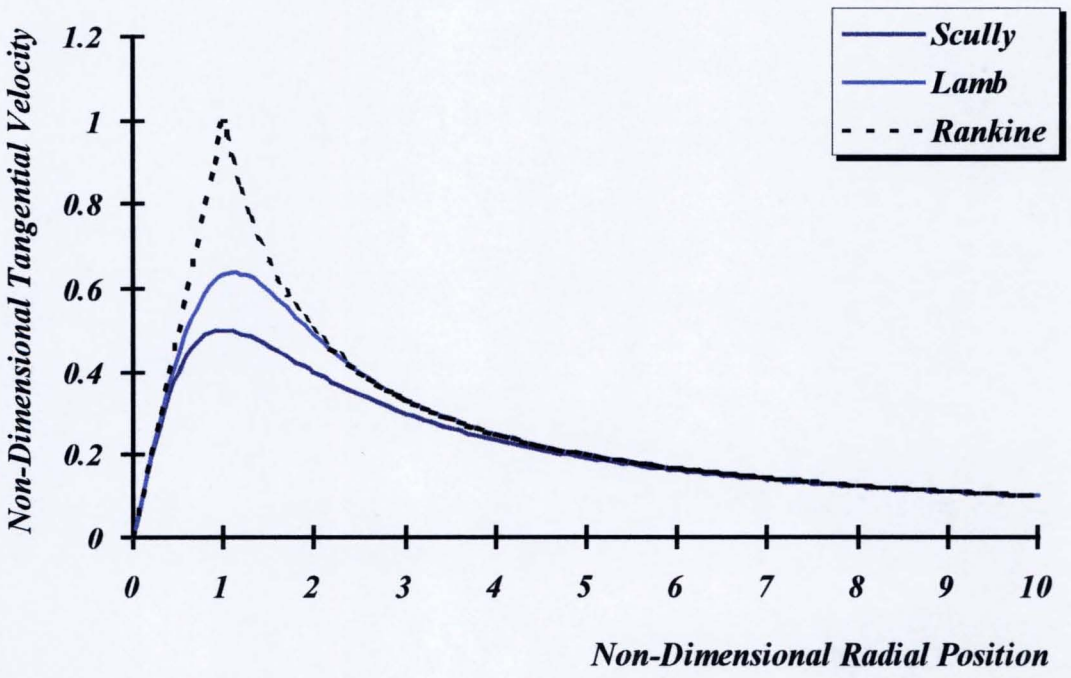

Figure 2.4- Comparison of Scully, Lamb and Rankine vortex core models.

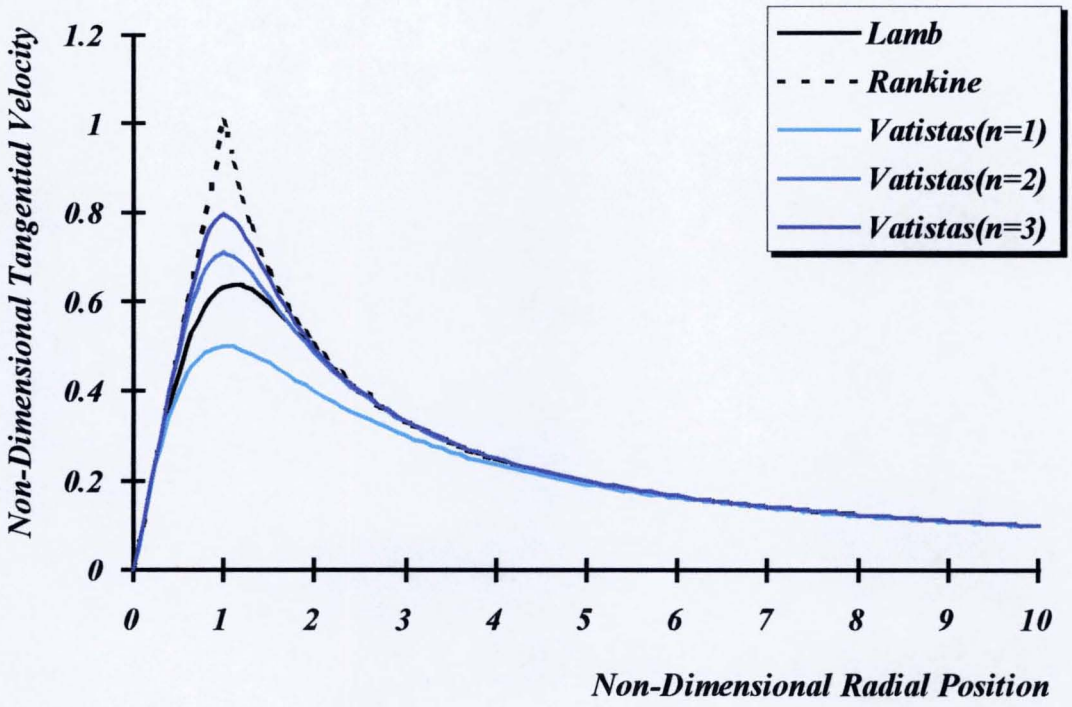

Figure 2.5- Comparison of Lamb, Rankine and Vastistas models.

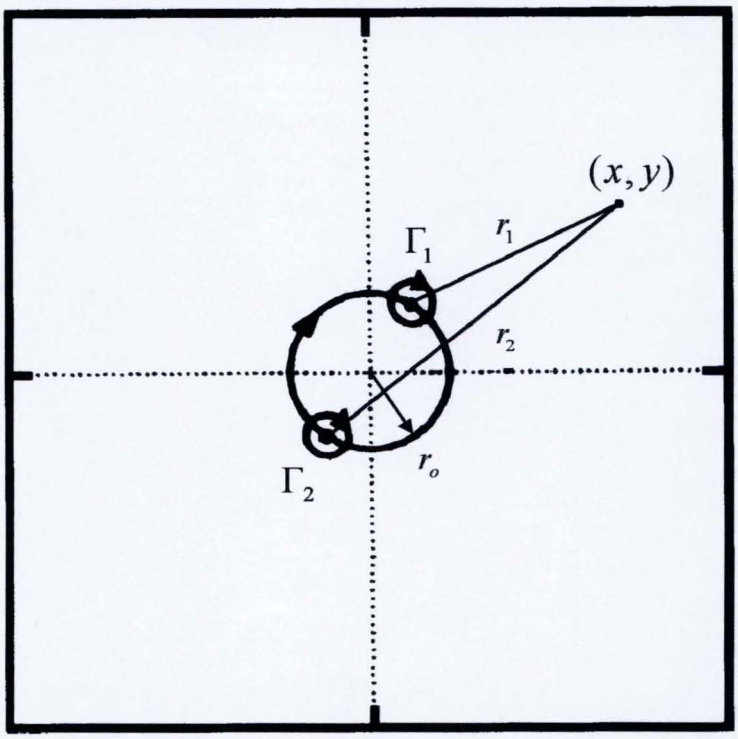

Figure 2.6- Illustration of two equal strength co-rotating point vortices.

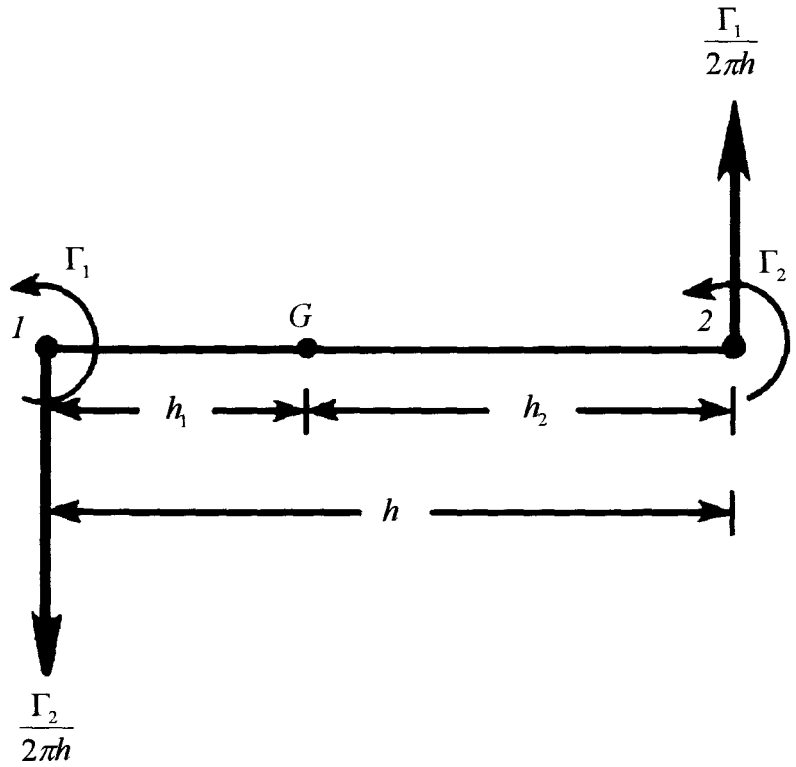

Figure 2.7- Illustration of two unequal strength co-rotating point vortices.

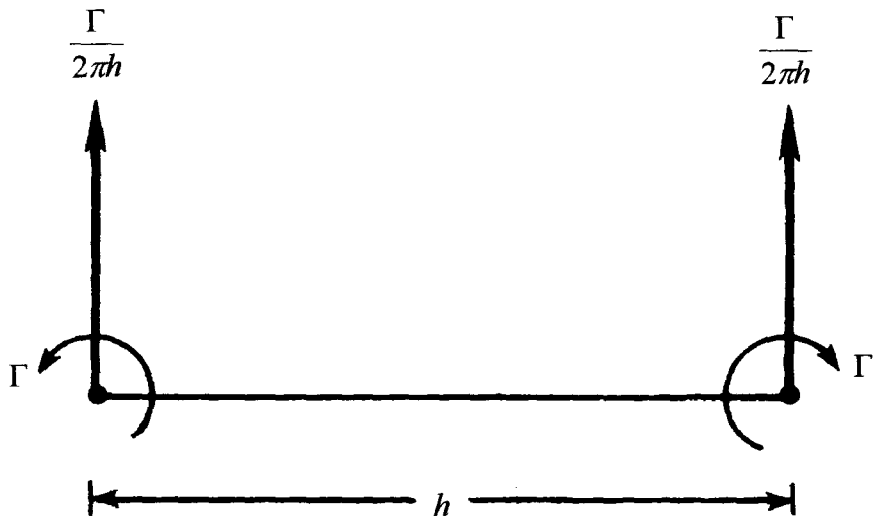

Figure 2.8- Illustration of two equal strength counter-rotating point vortices.

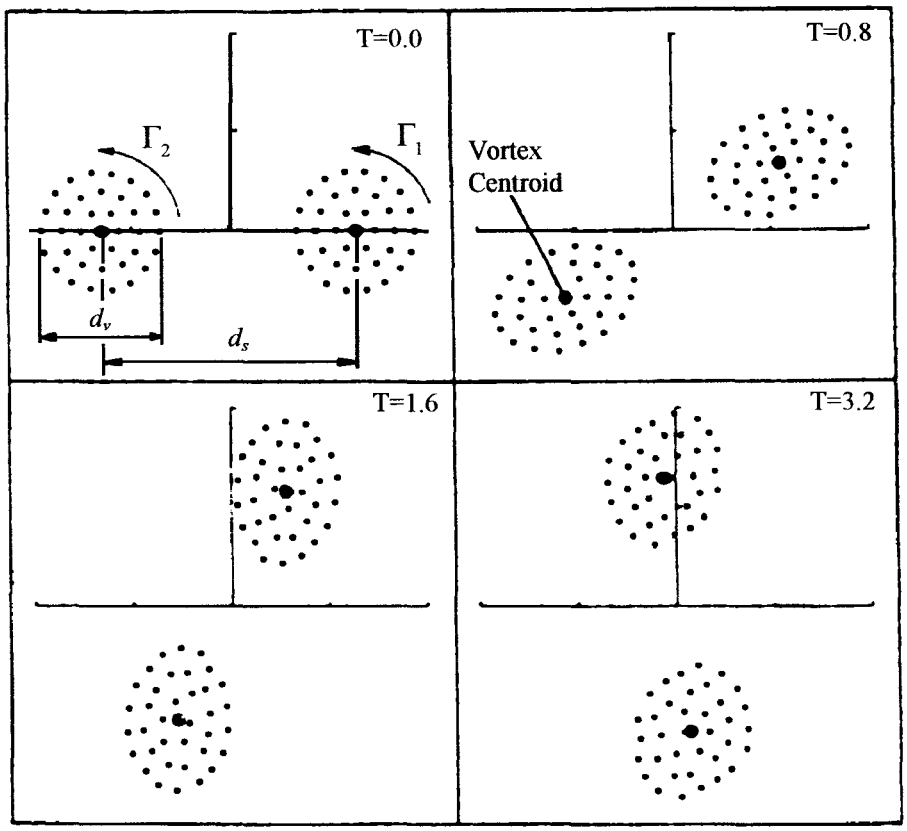

Figure 2.9- Illustration of the numerical analysis of two equal strength vortices, by Rossow (1977).

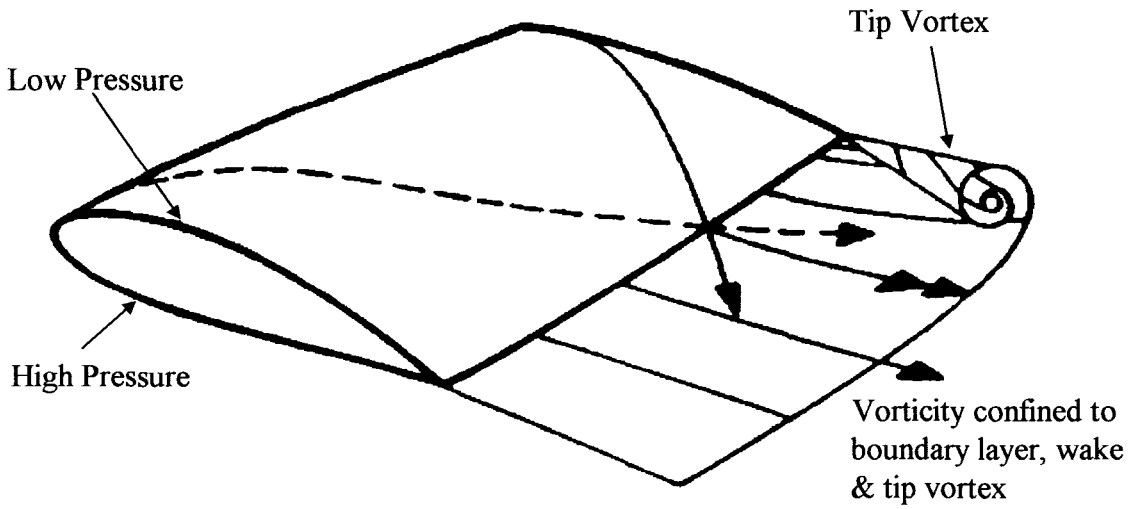

Figure 2.10- Wake and trailing tip vortex formed from the trailing edge of a finite wing.

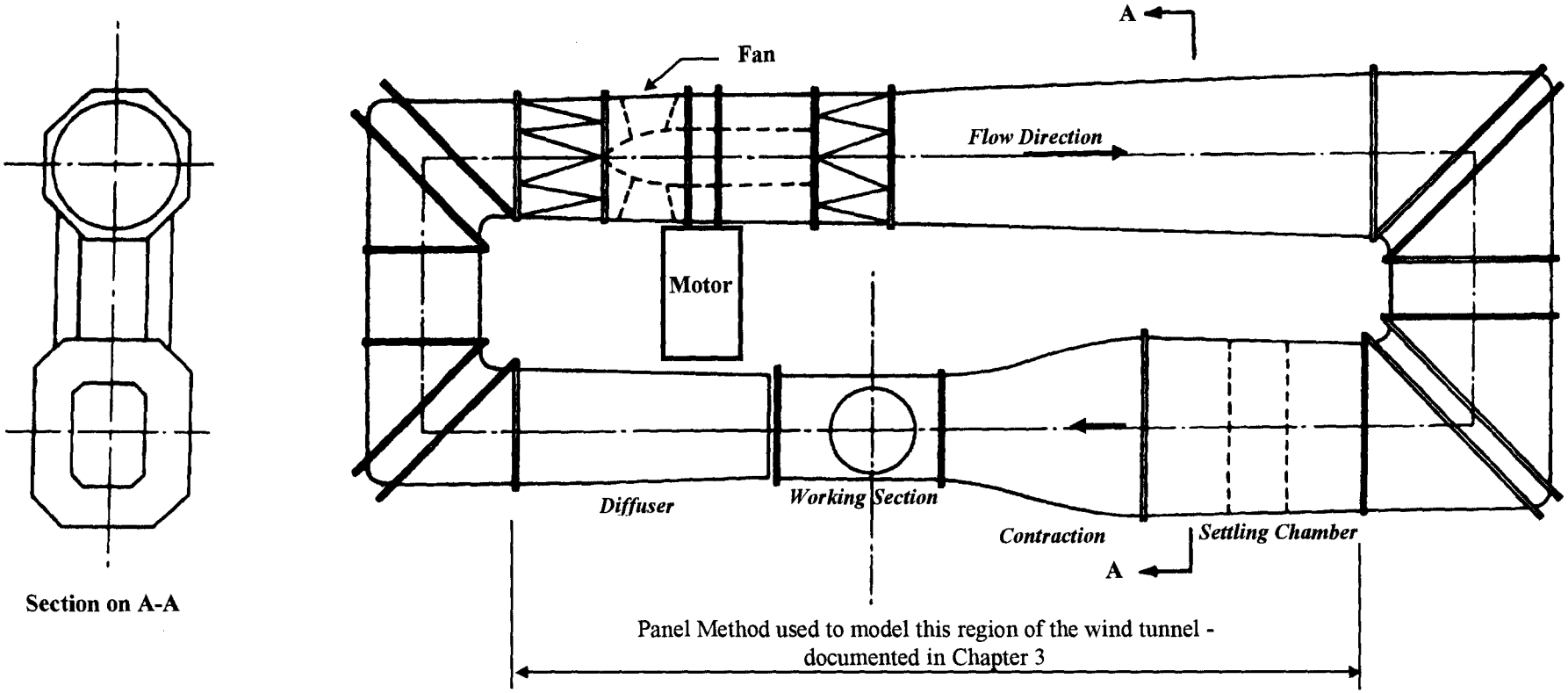

Figure 3.1- Illustration of the Glasgow University 1.15m x 0.8m low speed wind tunnel.

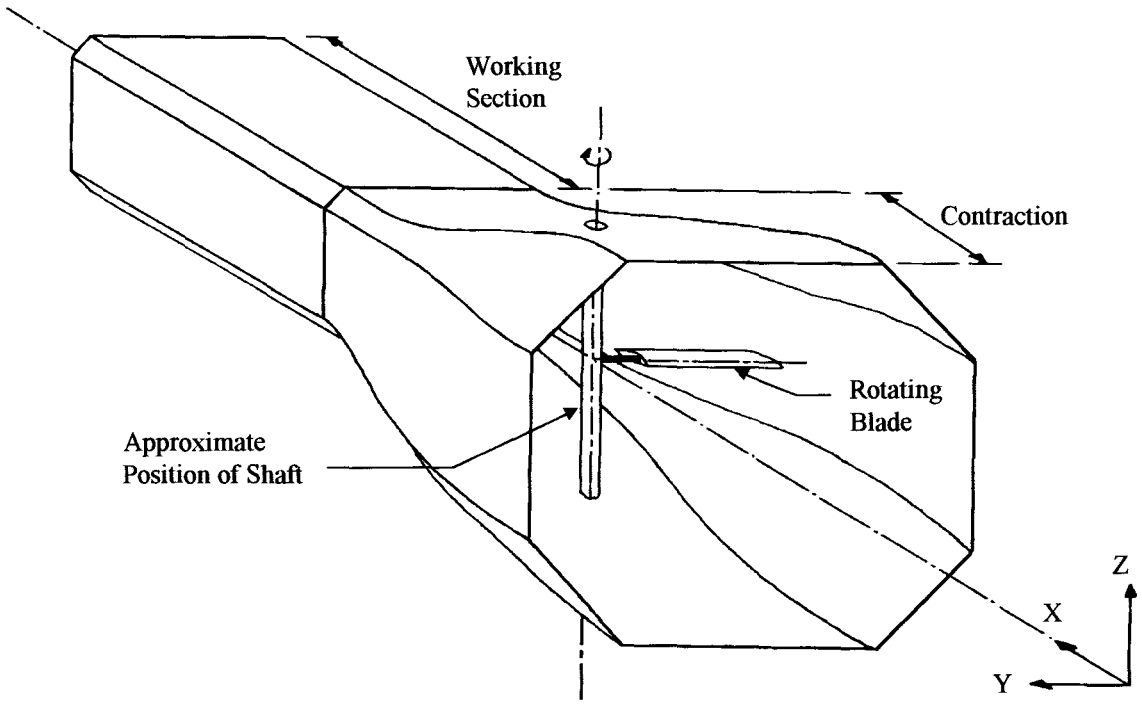

Figure 3.2- Schematic of rotor blade positioned in the contraction of the 1.15m x 0.8m low speed wind tunnel.

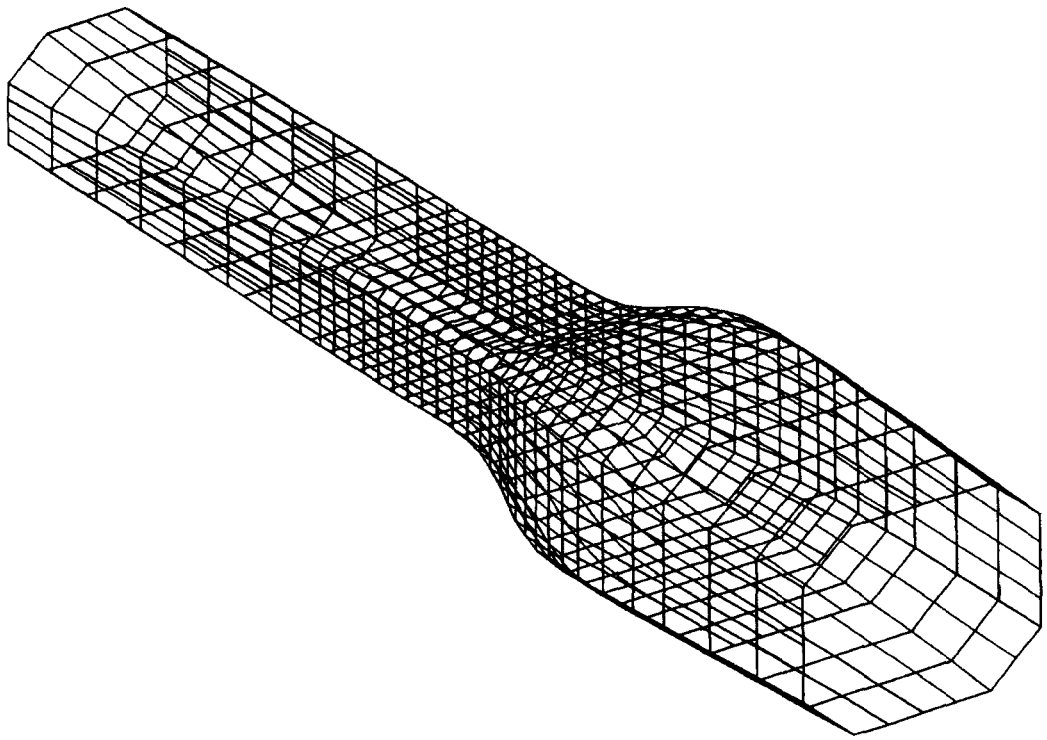

Figure 3.3- Illustration of the panel discretisation the 1.15m x0.8m wind tunnel (consisting of settling chamber, contraction, working section and diffuser).

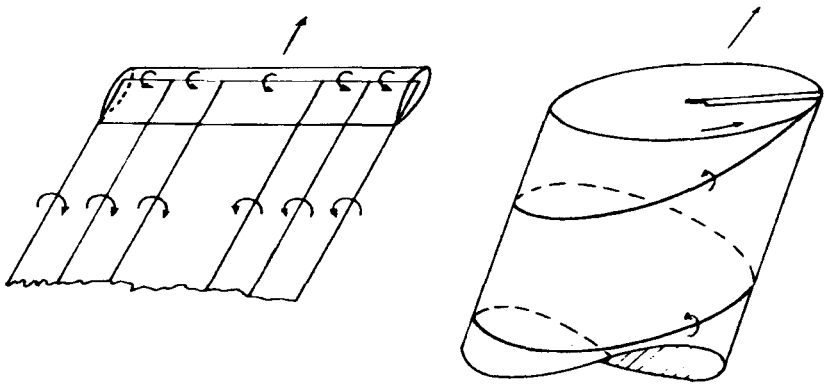

Figure 3.4- Illustration of Classical Rigid Wake for fixed and rotary wings (Landgrebe (1969)).

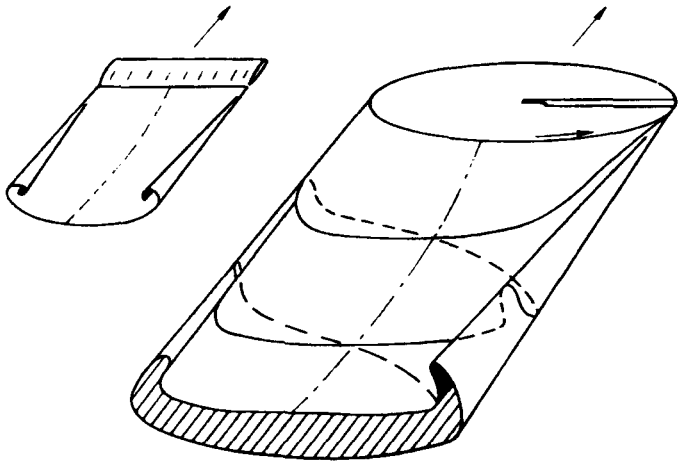

Figure 3.5- Illustration of the distorted wakes generated by fixed and rotary wings (Landgrede(1969)).

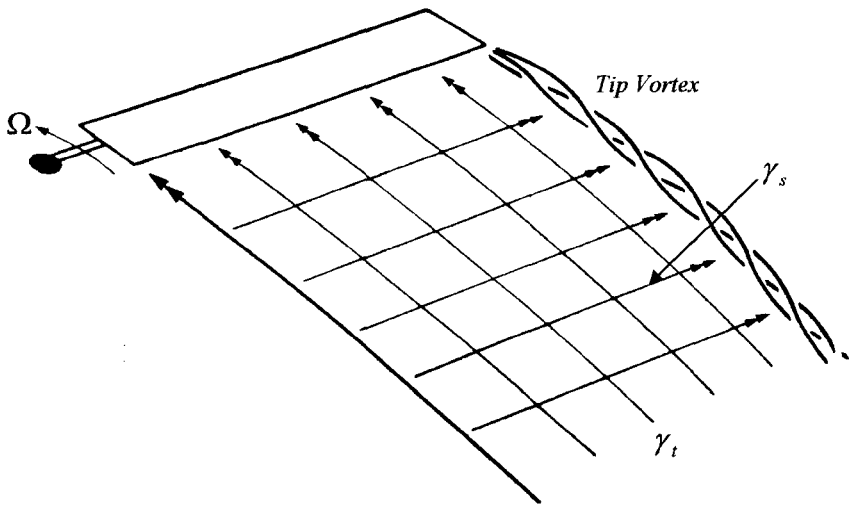

Figure 3.6- Illustration of athediscretised wake lattice generated by a rotating blade. (Johnson (1980))

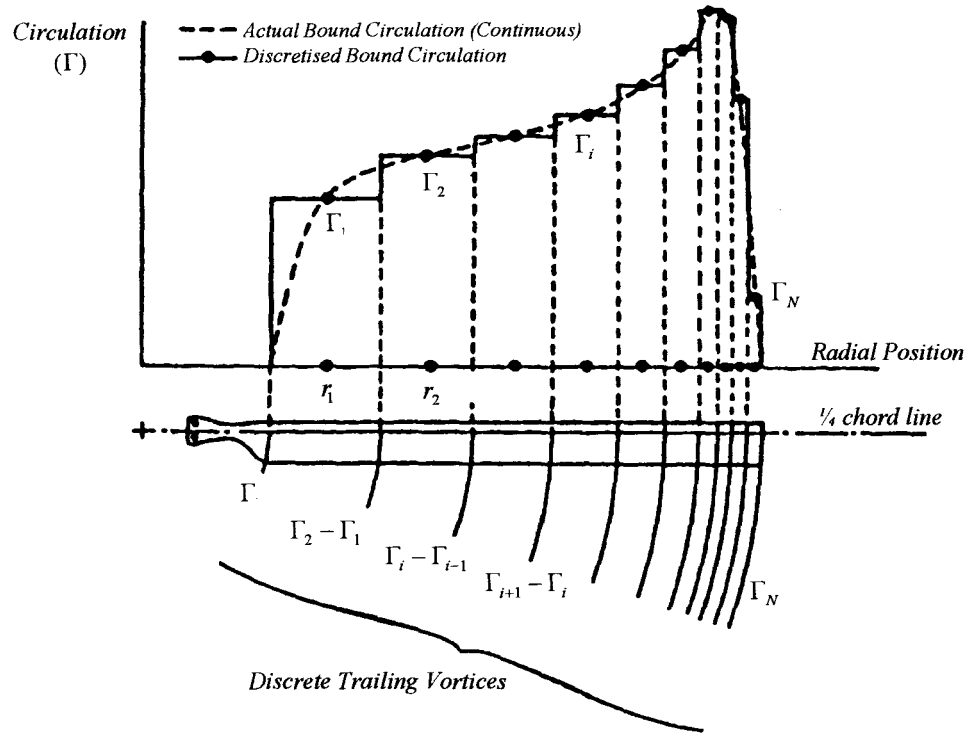

Figure 3.7 - Discretisation of the blade circulation distribution and the generation of discrete trailing vortices (Vuillet (1990)).

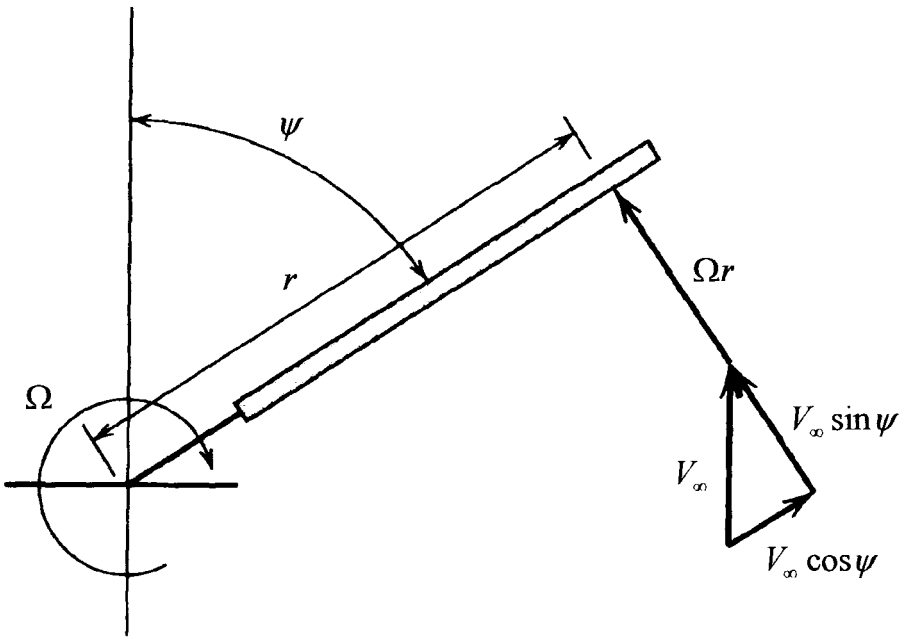

Figure 3.8- Primary velocity components (from freestream velocity and rotation of the blade) which act on a rotor blade in uniform flow - neglecting any induced effects from the wake.

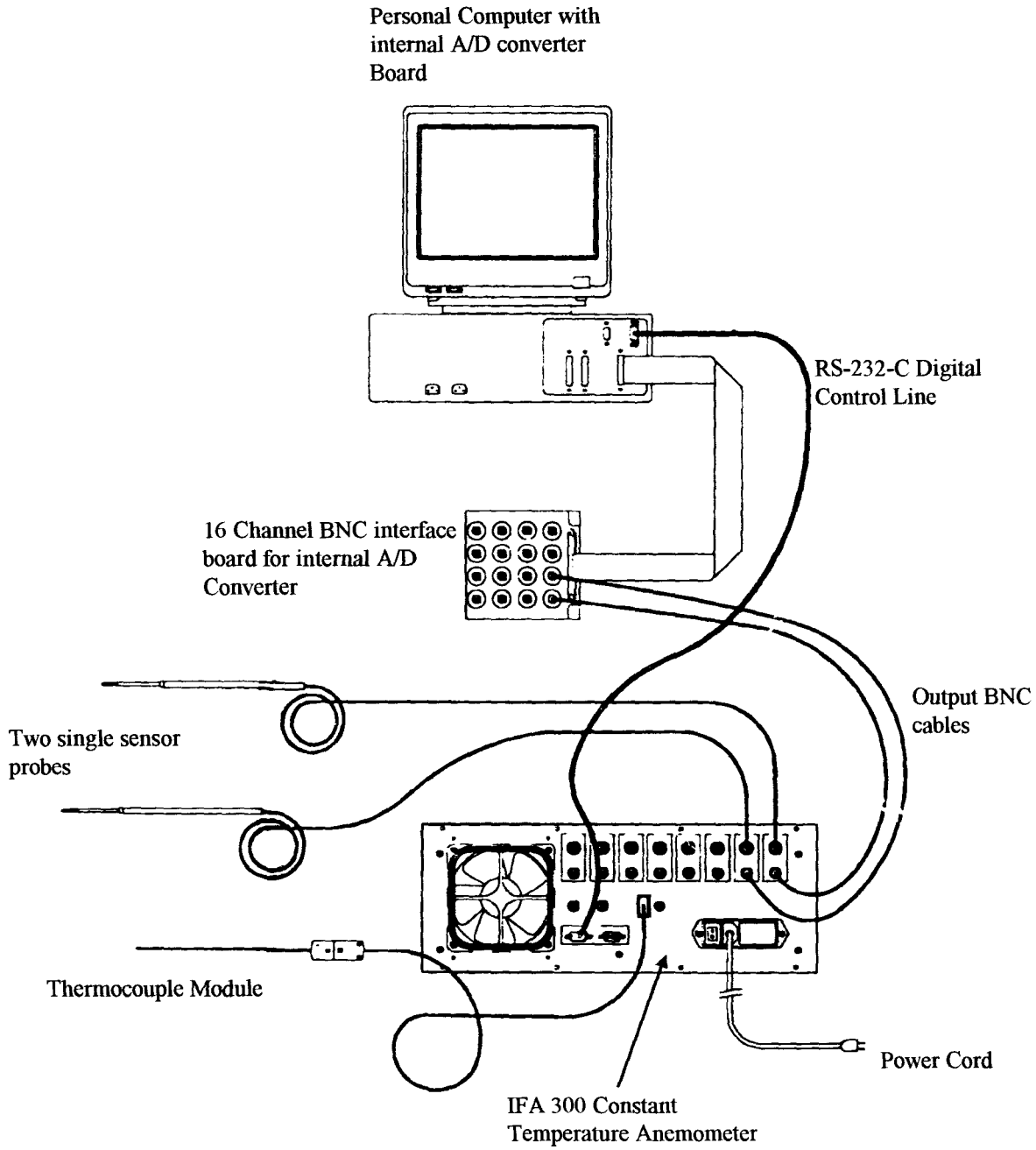

Figure 4.1- Illustration of the TSI IFA300 hot-wire data acquisition system with two single sensors. The same set-up applies for one x-wire probe.

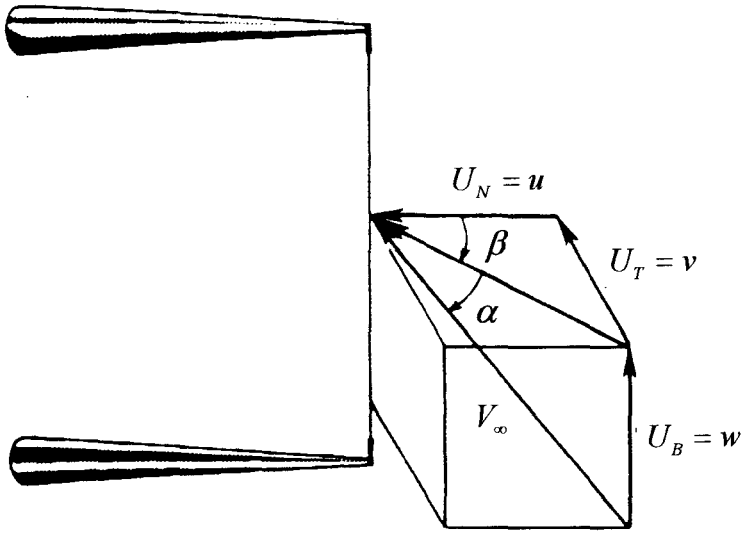

Figure 4.2- Illustration of the velocity components which act on a single normal hot-wire probe.

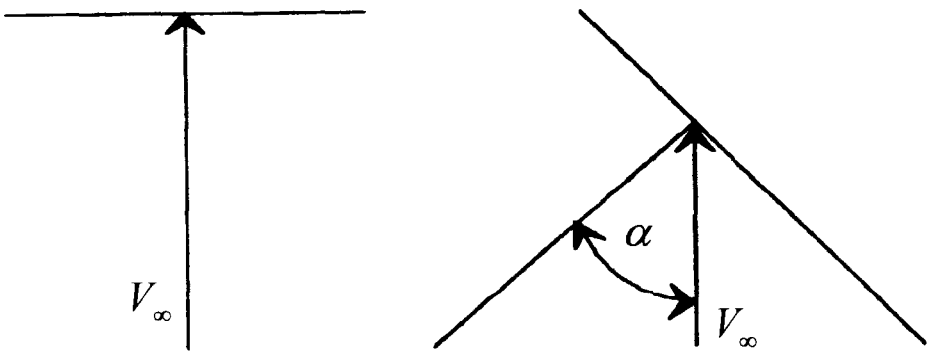

Figure 4.3- Illustration of the effective velocity which acts on normal and inclined hot-wires.

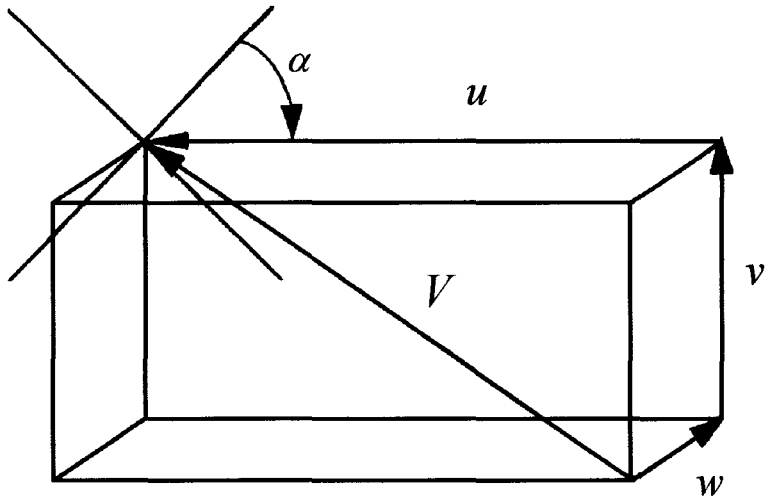

Figure 4.4- Illustration of the velocity components which act on a x-wire probe.

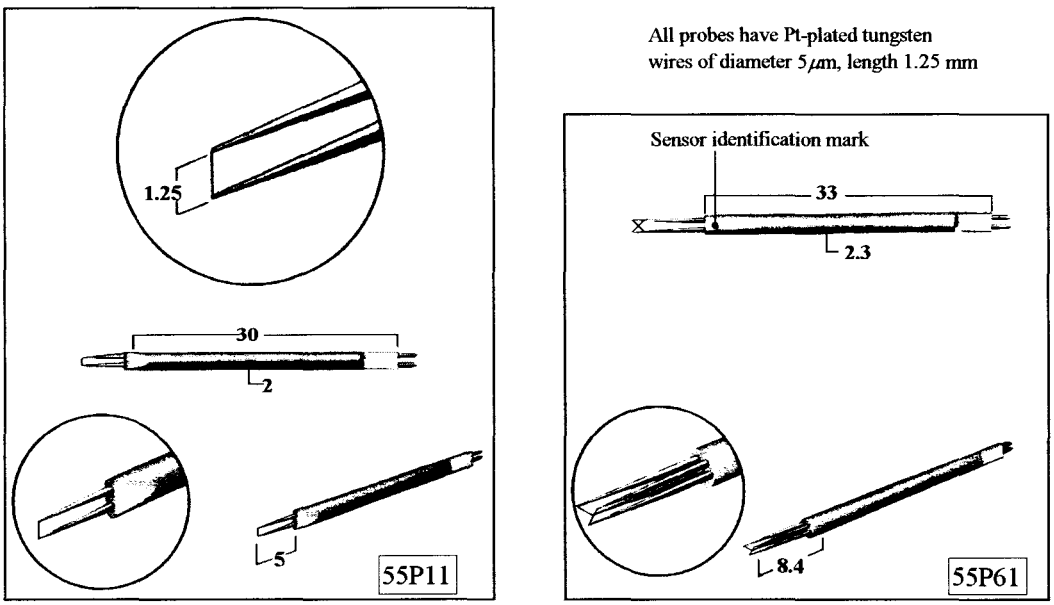

Figure 4.5- Illustration of DANTEC hot-wire probes available for the present study.

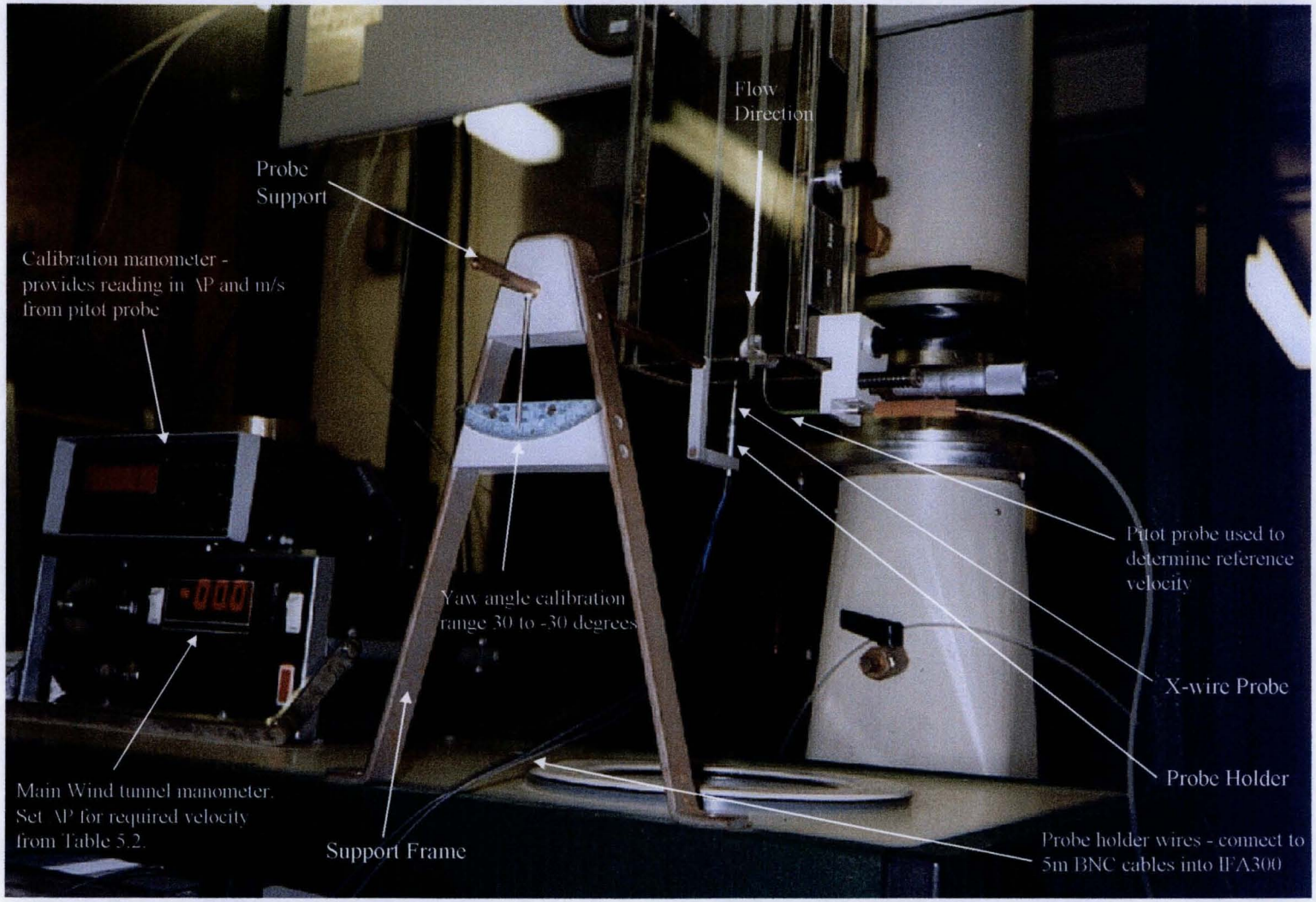

Figure 4.6- Photograph of the calibration facility illustrating the support frame and probe support.

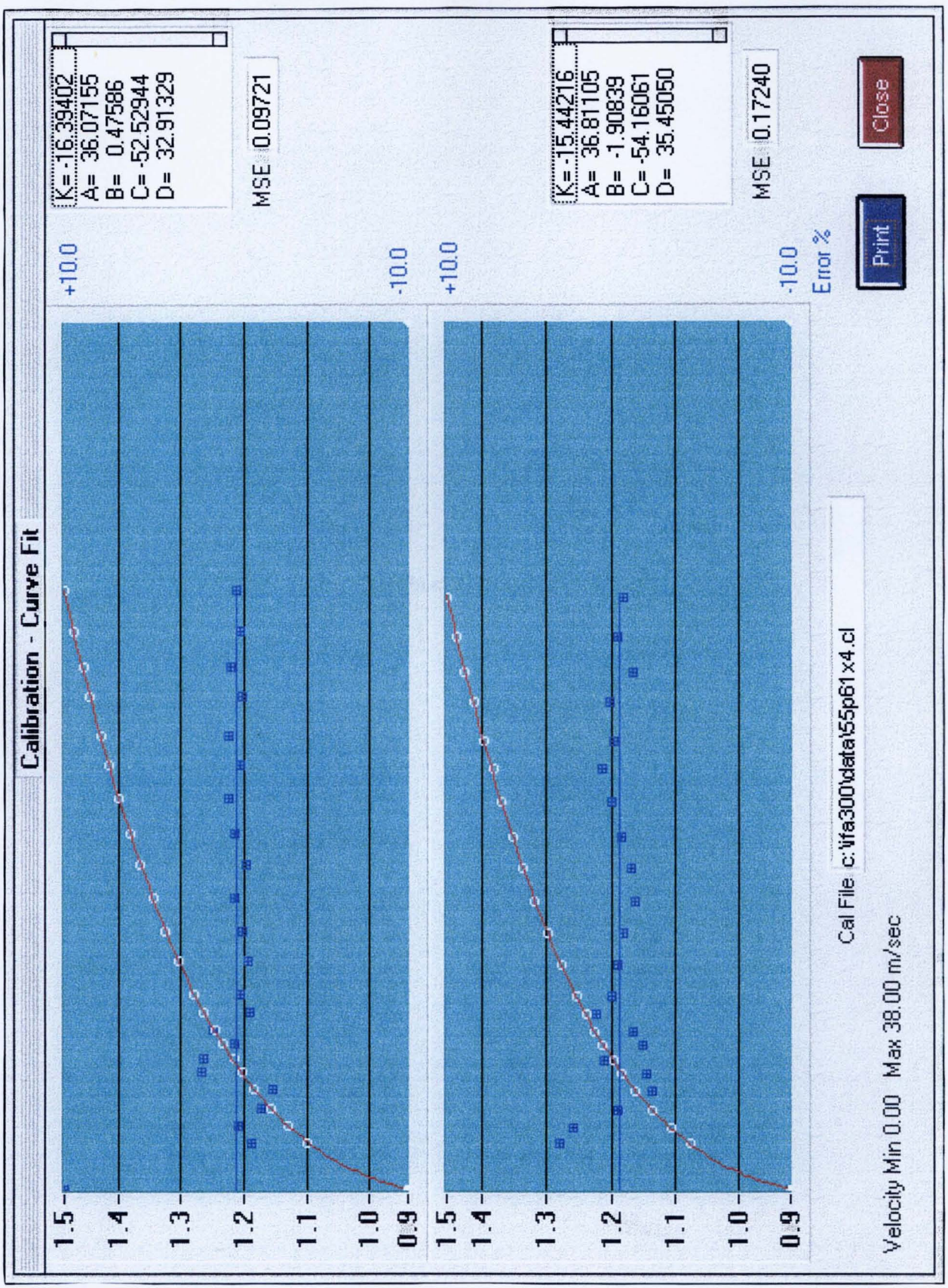

Figure 4.7- Calibration curve fits (with errors) depicting the relationship between the voltage and the effective velocity. The coefficients of the polynomial curve fit are presented on the right hand side of the graphs.

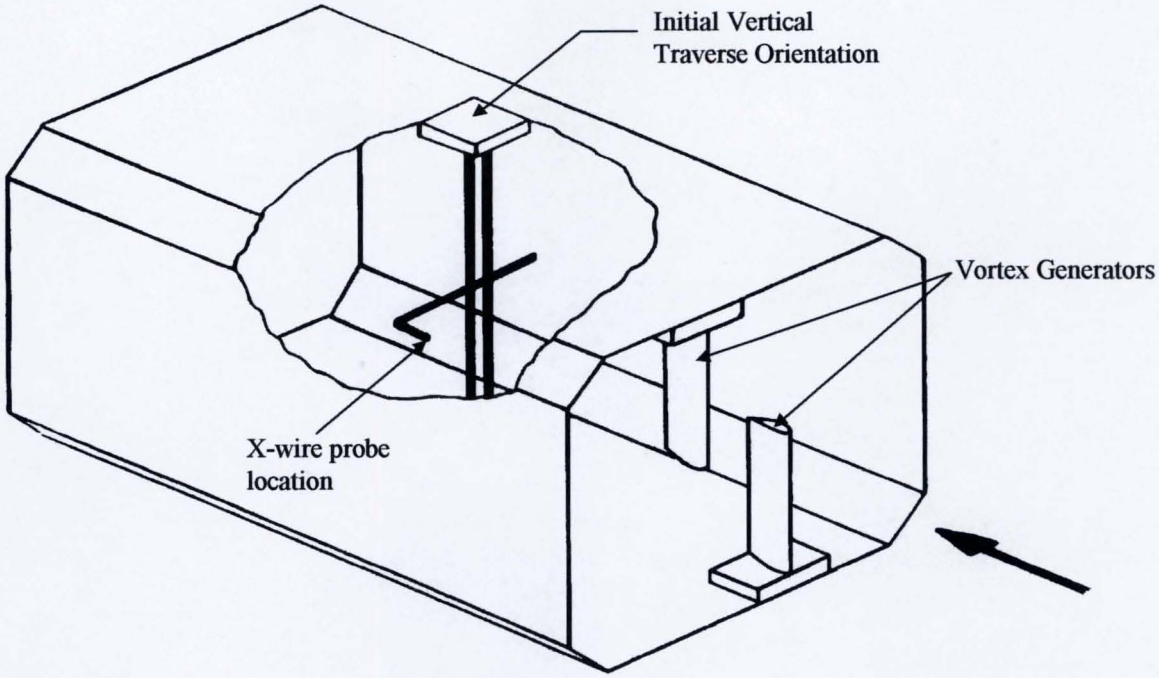

Figure 5.1- Schematic of the twin vortex experimental set-up in the1.15m x 0.8m low speed wind tunnel depicting the initial vertical traverse orientation.

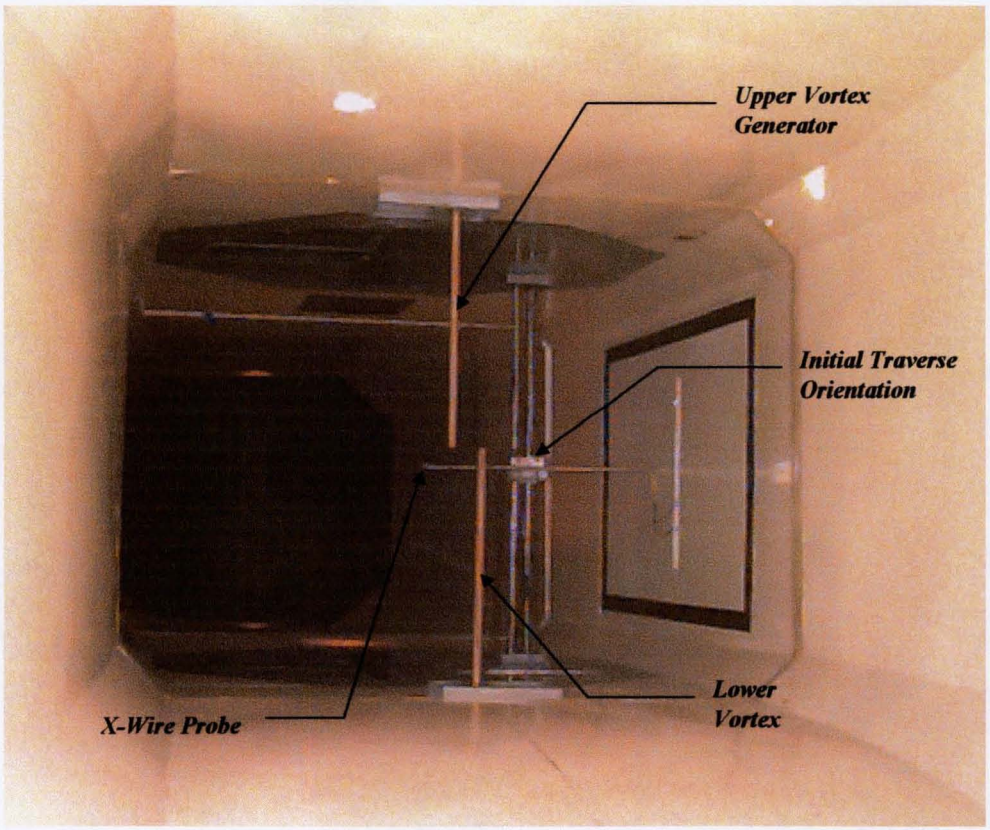

Figure 5.2- Photograph of the twin vortex generators and the initial vertical traverse orientation.

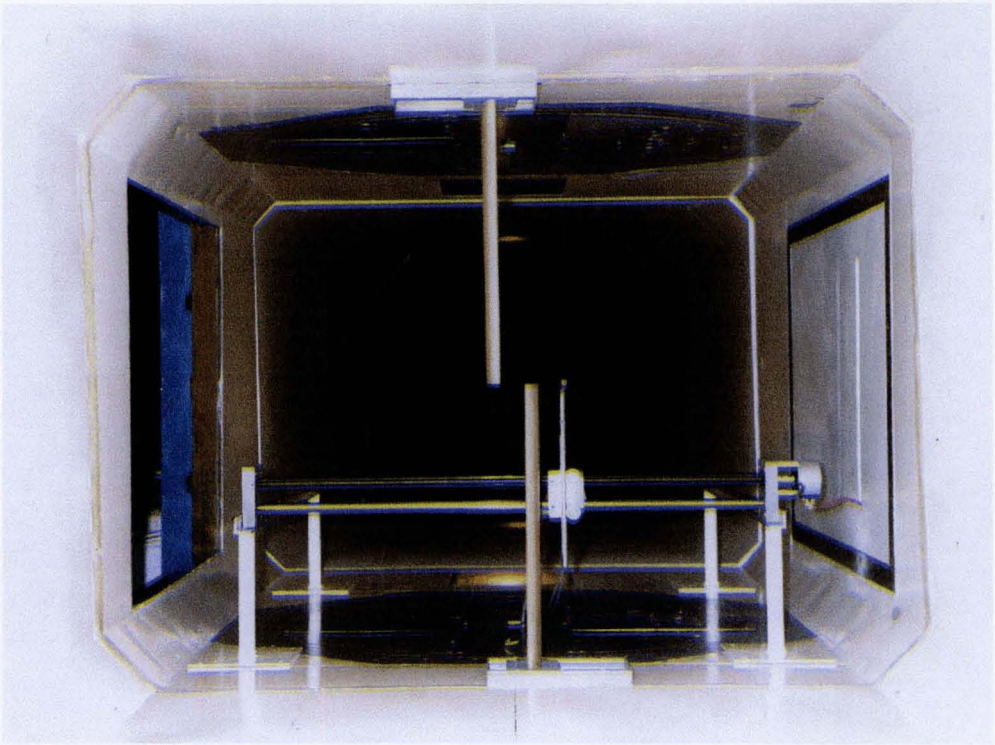

Figure 5.3- Photograph of the twin vortex generators and final horizontal traverse orientation.

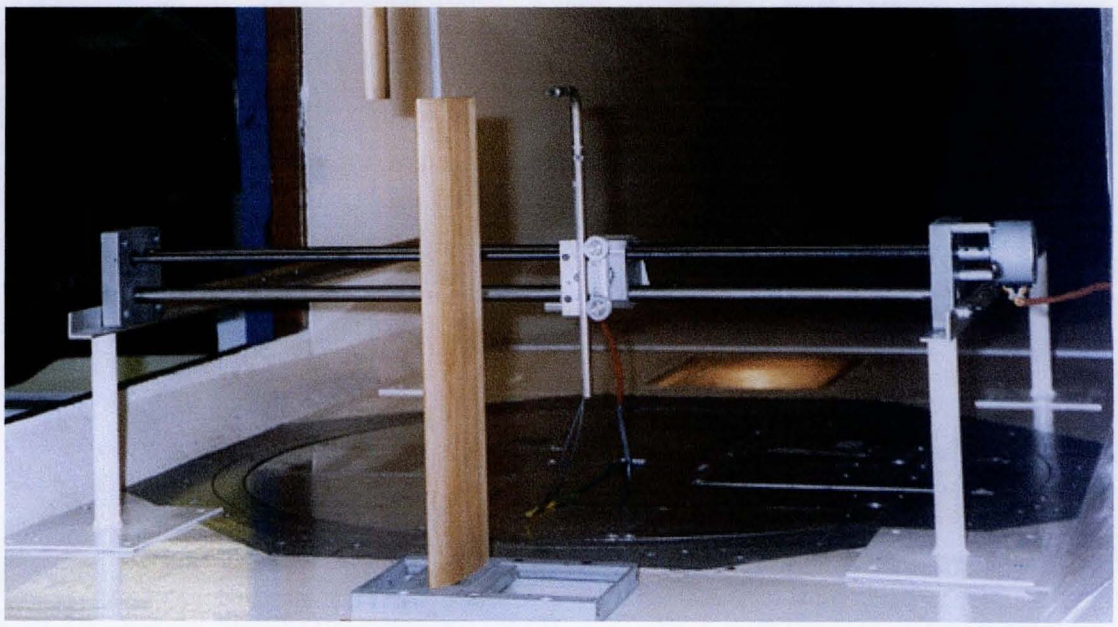

Figure 5.4- Close-up photograph of the horizontal traverse with support.

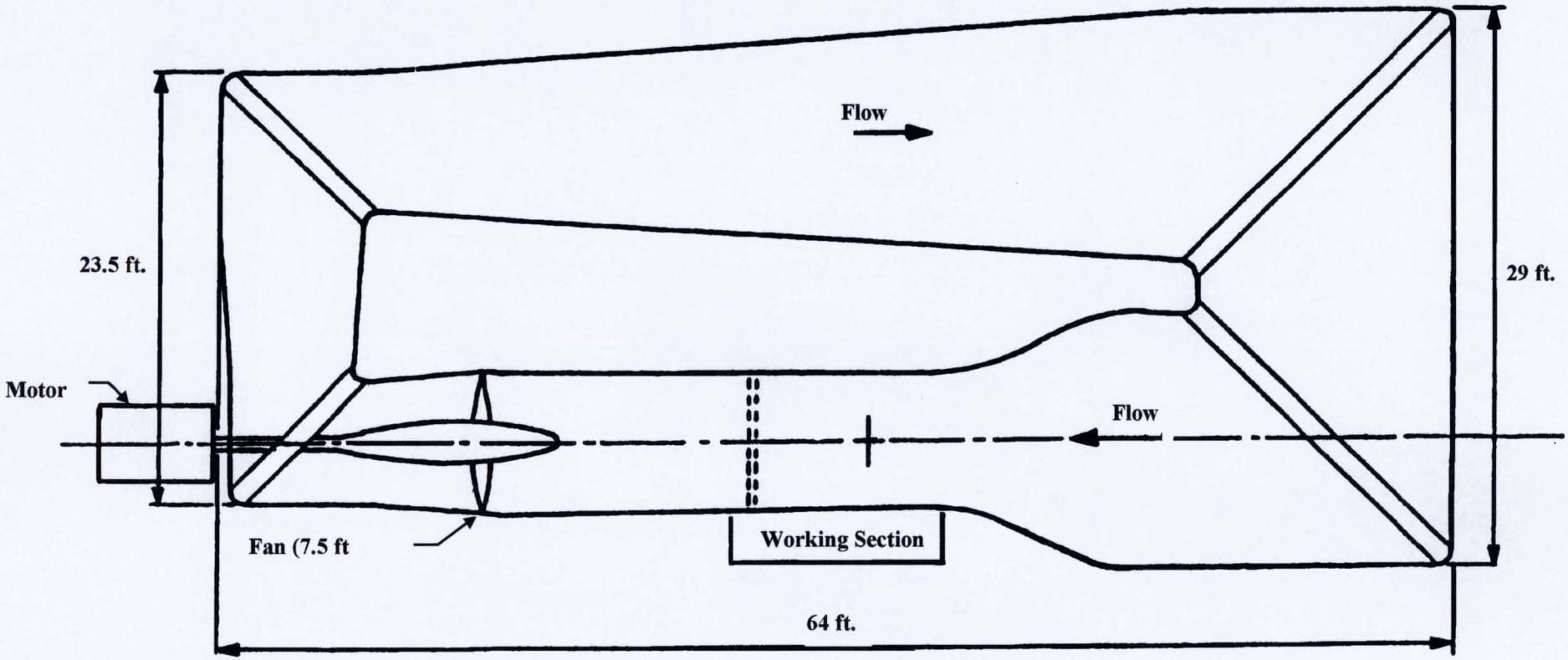

Figure 5.5- Illustration of the Glasgow University 2.1m x 1.6m low speed wind tunnel.

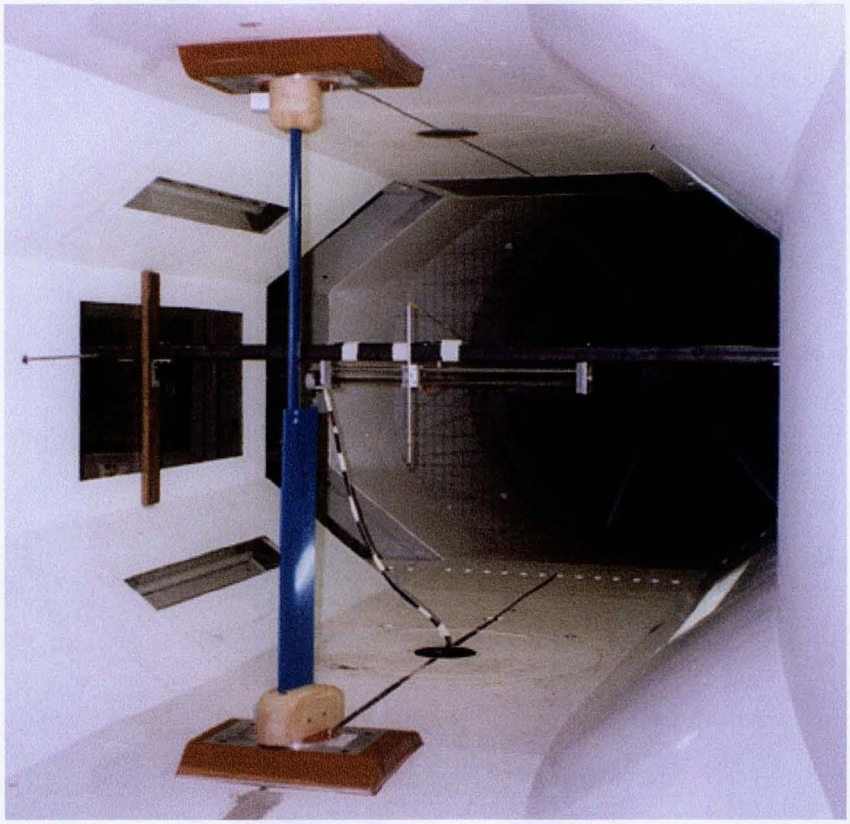

Figure 5.6- Photograph of the single vortex generator in the 2.1m x 1.6m wind tunnel.

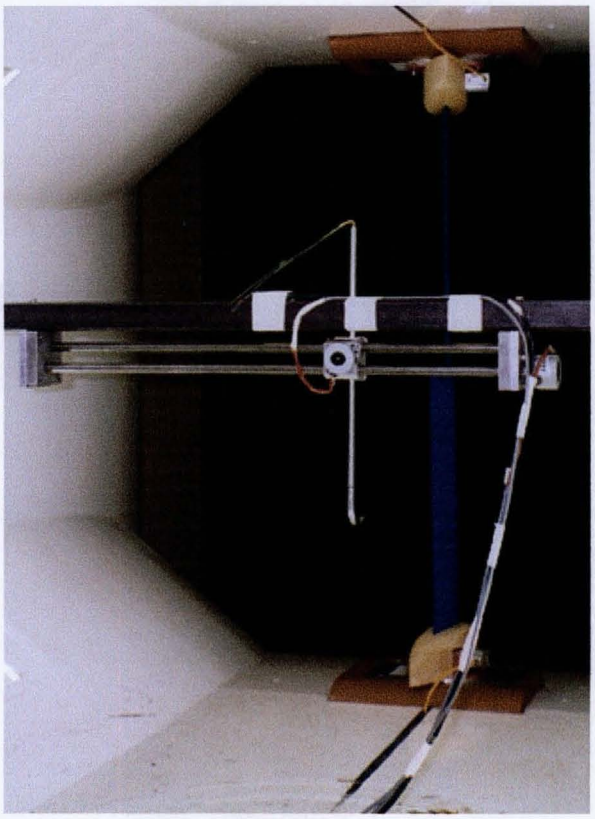

Figure 5.7- Photograph of the inverted traverse orientation and the traverse support.

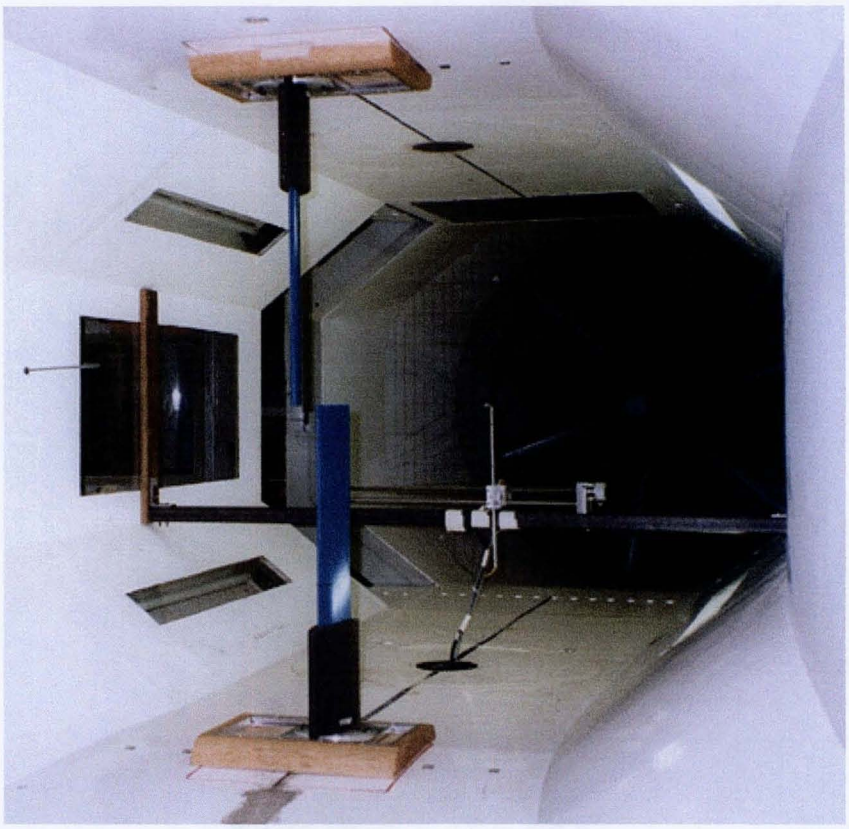

Figure 5.8- Photograph of twin vortex generators in the 2.1m x 1.6m wind tunnel.

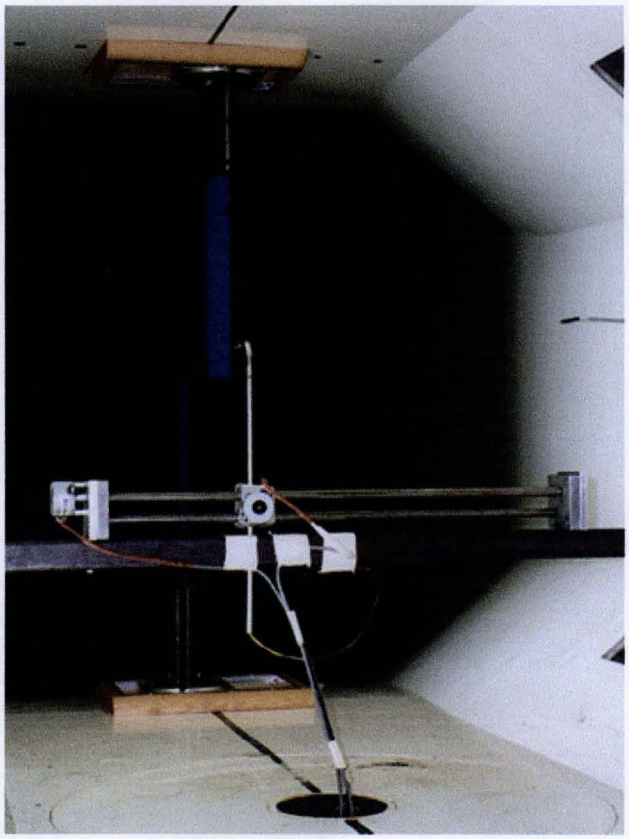

Figure 5.9- Photograph of the traverse in its 'normal' orientation.

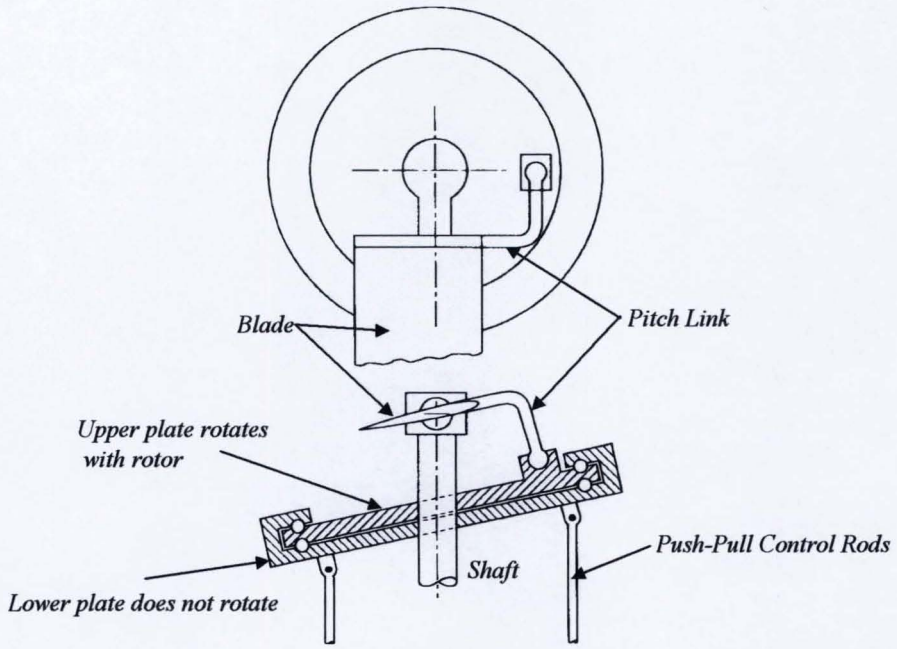

Figure 6.1- Idealisation of the helicopter swashplate mechanism to provide cyclic pitch.

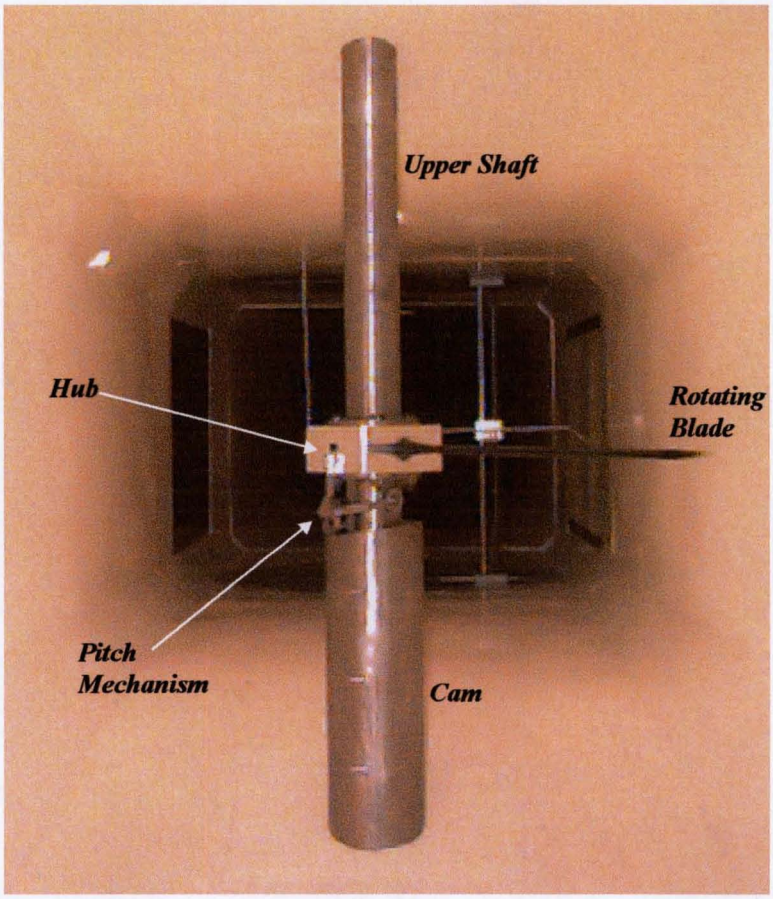

Figure 6.2- Photograph illustrating the transverse vortex generator. All subsequent tests had traverse horizontally orientated (Fig.5.4), the hub machined to a circular profile, and fairings around the upper shaft and cam.

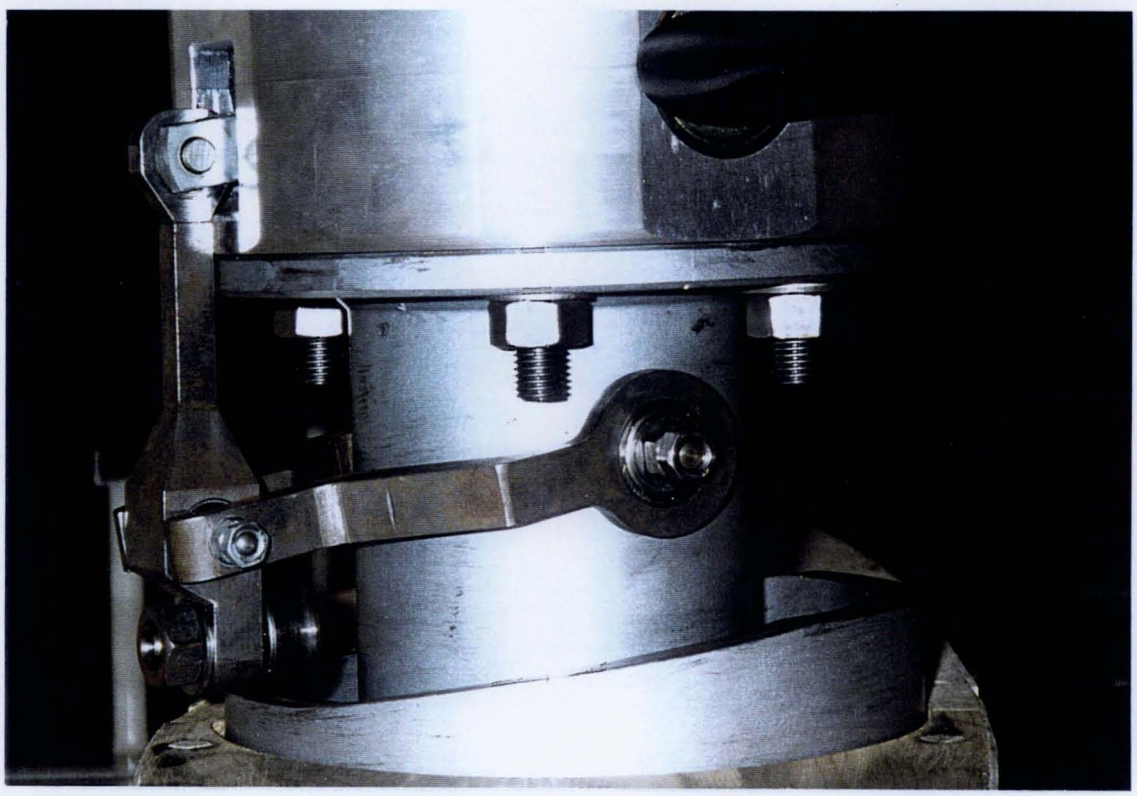

Figure 6.3- Close-up photograph of the roller/cam pitching mechanism. The blade is at zero incidence corresponding to the lowest position of the roller.

Figure 6.4- Photograph of the hub after final machining from square to circular profile.

Figure 6.5- Photograph of hub with upper flange removed. This allows removal and replacement of the spring which forces the roller onto the cam.

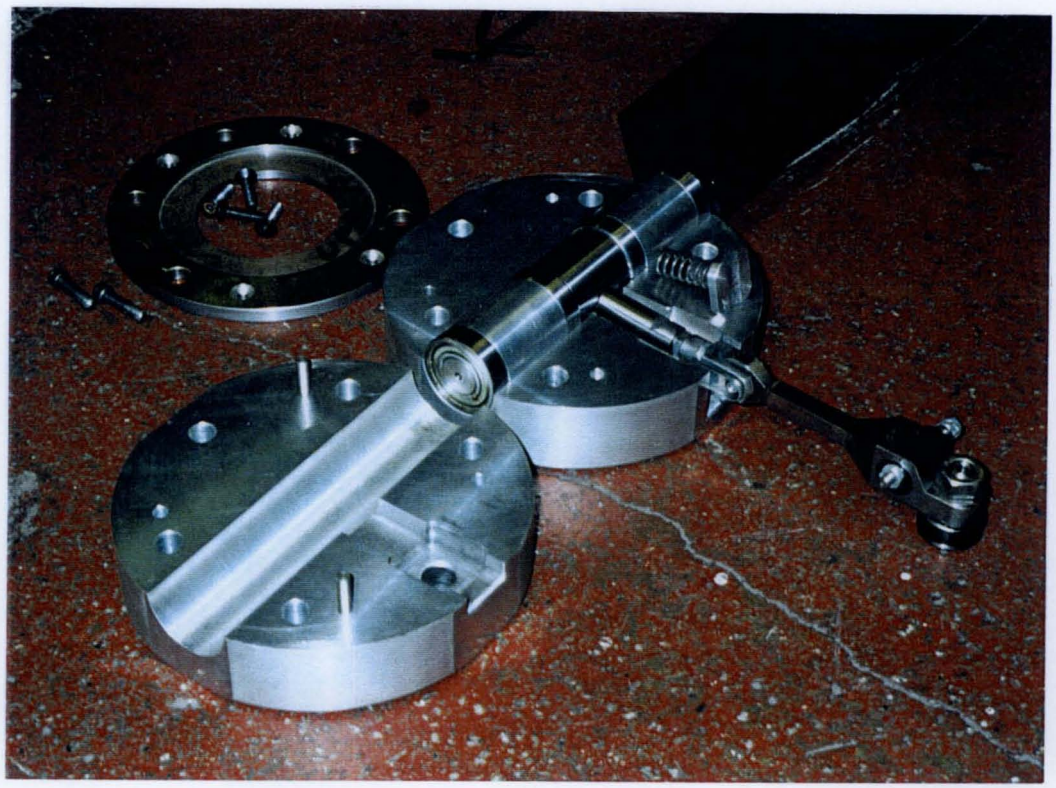

Figure 6.6- Photograph of hub split in two showing the main pitch barrel and the four pitch bearings.

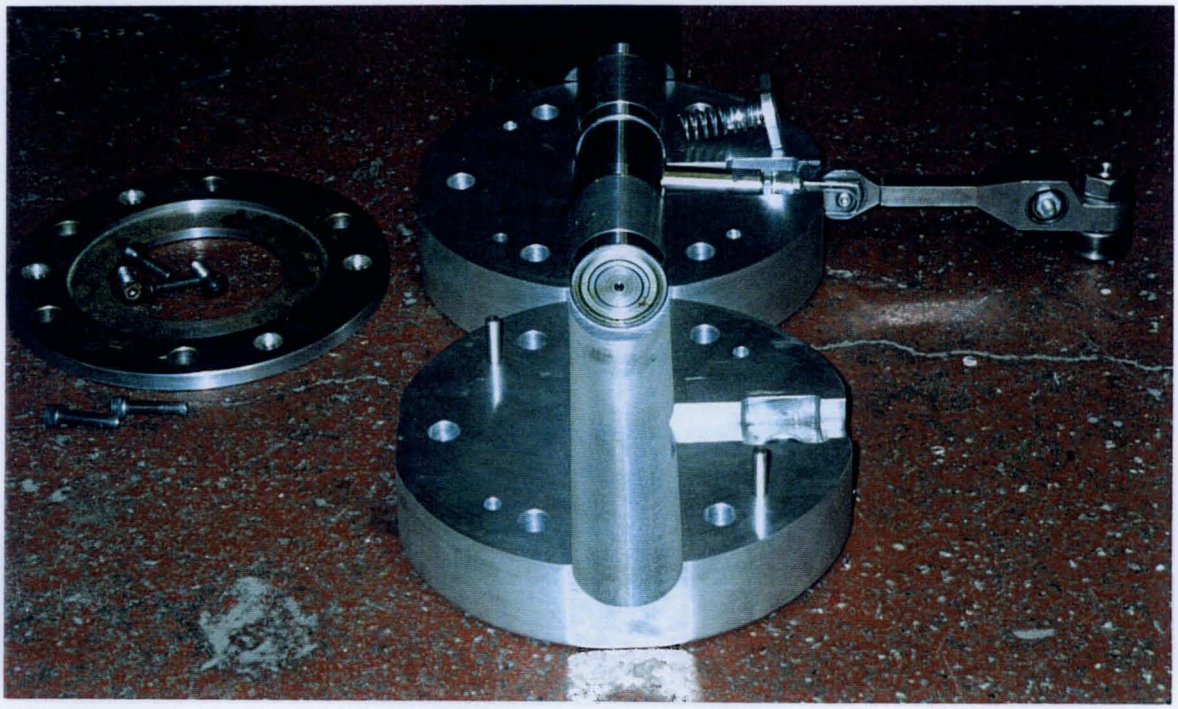

Figure 6.7- Another photograph of the internal arrangement of the hub.

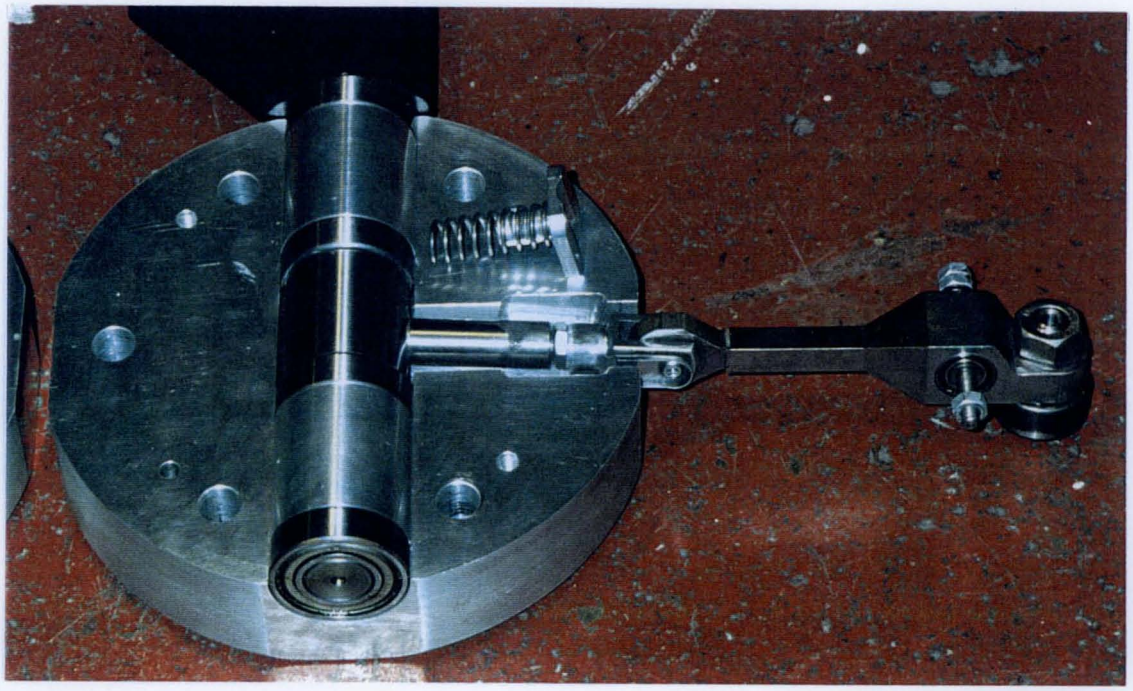

Figure 6.8- Close-up of the pitch arm (and spring) connected to the pitch link (with roller).

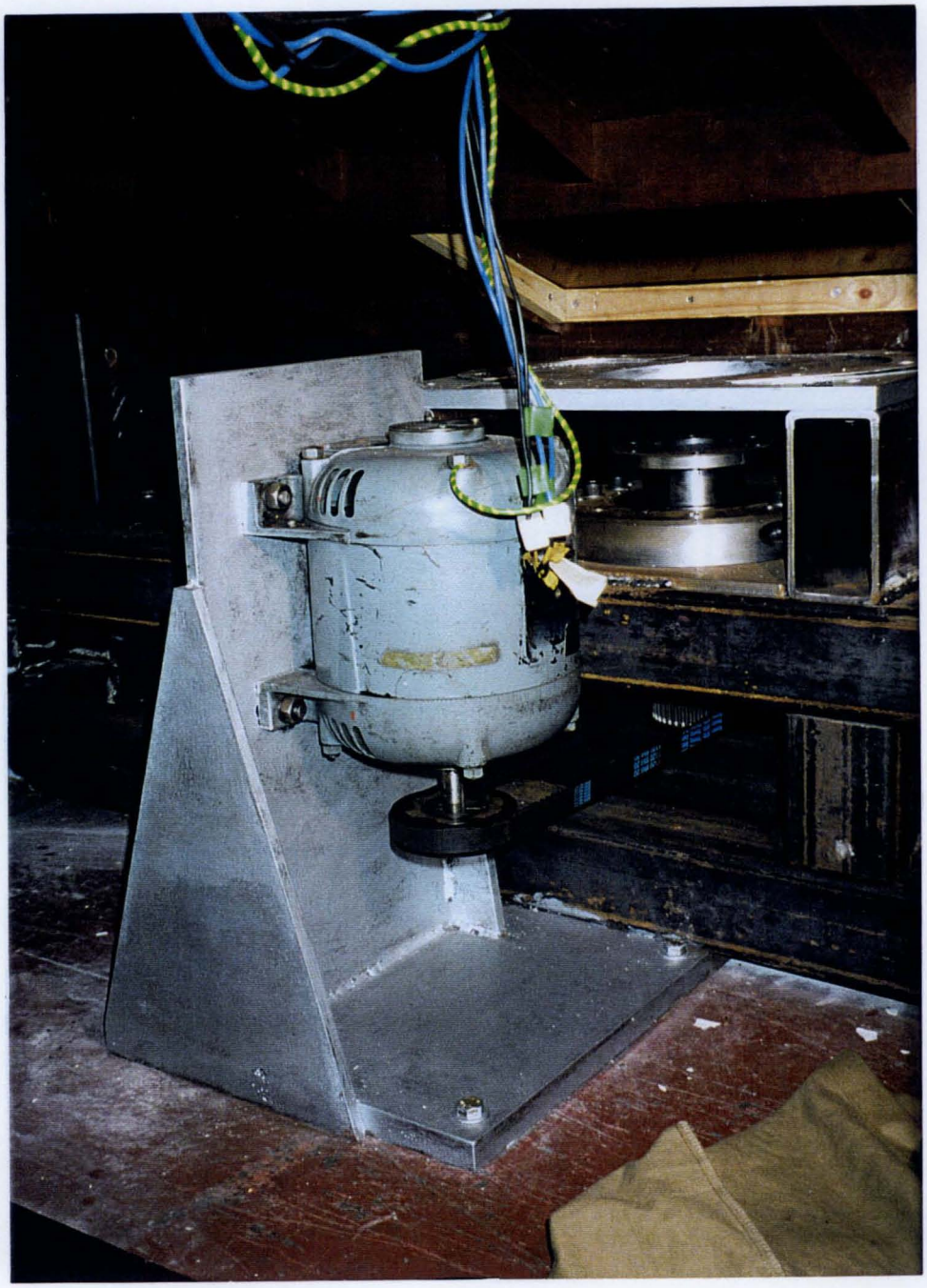

Figure 6.9- Photograph of the lower part of the main structure with motor, motor support and lower drive assembly (consisting of ball bearing and housing, belt drive with 1:1 gearing and plate on which the cam rests).

Figure 6.10- Photograph of upper part of the main structure with roller bearing and housing below the transverse beams. Optical sensors, to determine the rotational speed (rpm) and trigger for the hot-wire system, are positioned above the beams with reflective strips on the rotating shaft.

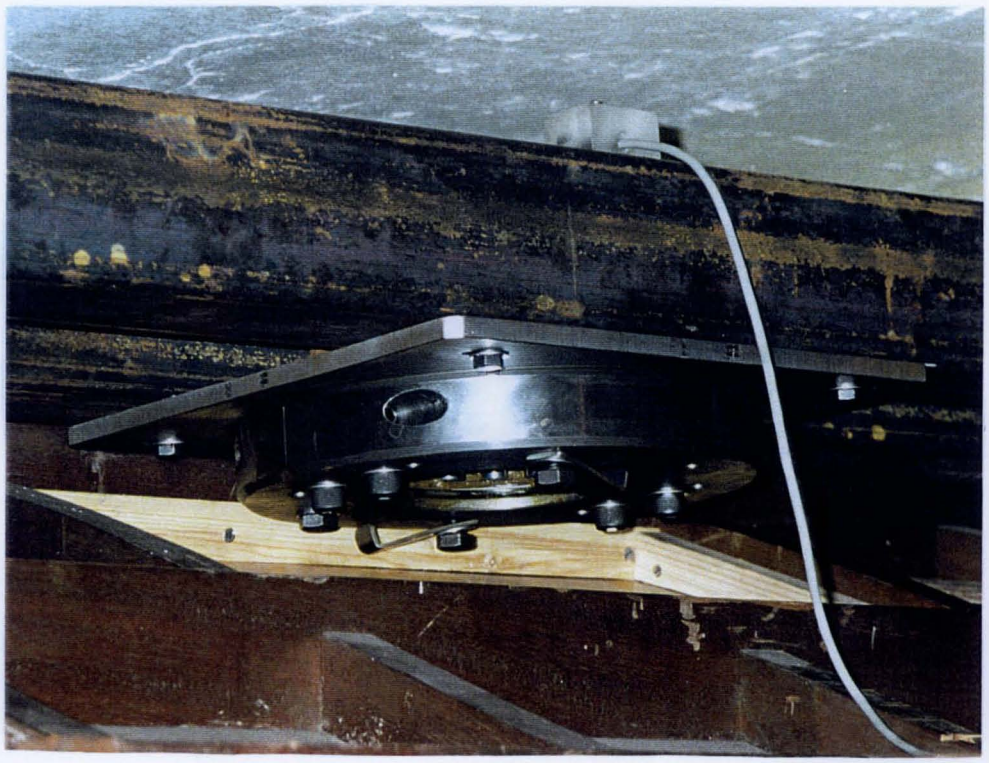

Figure 6.11- Close-up of upper roller bearing assembly. The two brackets, on the lower face of the bearing housing, hold the upper rotating shaft in place when installation takes place. The rpm sensor location is also evident on the upper surface of the transverse beams.

Figure 6.12- Photograph of the main factor which determined the final position of the rotating blade axis - a heating pipe which could not be moved of altered.

TABLES

Case	c (m)	R (m)	X (m)	Y (m)	WSVel (m/s)	TV1 (m/s)	TV2 (m/s)	AOA1 (°)	AOA2 (°)	Start (°)	AZI1 (°)	AZI2 (°)	Stop (°)	Start (°)	ALP1 (°)	ALP2 (°)	Stop (°)	tmax (secs)	tstep (secs)	nplot
1	0.09	0.7	3.0	0.0	20.0	70.0	70.0	5.0	5.0	225	300	420	500	270	315	390	450	0.15	0.0035	15
2	0.09	0.6	3.3	0.0	20.0	70.0	70.0	5.0	5.0	225	300	420	500	270	315	390	450	0.15	0.0035	13
3	0.09	0.6	3.3	0.0	30.0	70.0	70.0	5.0	5.0	225	300	420	500	270	315	390	450	0.15	0.0035	15
4	0.09	0.6	3.3	0.0	30.0	50.0	70.0	5.0	5.0	225	300	420	500	270	315	390	450	0.17	0.0035	20
5	0.09	0.6	3.3	0.1	30.0	50.0	70.0	5.0	5.0	225	300	420	500	270	315	390	450	0.17	0.0035	20
6	0.09	0.6	3.3	0.0	20.0	50.0	70.0	5.0	5.0	225	300	420	500	270	315	390	450	0.2	0.0035	20
7	0.09	0.6	3.3	0.0	20.0	50.0	50.0	5.0	5.0	225	300	420	500	270	315	390	450	0.2	0.0035	20
8	0.09	0.6	3.3	0.0	25.0	50.0	50.0	5.0	5.0	225	300	420	500	270	315	390	450	0.2	0.0035	15
9	0.09	0.6	3.3	0.0	25.0	50.0	50.0	5.0	5.0	180	270	345	500	270	315	350	400	0.2	0.0025	15
10	0.09	0.6	3.3	0.0	20.0	50.0	50.0	5.0	5.0	180	270	345	500	270	315	350	450	0.2	0.0025	20
11	0.09	0.6	3.3	0.0	20.0	50.0	90.0	5.0	5.0	180	270	370	500	270	315	350	450	0.2	0.0025	20
12	0.09	0.6	3.3	0.0	20.0	70.0	110.0	5.0	5.0	180	270	390	500	270	315	350	450	0.2	0.0025	20
13	0.09	0.6	3.3	0.0	20.0	50.0	100.0	5.0	5.0	180	300	390	500	270	315	350	450	0.2	0.0025	20
14	0.09	0.55	3.3	-0.2	20.0	50.0	100.0	5.0	5.0	180	300	390	540	270	315	350	450	0.2	0.0025	20
15	0.09	0.6	3.3	0.0	20.0	50.0	100.0	5.0	5.0	180	300	390	540	250	300	405	540	0.2	0.0025	20
16	0.09	0.6	3.3	0.0	20.0	50.0	100.0	5.0	5.0	180	300	390	540	250	300	405	540	0.2	0.0025	20
17	0.09	0.6	3.3	0.0	20.0	50.0	100.0	5.0	5.0	180	300	390	540	250	300	450	540	0.2	0.0025	20

Table 3.1- List of numerical model acceleration/deceleration (fixed rotation) test cases.

Case	c (m)	R (m)	X (m)	Y (m)	WSVel (m/s)	TV1 (m/s)	TV2 (m/s)	AOA1 (°)	AOA2 (°)	Start (°)	AZI1 (°)	AZI2 (°)	Stop (°)	Start (°)	ALP1 (°)	ALP2 (°)	Stop (°)	tmax (secs)	tstep (secs)	nplot
18	0.09	0.6	3.2	0	20.0	50.0	100.0	5.0	5.0	180	300	390	540	250	300	450	540	0.2	0.0025	20
19	0.09	0.6	3.2	0	20.0	50.0	100.0	5.0	2.0	180	300	390	540	250	300	390	540	0.2	0.0025	20
20	0.09	0.6	3.3	0	20.0	50.0	100.0	5.0	2.5	180	300	390	540	250	300	390	540	0.2	0.0025	20
21	0.09	0.6	3.4	0	20.0	50.0	100.0	5.0	3.0	180	300	390	540	250	300	390	540	0.2	0.0025	20
22	0.09	0.6	3.45	0	20.0	50.0	100.0	5.0	2.75	180	300	420	540	250	300	390	490	0.2	0.0025	20
23	0.09	0.6	3.45	0	20.0	50.0	100.0	5.0	2.75	180	300	440	540	250	300	390	490	0.2	0.0025	20
24	0.09	0.6	3.45	0	20.0	50.0	100.0	5.0	2.75	0	300	440	720	250	300	390	490	0.4	0.0035	20
25	0.09	0.6	3.45	0	15.0	60.0	100.0	5.0	2.75	180	300	420	540	250	300	390	490	0.2	0.0025	20
26	0.09	0.6	3.45	0	20.0	60.0	100.0	5.0	2.75	180	300	420	540	250	300	390	490	0.2	0.0025	20
27	0.09	0.8	3.0	0	20.0	30.0	60.0	5.0	2.75	180	300	420	540	280	320	400	450	0.4	0.0035	20
28	0.09	0.6	3.45	0	20.0	50.0	100.0	10.0	5.0	180	300	420	540	280	330	400	450	0.2	0.0025	20
29	0.09	0.75	3.2	0	20.0	50.0	90.0	5.0	2.75	180	300	420	540	280	330	400	450	0.2	0.0025	20
30	0.09	0.75	3.2	0	15.0	50.0	90.0	5.0	2.75	180	300	420	540	280	330	400	450	0.35	0.003	20
31	0.1	0.6	3.45	0	20.0	50.0	50.0	5.0	2.75	0	300	420	730	250	330	380	490	0.3	0.0025	20
32	0.1	0.6	3.45	0	20.0	35.0	50.0	5.0	2.75	0	300	420	730	250	330	380	440	0.2	0.0015	20
33	0.1	0.6	3.45	0	20.0	50.0	50.0	5.0	2.75	0	300	420	730	250	330	380	440	0.2	0.0015	20
34	0.1	0.65	3.45	0	20.0	50.0	50.0	5.0	2.75	0	300	420	730	250	330	380	440	0.2	0.0015	20

Table 3.1- List of numerical model acceleration/deceleration (fixed rotation) test cases (Continued).

Case	c (m)	R (m)	X (m)	Y (m)	WSVel (m/s)	TV1 (m/s)	TV2 (m/s)	AOA1 (°)	AOA2 (°)	Start (°)	AZI1 (°)	AZI2 (°)	Stop (°)	Start (°)	ALP1 (°)	ALP2 (°)	Stop (°)	tmax (secs)	tstep (secs)	nplot
35	0.15	0.65	3.45	0	20.0	50.0	---	5.0	2.75	0	---	---	---	250	330	380	440	0.4	0.0025	20
36	0.15	0.7	3.0	0	20.0	50.0	---	5.0	2.75	0	---	---	---	250	330	380	440	0.4	0.0025	20
37	0.15	0.8	2.5	0	20.0	50.0	---	5.0	2.75	0	---	---	---	250	330	380	440	0.3	0.0035	20
38	0.15	0.8	2.5	0	30.0	50.0	---	5.0	2.75	0	---	---	---	250	330	380	440	0.3	0.0035	20
39	0.15	0.75	3.2	0	30.0	50.0	---	5.0	2.75	0	---	---	---	250	330	380	440	0.3	0.003	20
40	0.15	0.75	2.8	0	30.0	50.0	---	5.0	2.75	0	---	---	---	250	330	380	440	0.3	0.003	20
41	0.15	0.75	2.8	0	20.0	50.0	---	5.0	2.75	0	---	---	---	250	330	380	440	0.3	0.003	20
42	0.15	0.75	3.2	0	20.0	50.0	---	5.0	2.75	0	---	---	---	250	330	380	440	0.3	0.003	20
43	0.09	0.75	3.2	0	20.0	50.0	---	5.0	2.75	0	---	---	---	250	330	380	440	0.3	0.003	20
44	0.09	0.75	3.2	0	20.0	50.0	---	8.0	4.0	0	---	---	---	250	330	380	440	0.3	0.003	20
45	0.09	0.75	3.2	0	20.0	50.0	---	10.0	5.0	0	---	---	---	250	330	380	440	0.3	0.003	20
46	0.09	0.75	3.2	0	20.0	50.0	---	10.0	10.0	0	---	---	---	250	330	380	440	0.3	0.003	20
47	0.15	0.75	3.2	0	20.0	50.0	---	5.0	5.0	0	---	---	---	250	330	380	440	0.3	0.003	20
48	0.15	0.75	3.1	0	20.0	50.0	---	10.0	10.0	0	---	---	---	250	330	380	440	0.3	0.003	20
49	0.15	0.75	3.1	0	20.0	50.0	---	5.0	5.0	0	---	---	---	250	330	380	440	0.3	0.003	20
50	0.09	0.75	3.1	0	20.0	50.0	---	5.0	5.0	0	---	---	---	250	330	380	440	0.3	0.003	20

Table 3.2 - List of numerical model continual running test cases.

Probe Serial		
	Sensor 1	***Sensor 2***
Cable Resistance R_c		
Total Resistance R_{tot}		
Sensor Resistance $R_s = R_{tot} - R_c$		
Operating Resistance $R_{op} = OHR \times R_s$		

OHR = Overheat Ratio = 1.8

	Sensor 1	***Sensor 2***
Minimum Voltage E_o		
Maximum Voltage E_M		
Span $Span = \frac{10}{E_M - E_o}$		
Offset $Offset = E_M - \frac{5}{Span}$		
Gain $Gain = \frac{5}{E_M - Offset}$		

E_o = Voltage at Zero Calibration Velocity

E_M = Voltage at Maximum Calibration Velocity

Table 4.1- Hot-wire calibration record for single (Ignore sensor 2 column) and x-wire probes.

Date	
Filename/s	
Probe Serial	
Probe Calibration File	
Probe Orientation (0°/90°)	
Sampling Frequency (*Hz*)	
Traverse Grid Size (*mm*)	
Blade Incidence *(degrees)*	
Blade Separation *(mm)*	
Measurement Position *(chord lengths behind T.E.)*	
Atmospheric Pressure (*mmHg*)	
Atmospheric Temperature ($^{\circ}C$)	
Reynolds Number	
Mano Reading $\Delta P\,(mmH_2O)$	
Working Section Velocity (m/s)	
Comments	

Table 5.1- Twin vortex data acquisition record.

T_{atms} $^{\circ}C$	P_{atms} $mmHg$	T_{atms} K	ρ kg/m^3	μ kg/ms	V m/s	c m	Re	ΔP mmH_2O
10	753	283.15	1.2352	1.7424E-05	30	0.1	212668	45.80
11	753	284.15	1.2308	1.7472E-05	30	0.1	211337	45.64
12	753	285.15	1.2265	1.7520E-05	30	0.1	210020	45.48
13	753	286.15	1.2222	1.7568E-05	30	0.1	208717	45.32
14	753	287.15	1.2180	1.7615E-05	30	0.1	207426	45.17
15	753	288.15	1.2137	1.7663E-05	30	0.1	206148	45.01
16	753	289.15	1.2095	1.7711E-05	30	0.1	204883	44.85
17	753	290.15	1.2054	1.7758E-05	30	0.1	203631	44.70
18	753	291.15	1.2012	1.7806E-05	30	0.1	202391	44.55
19	753	292.15	1.1971	1.7853E-05	30	0.1	201163	44.39
20	753	293.15	1.1930	1.7900E-05	30	0.1	199947	44.24
21	753	294.15	1.1890	1.7947E-05	30	0.1	198744	44.09
22	753	295.15	1.1850	1.7995E-05	30	0.1	197552	43.94
23	753	296.15	1.1809	1.8042E-05	30	0.1	196371	43.79
24	753	297.15	1.1770	1.8089E-05	30	0.1	195202	43.65
25	753	298.15	1.1730	1.8135E-05	30	0.1	194045	43.50
26	753	299.15	1.1691	1.8182E-05	30	0.1	192898	43.35
27	753	300.15	1.1652	1.8229E-05	30	0.1	191762	43.21
28	753	301.15	1.1613	1.8276E-05	30	0.1	190638	43.07
29	753	302.15	1.1575	1.8322E-05	30	0.1	189524	42.92
30	753	303.15	1.1537	1.8369E-05	30	0.1	188420	42.78
31	753	304.15	1.1499	1.8415E-05	30	0.1	187327	42.64
32	753	305.15	1.1461	1.8462E-05	30	0.1	186244	42.50
33	753	306.15	1.1424	1.8508E-05	30	0.1	185172	42.36
34	753	307.15	1.1387	1.8554E-05	30	0.1	184109	42.22
35	753	308.15	1.1350	1.8600E-05	30	0.1	183057	42.09

Table 5.2- Calculation of manometer setting and Reynolds Number for specified working section velocity.

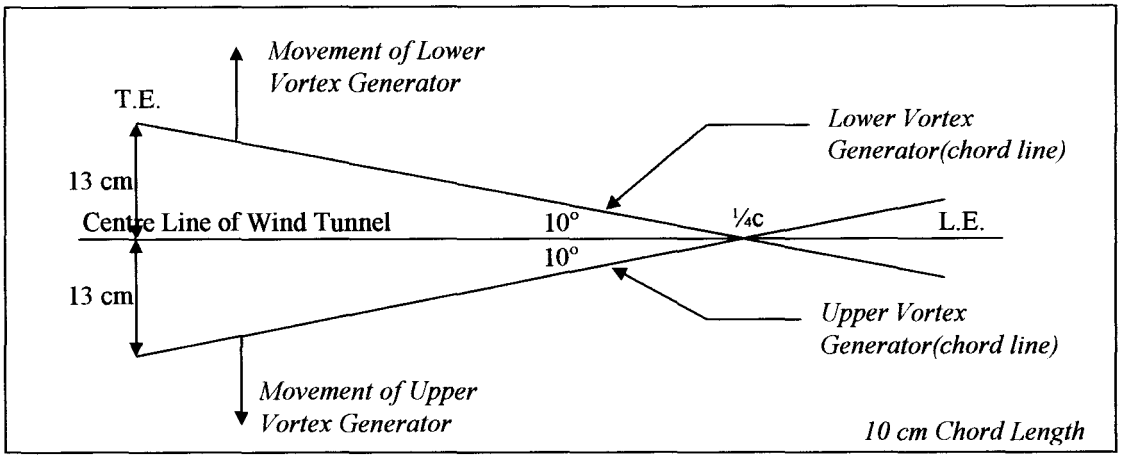

Illustration of the initial position of vortex generators (looking down) which corresponds to 0.0c quarter chord (¼ c) separation and 10° incidence (case 4). This configuration generates a single vortex similar to that generated by Kokkalis and Horner. To generate the twin vortex system, the upper generator moves to the right (looking upstream) and the lower to the left.

Test Conducted	*Description of Test*
General Blade Orientations	Single and co/counter rotating twin vortex measurements conducted at 2.5c and 6c downstream of trailing edges.
Incidence Variation	2-12 degree incidence variation at 4.3c downstream. Blade separation of 0.5c between ¼c positions
Downstream Position	Variation in downstream measurement position 0.1c-10c. Vortex Generator separation held constant at 0.5c between ¼ c positions and 10 degrees incidence.
Blade Separation	Variation of ¼ c separation position from 0c to 1c every 0.25c. Measurements conducted at 4c and 8c downstream of trailing edges at 10 degrees incidence.

Table 5.3- Chronological list of tests conducted in the 1.15m x 0.8m wind tunnel.

General Blade Orientation

Case	Measurement Position	Blade Incidence $\alpha(^o)$	Blade Separation	Blade Orientation	Traverse Orientation	Grid Size (mm)
1	2.5c	10°	0.5c (¼c)	T.E. Outwards	Vertical	100x200
2	2.5c	10°	0.5c (¼c)	T.E. Inwards	Vertical	100x200
3	2.5c	2°	0.5c (¼c)	T.E. Outwards	Vertical	100x200
4	2.5c	10°	0.0c	Same Sense as 1	Vertical	100x200
5	2.5c	10°	0.0c	Same Sense as 2	Vertical	100x200
6	2.5c	10°	0.5c (T.E.)	T.E. Outwards	Vertical	100x200
7	2.5c	10°	0.5c (T.E.)	T.E. Inwards	Vertical	100x200
8	2.5c	10°	0.5c	Opposite Sense	Vertical	100x200
9	6c	10°	0.5c (¼c)	T.E. Outwards	Vertical	100x200
10	6c	10°	0.5c (¼c)	T.E. Inwards	Vertical	100x200
11	6c	2°	0.5c (¼c)	T.E. Outwards	Vertical	100x200
12	6c	10°	0.0c	Same Sense as 1	Vertical	100x200
13	6c	10°	0.0c	Same Sense as 2	Vertical	100x200
14	6c	10°	0.5c (T.E.)	T.E. Outwards	Vertical	100x200
15	6c	10°	0.5c (T.E.)	T.E. Inwards	Vertical	100x200
16	6c	10°	0.5c	Opposite Sense	Vertical	100x200

Table 5.4- General test configurations for single and twin co and counter rotating vortices.

Variation of Blade Incidence

Case	Measurement Position	Blade Incidence $\alpha(^o)$	Blade Separation	Blade Orientation	Traverse Orientation	Grid Size (mm)
17	4.3c	10°	0.0c	Same sense as 1	Vertical	100x200
18	4.3c	10°	0.5c (¼c)	T.E. Outwards	Vertical	100x200
19	4.3c	12°	0.5c (¼c)	T.E. Outwards	Vertical	100x200
20	4.3c	8°	0.5c (¼c)	T.E. Outwards	Vertical	100x200
21	4.3c	6°	0.5c (¼c)	T.E. Outwards	Vertical	100x200
22	4.3c	4°	0.5c (¼c)	T.E. Outwards	Vertical	100x200
23	4.3c	2°	0.5c (¼c)	T.E. Outwards	Vertical	100x200

Table 5.5- Twin vortex test configurations to investigate the influence of blade incidence setting (Case 17 for verification with previous tests in Table 5.4).

Variation of Downstream Measurement Position

Case	Measurement Position	Blade Incidence $\alpha(^o)$	Blade Separation	Blade Orientation	Traverse Orientation	Grid Size (mm)
24	0.1c	10°	0.5c (¼c)	T.E. Outwards	Horizontal	100x160
25	1.0c	10°	0.5c (¼c)	T.E. Outwards	Horizontal	100x160
26	0.1c	10°	0.5c (¼c)	T.E. Outwards	Horizontal	160x160
27	0.5c	10°	0.5c (¼c)	T.E. Outwards	Horizontal	160x160
28	1.0c	10°	0.5c (¼c)	T.E. Outwards	Horizontal	160x160
29	2.0c	10°	0.5c (¼c)	T.E. Outwards	Horizontal	160x160
30	3.0c	10°	0.5c (¼c)	T.E. Outwards	Horizontal	160x160
31	4.0c	10°	0.5c (¼c)	T.E. Outwards	Horizontal	160x160
32	5.0c	10°	0.5c (¼c)	T.E. Outwards	Horizontal	160x160
33	6.0c	10°	0.5c (¼c)	T.E. Outwards	Horizontal	160x160
34	7.0c	10°	0.5c (¼c)	T.E. Outwards	Horizontal	160x160
35	8.0c	10°	0.5c (¼c)	T.E. Outwards	Horizontal	160x160
36	9.0c	10°	0.5c (¼c)	T.E. Outwards	Horizontal	160x160
37	10.0c	10°	0.5c (¼c)	T.E. Outwards	Horizontal	160x160

Table 5.6- Tests configurations for the investigation of downstream measurement position.

Variation of Blade Separation

Case	Measurement Position	Blade Incidence $\alpha(^o)$	Blade Separation	Blade Orientation	Traverse Orientation	Grid Size (mm)
38	4.0c	10°	0.0c	T.E. Outwards	Horizontal	160x160
39	4.0c	10°	0.25c (¼c)	T.E. Outwards	Horizontal	160x160
40	4.0c	10°	0.0c	T.E. Outwards	Horizontal	160x160
41	4.0c	10°	0.25c (¼c)	T.E. Outwards	Horizontal	160x160
42	4.0c	10°	0.5c (¼c)	T.E. Outwards	Horizontal	160x160
43	4.0c	10°	0.75c (¼c)	T.E. Outwards	Horizontal	160x160
44	4.0c	10°	1.0c (¼c)	T.E. Outwards	Horizontal	160x160
45	8.0c	10°	0.0c (¼c)	T.E. Outwards	Horizontal	160x160
46	8.0c	10°	0.25c (¼c)	T.E. Outwards	Horizontal	160x160
47	8.0c	10°	0.5c (¼c)	T.E. Outwards	Horizontal	160x160
48	8.0c	10°	0.75c (¼c)	T.E. Outwards	Horizontal	160x160
49	8.0c	10°	1.0c (¼c)	T.E. Outwards	Horizontal	160x160
50	0.5c	10°	0.5c (¼c)	T.E. Outwards	Horizontal	160x160
51	2.0c	10°	0.5c	Opposite Sense	Horizontal	160x160
52	2.0c	10°	0.5c	Opposite Sense	Horizontal	160x160

Table 5.7- Tests configurations for the investigation of the influence of blade ¼c separation.

Single Vortex Measurements (2.1m x 1.6m tunnel)

Case	*Blade Incidence*	*Generator Vertical Position*		*Grid Size*	*Traverse Orientation*
	α(°)	*(mm)*	*(/c)*	*(mm)*	
1	*12.5*	*0.0*	*0.0*	*240x240*	*Horizontal*
2	*10.0*	*0.0*	*0.0*	*240x240*	*Horizontal*
3	*7.5*	*0.0*	*0.0*	*240x240*	*Horizontal*
4	*5.0*	*0.0*	*0.0*	*240x240*	*Horizontal*
5	*2.5*	*0.0*	*0.0*	*240x240*	*Horizontal*
6	*12.5*	*228.6*	*1.5*	*240x240*	*Horizontal*
7	*12.5*	*-228.6*	*-1.5*	*240x240*	*Horizontal/Inverted*
8	*12.5*	*0.0*	*0.0*	*240x240*	*Horizontal/Inverted*

Table 5.8- Single vortex test configurations implemented in the 2.1m x 1.6m low speed wind tunnel.

Case	Blade Incidence	Top Generator Vertical Position		Top Generator Lateral Position		Bottom Generator Vertical Position		Bottom Generator Lateral Position		Grid Size	Tip Separation (between ¼c)	Angle between Tips
	$\alpha(^{o})$	(mm)	(/c)	(mm)	(/c)	(mm)	(/c)	(mm)	(/c)	(mm)		
9	12.5	0.0	0.0	46.35	0.30	0.0	0.0	-46.35	-0.30	300x300	0.5c	0°
10	10.0	0.0	0.0	44.72	0.29	0.0	0.0	-44.72	-0.29	300x300	0.5c	0°
11	7.5	0.0	0.0	43.07	0.28	0.0	0.0	-43.07	-0.28	300x300	0.5c	0°
12	5.0	0.0	0.0	41.42	0.27	0.0	0.0	-41.42	-0.27	300x300	0.5c	0°
13	12.5	26.94	0.18	35.19	0.23	-26.94	-0.18	-35.19	-0.23	300x300	0.5c	45°
14	12.5	38.1	0.25	0.0	0.0	-38.1	-0.25	0.0	0.0	300x300	0.5c	90°
15	12.5	19.05	0.13	0.0	0.0	-19.05	-0.13	0.0	0.0	300x300	0.25c	90°
16	12.5	0.0	0.0	27.30	0.179	0.0	0.0	-27.30	-0.179	300x300	0.25c	0°
17	12.5	0.0	0.0	65.40	0.43	0.0	0.0	-65.40	-0.43	300x300	0.75c	0°
18	12.5	0.0	0.0	89.42	0.59	0.0	0.0	-89.42	-0.59	300x300	1.0c	0°
19	7.5	0.0	0.0	81.17	0.53	0.0	0.0	-81.17	-0.53	300x300	1.0c	0°
20	7.5	76.2	0.5	0.0	0.0	-76.2	-0.5	0.0	0.0	300x300	1.0c	90°
21	12.5	57.15	0.38	0.0	0.0	-57.15	-0.38	0.0	0.0	300x300	0.75c	90°
22	7.5	26.94	0.18	31.91	0.21	-26.94	-0.18	-31.91	-0.21	300x300	0.5c	45°
23	7.5	40.41	0.27	45.38	0.297	-40.41	-0.27	-45.38	-0.297	300x300	0.75c	45°
24	12.5	40.41	0.27	48.65	0.32	-40.41	-0.27	-48.65	-0.32	300x300	0.75c	45°
25	7.5	53.88	0.35	58.85	0.39	-53.88	-0.35	-58.85	-0.39	300x300	1.0c	45°
26	7.5	38.1	0.25	0.0	0.0	-38.1	-0.25	0.0	0.0	300x300	0.5c	90°
27	12.5	26.94	0.18	-18.69	-0.47	-26.94	-0.18	18.69	0.47	300x300	0.5c	135°
28	7.5	26.94	0.18	-21.97	-0.38	-26.94	-0.18	21.97	0.38	300x300	0.5c	135°
29	7.5	0.0	0.0	62.12	0.41	0.0	0.0	-65.4	-0.43	300x300	0.75c	0°

Table 5.9- Twin vortex test configurations implemented in the 2.1m x 1.6m low speed wind tunnel (refer to Fig. B.5).

Case	Meas. Pos.	α (°)	Γ1 (m^2/s)	X1 (m)	Y1 (m)	RC1 (m)	Γ2 (m^2/s)	X2 (m)	Y2 (m)	RC2 (m)
1	2.5c	10	-0.85	0.014	-0.021	0.008	-0.9	-0.012	0.027	0.008
2	2.5c	10	0.9	-0.024	-0.002	0.0075	0.9	0.03	0.005	0.008
3	2.5c	2	-0.25	0.003	-0.023	0.01	-0.3	0.004	0.024	0.01
4	2.5c	10	-0.8	0.001	0.0	0.01	-0.85	-0.001	0.006	0.008
5	2.5c	10	0.8	0.001	0.0	0.01	0.85	-0.001	0.006	0.008
6	2.5c	10	-0.9	0.013	0.015	0.0075	-0.98	-0.01	-0.004	0.0079
7	2.5c	10	1.0	-0.026	-0.022	0.009	0.95	0.032	0.028	0.009
8	2.5c	10	-1.0	-0.039	-0.018	0.007	0.95	-0.017	0.032	0.0076
9	6c	10	-0.9	0.027	0.0085	0.011	-0.98	-0.021	0.0019	0.011
10	6c	10	1.0	-0.017	0.023	0.014	0.95	0.02	-0.023	0.014
11	6c	2	-0.16	0.01	-0.02	0.013	-0.24	0.004	0.022	0.013
12	6c	10	-0.9	0.0	0.008	0.013	-1.0	0.0	0.008	0.013
13	6c	10	0.85	0.003	0.0075	0.014	0.9	0.008	0.0075	0.014
14	6c	10	-0.9	-0.005	-0.005	0.013	-0.95	0.01	0.02	0.013
15	6c	10	1.0	-0.032	-0.002	0.013	0.93	0.049	0.007	0.013
16	6c	10	-1.05	-0.07	-0.006	0.012	1.0	-0.045	0.043	0.012

Table 5.10- Results of the general blade orientation tests (Table 5.4) as determined from the two-dimensional numerical model.

Case	Meas. Pos.	α (°)	Γ1 (m^2/s)	X1 (m)	Y1 (m)	RC1 (mm)	Γ1 (m^2/s)	X2 (m)	Y2 (m)	RC2 (m)
17	4.3c	10	-0.9	0.0	0.002	0.01	-0.9	0.001	0.009	0.01
18	4.3c	10	-0.95	0.032	-0.007	0.009	-1.03	-0.017	0.017	0.009
19	4.3c	12	-1.1	0.032	-0.007	0.009	-1.2	-0.017	0.011	0.009
20	4.3c	8	-0.65	0.028	-0.009	0.009	-0.87	-0.013	0.019	0.009
21	4.3c	6	-0.55	0.0265	-0.013	0.01	-0.65	-0.003	0.022	0.009
22	4.3c	4	-0.35	0.018	-0.018	0.01	-0.4	0.03	0.024	0.009
23	4.3c	2	-0.2	0.013	-0.018	0.01	-0.2	0.008	0.024	0.01

Table 5.11- Results of the incidence variation tests (Table 5.5) as determined from the two-dimensional numerical model.

Case	Meas. Pos.	α (^{o})	Γ1 (m^2/s)	X1 (m)	Y1 (m)	RC1 (mm)	Γ1 (m^2/s)	X2 (m)	Y2 (m)	RC2 (m)
24	0.1c	10	-0.7	0.001	-0.032	0.005	-0.7	0.003	0.028	0.005
25	1.0c	10	-0.8	0.0075	-0.025	0.006	-0.85	-0.001	0.027	0.006
26	0.1c	10	-0.7	0.001	-0.031	0.005	-0.73	0.003	0.029	0.005
27	0.5c	10	-0.72	0.001	-0.031	0.005	-0.76	0.0005	0.028	0.004
28	1.0c	10	-0.8	0.0075	-0.027	0.0059	-0.85	-0.001	0.025	0.0058
29	2.0c	10	-0.85	0.018	-0.024	0.0075	-0.9	-0.0035	0.024	0.0067
30	3.0c	10	-0.85	0.023	-0.018	0.009	-0.9	-0.011	0.02	0.009
31	4.0c	10	-0.9	0.028	-0.013	0.009	-0.95	-0.015	0.013	0.009
32	5.0c	10	-0.9	0.029	-0.004	0.012	-0.95	-0.017	0.0025	0.01
33	6.0c	10	-0.9	0.029	0.004	0.012	-0.95	-0.015	-0.008	0.011
34	7.0c	10	-0.9	0.026	0.012	0.014	-0.95	-0.013	-0.015	0.014
35	8.0c	10	-0.9	0.024	0.017	0.016	-0.95	-0.01	-0.023	0.016
36	9.0c	10	-0.9	0.013	0.02	0.017	-0.95	0.02	-0.027	0.017
37	10.0c	10	-0.9	0.006	0.02	0.017	-0.95	0.008	-0.027	0.017

Table 5.12- Results of the downstream measurement position tests (Table 5.6) as determined from the two-dimensional numerical model.

Case	Meas. Pos.	Blade Sep.	Γ1 (m^2/s)	X1 (m)	Y1 (m)	RC1 (m)	Γ2 (m^2/s)	X2 (m)	Y2 (m)	RC2 (m)
38	4.0c	0.0c	-0.95	0.005	0.005	0.013	-0.95	0.005	0.005	0.013
39	4.0c	0.25c	-0.9	-0.004	0.016	0.01	-0.95	0.015	-0.01	0.01
40	4.0c	0.0c	-1.0	0.001	0.0	0.013	-0.95	0.0	0.0	0.013
41	4.0c	0.25c	-0.95	0.014	-0.01	0.01	-0.95	-0.007	0.013	0.01
42	4.0c	0.5c	-0.95	0.03	-0.01	0.01	-1.0	-0.017	0.012	0.01
43	4.0c	0.75c	-0.95	0.02	-0.0345	0.01	-1.0	-0.01	0.032	0.01
44	4.0c	1.0c	-0.95	0.013	-0.052	0.01	-1.0	-0.004	0.048	0.01
45	8.0c	0.0c	-0.95	0.0	0.0	0.017	-1.0	0.0	0.0	0.017
46	8.0c	0.25c	-0.95	0.01	0.0	0.02	-1.0	0.015	0.0	0.02
47	8.0c	0.5c	-0.95	0.015	0.023	0.015	-1.0	-0.01	-0.02	0.015
48	8.0c	0.75c	-0.95	0.04	-0.02	0.015	-1.0	-0.025	0.01	0.015
49	8.0c	1.0c	-0.95	0.035	-0.043	0.015	-1.0	-0.02	0.039	0.015
50	0.5c	0.5c	-0.75	0.002	-0.026	0.006	-0.8	0.0005	0 .029	0.006
51	2.0c	0.5c	0.95	0.018	-0.03	0.008	-1.0	0.04	0.023	0.008
52	2.0c	0.5c	0.95	-0.03	-0.028	0.007	-0.95	-0.01	0.023	0.008

Table 5.13- Results of the blade ¼c separation tests (Table 5.7) as determined from the two-dimensional numerical model.

Case	α (°)	Γ (m^2/s)	X (m)	Y (m)	RC (m)
1	12.5	-5.8	0.026	-0.005	0.023
2	10.0	-4.4	0.026	-0.007	0.022
3	7.5	-3.2	0.032	-0.005	0.022
4	5.0	-2.2	0.032	-0.0115	0.024
5	2.5	-1.1	0.032	-0.0115	0.024
6	12.5	-5.8	-0.026	-0.005	0.023
7	12.5	-5.8	-0.025	-0.033	0.024
8	12.5	-5.8	-0.028	-0.013	0.023

Table 5.14- Results of the 2.1m x 1.6m single vortex tests (Table 5.8) as determined from the two-dimensional numerical model.

Case	α (°)	Γ1 (m^2/s)	X1 (m)	Y1 (m)	RC1 (m)	Γ2 (m^2/s)	X2 (m)	Y2 (m)	RC2 (m)
9	12.5	-2.9	0.02	-0.038	0.017	-2.9	0.02	0.035	0.017
10	10	-2.4	0.008	-0.035	0.019	-2.4	0.035	0.033	0.019
11	7.5	-1.6	-0.001	-0.028	0.018	-1.6	0.04	0.023	0.018
12	5.0	-1.1	0.0	-0.001	0.018	-1.1	0.05	0.005	0.018
13	12.5	-2.9	-0.013	0.004	0.02	-2.9	0.06	-0.015	0.02
14	12.5	-2.9	0.045	0.055	0.017	-2.9	0.007	-0.06	0.017
15	12.5	-2.7	0.028	-0.005	0.026	-2.7	0.018	-0.005	0.026
16	12.5	-2.9	0.045	0.01	0.02	-2.9	0.02	-0.01	0.02
17	12.5	-2.9	0.08	-0.005	0.016	-2.9	-0.005	-0.005	0.017
18(u)	12.5	-2.9	0.105	-0.053	0.017	-2.9	0.025	0.047	0.017
18(v)	12.5	-2.9	0.085	-0.055	0.016	-2.9	-0.003	0.04	0.016
19	7.5	-1.6	0.091	-0.055	0.02	-1.6	0.043	0.054	0.02
20(u)	7.5	-1.6	0.21	0.02	0.021	-1.6	0.05	-0.025	0.021
20(v)	7.5	-1.6	0.17	0.02	0.02	-1.6	-0.03	-0.02	0.02
21	12.5	-2.9	0.125	0.05	0.02	-2.9	0.005	-0.055	0.02
22	7.5	-1.9	0.06	0.04	0.021	-1.9	0.073	-0.035	0.019
23	7.5	-1.6	0.099	0.05	0.015	-1.6	0.035	-0.07	0.015
24	12.5	-2.9	0.065	0.07	0.019	-2.9	0.065	-0.07	0.019
25	7.5	-1.6	0.129	0.07	0.02	-1.6	0.015	-0.07	0.02
26	7.5	-1.6	0.125	0.03	0.018	-1.6	0.02	-0.03	0.016
27	12.5	-2.9	0.155	-0.028	0.018	-2.9	-0.025	0.026	0.018
28	7.5	-1.6	0.1	-0.04	0.018	-1.6	-0.045	0.025	0.016
29	7.5	-1.6	0.065	-0.03	0.018	-1.6	-0.01	0.028	0.015

Table 5.15- Results of 2.1m x 1.6m twin vortex tests (Table 5.9) as determined from two-dimensional numerical model.

Date	
Filename/s	
Probe Serial	
Probe Calibration File	
Probe Orientation (0°/90°)	
Sampling Frequency (*Hz*)	
Measurement Location (*mm*)	
Blade Rotational Speed *(rpm)*	
Atmospheric Pressure (*mmHg*)	
Atmospheric Temperature (°*C*)	
Reynolds Number	
Mano Reading (mmH_2O)	
Working Section Velocity (m/s)	
Comments	

Table 6.1- Transverse vortex data acquisition record.

Test Case	*Working Section Velocity*	*Rotational speed*	*Sampling Time*	*Measurement Position*
	(m/s)	*rpm*	*secs*	*x,y (mm)*
1	*10*	*400*	*0.4*	*-30,150*
2	*10*	*400*	*0.8*	"
3	*20*	*520*	*0.4*	"
4	*20*	*600*	*0.8*	"

Table 6.2- Initial transverse vortex test cases. Measurement position related to centre line of working section with *x* corresponding to a vertical movement from the centre line and *y* a horizontal. Sampling rate set at 5000Hz for all tests.

Test Case	*Working Section Velocity*	*Rotational speed*	*Sampling Time*	*Measurement Position*
	(m/s)	*rpm*	*secs*	*x,y (mm)*
5	*10*	*0*	*0.8*	*-30,150*
6	*10*	*300*	"	"
7	*10*	*375*	"	"
8	*10*	*500*	"	"
9	*10*	*600*	"	"
10	*10*	*500*	*0.8*	*-30,150*
11	*10*	*500*	"	*-30,75*
12	*10*	*500*	"	*-30,0*
13	*10*	*500*	"	*-30,-75*
14	*10*	*500*	"	*-30,-150*

Table 6.3- Transverse vortex test cases with working section velocity of 10 m/s. Measurement position related to centre line of working section with *x* corresponding to a vertical movement from the centre line and *y* a horizontal. Sampling rate set at 5000Hz for all tests.

Test Case	*Working Section Velocity*	*Rotational speed*	*Sampling Time*	*Measurement Position*
	(m/s)	*rpm*	*secs*	*x,y (mm)*
15	*20*	*0*	*0.8*	*-30,-150*
16	*20*	*300*	"	"
17	*20*	*375*	"	"
18	*20*	*500*	"	"
19	*20*	*600*	"	"
20	*20*	*500*	*0.8*	*-30,150*
21	*20*	*500*	"	*-30,75*
22	*20*	*500*	"	*-30,0*
23	*20*	*500*	"	*-30,-75*
24	*20*	*500*	"	*-30,-150*

Table 6.4- Transverse vortex test cases with a working section velocity of 20 m/s. Measurement position related to centre line of working section with *x* corresponding to a vertical movement from the centre line and *y* a horizontal. Sampling rate set at 5000Hz for all tests.

Test Case	*Working Section Velocity*	*Rotational speed*	*Sampling Time*	*Measurement Position*
	(m/s)	*rpm*	*secs*	*x,y (mm)*
25	*15*	*0*	*0.8*	*-30,-150*
26	*15*	*300*	"	"
27	*15*	*375*	"	"
28	*15*	*500*	"	"
29	*15*	*600*	"	"
30	*15*	*500*	*0.8*	*-30,150*
31	*15*	*500*	"	*-30,75*
32	*15*	*500*	"	*-30,0*
33	*15*	*500*	"	*-30,-75*
34	*15*	*500*	"	*-30,-150*

Table 6.5- Transverse vortex test cases with a working section velocity of 15 m/s. Measurement position related to centre line of working section with *x* corresponding to a vertical movement from the centre line and *y* a horizontal. Sampling rate set at 5000Hz for all tests.

Dial Setting	*1000*	*1200*	*1500*	*1600*	*2000*	*2400*
Rotational Speed (rpm)	*250*	*300*	*375*	*400*	*500*	*600*
Frequency, f (Hz)	*4.16*	*5*	*6.25*	*6.67*	*8.33*	*10*
Period, T (secs/rev)	*0.24*	*0.2*	*0.16*	*0.15*	*0.12*	*0.1*

Table 6.6- Specification of the rotational speed of the blade from the dial setting. The dial setting corresponds to 4 times the rpm due to 4 reflective strips being positioned at 90 degree intervals around the rotating shaft. The corresponding period of rotation is also given for comparison with the period of the convecting transverse vortex.

RESULTS

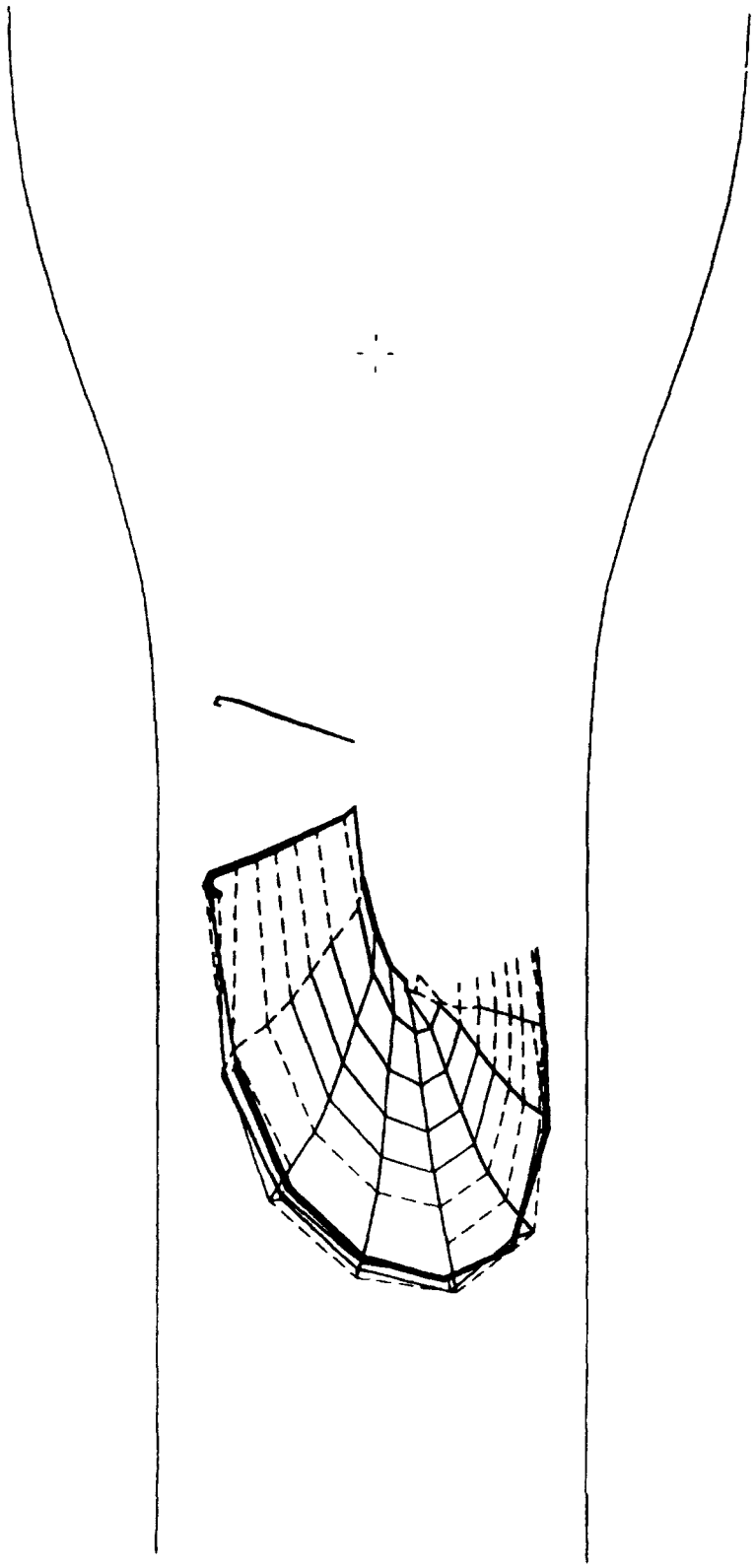

Figure R3.1- Single rotation convecting wake with 30 m/s working section velocity - tip velocity constant at 70 m/s across working section.

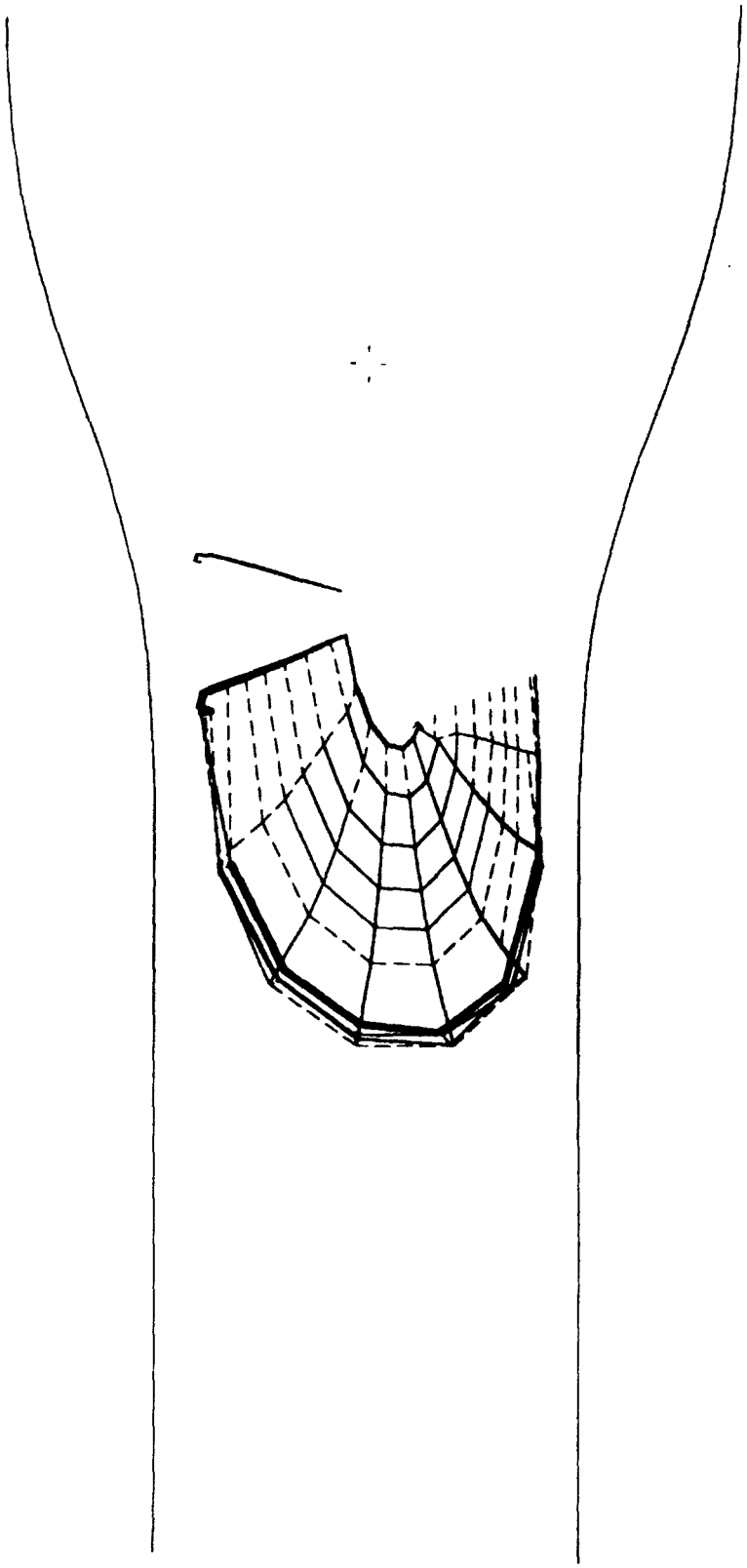

Figure R3.2- Single rotation convecting wake with 20 m/s working section velocity - tip velocity constant at 70 m/s across working section.

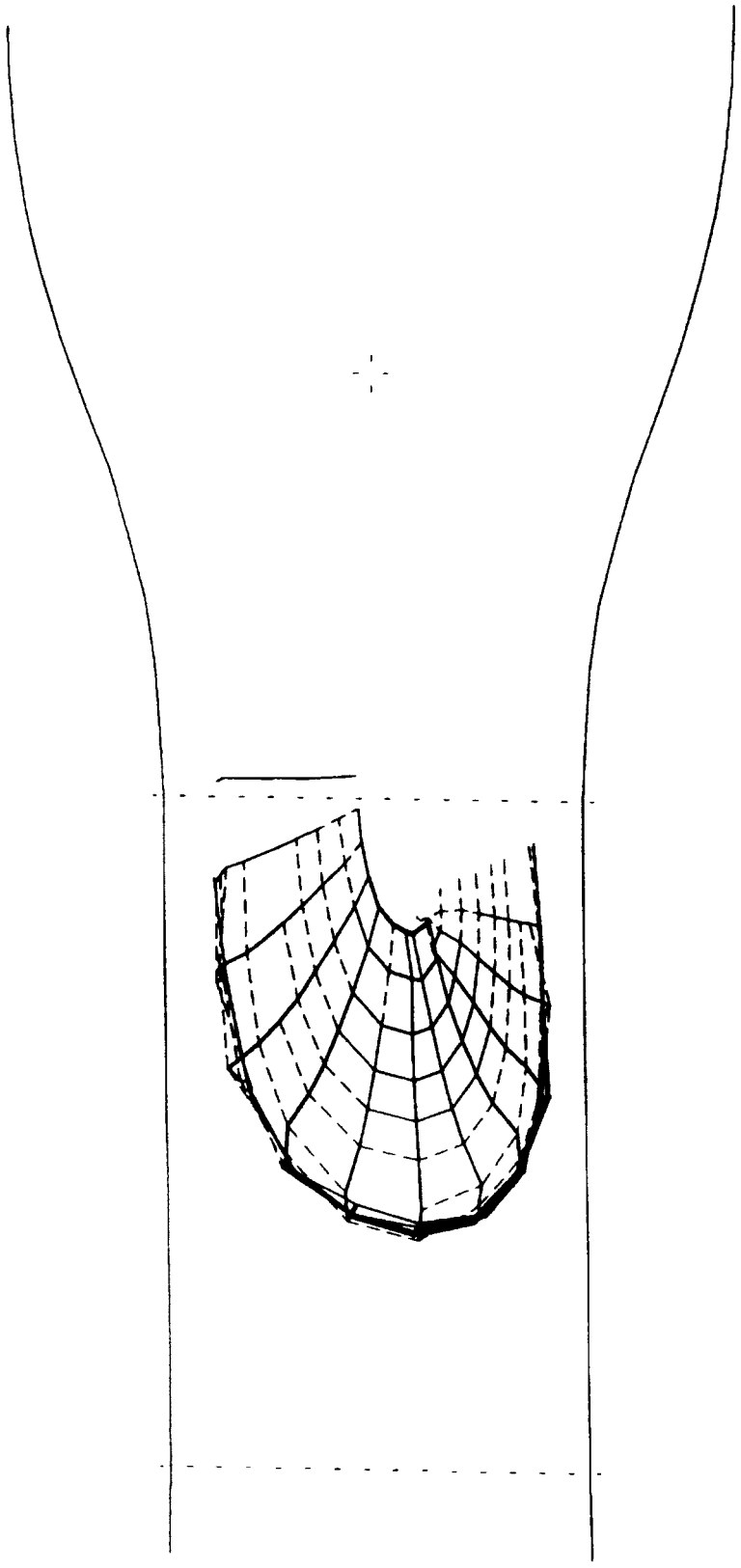

Figure R3.3- Single rotation convecting wake with 20 m/s working section velocity - tip velocity increasing from 50 to 90 m/s across working section incidence held constant at 5 degrees.

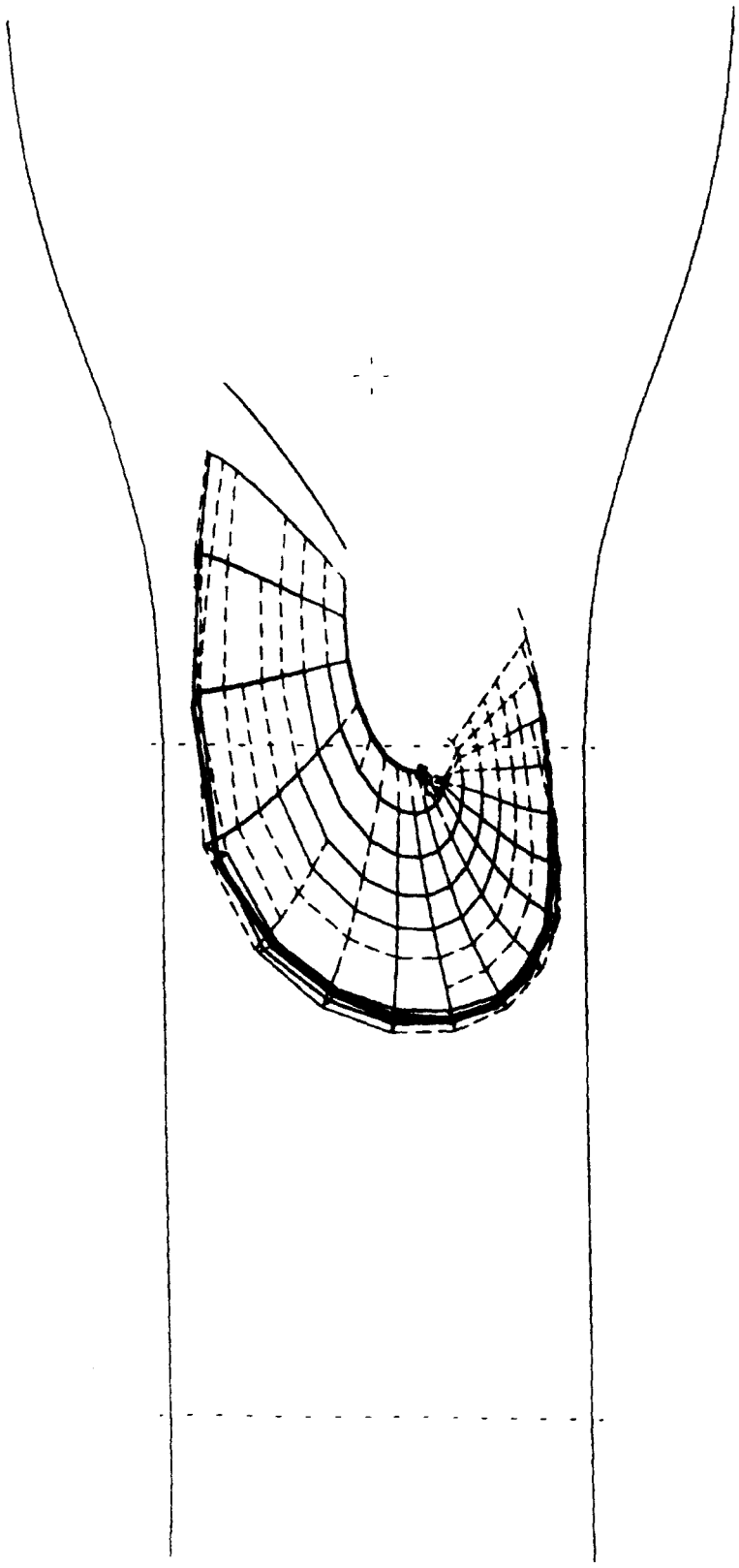

Figure R3.4- Single rotation convecting wake- tip velocity increasing from 50 to 90 m/s across working section with pitch down from 5 to 2.75 degrees.

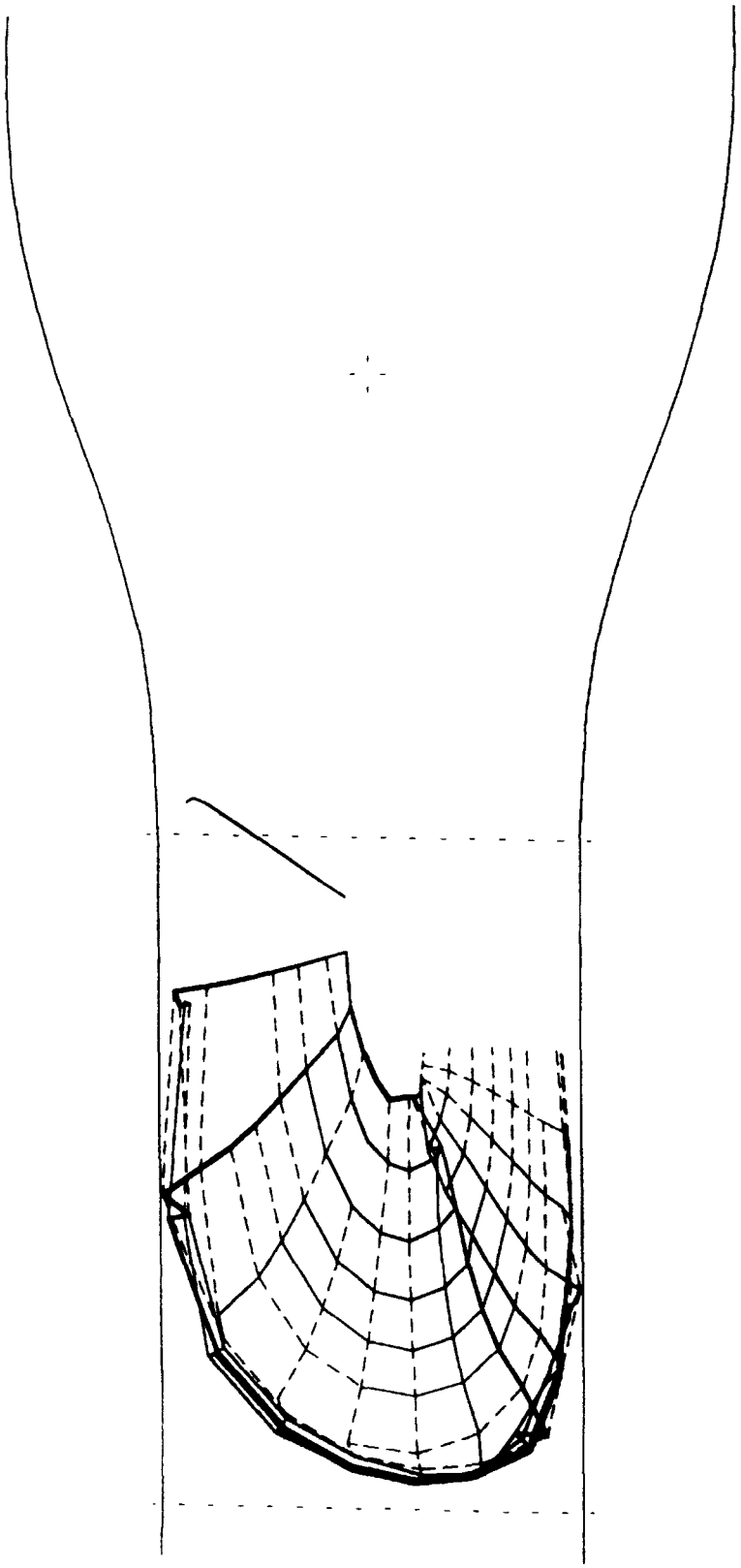

Figure R3.5- Single rotation convecting wake with a blade of radius 0.75m positioned at 3.2m from tunnel model origin- working section velocity 15m/s.

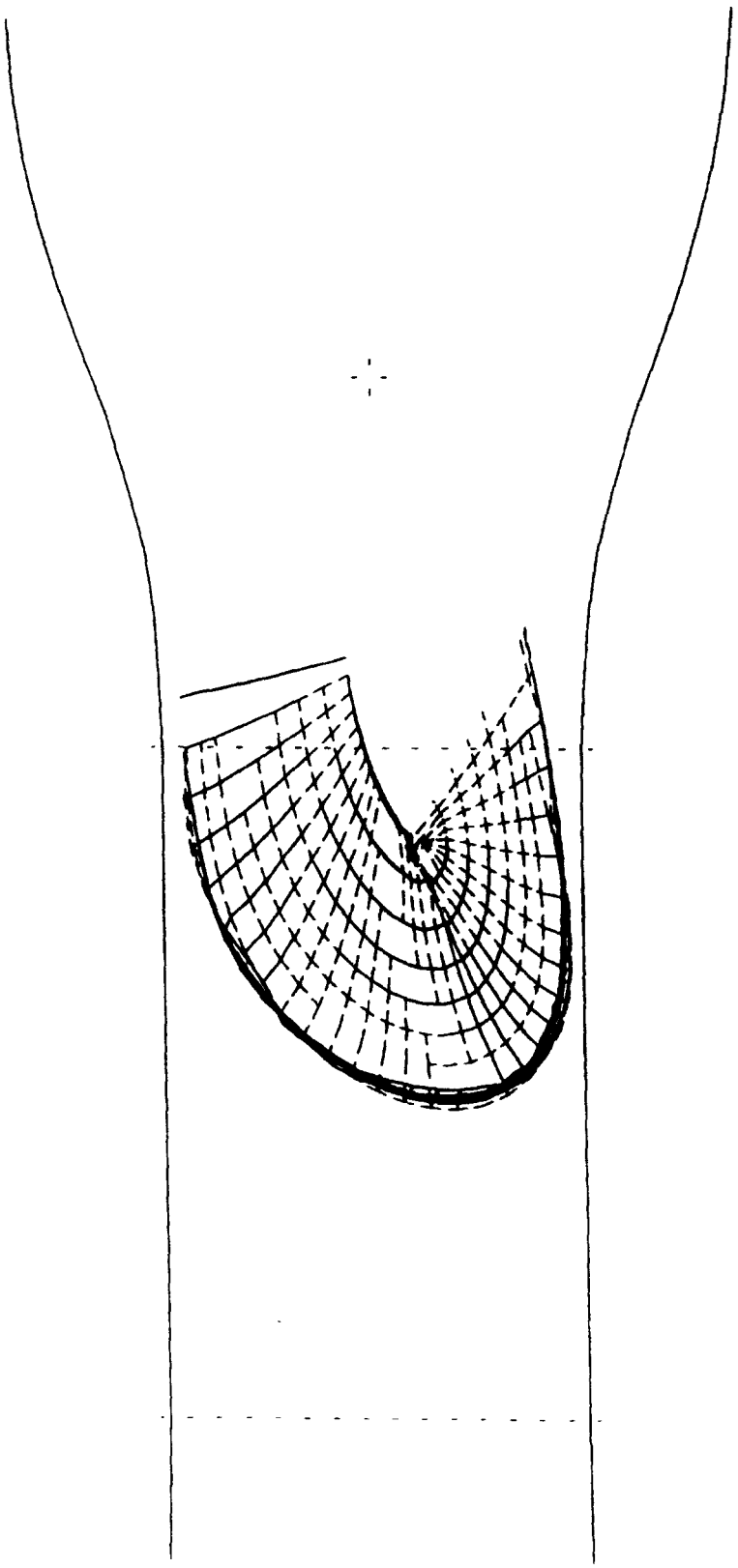

Figure R3.6- Single rotation convecting wake with tip velocity constant at 50 m/s across working section. Blade radius 0.65m positioned at 3.45m from origin.

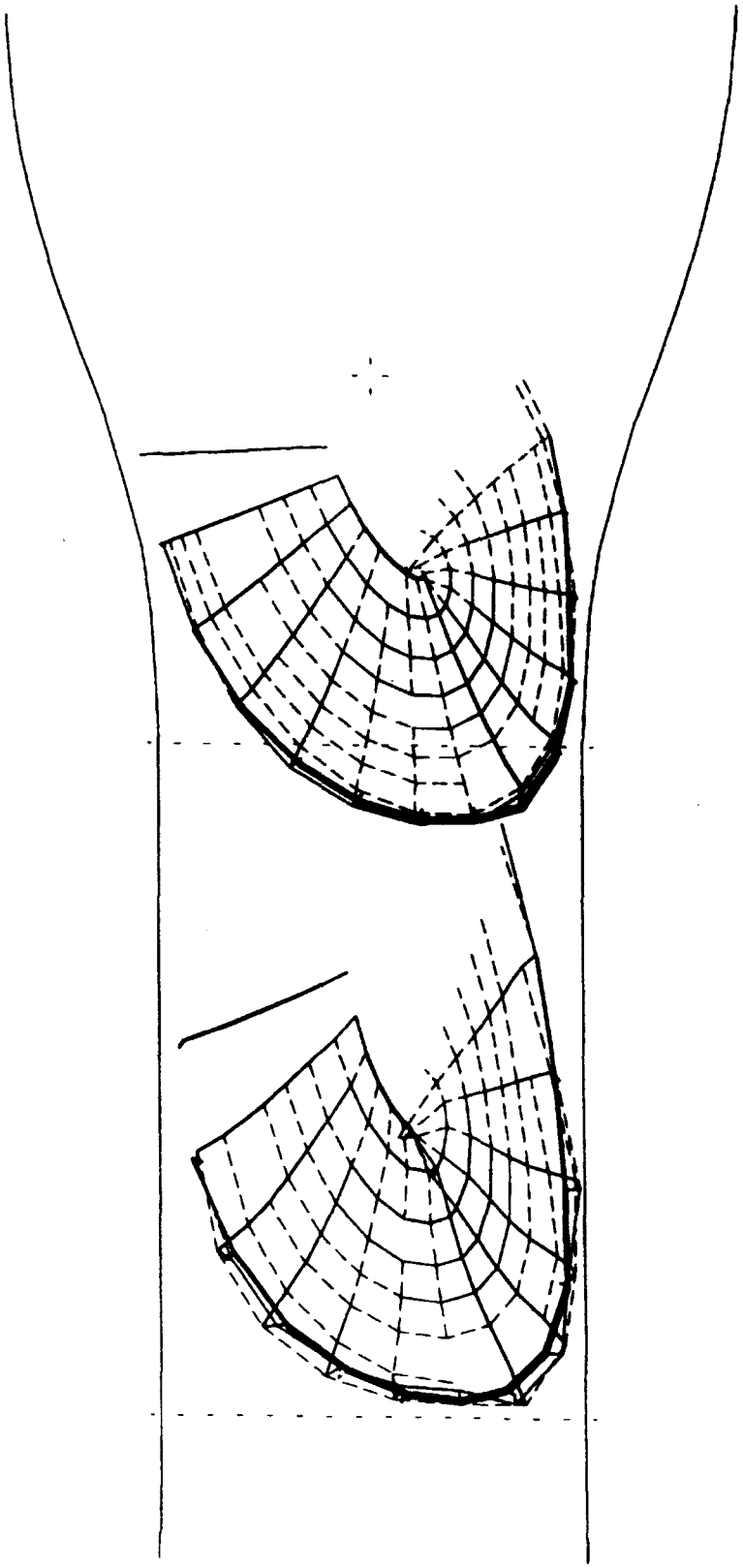

Figure R3.7- Continuous running wake development with a blade of radius 0.65m positioned at 3.45m from tunnel origin.

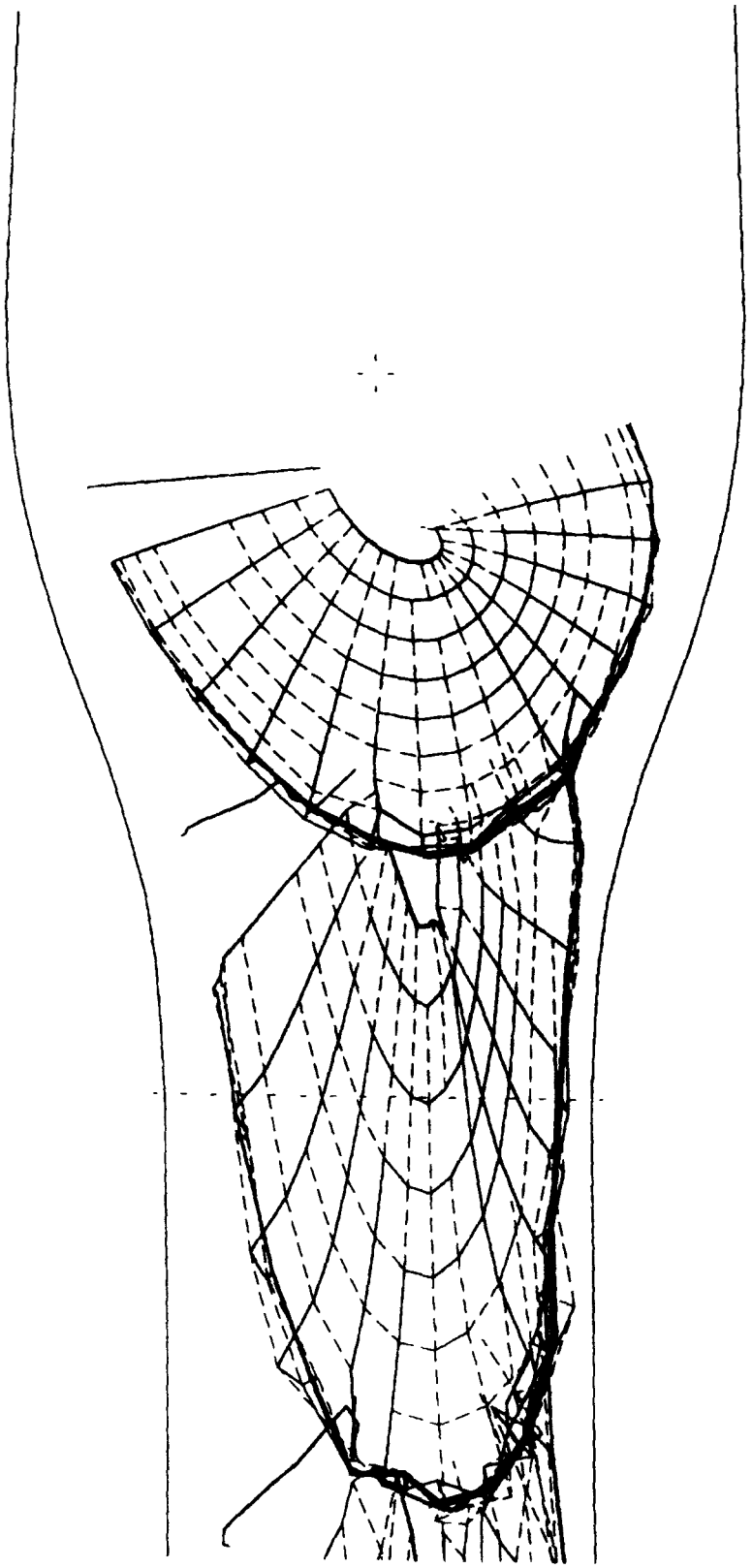

Figure R3.8- Continuous running wake development with a blade of radius 0.8m positioned at 2.5m from tunnel origin- 20m/s working section velocity.

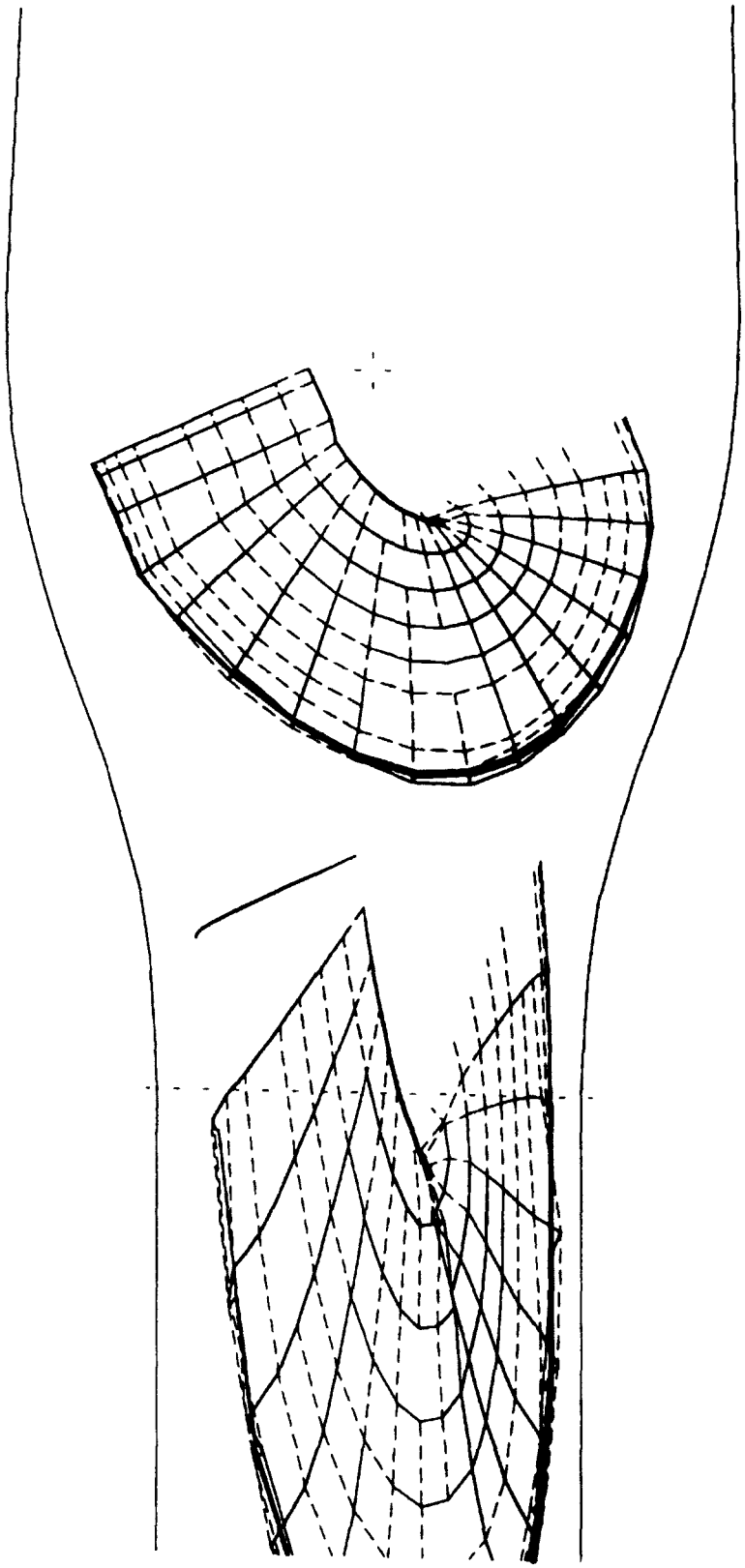

Figure R3.9- Continuous running wake development with a blade of radius 0.8m positioned at 2.5m from tunnel origin- 30m/s working section velocity.

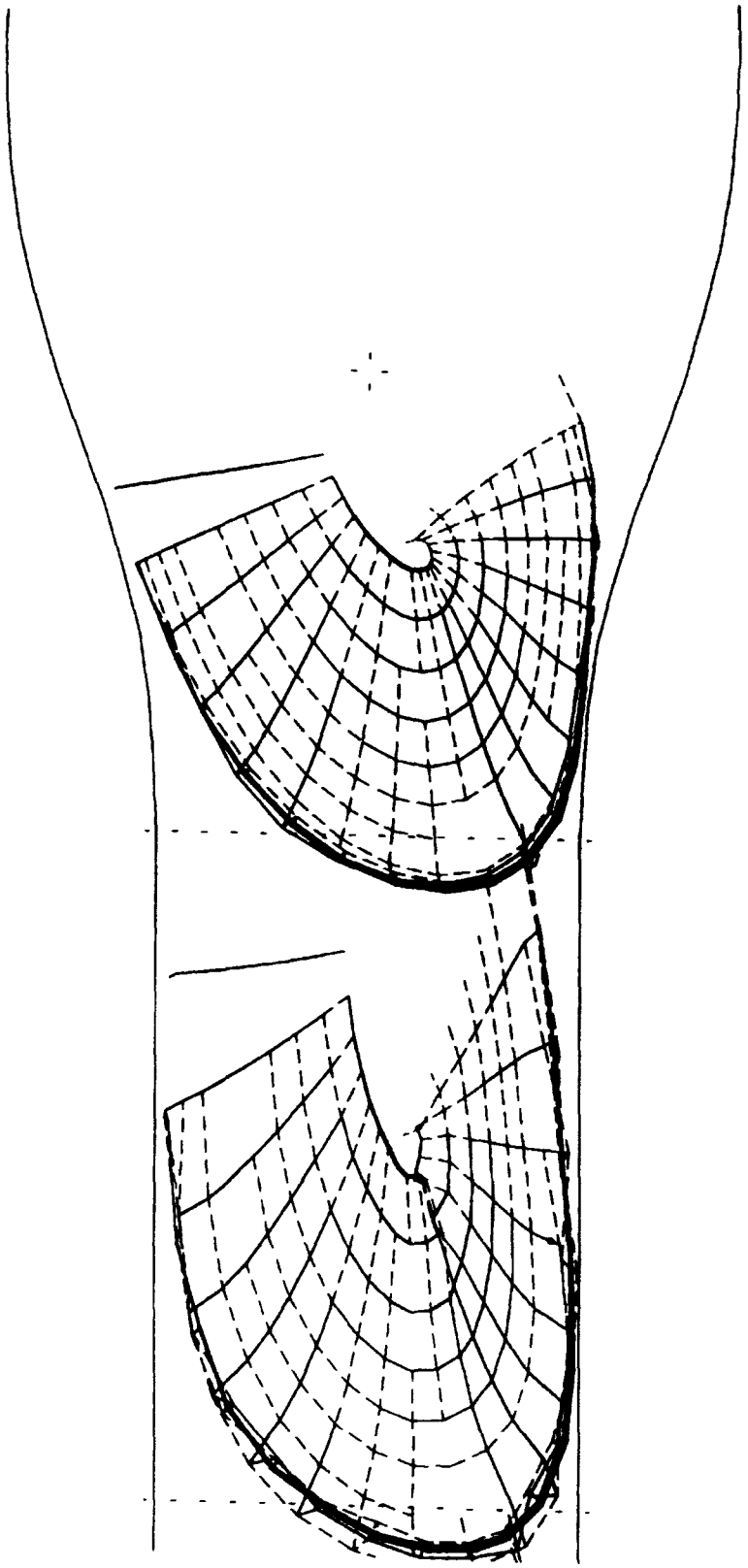

Figure R3.10- Continuous running wake development with a blade of radius 0.75m positioned at 3.2m from tunnel origin.

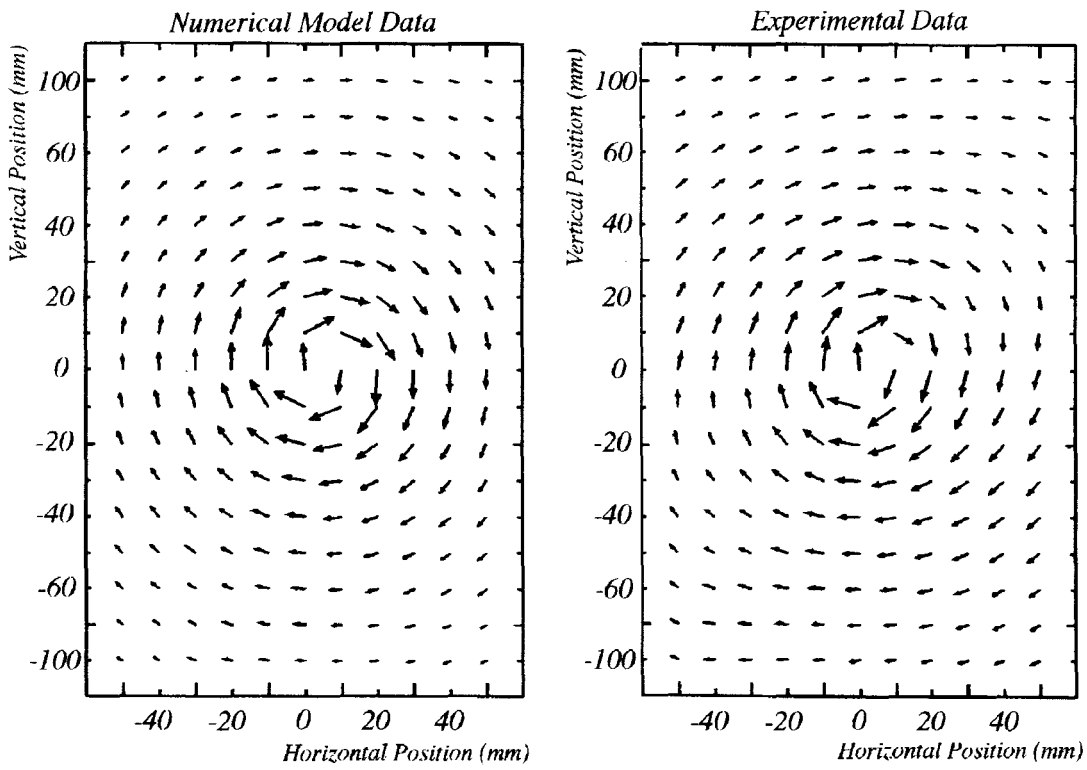

Figure R5.1- Comparison of numerical model and experimental data vector plots for single vortex Case 17.

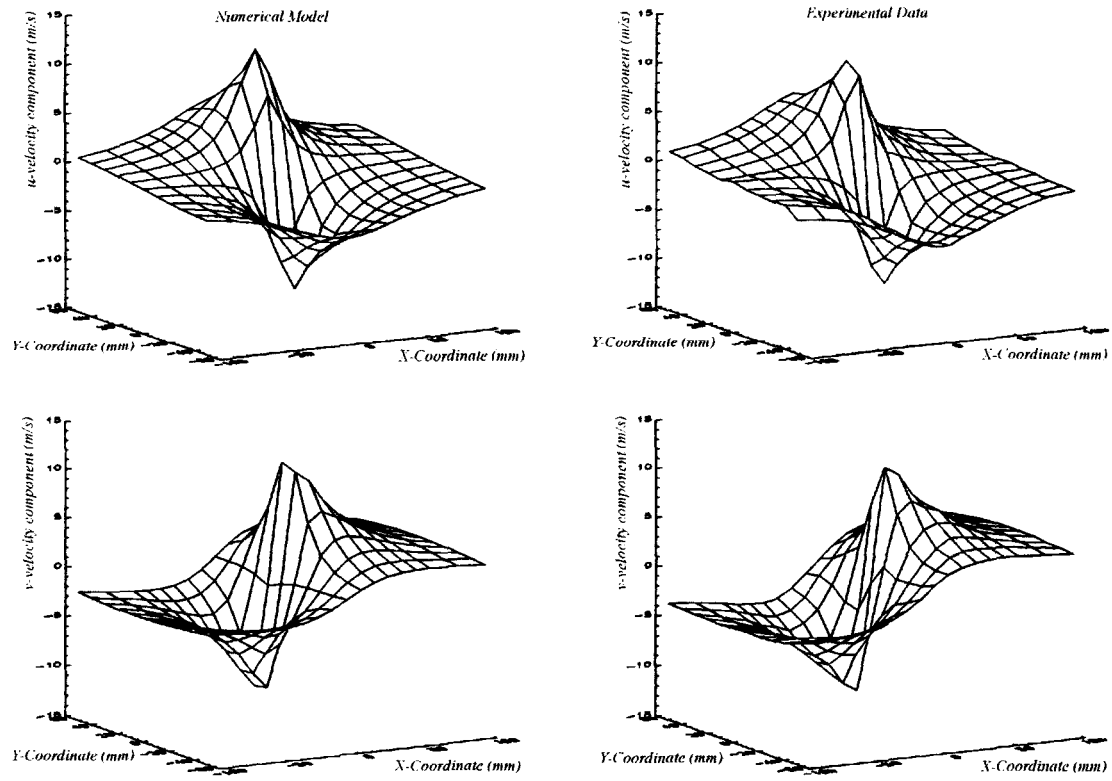

Figure R5.2- Surface plots of *u* (top) and *v* (bottom) velocity components for numerical model (left) and experimental data (right) for Case 17.

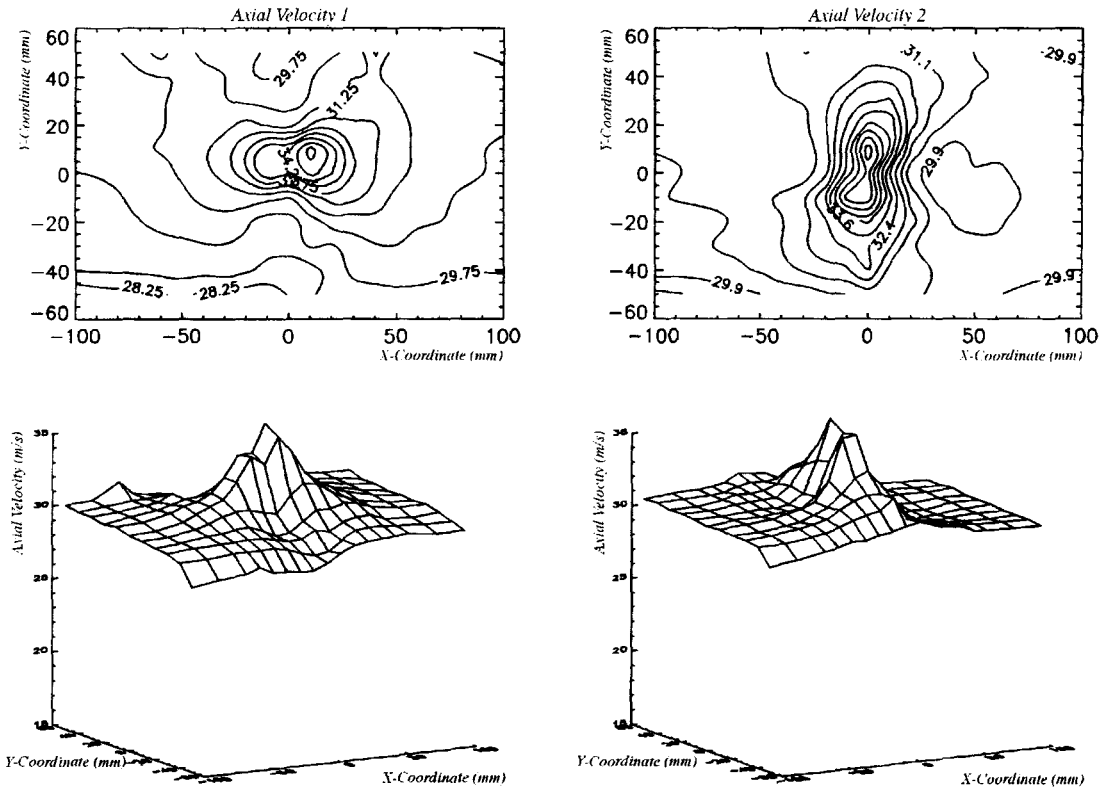

Figure R5.3- Contour and surface plots of the two measured axial velocity distributions for Case 17.

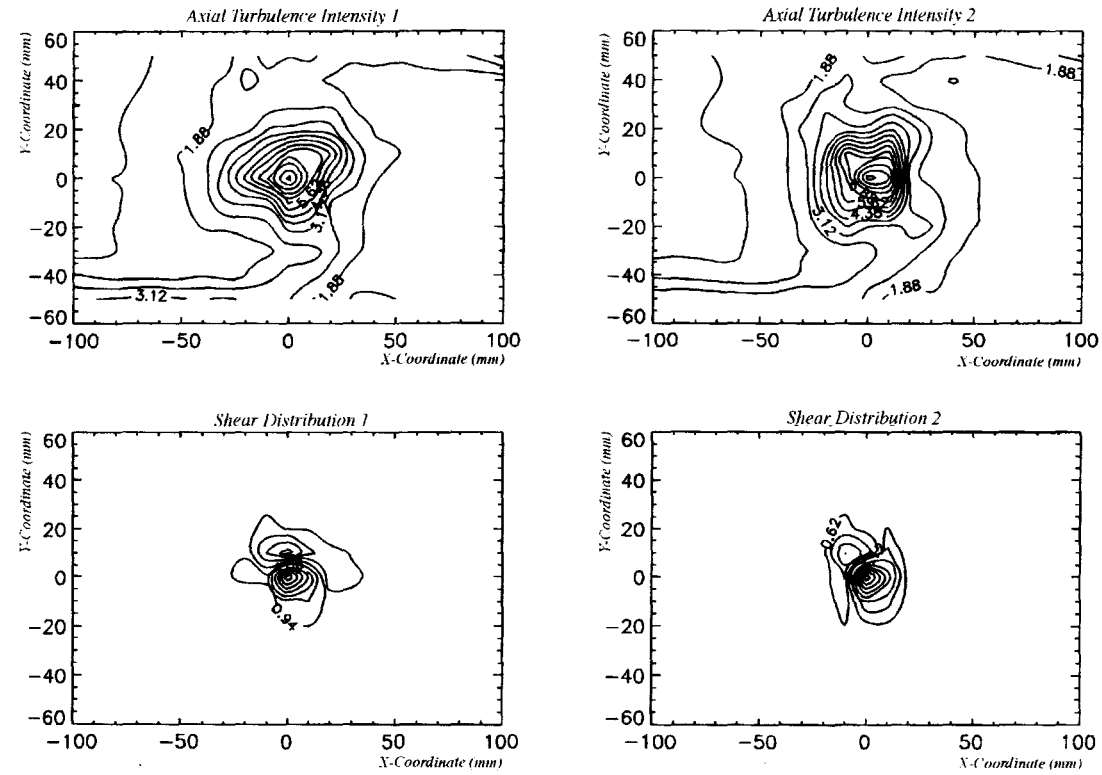

Figure R5.4- Turbulence intensity and shear distribution for Case 17.

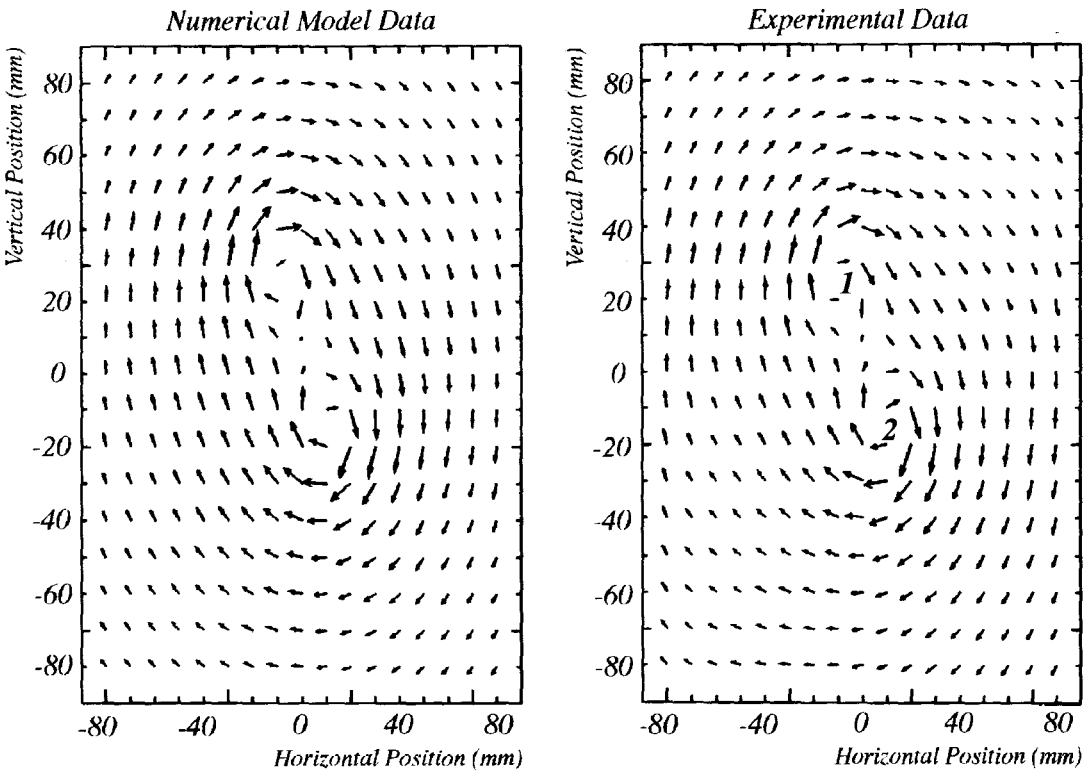

Figure R5.5- Comparison of numerical model and experimental data vector plots for twin vortex Case 42.

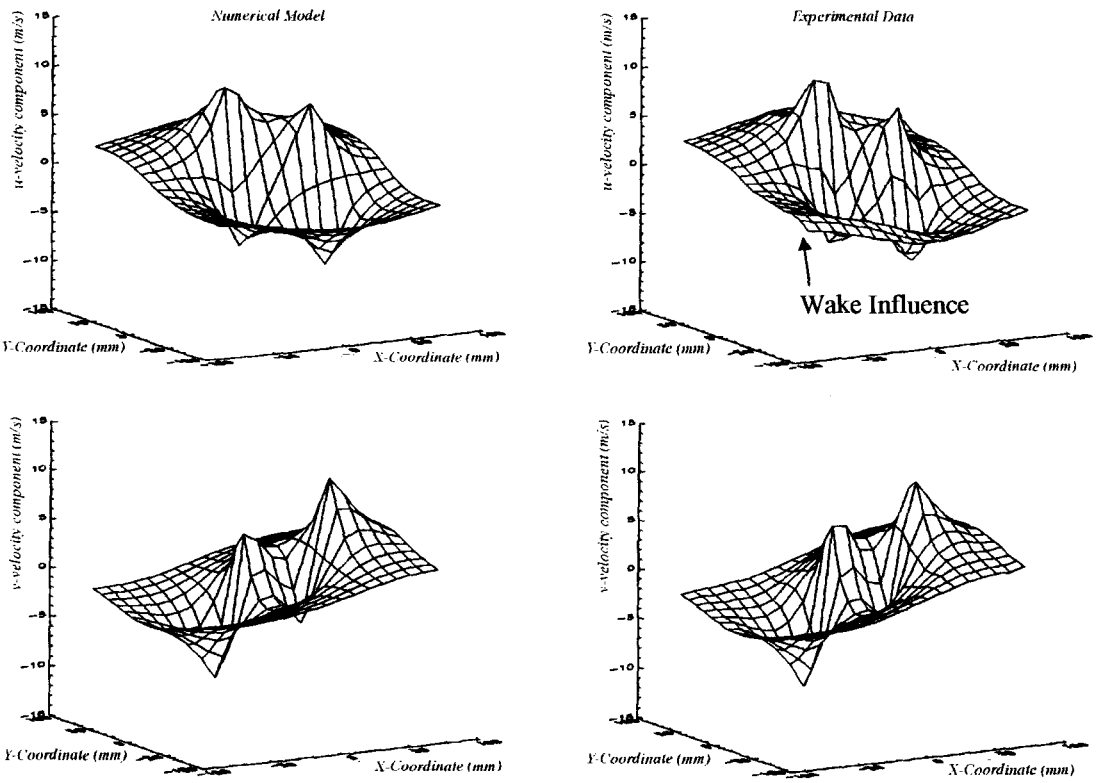

Figure R5.6- Surface plots of u (top) and v (bottom) velocity components for numerical model (left) and experimental data (right) for Case 42.

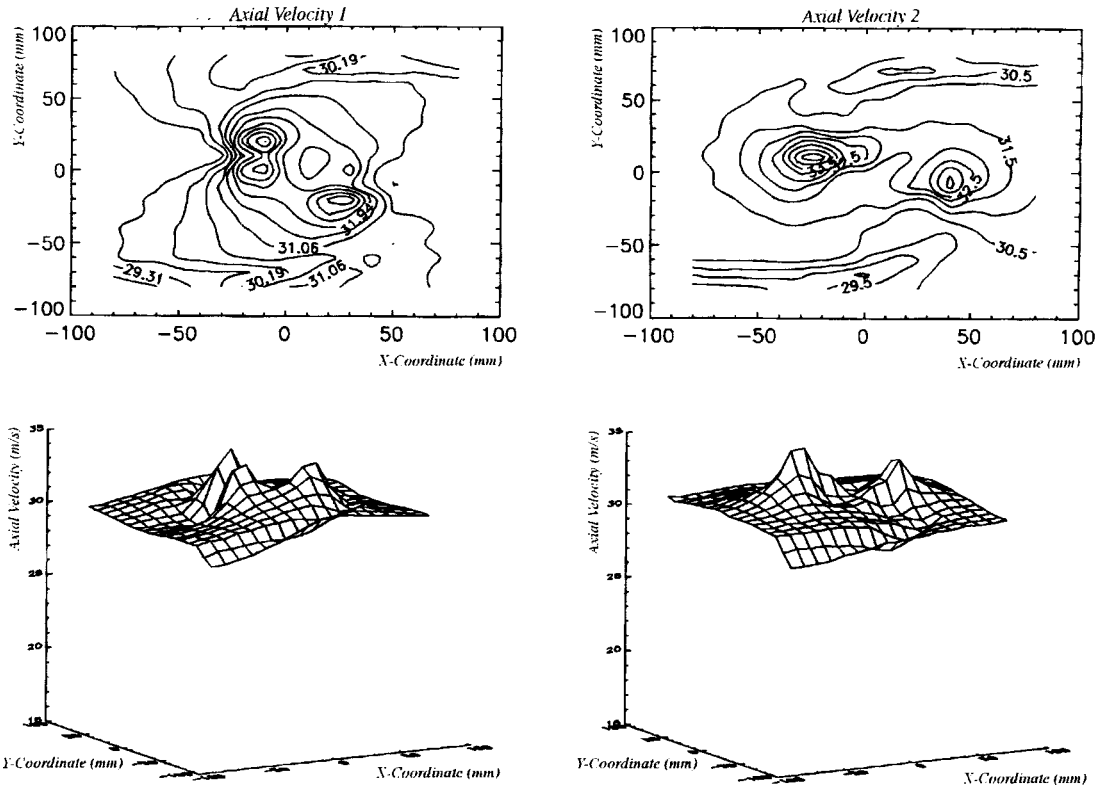

Figure R5.7- Contour and surface plots of the axial velocity distribution for Case 42.

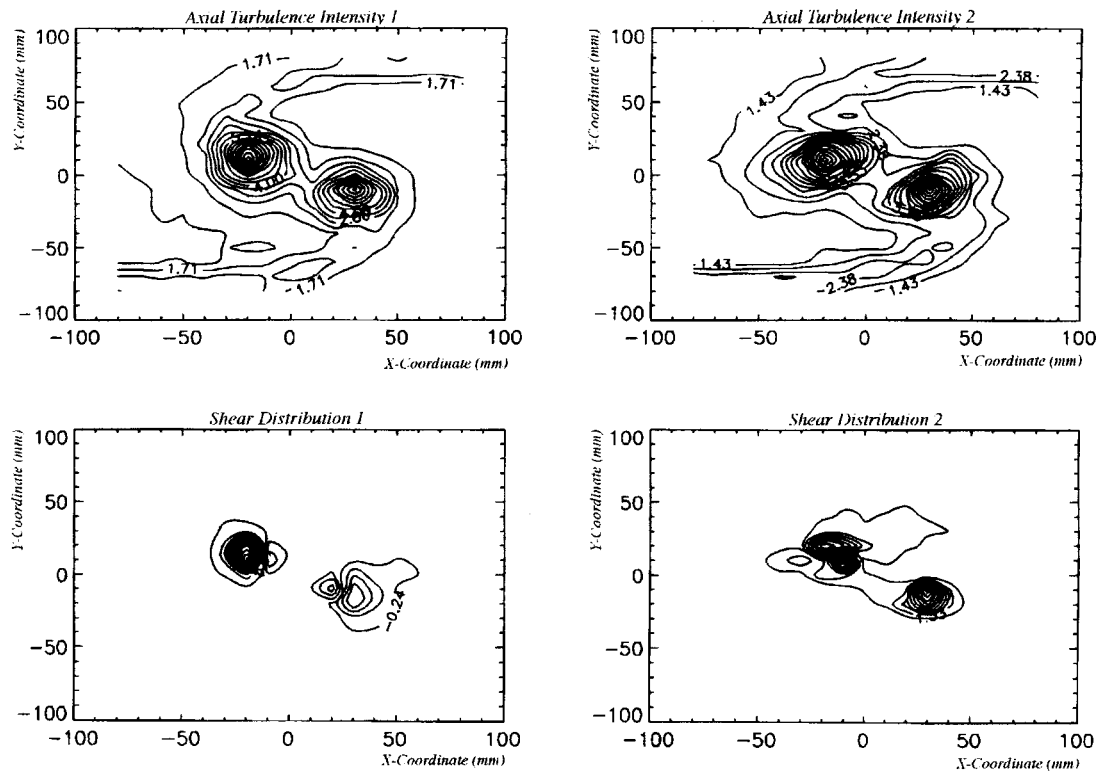

Figure R5.8- Turbulence intensity and shear distribution for Case 42.

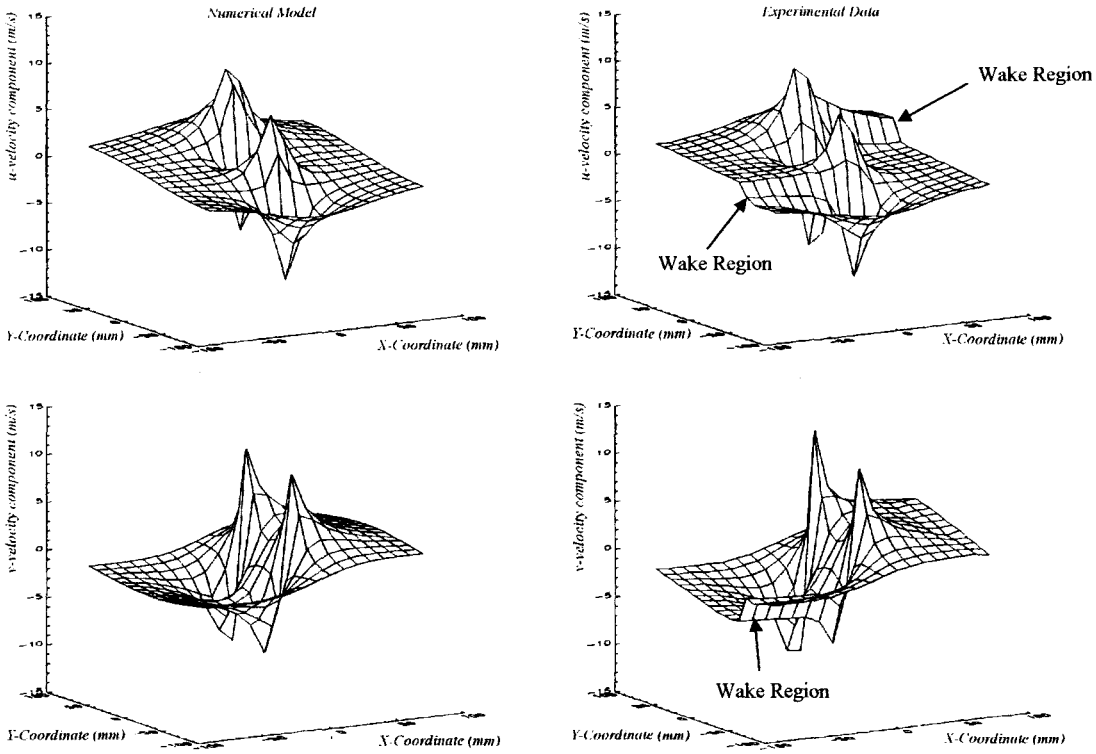

Figure R5.9- Surface plots of cross-flow velocity components for Case 26, 0.1c downstream of the trailing edge.

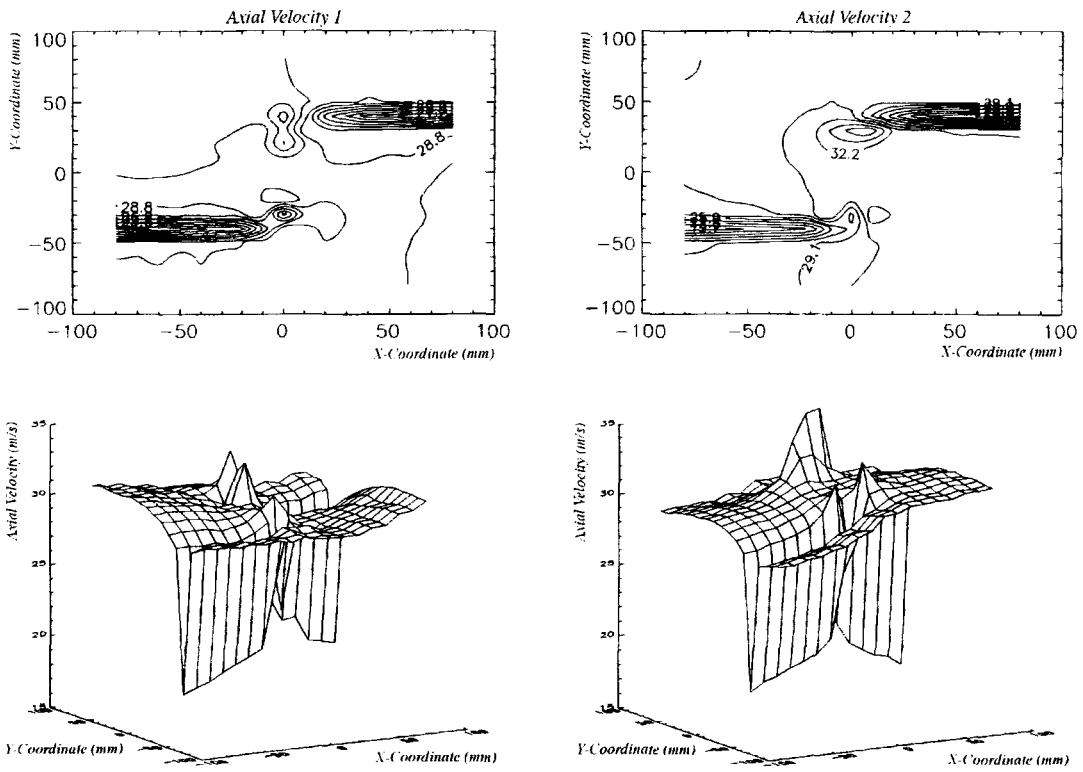

Figure R5.10- Contour and surface plots of the axial velocity distribution for case 26.

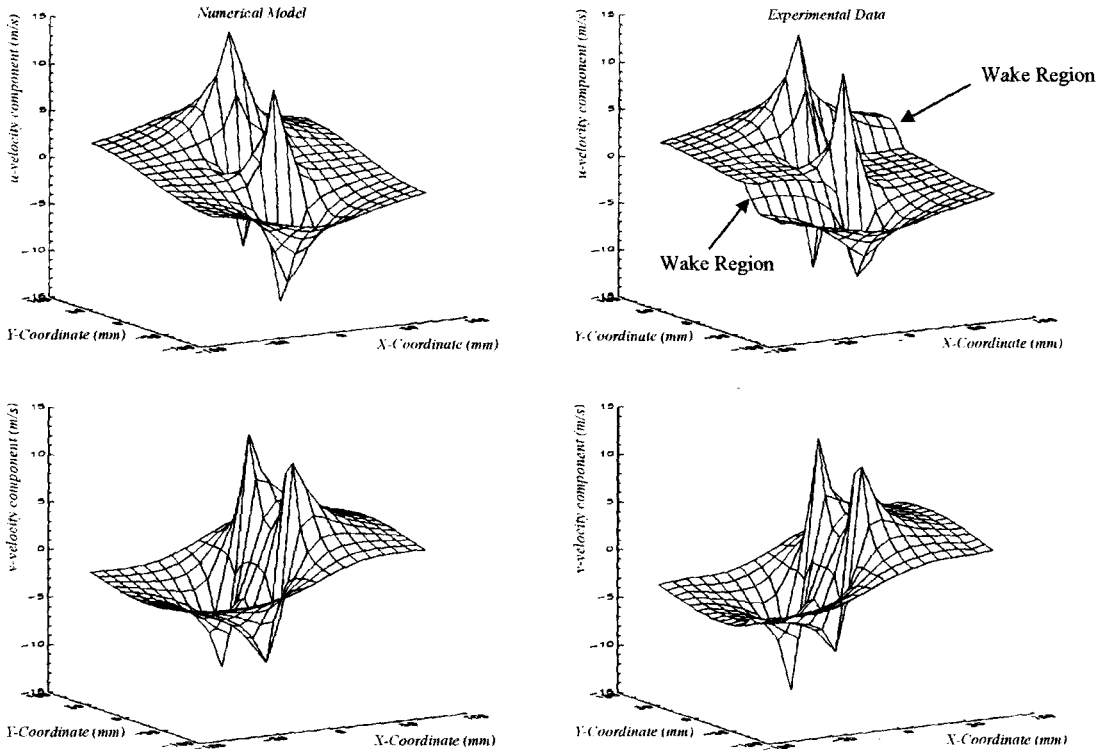

Figure R5.11- Surface plots of cross-flow velocity components for Case 27, 0.5c downstream of the trailing edge.

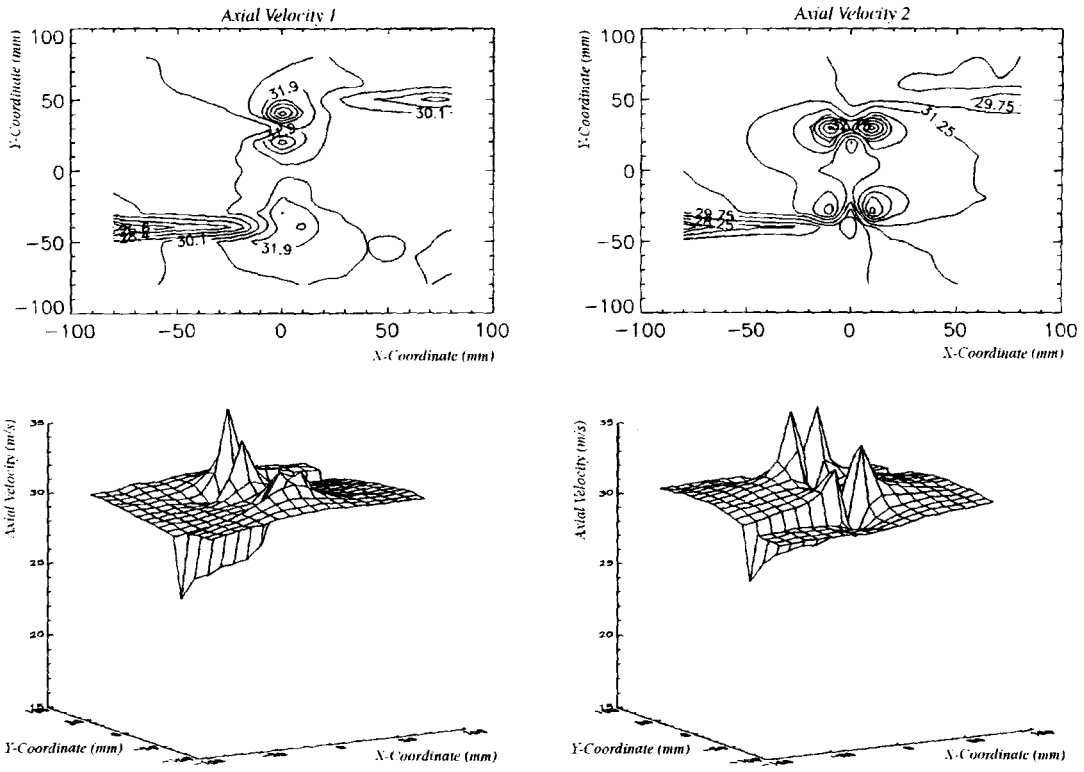

Figure R5.12- Contour and surface plots of the axial velocity distribution for case 27.

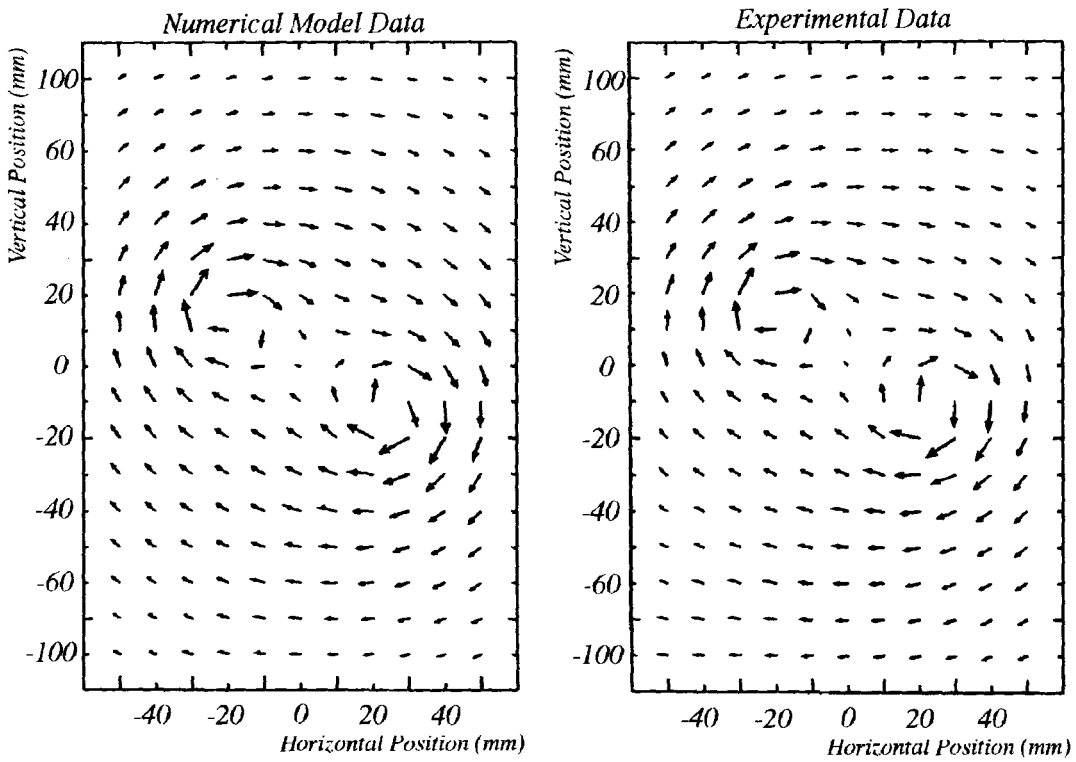

Figure R5.13- Comparison of numerical model and experimental data vector plots for single vortex Case 1, measurement position 2.5c downstream of trailing edge.

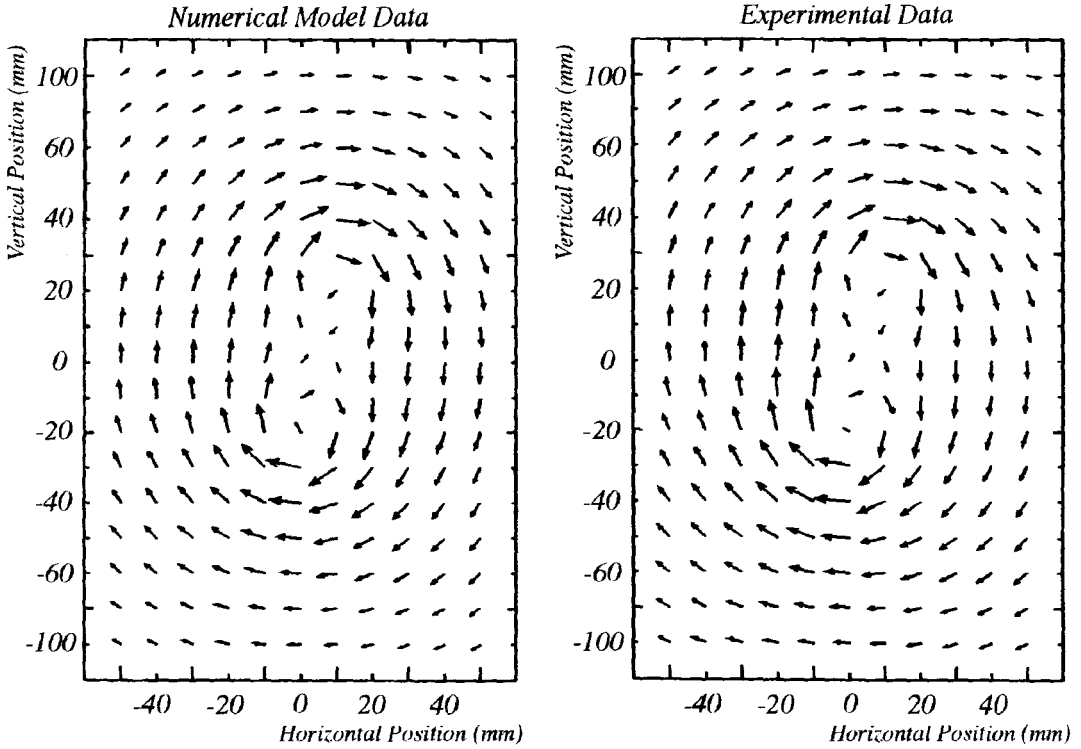

Figure R5.14- Comparison of numerical model and experimental data vector plots for single vortex Case 9, measurement position 6c downstream of trailing edge, illustrating rotation of twin co-rotating vortex system from Fig. 5.13.

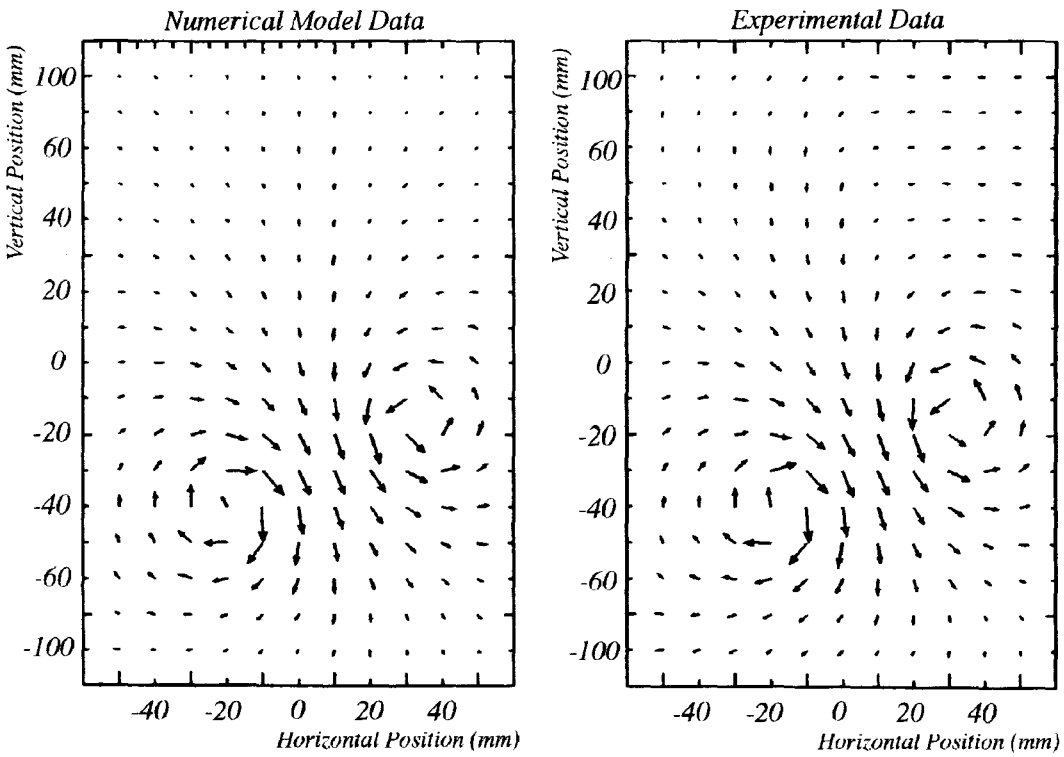

Figure R5.15- Comparison of numerical model and experimental data vector plots for counter rotating twin vortex Case 8, measurement position 2.5c downstream of trailing edge.

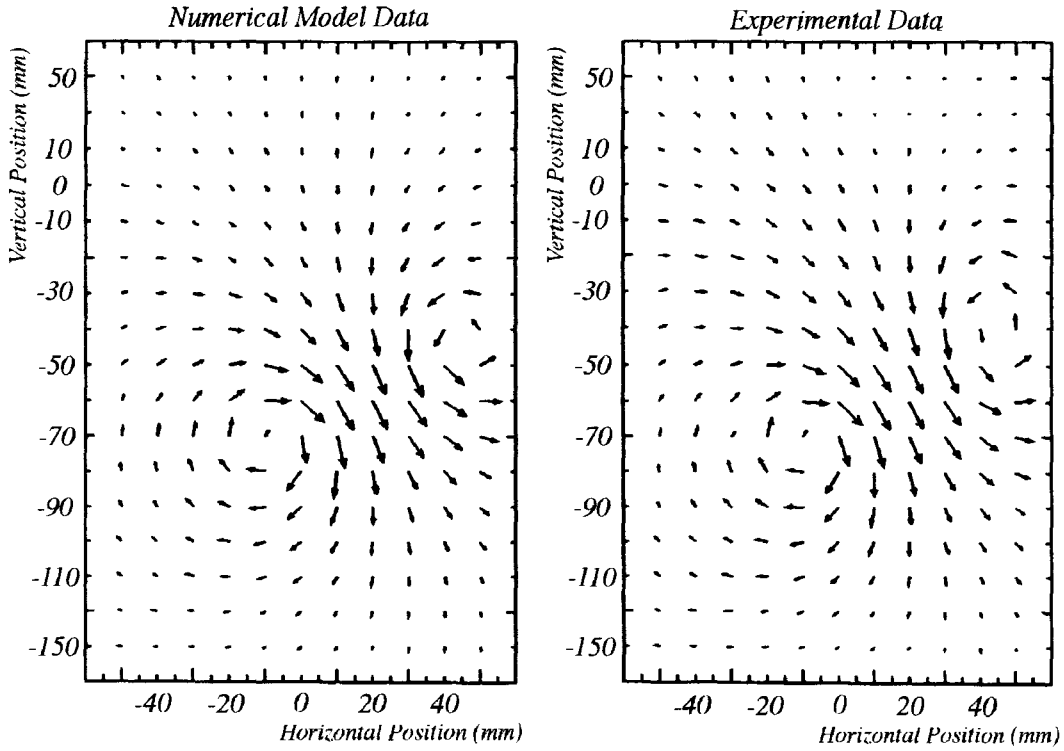

Figure R5.16- Comparison of numerical model and experimental data vector plots for twin vortex Case 16, measurement position 6c downstream of trailing edge, illustrating downward convection of twin counter-rotating vortex system from Fig.5.15.

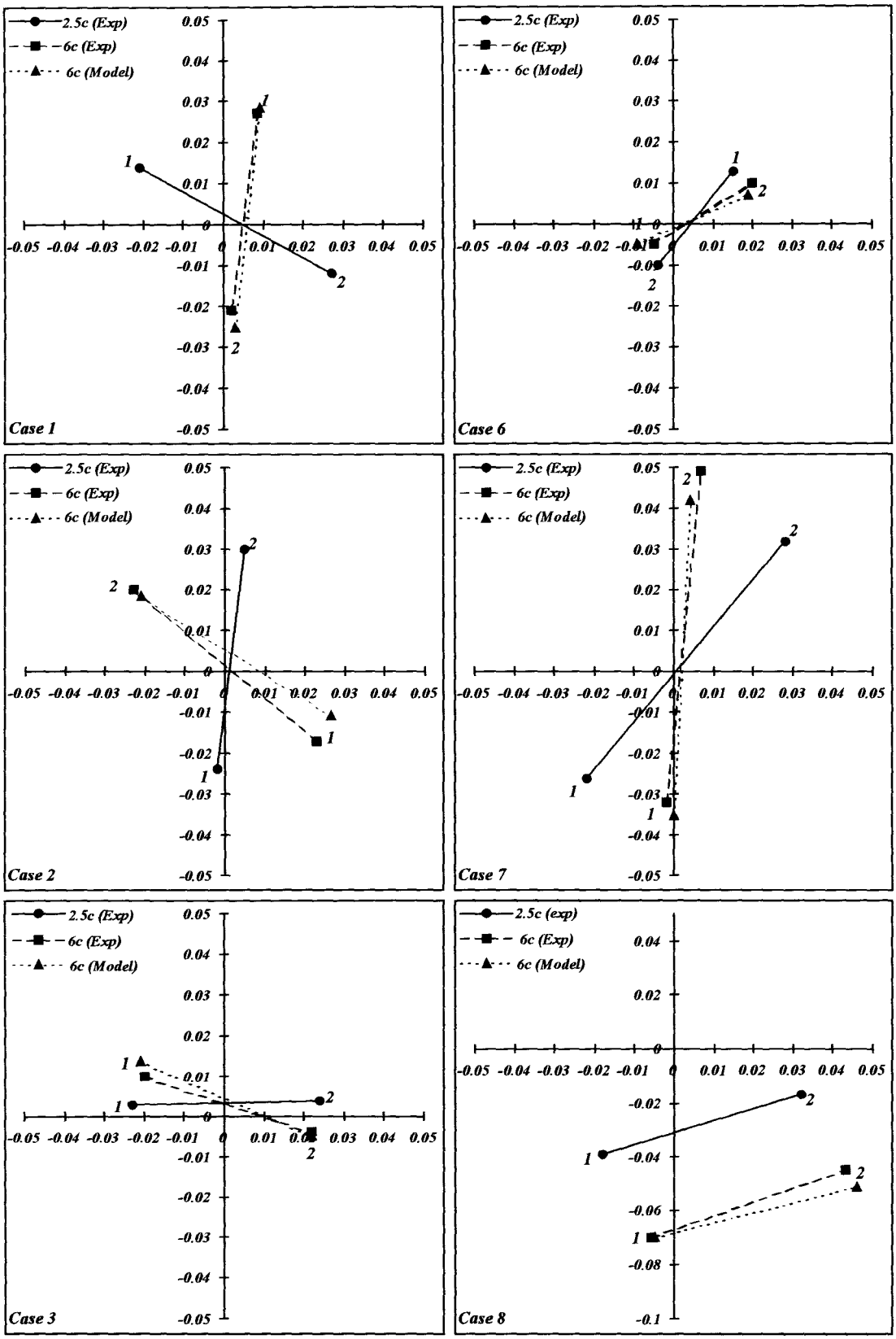

Figure R5.17- Comparison of vortex locations at 2.5 chord lengths downstream of trailing edge with comparison to experimental locations at 6c and predicted position at 6c from 3D numerical model (for twin vortex cases 1,2,3,6,7,8). The 2.5c experimental data is used for input parameters for the 3D numerical model.

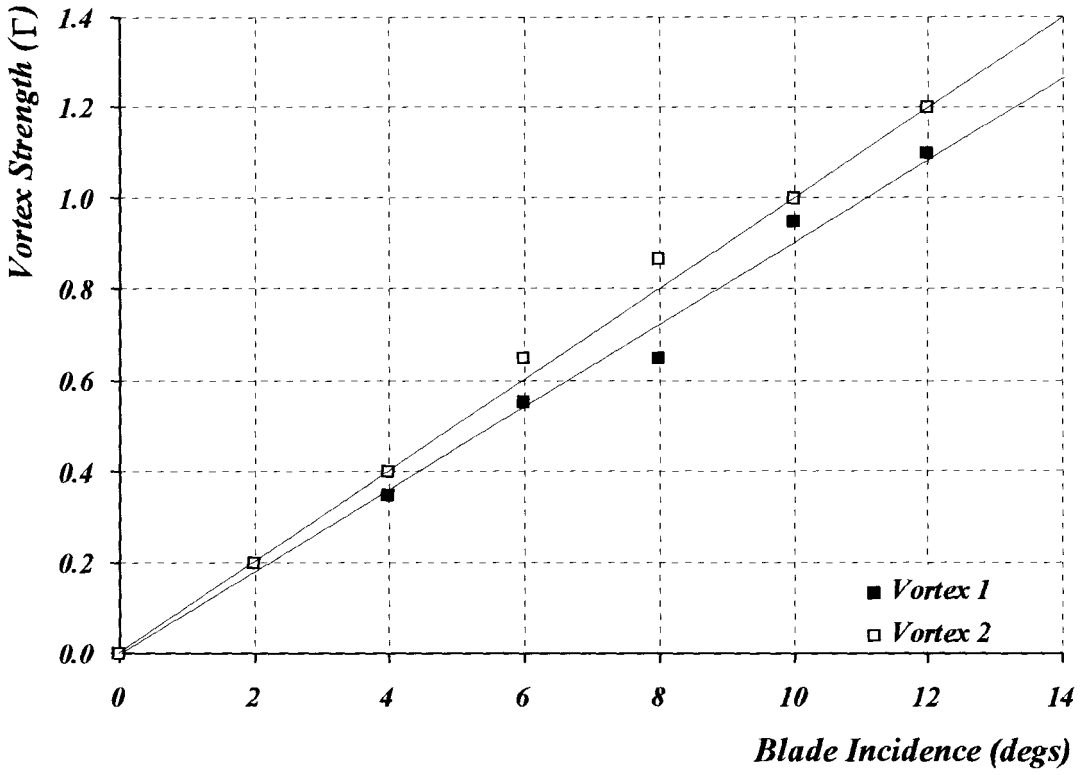

Figure R5.18- Variation in vortex strength with change in incidence at 4.3c downstream of trailing edge.

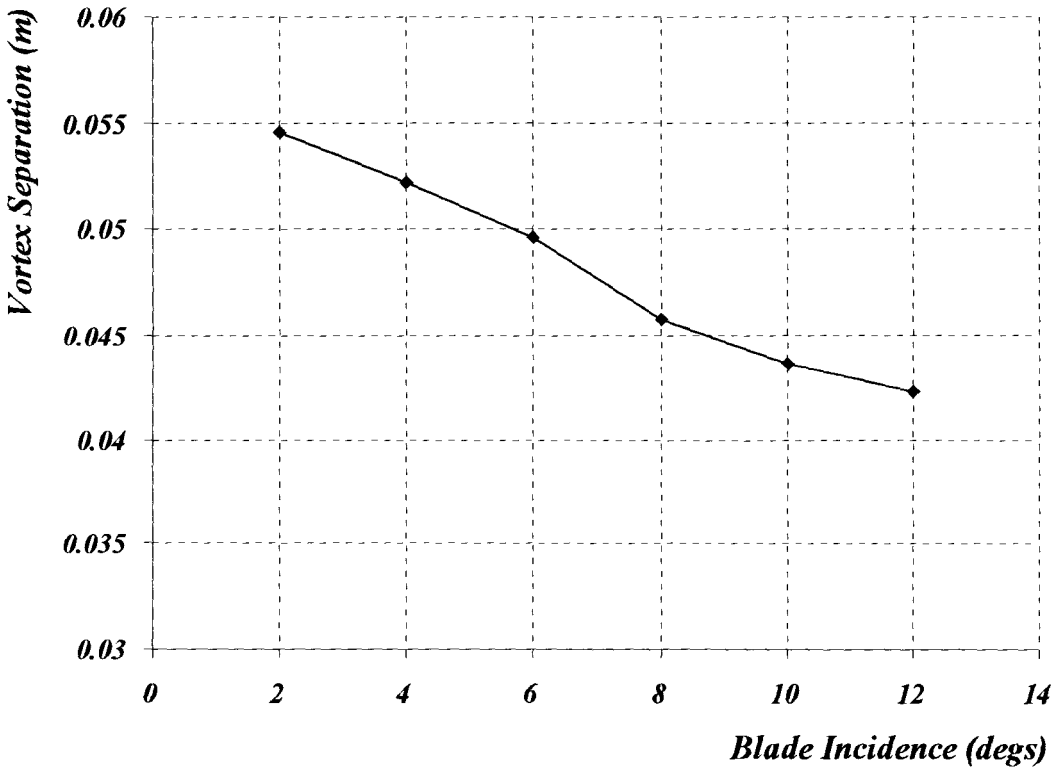

Figure R5.19- Variation in vortex core separation with a change in incidence at 4.3c downstream.

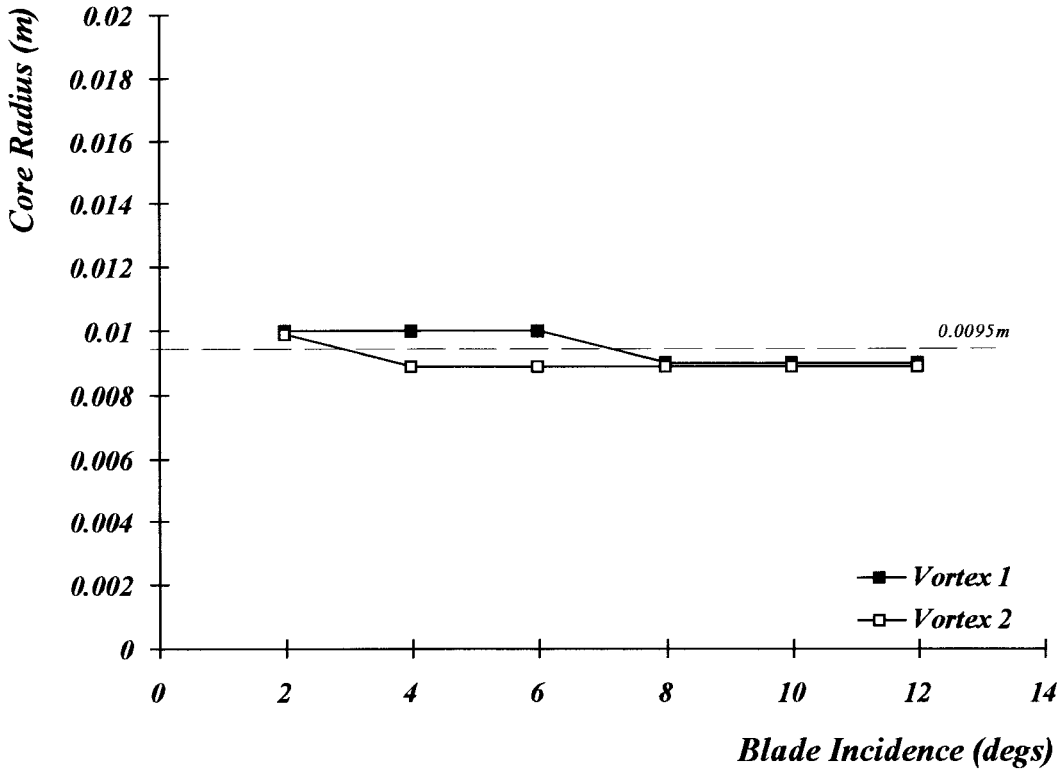

Figure R5.20- Variation in core size with a change in incidence at 4.3 chord lengths downstream.

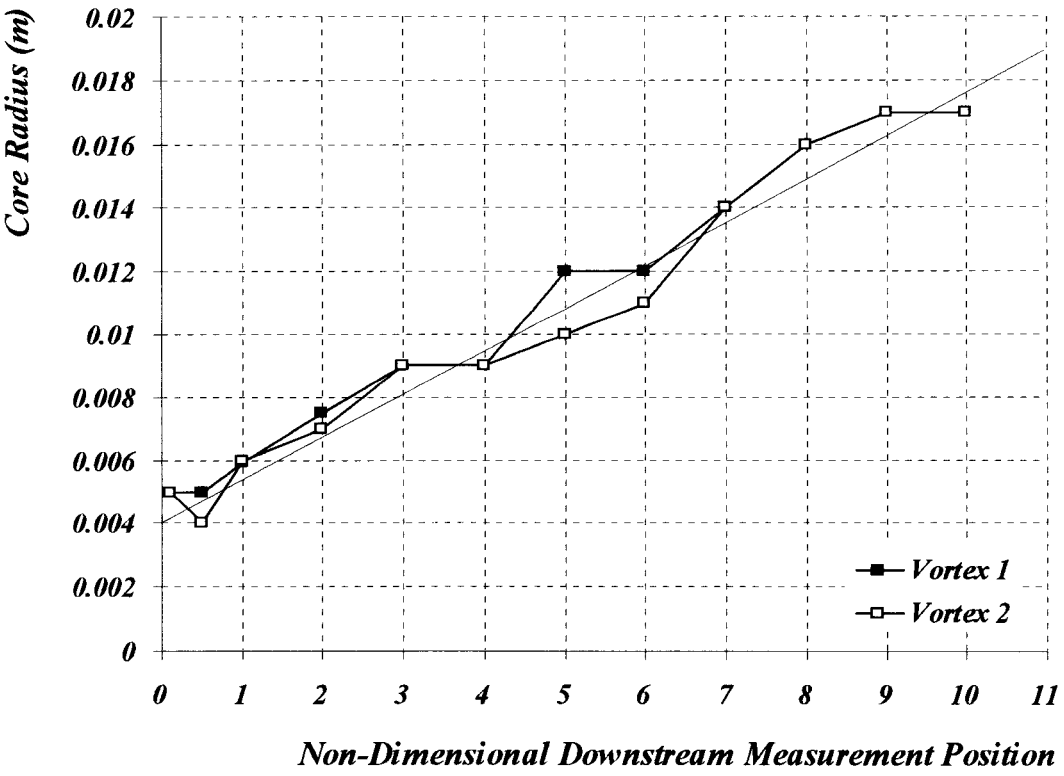

Figure R5.21- Variation in core radius with downstream measurement position.

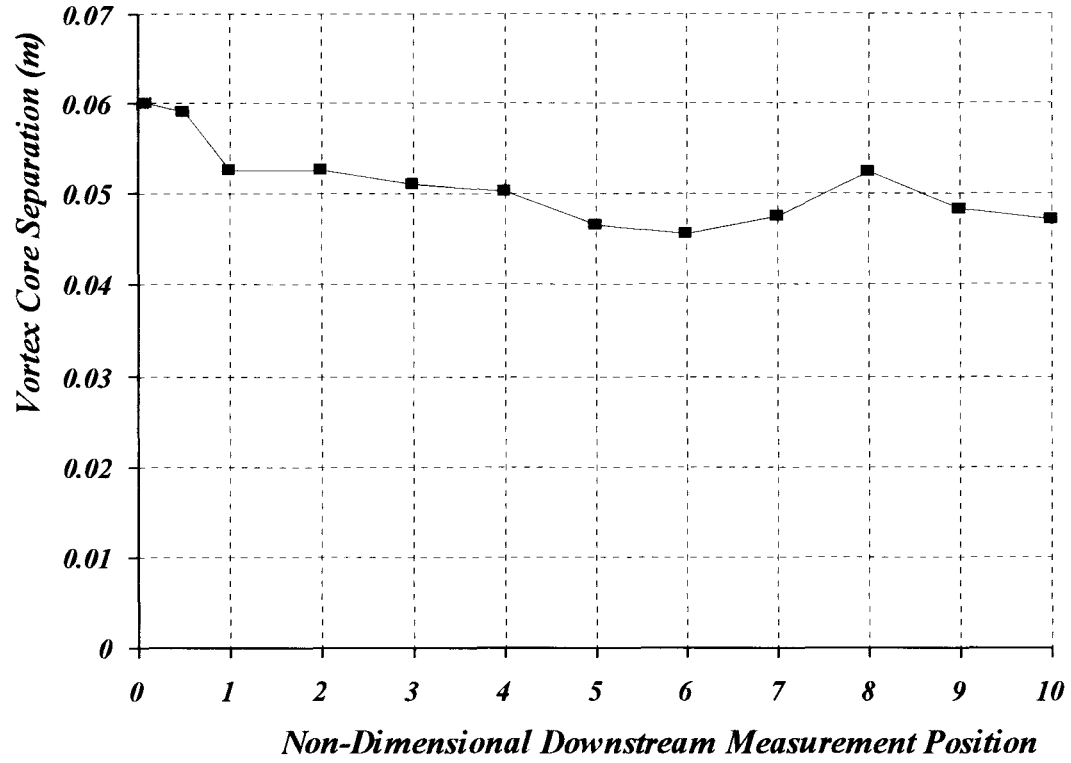

Figure R5.22- Variation in vortex separation with downstream measurement position.

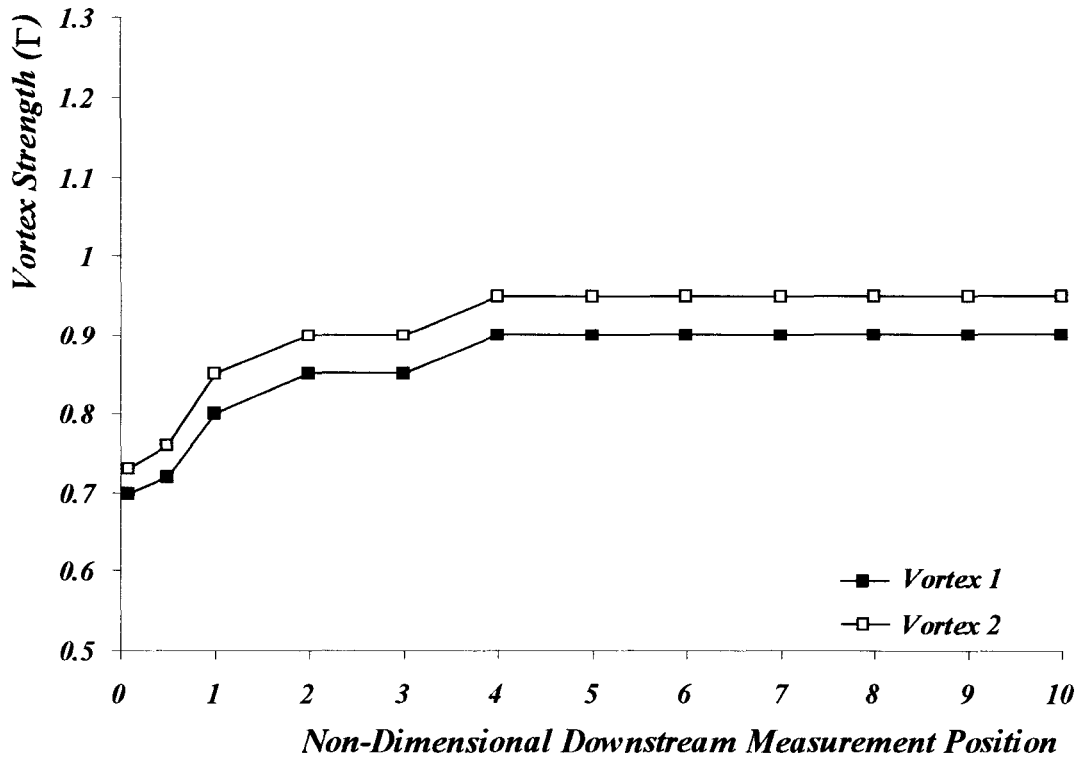

Figure R5.23- Variation of vortex strength with downstream measurement position.

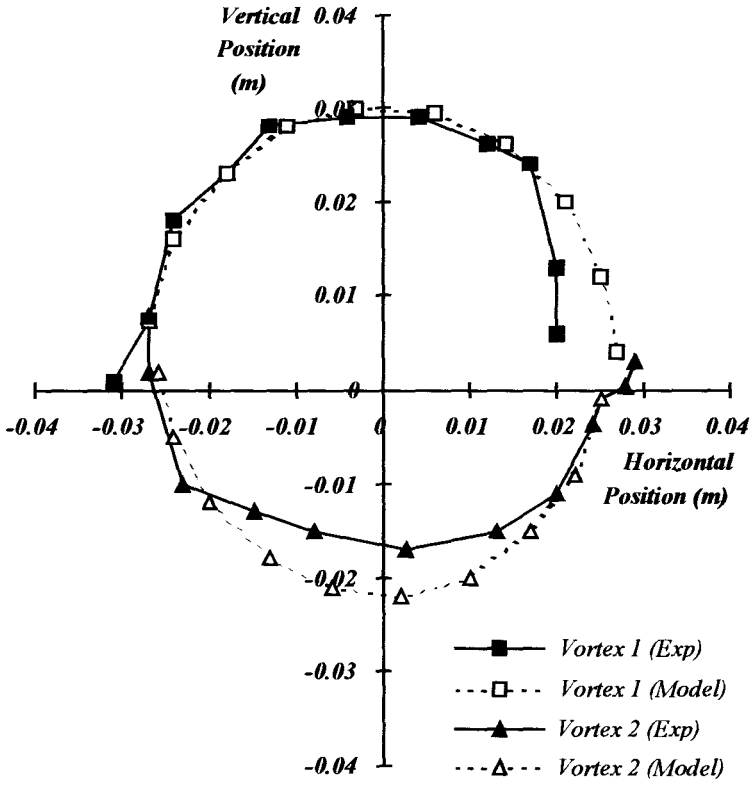

Figure R5.24- Location of twin vortices with respect to test section centre for variation in downstream position and comparison with numerical model.

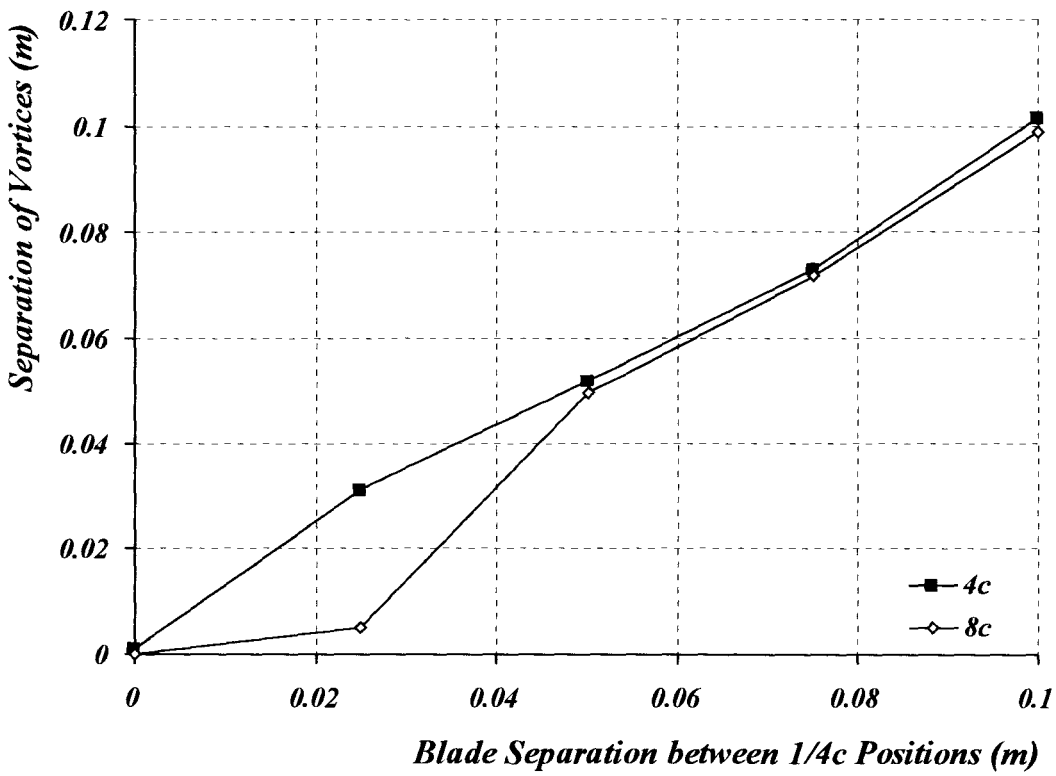

Figure R5.25- Variation of vortex separation with respect to blade separation for downstream measurements positions of 4c and 8c.

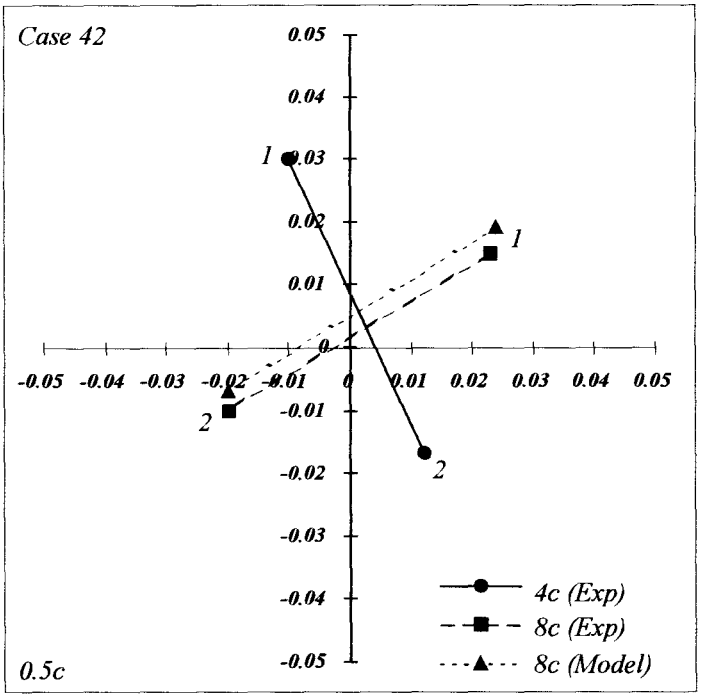

Figure R5.26- Comparison of experimental data at 8c with quasi 3D numerical model prediction at 8c (input parameters specified at 4c as determined from experimental data) for 0.5c blade ¼c separation.

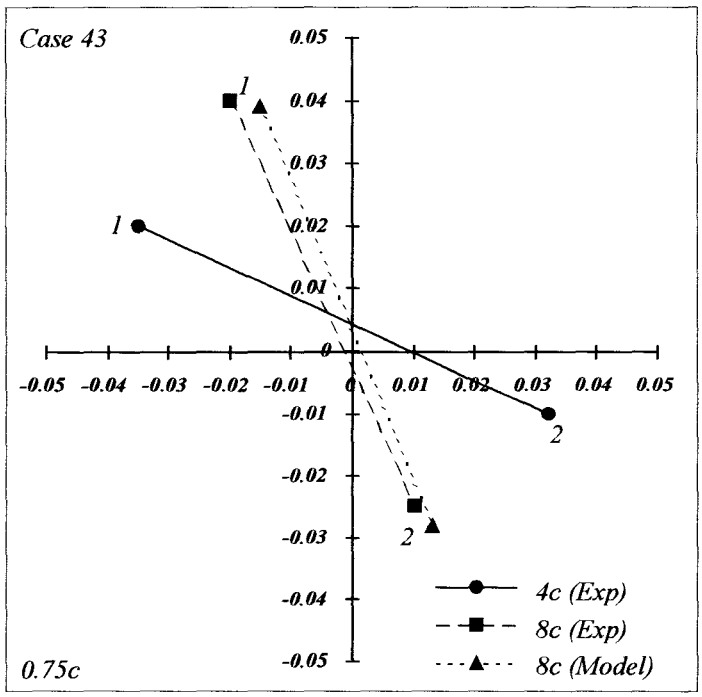

Figure R5.27- Comparison of experimental data at 8c with quasi 3D numerical model prediction at 8c (input parameters specified at 4c as determined from experimental data) for 0.75c blade ¼c separation.

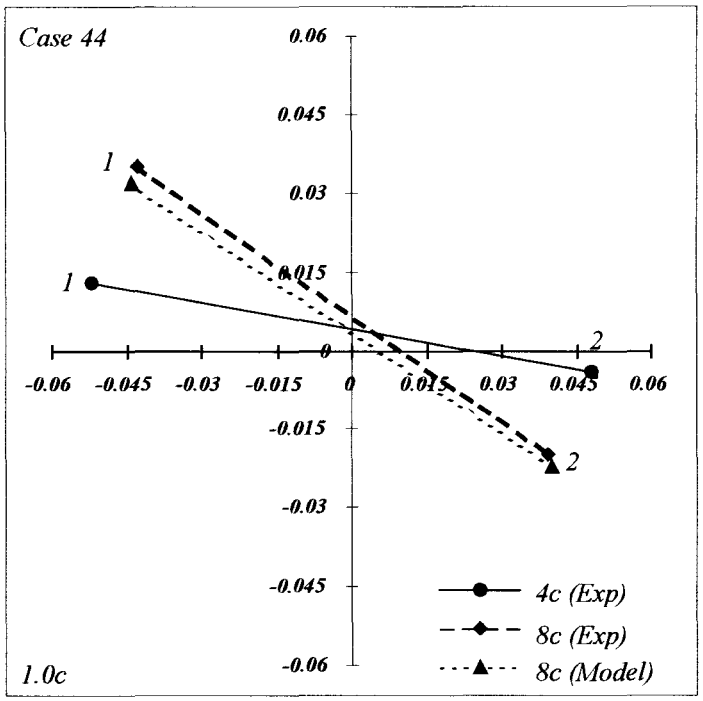

Figure R5.28- Comparison of experimental data at 8c with quasi 3D numerical model prediction at 8c (input parameters specified at 4c as determined from experimental data) for 1c blade ¼c separation.

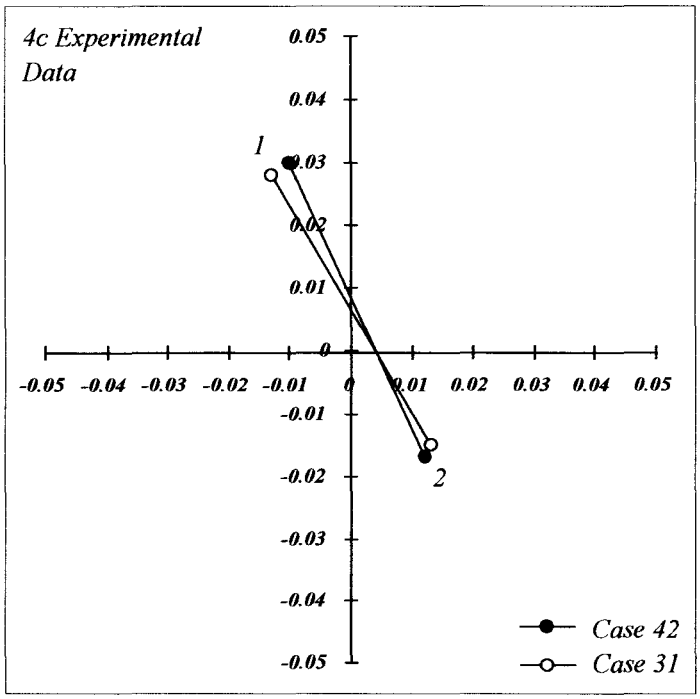

Figure R5.29- Comparison of two experimental cases (31 & 42) conducted with the same blade geometry and measurement position (4c).

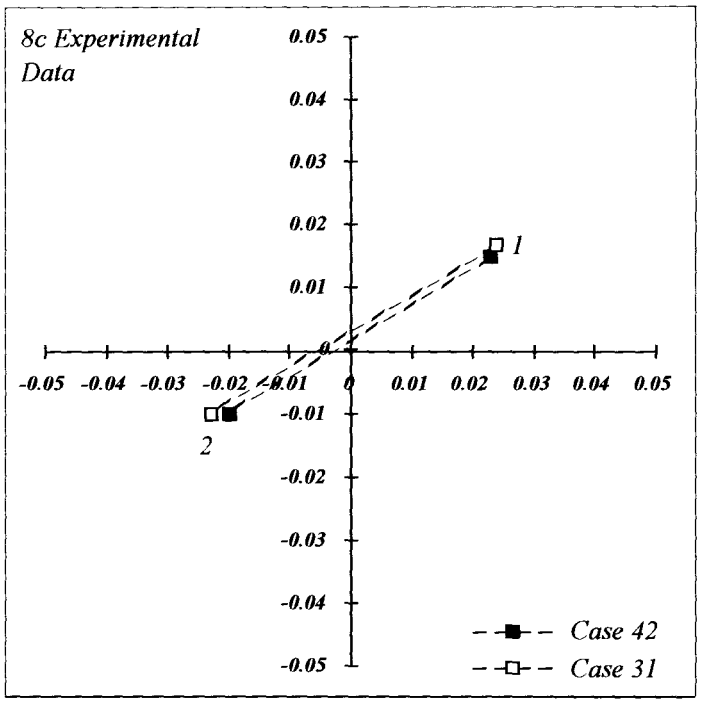

Figure R5.30- Comparison of two experimental cases (31 & 42) conducted with the same blade geometry and measurement position (8c).

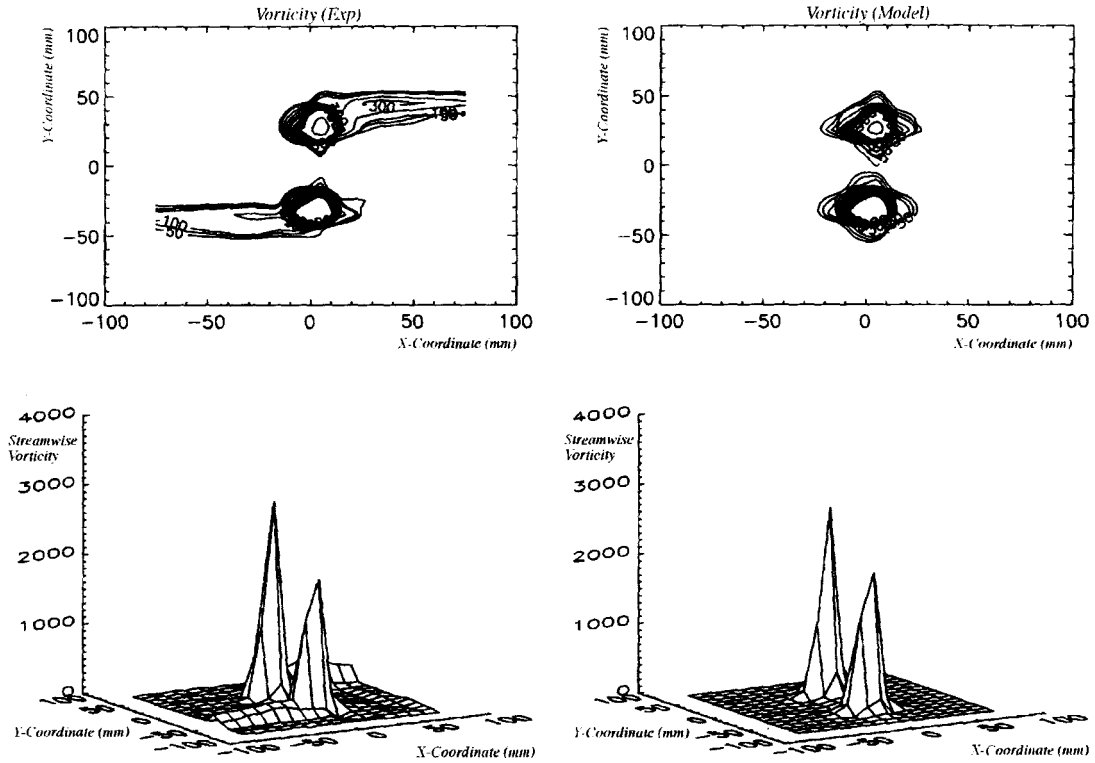

Figure R5.31- Streamwise vorticity calculated from experimental data and numerical model curve fit data for twin vortex case 26 (0.1c downstream measurement position).

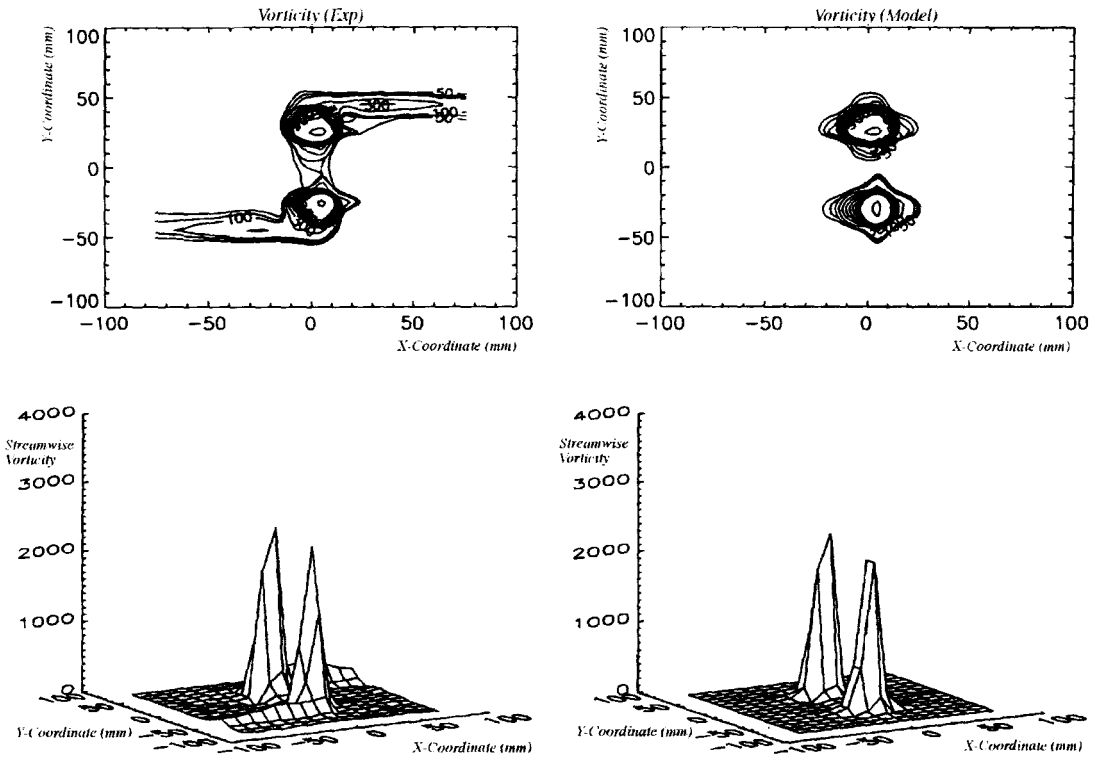

Figure R5.32- Streamwise vorticity calculated from experimental data and numerical model curve fit data for twin vortex case 27 (0.5c downstream measurement position).

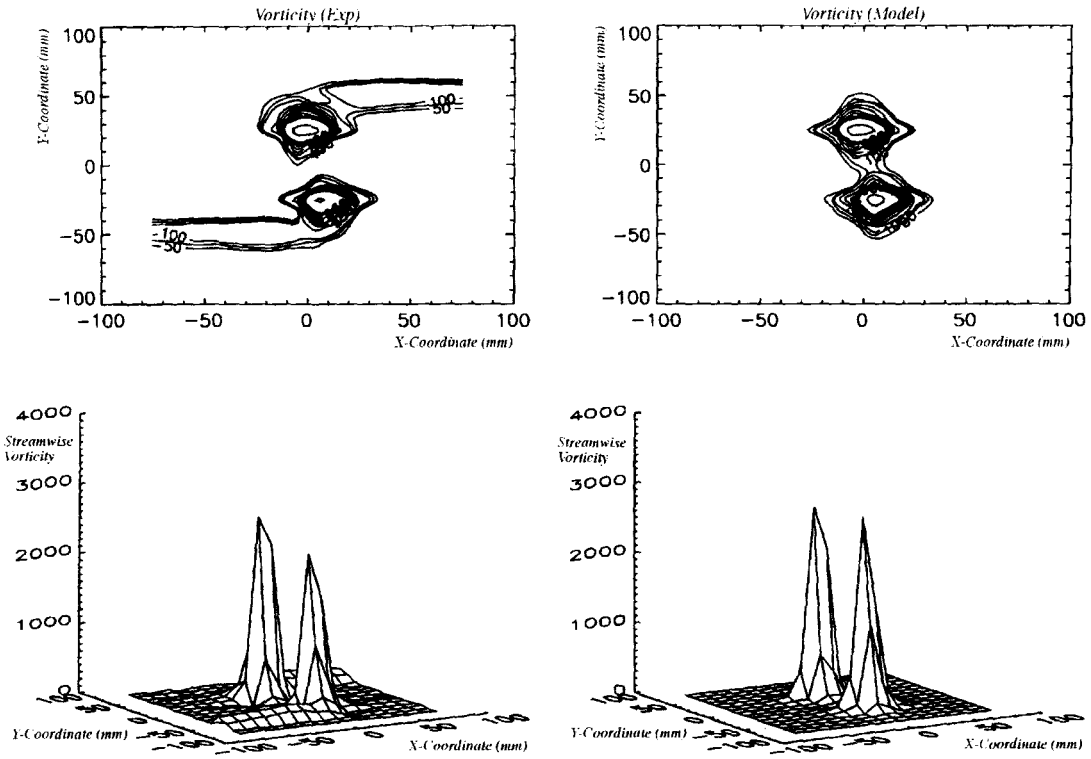

Figure R5.33- Streamwise vorticity calculated from experimental data and numerical model curve fit data for twin vortex case 28 (1c downstream measurement position).

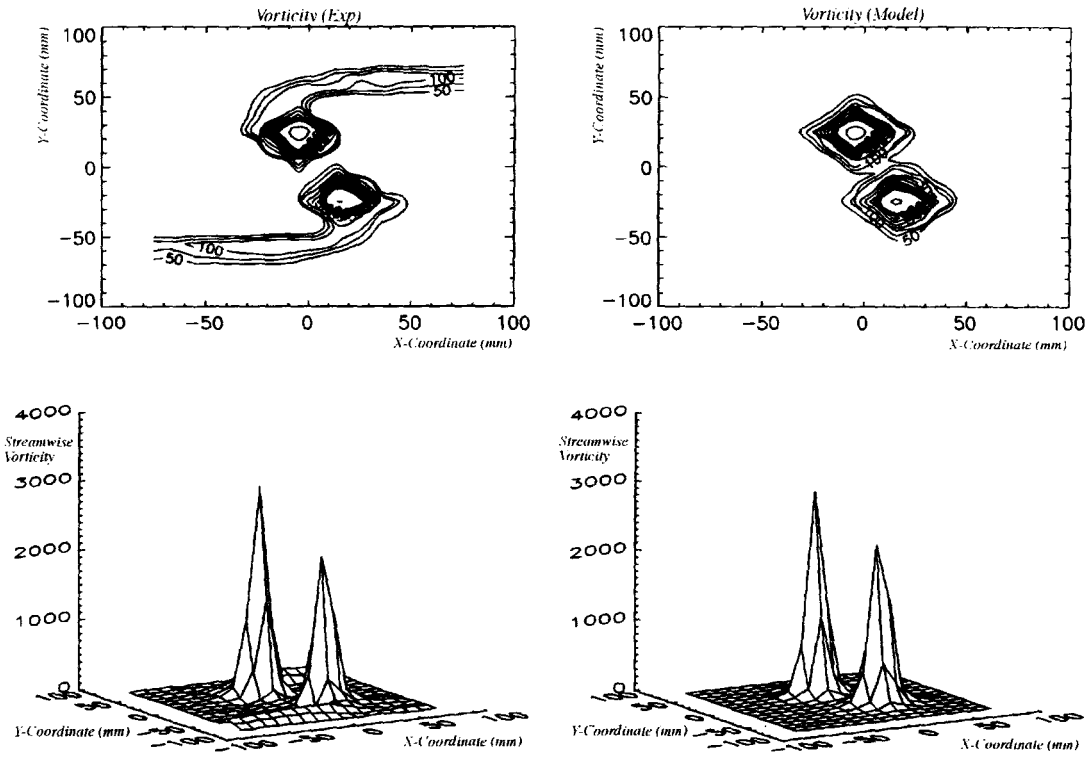

Figure R5.34- Streamwise vorticity calculated from experimental data and numerical model curve fit data for twin vortex case 29 (2c downstream measurement position).

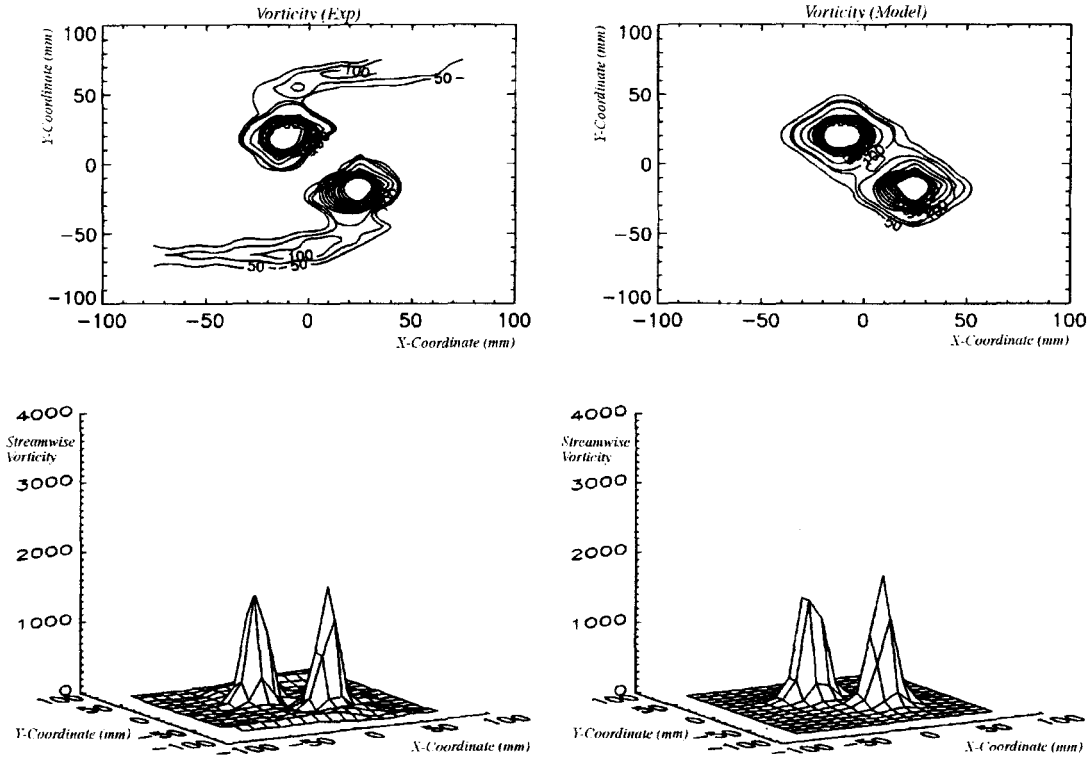

Figure R5.35- Streamwise vorticity calculated from experimental data and numerical model curve fit data for twin vortex case 30 (3c downstream measurement position).

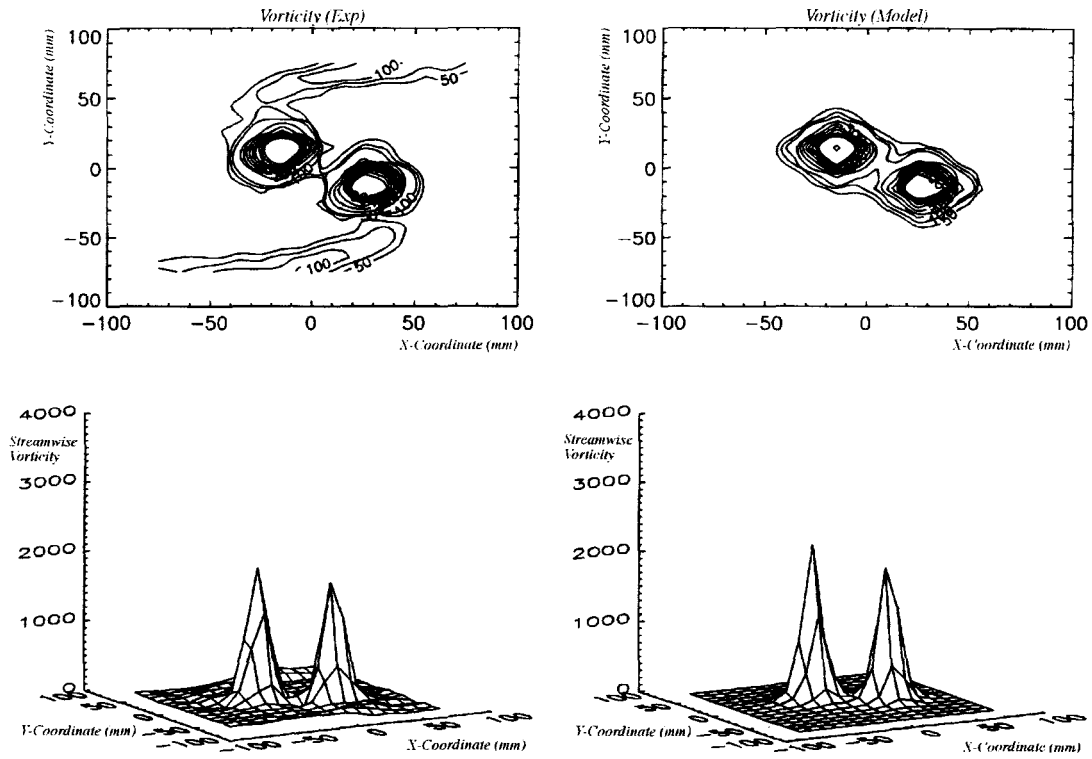

Figure R5.36- Streamwise vorticity calculated from experimental data and numerical model curve fit data for twin vortex case 31 (4c downstream measurement position).

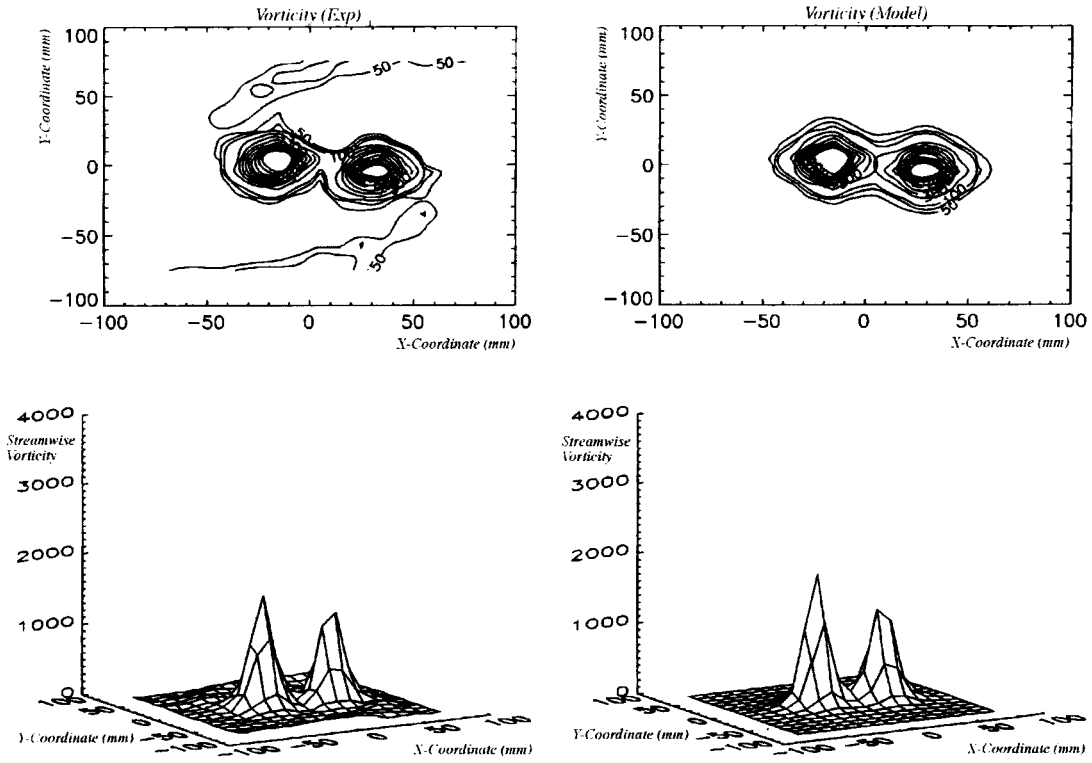

Figure R5.37- Streamwise vorticity calculated from experimental data and numerical model curve fit data for twin vortex case 32 (5c downstream measurement position).

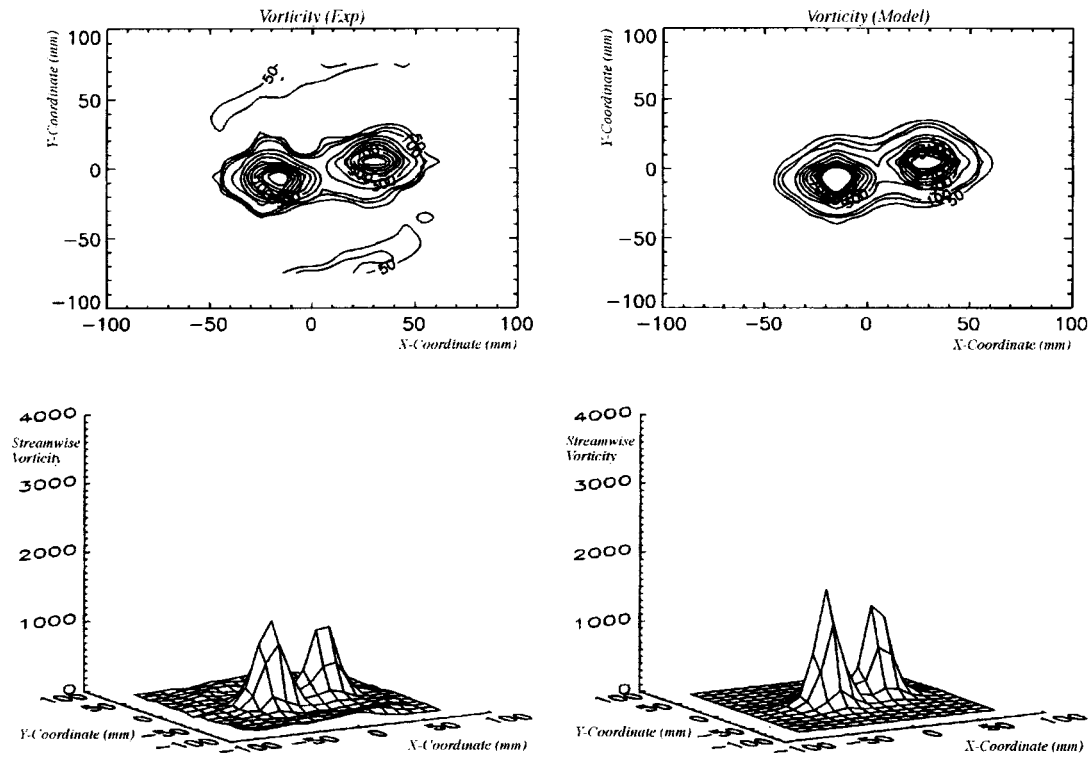

Figure R5.38- Streamwise vorticity calculated from experimental data and numerical model curve fit data for twin vortex case 33 (6c downstream measurement position).

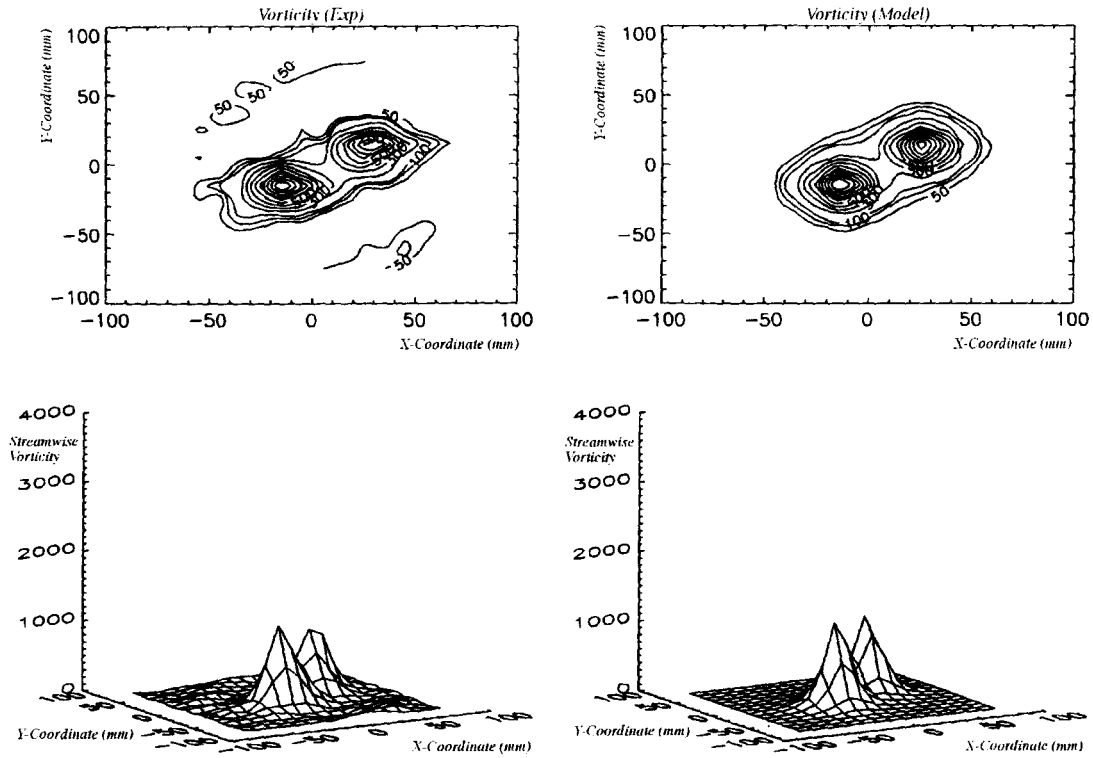

Figure R5.39- Streamwise vorticity calculated from experimental data and numerical model curve fit data for twin vortex case 34 (7c downstream measurement position).

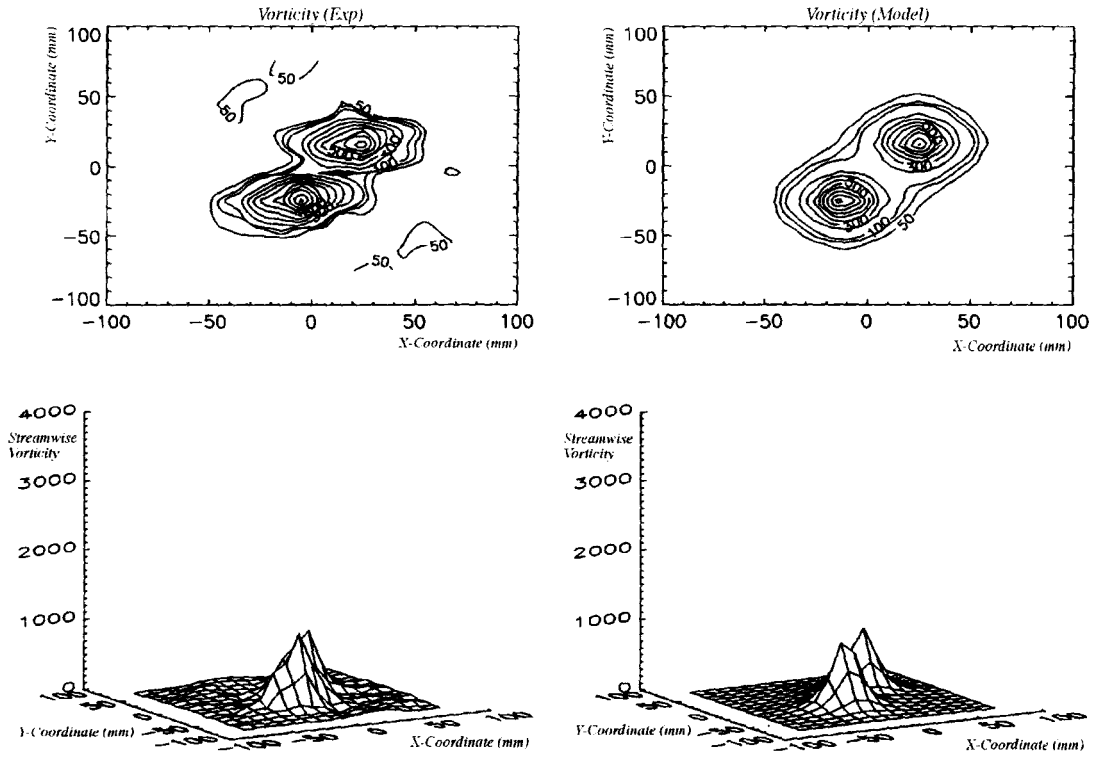

Figure R5.40- Streamwise vorticity calculated from experimental data and numerical model curve fit data for twin vortex case 35 (8c downstream measurement position).

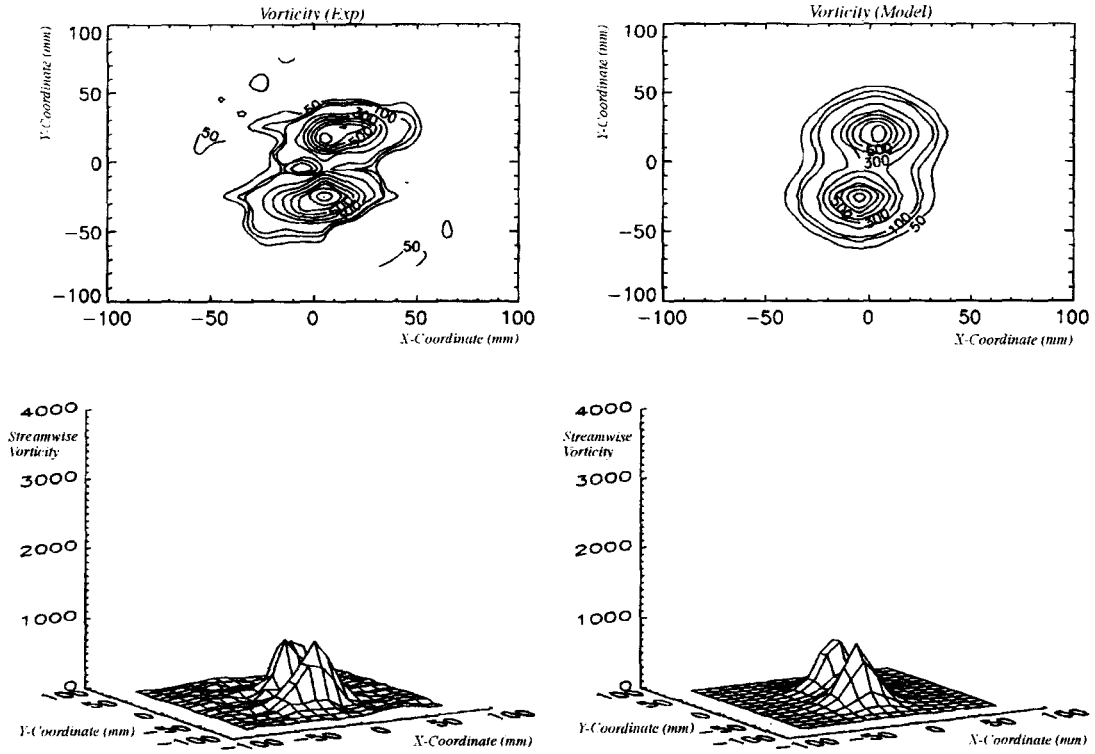

Figure R5.41- Streamwise vorticity calculated from experimental data and numerical model curve fit data for twin vortex case 36 (9c downstream measurement position).

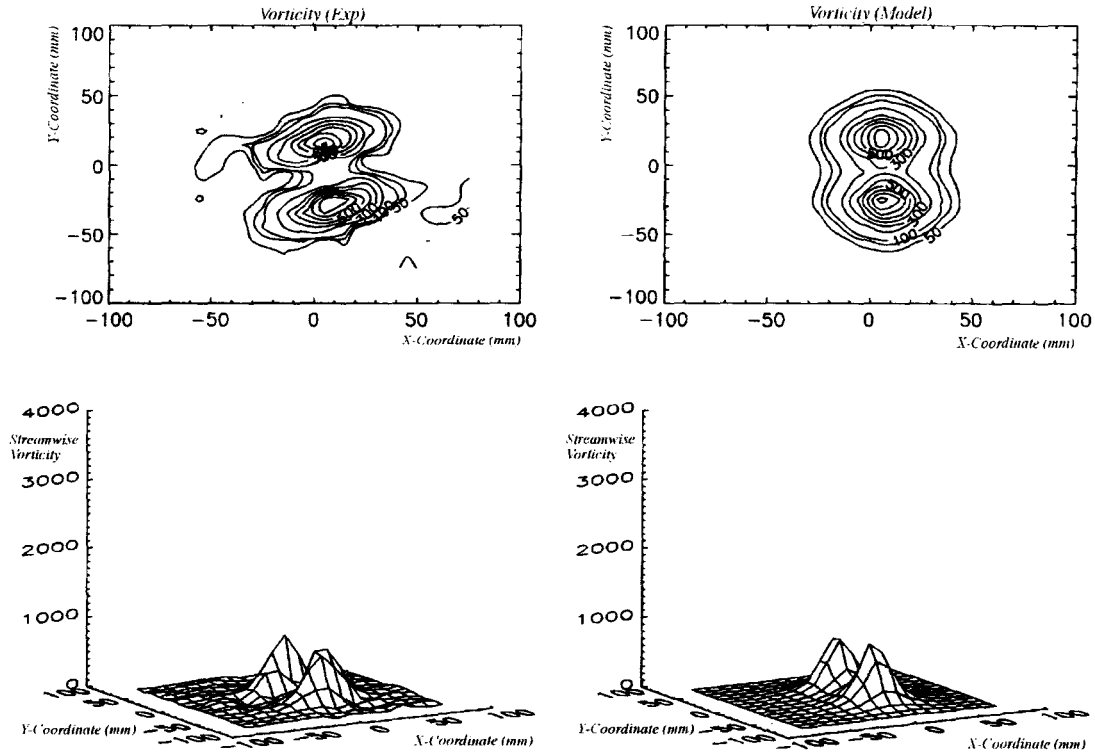

Figure R5.42- Streamwise vorticity calculated from experimental data and numerical model curve fit data for twin vortex case 37 (10c downstream measurement position).

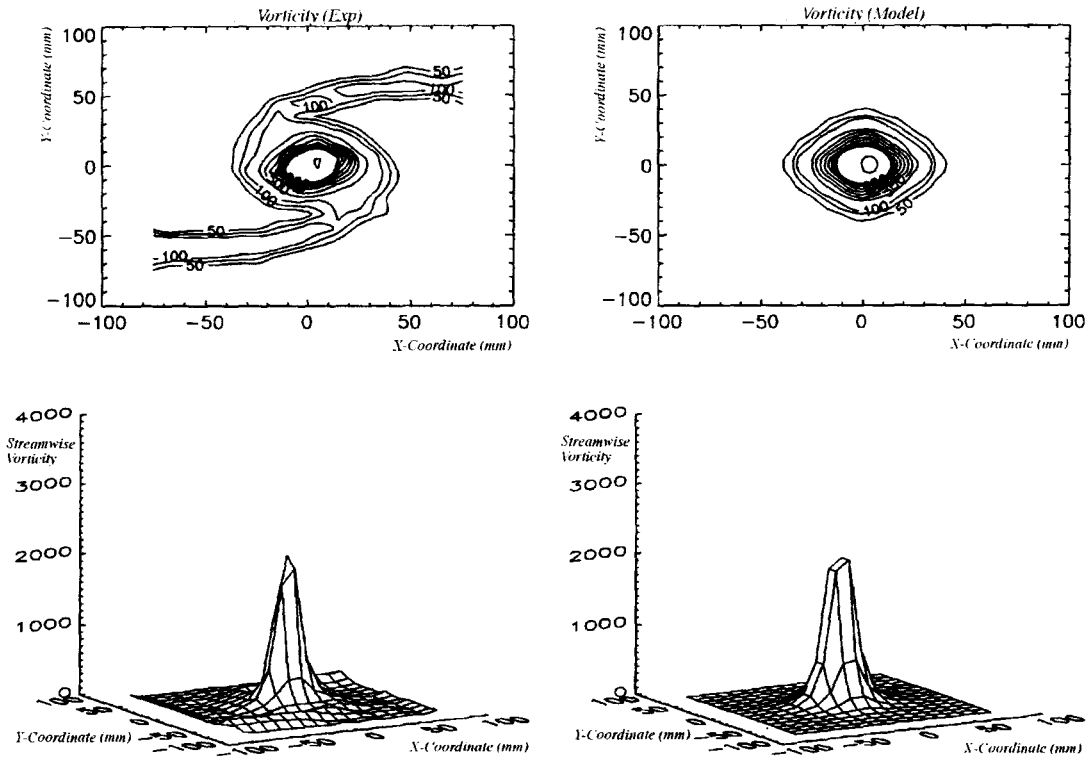

Figure R5.43- Streamwise vorticity calculated from experimental data and numerical model curve fit data for single vortex case 40 (4c downstream measurement position with 0.0c blade separation).

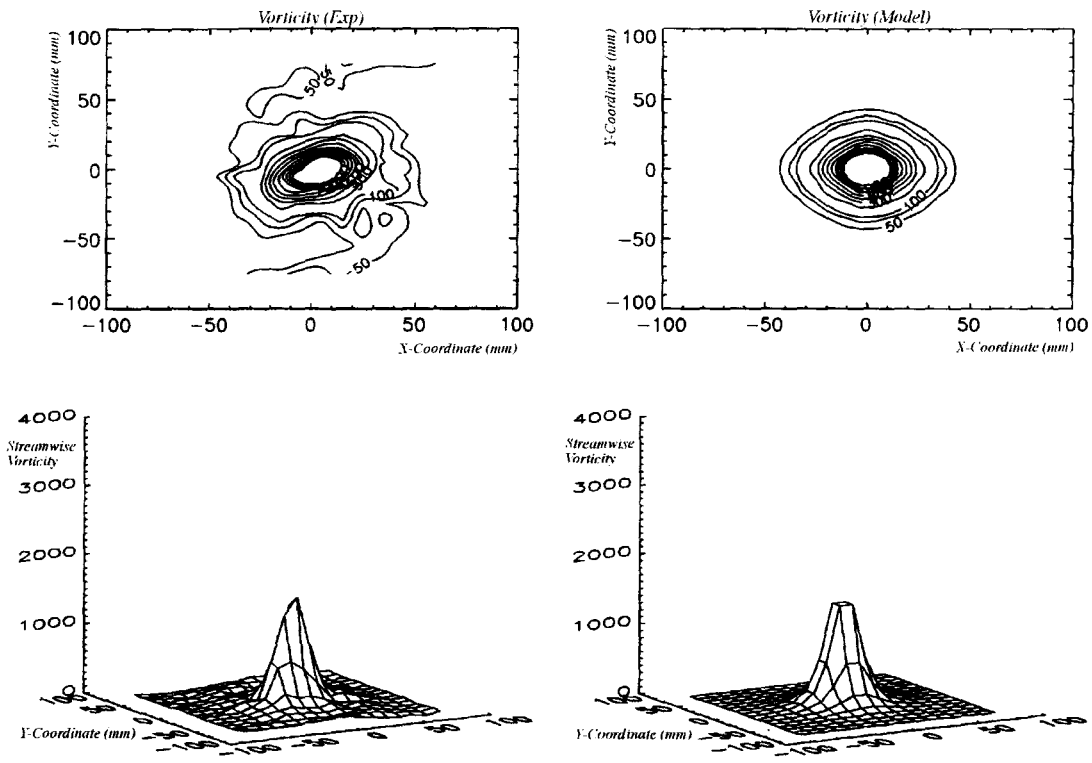

Figure R5.44- Streamwise vorticity calculated from experimental data and numerical model curve fit data for single vortex case 45 (8c downstream measurement position with 0.0c blade separation).

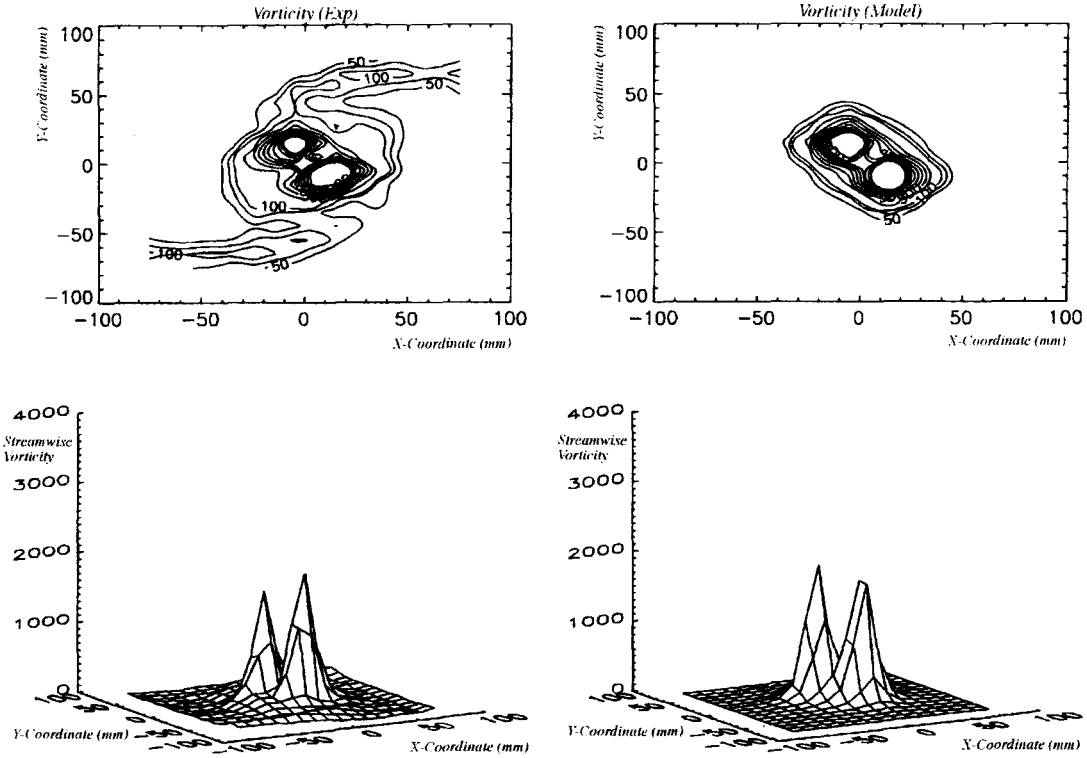

Figure R5.45- Streamwise vorticity calculated from experimental data and numerical model curve fit data for twin vortex case 41 (4c downstream measurement position with 0.25c blade separation).

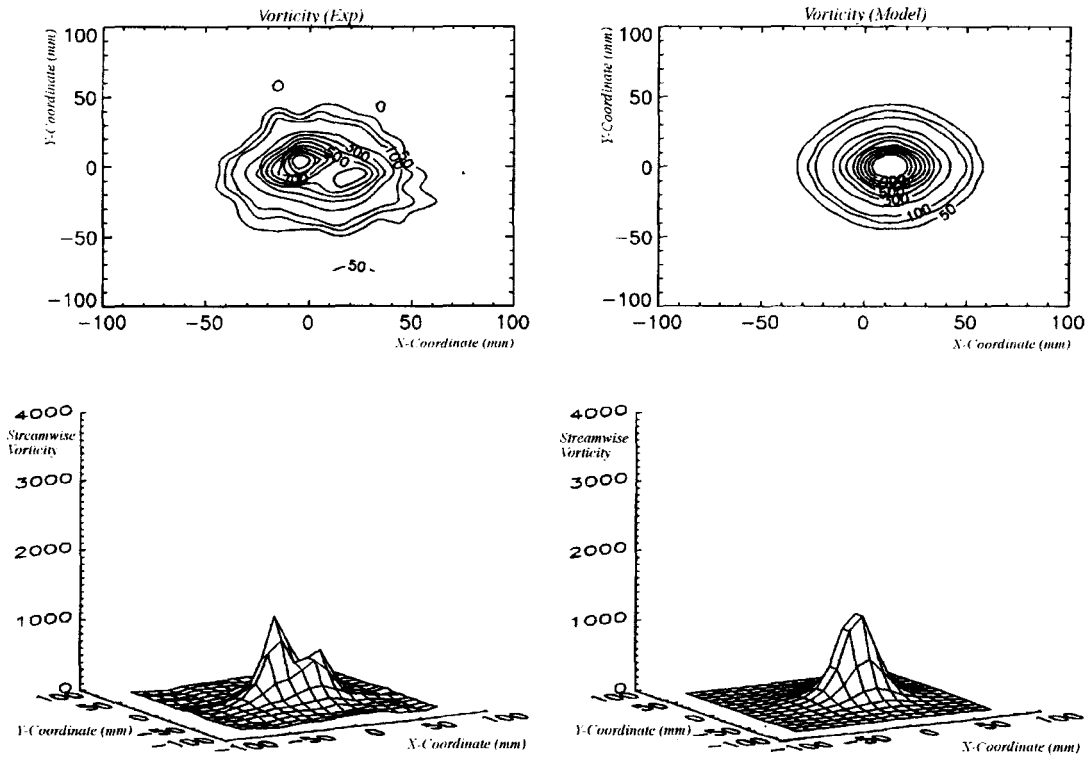

Figure R5.46- Streamwise vorticity calculated from experimental data and numerical model curve fit data for twin vortex case 46 (8c downstream measurement position with 0.25c blade separation).

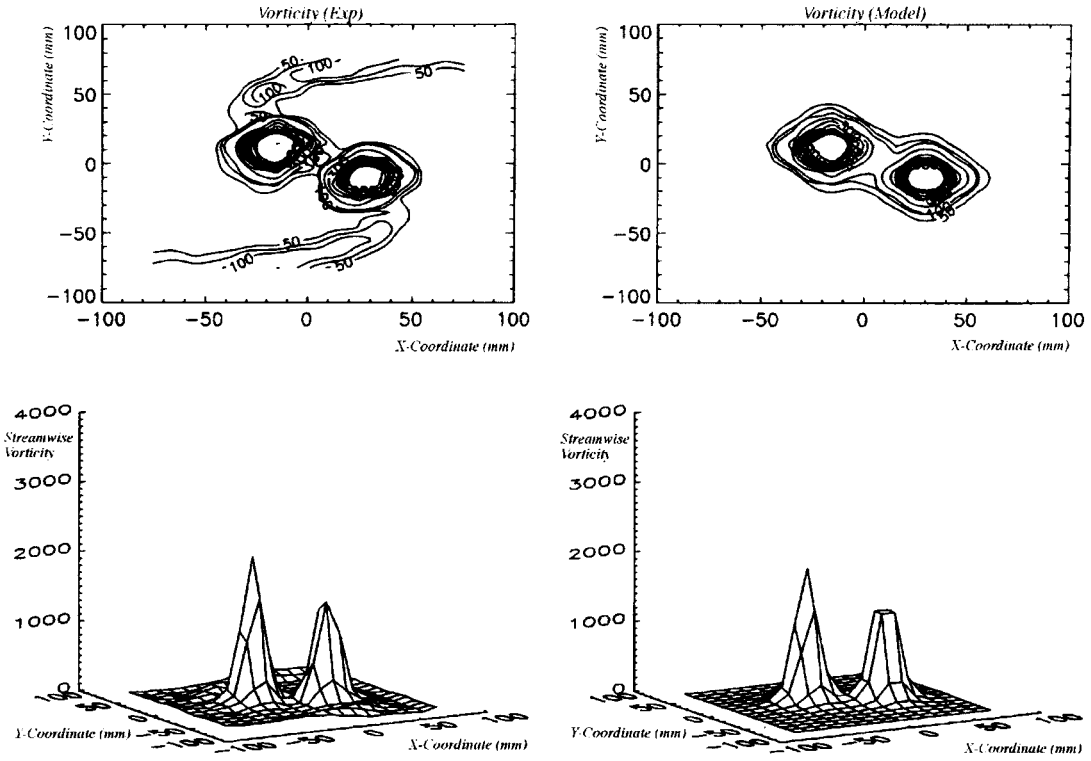

Figure R5.47- Streamwise vorticity calculated from experimental data and numerical model curve fit data for twin vortex case 42 (4c downstream measurement position with 0.75c blade separation).

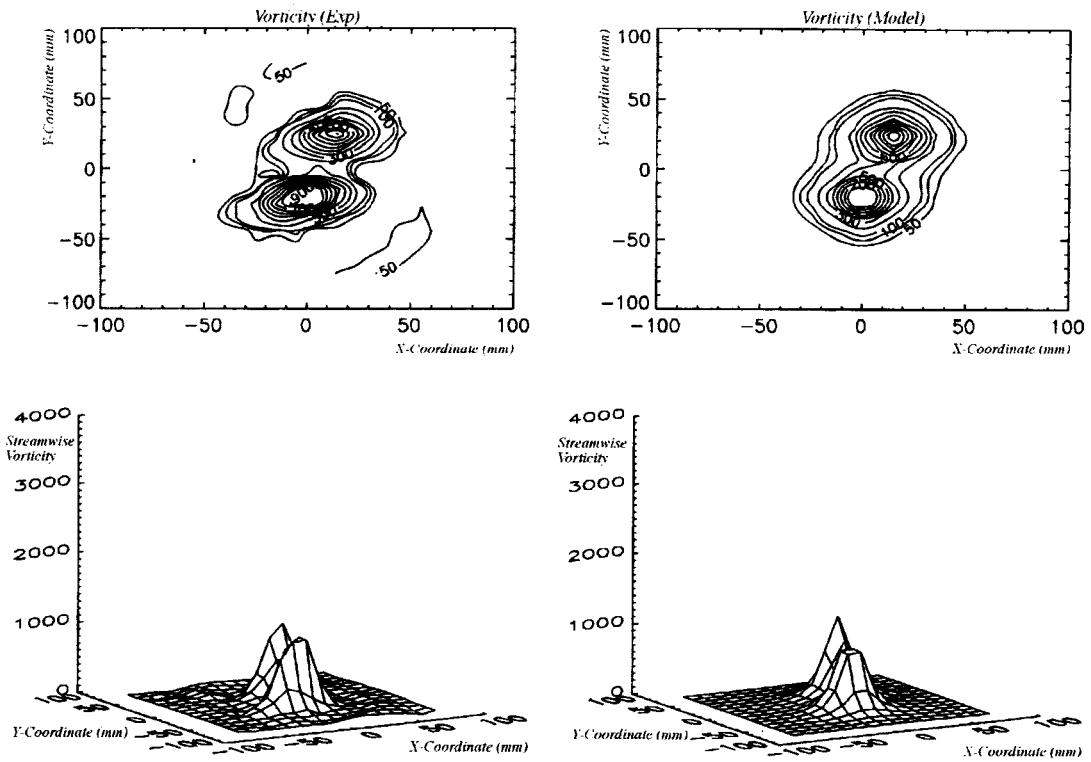

Figure R5.48- Streamwise vorticity calculated from experimental data and numerical model curve fit data for twin vortex case 47 (8c downstream measurement position with 0.5c blade separation).

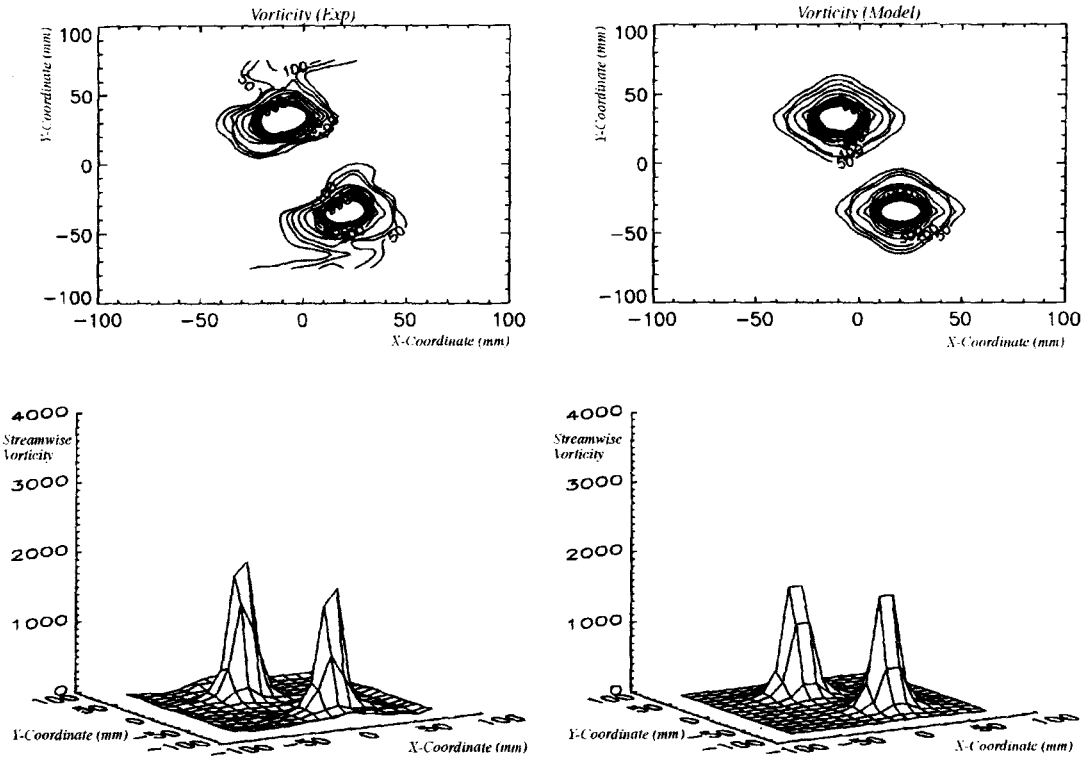

Figure R5.49- Streamwise vorticity calculated from experimental data and numerical model curve fit data for twin vortex case 43 (4c downstream measurement position with 0.75c blade separation).

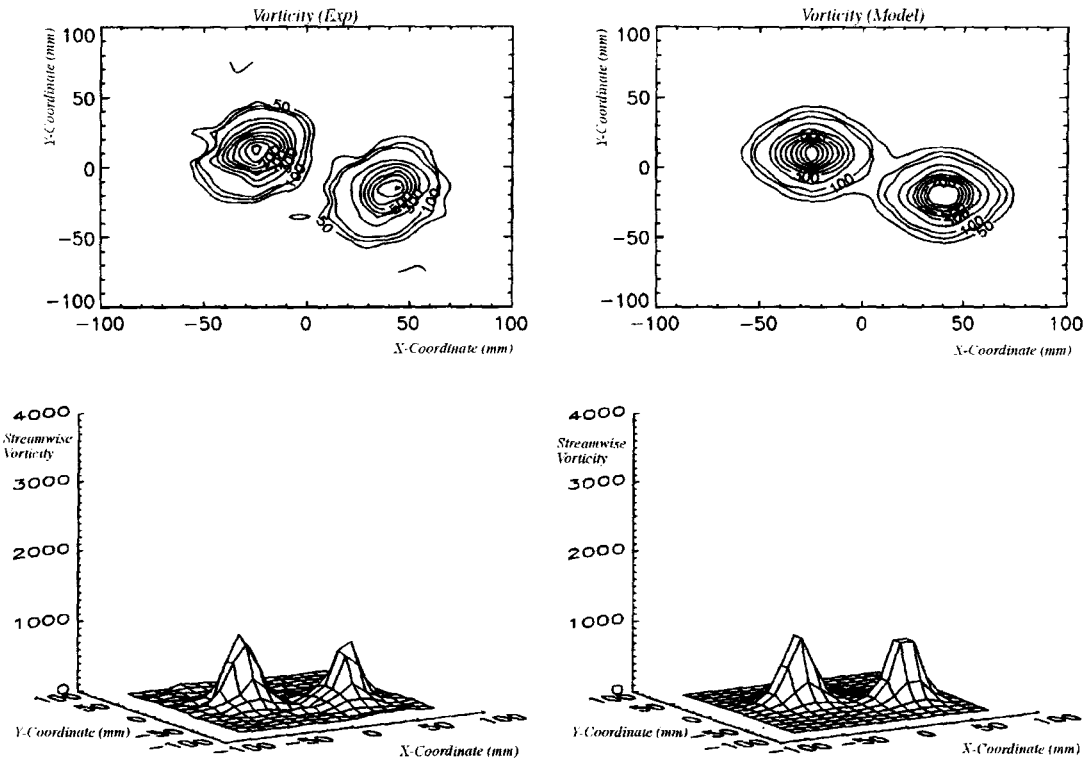

Figure R5.50- Streamwise vorticity calculated from experimental data and numerical model curve fit data for twin vortex case 48 (8c downstream measurement position with 0.75c blade separation).

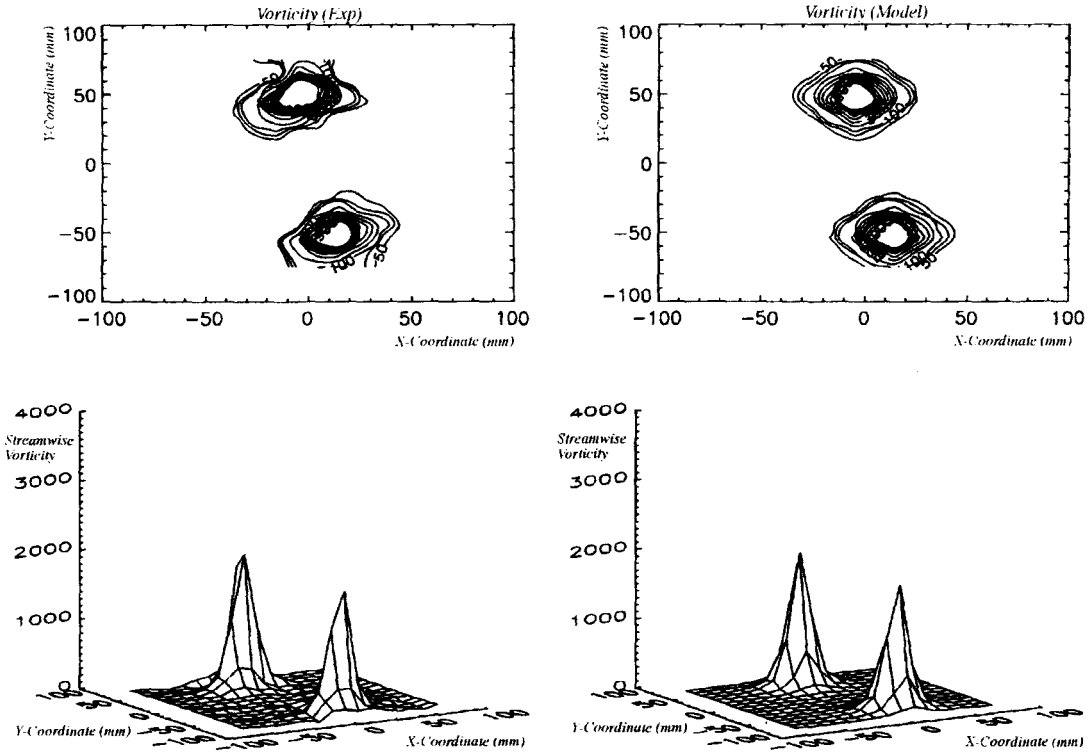

Figure R5.51- Streamwise vorticity calculated from experimental data and numerical model curve fit data for twin vortex case 44 (4c downstream measurement position with 1.0c blade separation).

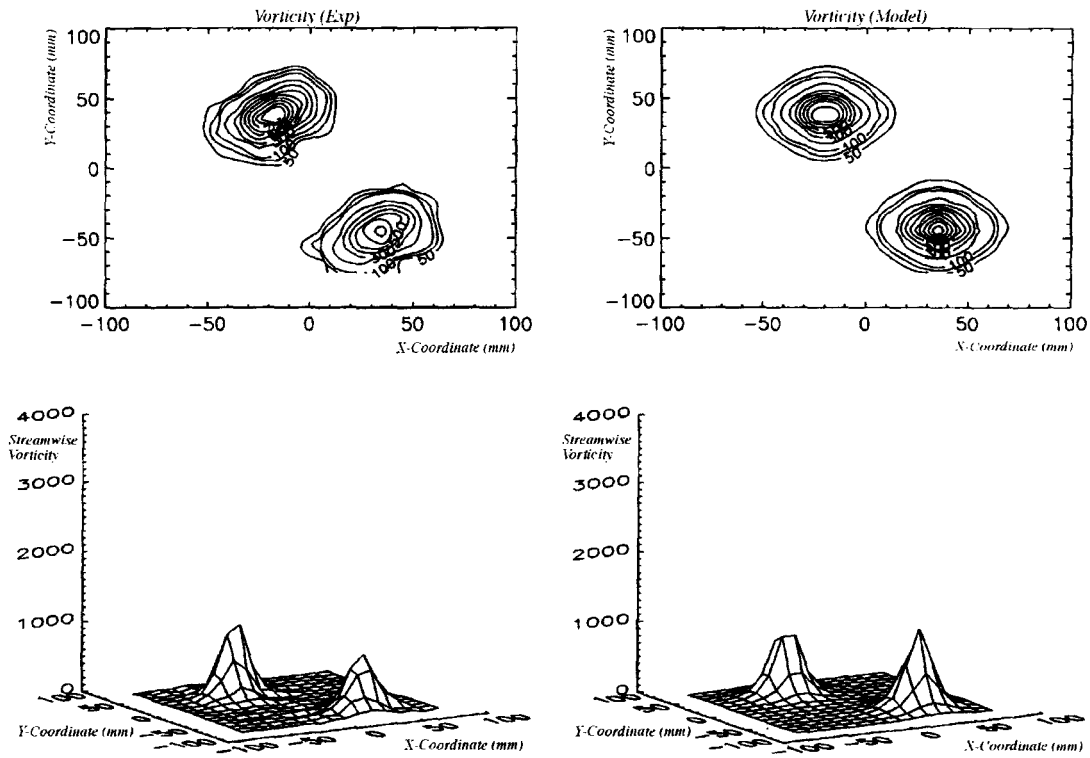

Figure R5.52- Streamwise vorticity calculated from experimental data and numerical model curve fit data for twin vortex case 49 (8c downstream measurement position with 1.0c blade separation).

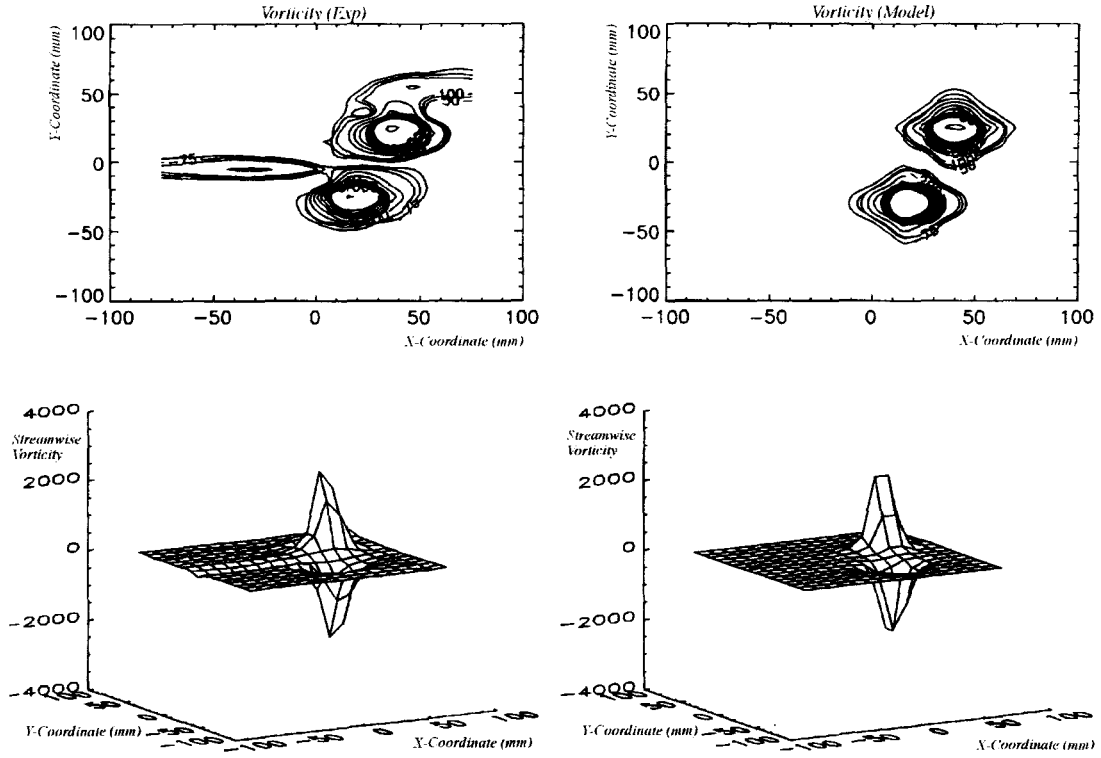

Figure R5.53- Streamwise vorticity calculated from experimental data and numerical model curve fit data for twin vortex case 51 (2.5c downstream measurement position and 0.5c blade separation).

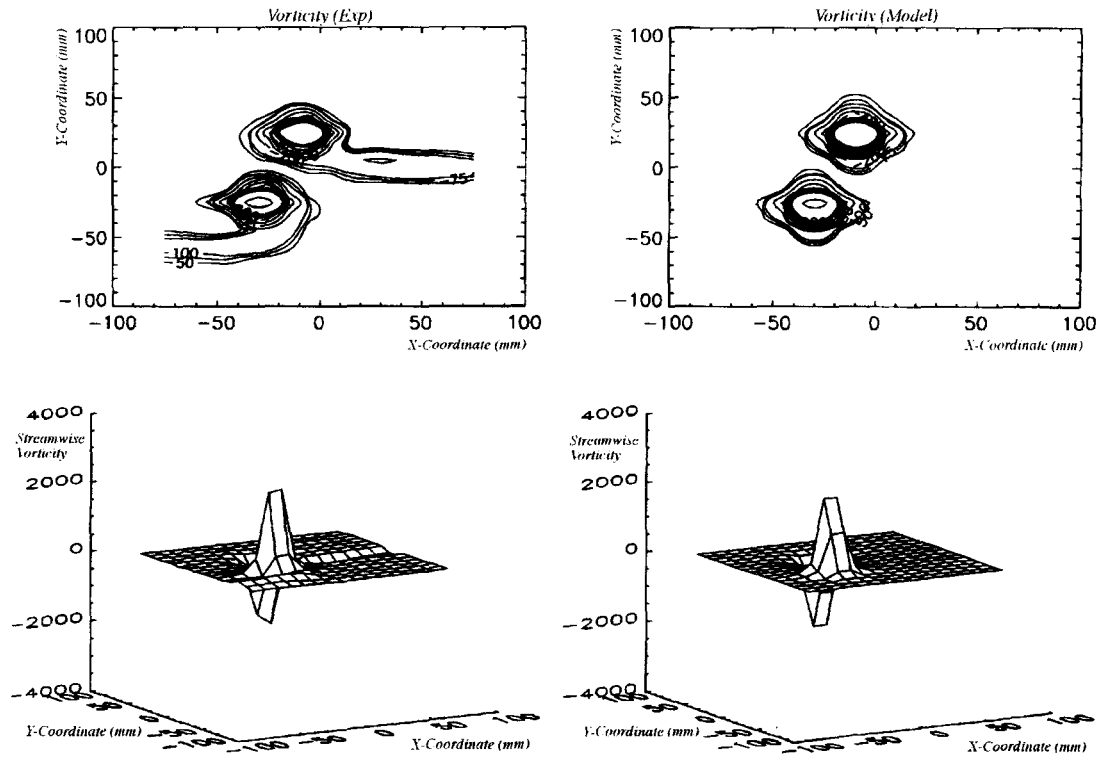

Figure R5.54- Streamwise vorticity calculated from experimental data and numerical model curve fit data for twin vortex case 52 (2.5c downstream measurement position and 0.5c blade separation- opposite sense vortices to Fig. 5.53).

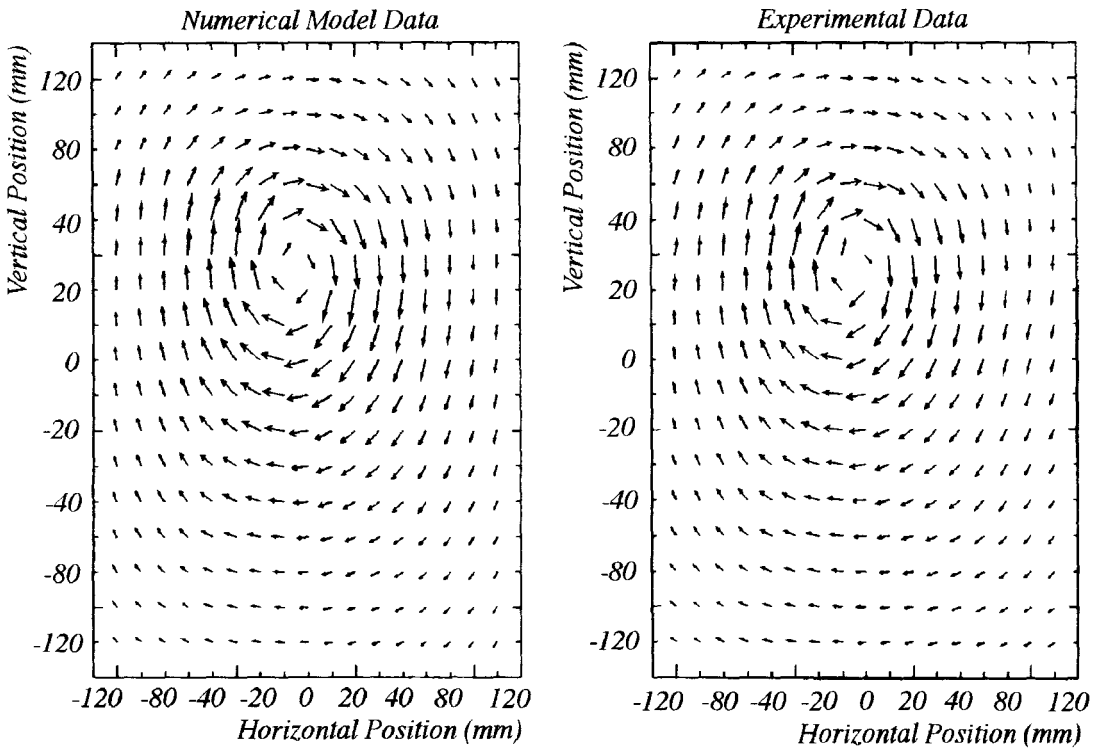

Figure R5.55- Comparison of numerical model and experimental data vector plots for single vortex Case 1 (Tables 5.8 & 5.14).

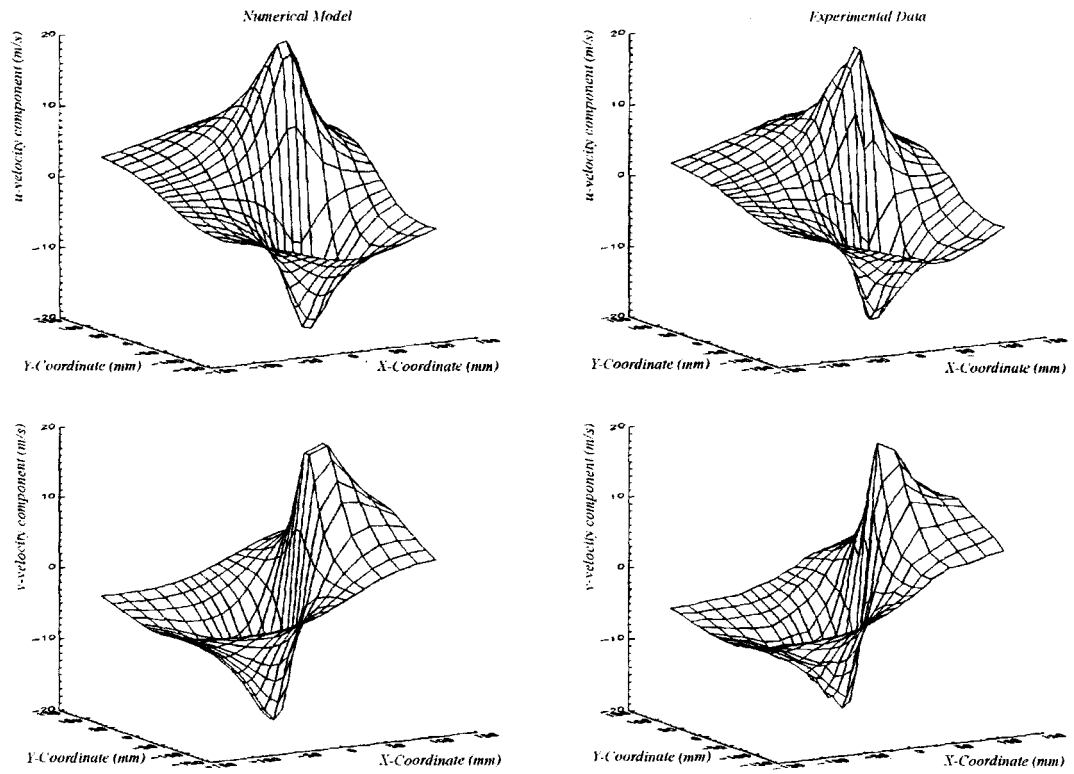

Figure R5.56- Surface plots of u (top) and v (bottom) velocity components for numerical model (left) and experimental data (right) for Case 1 (Tables 5.8 & 5.14).

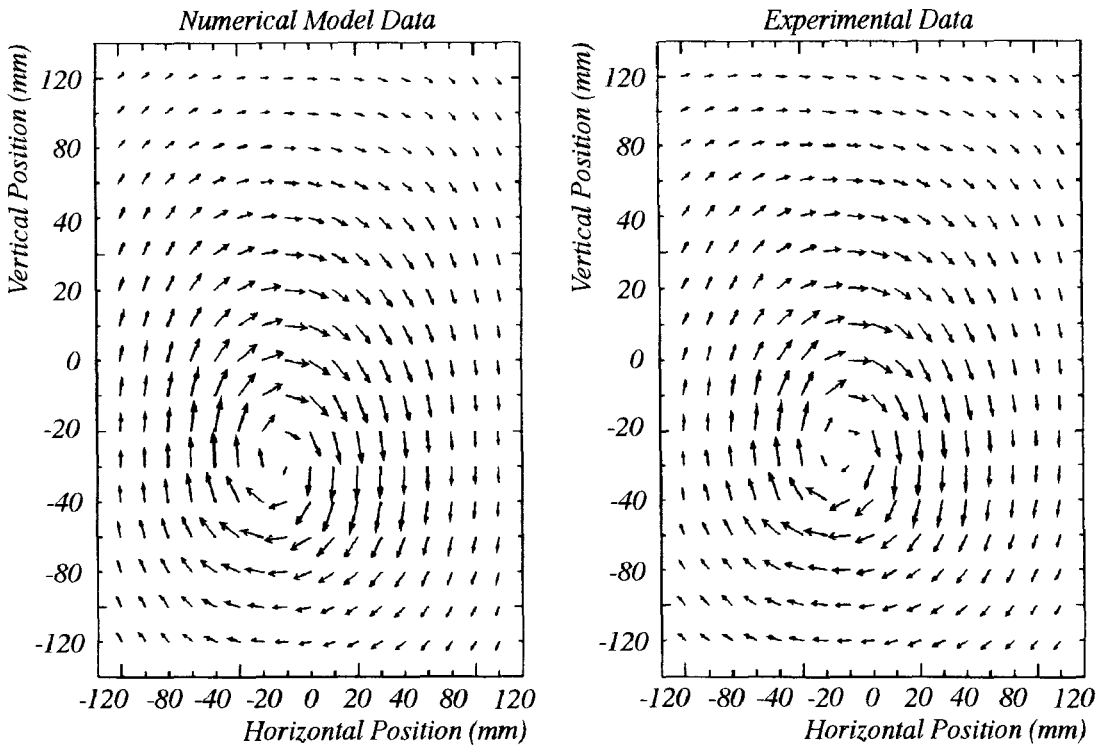

Figure R5.57- Comparison of numerical model and experimental data vector plots for single vortex Case 8 (Tables 5.8 & 5.14).

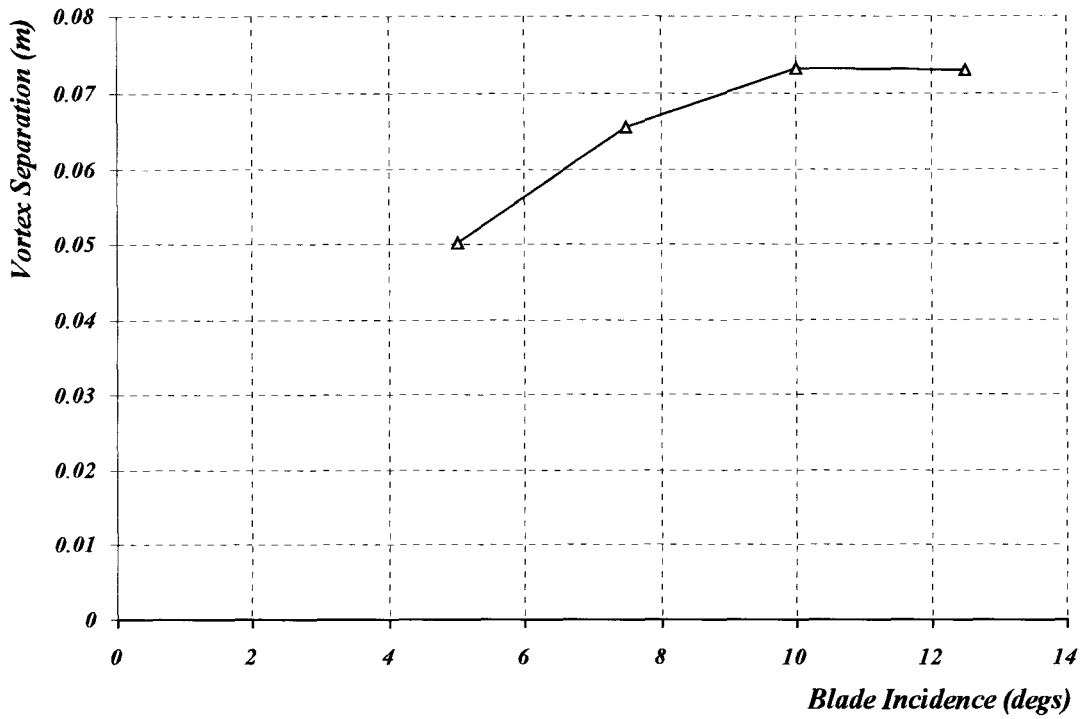

Figure R5.58- Variation in vortex core separation with a change in incidence for twin vortex cases 9-12 (Tables 5.9 & 5.15).

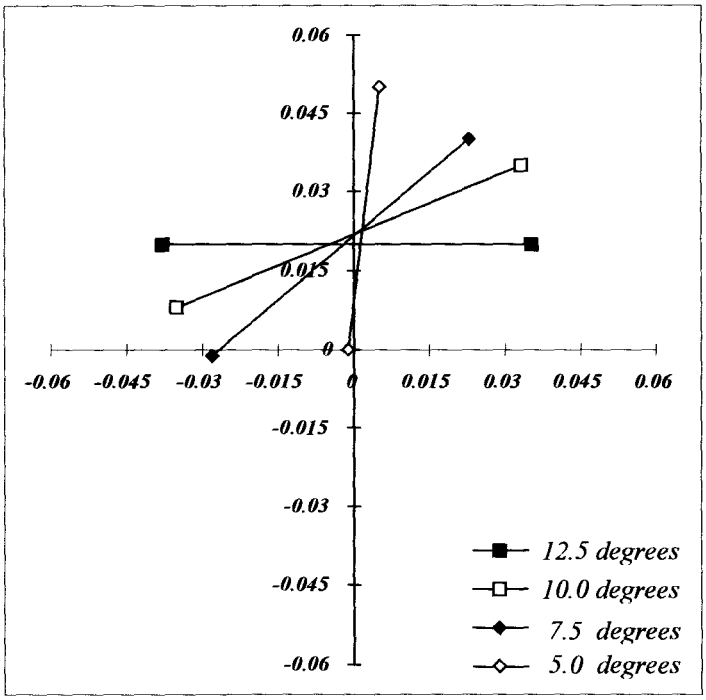

Figure R5.59- Vortex locations at different incidence settings with a downstream measurement position of 7.1c (0.5c separation between ¼c aerofoil locations). The lower vortices are convected upward due to traverse interference and so the separation is reduced - as indicated in the preceding figure. This effect is most significant in the 5 degree case where the vortices are vertically aligned.

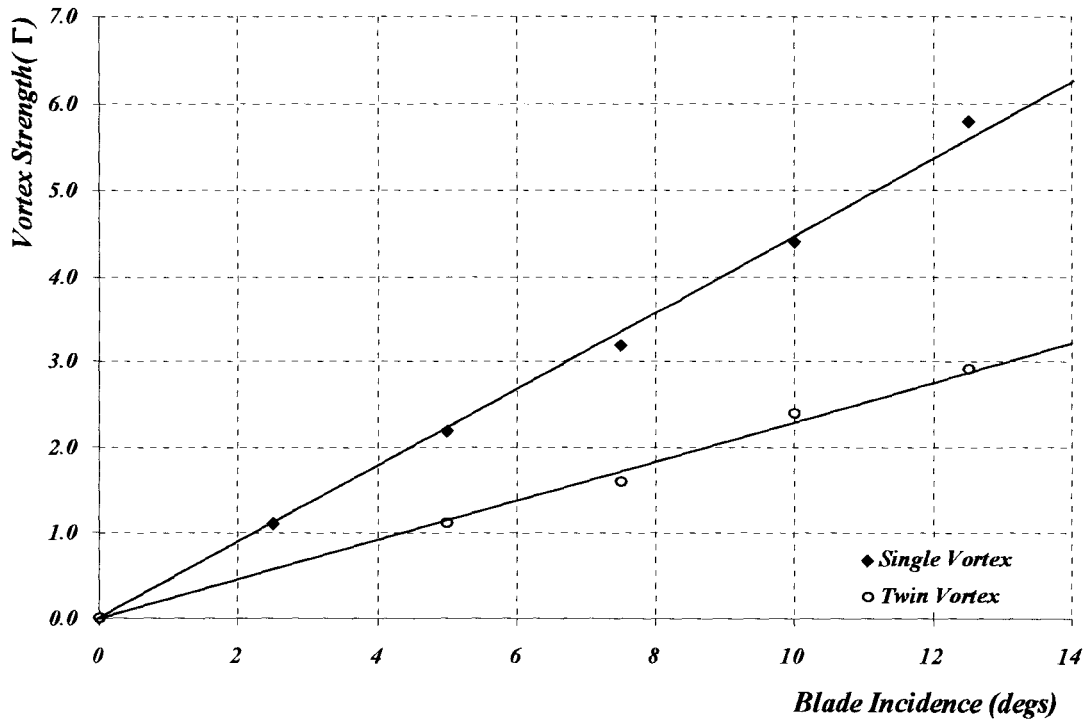

Figure R5.60- Variation in vortex strength with incidence for the single vortex generator (cases 1-5) and the twin vortex generator (cases 9-12 in Tables 5.14 & 5.15).

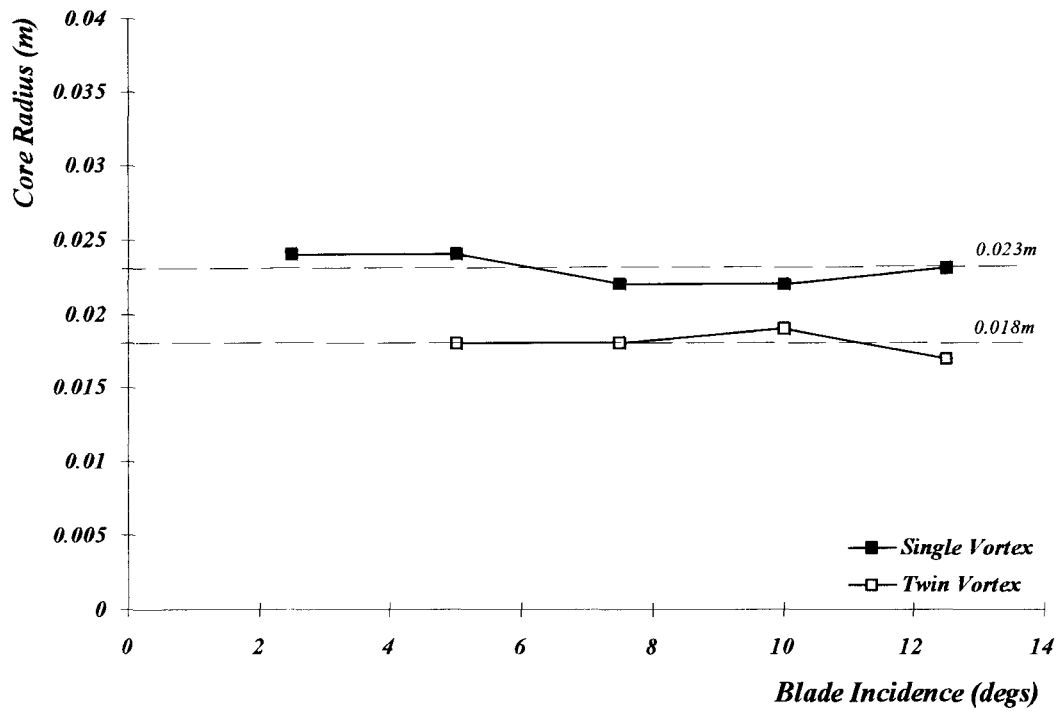

Figure R5.61- Variation in core size with a change in incidence for single vortex cases 1-5 and twin vortex cases 9-12. The core size is, approximately, invarient with incidence and this agrees with the previous data depicted in Fig.R5.20.

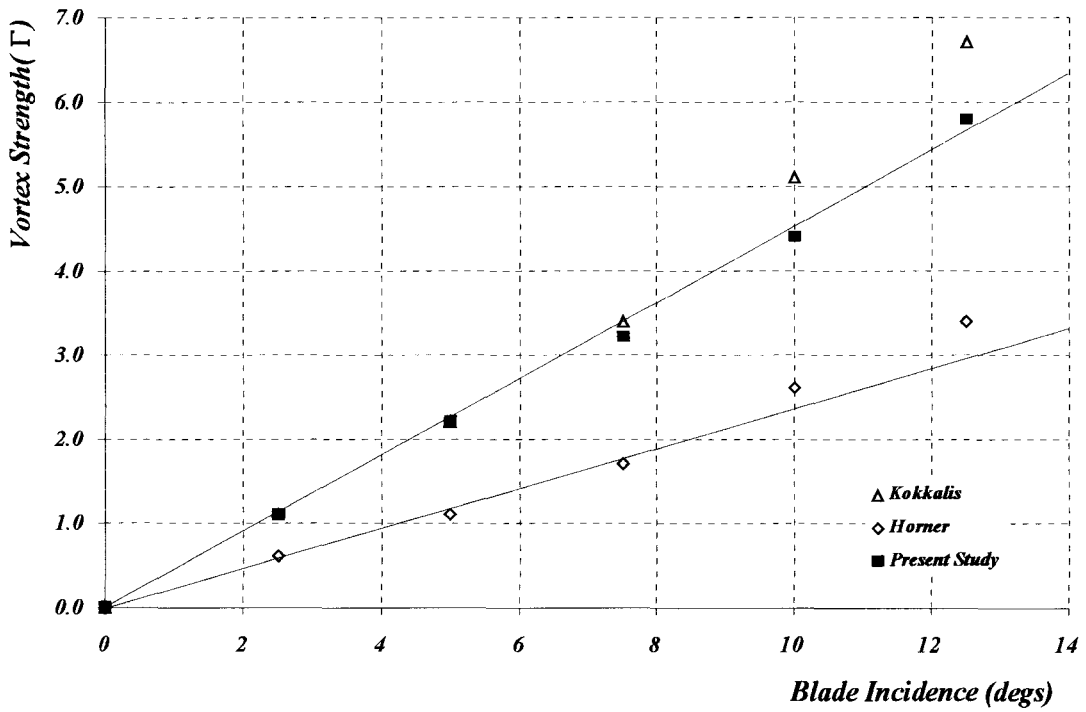

Figure R5.62- Comparison of the single vortex strengths documented by Kokkalis, Horner (see Appendix E) and in Fig. R5.60 of the present study.

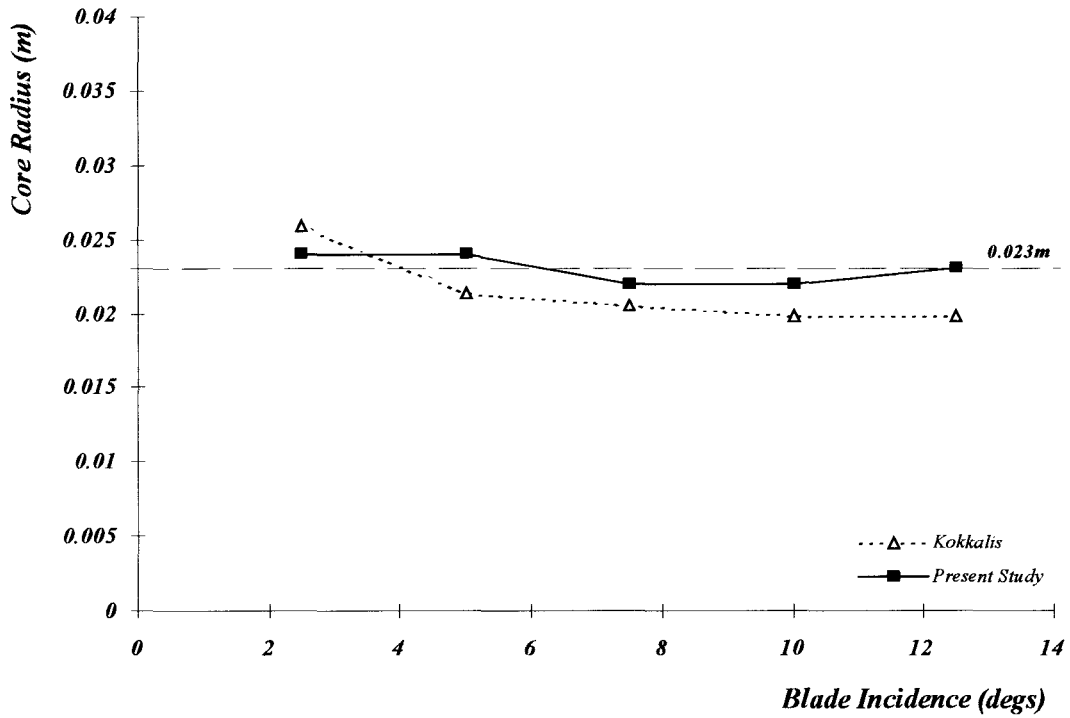

Figure R5.63- Comparison of the core radius as documented by Kokkalis (see Appendix E) and in Fig. R5.61 of the present study. Horner obtained a core radius of 0.025m, from the PIV data depicted in Appendix E, for a generator incidence of 12.5 degrees.

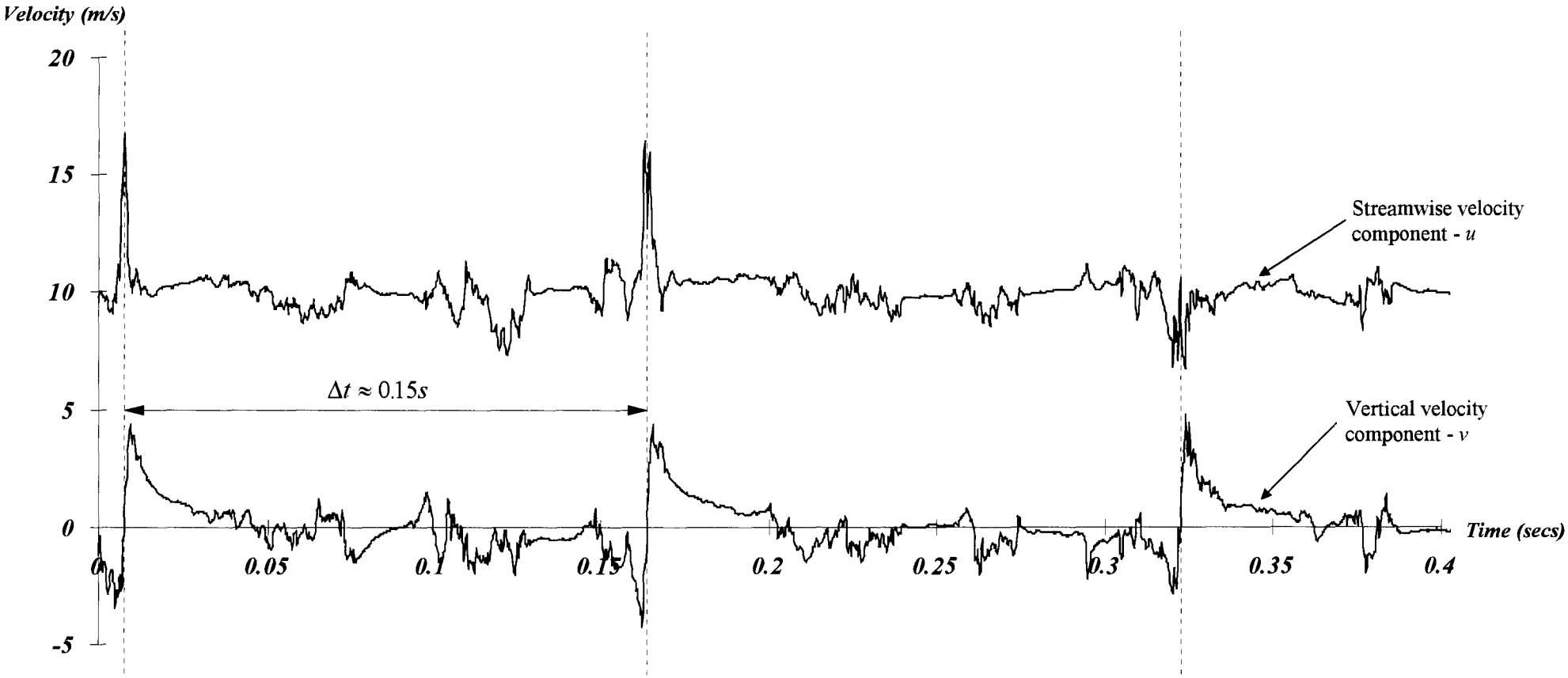

Figure R6.1- Transverse vortex test case 1 - working section velocity 10m/s, rotational speed 400rpm.

Sampling Frequency 5000 Hz for 0.4seconds.

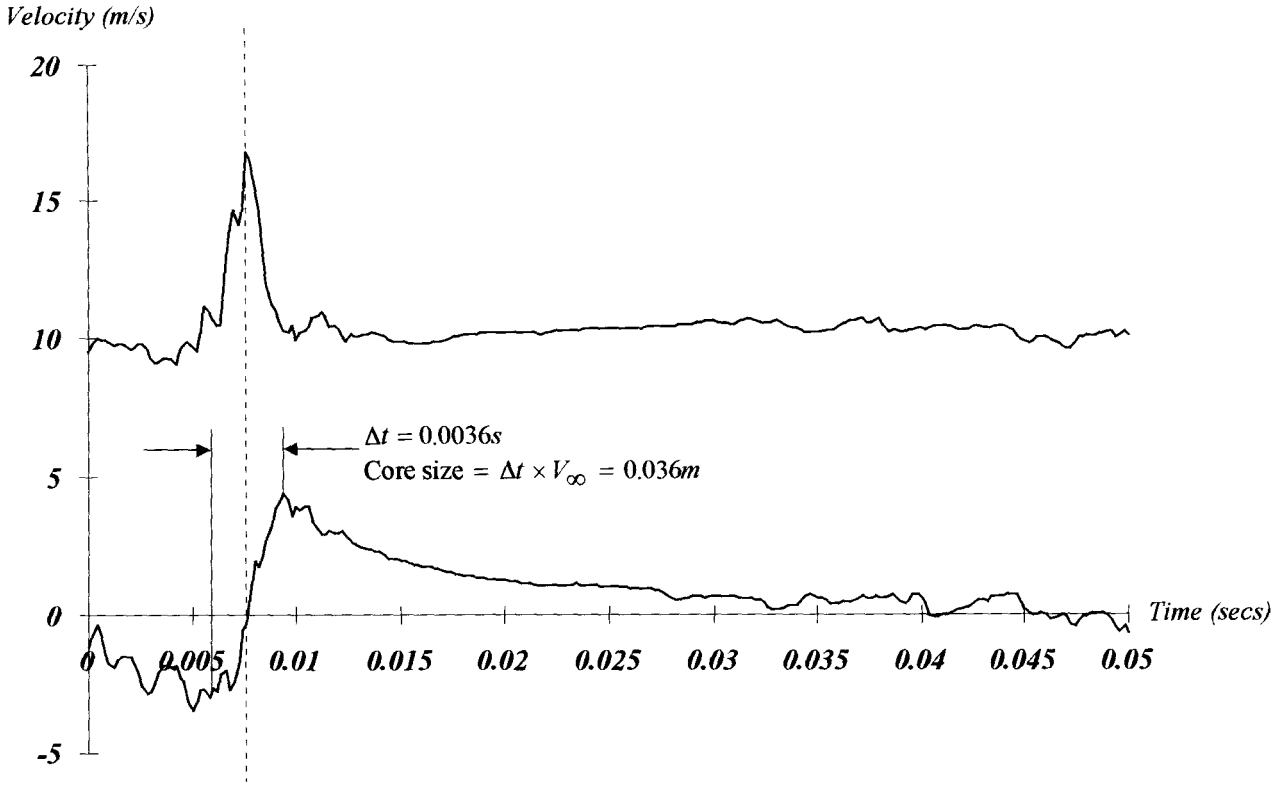

Figure R6.2- Close-up of first vortex in Fig. 6.1 illustrating peak to peak change in time (Δt) and corresponding core size.

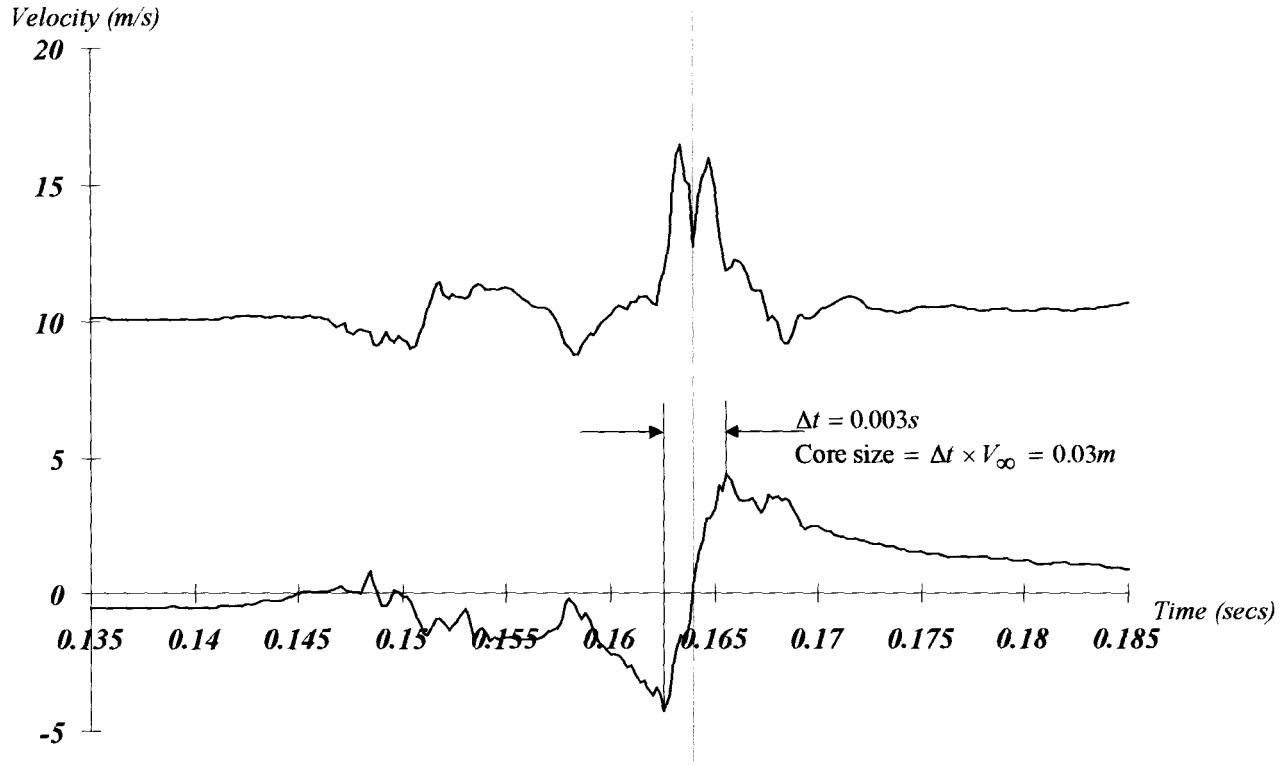

Figure R6.3- Close-up of second vortex in Fig. 6.1 illustrating peak to peak change in time (Δt) and corresponding core size.

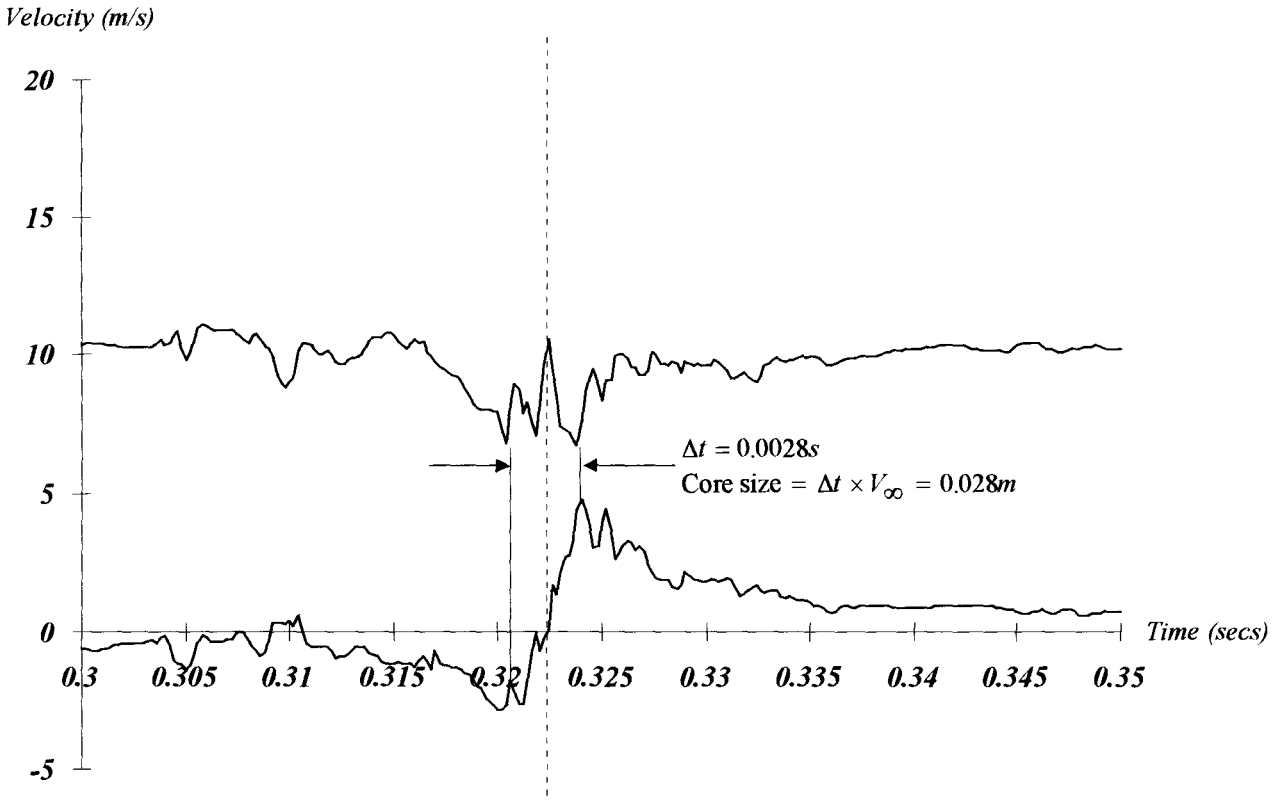

Figure R6.4- Close-up of third vortex in Fig. 6.1 illustrating peak to peak change in time (Δt) and corresponding core size.

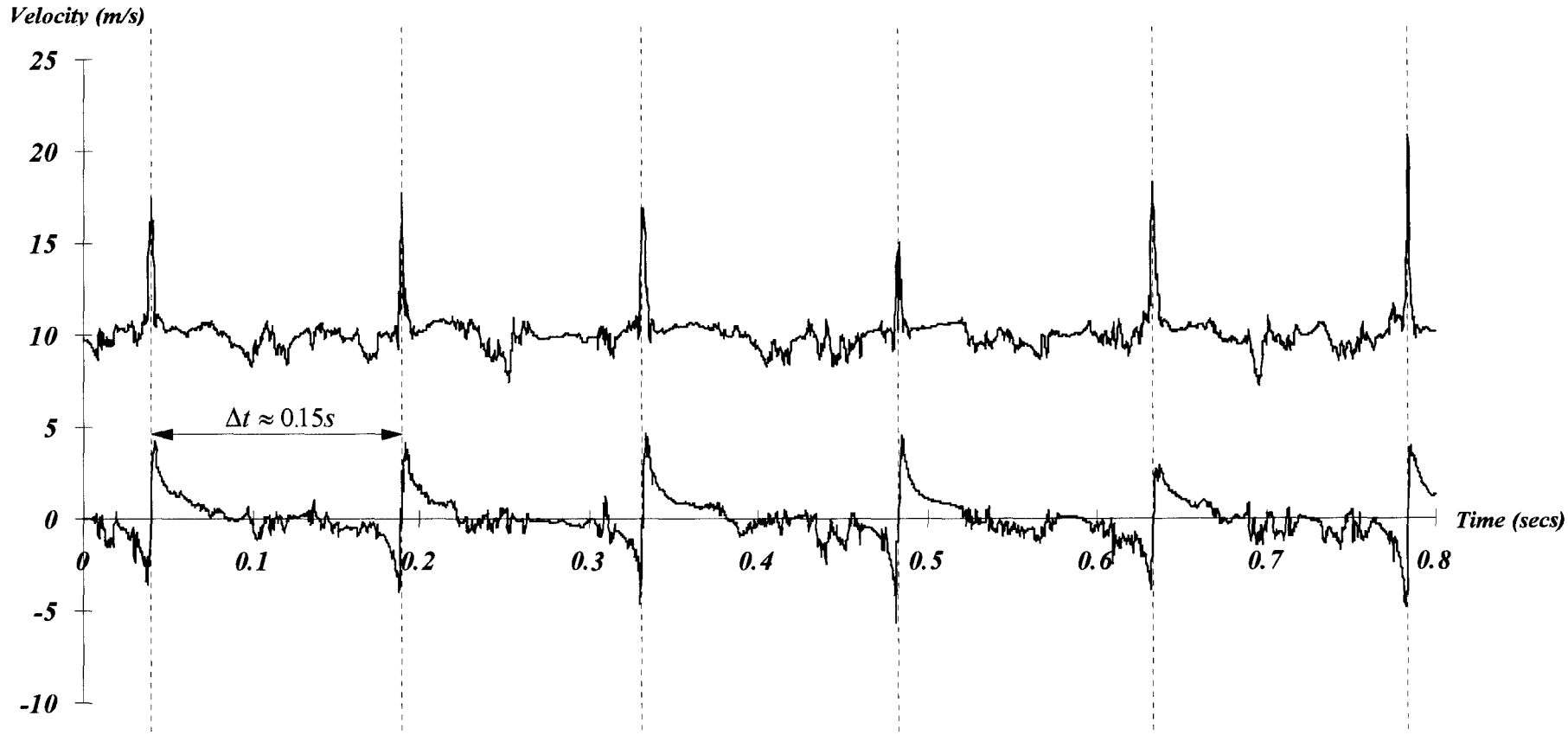

Figure R6.5- Transverse vortex test case 2 - working section velocity 10 m/s, rotational speed approximately 400rpm. Sampling frequency 5000Hz for 0.8seconds.

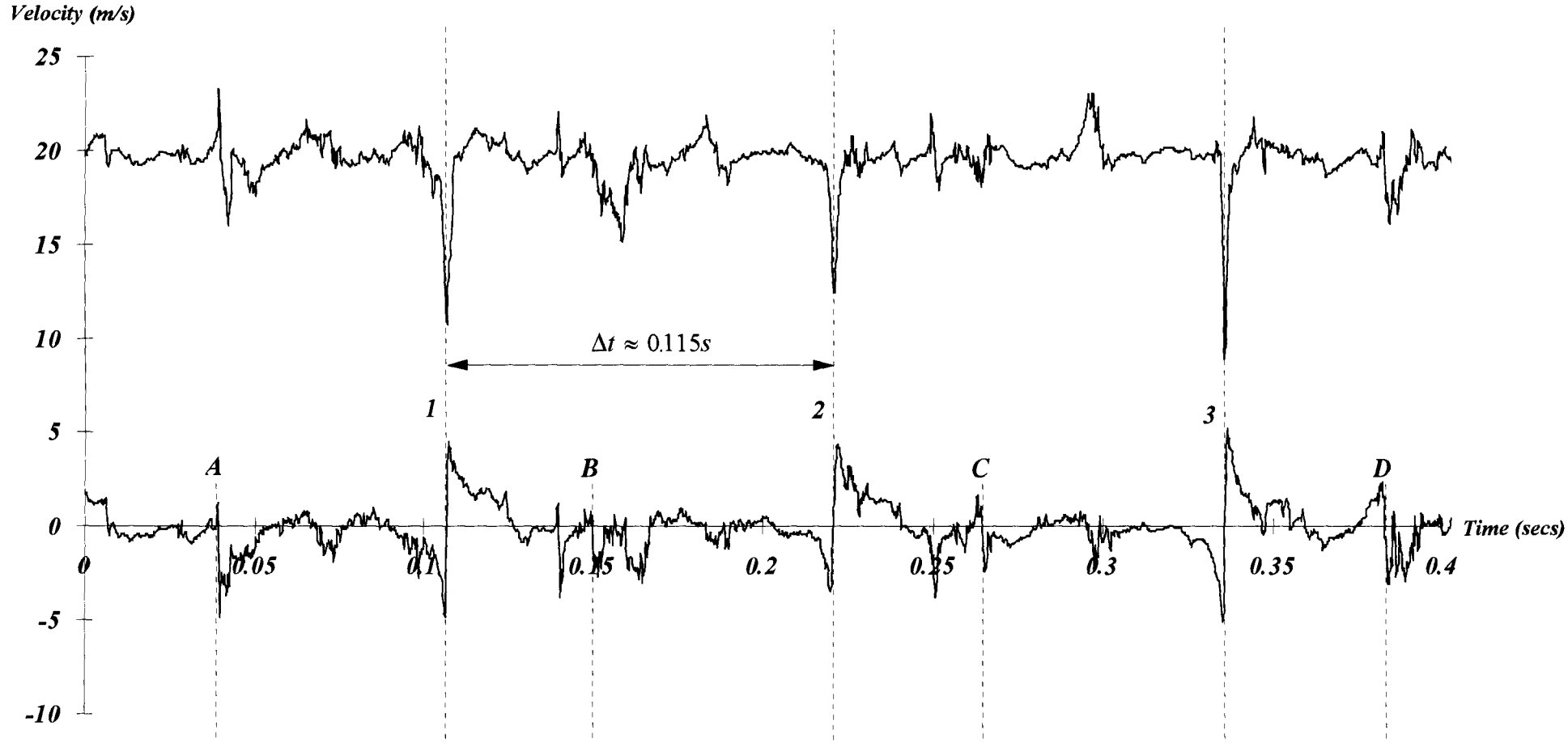

Figure R6.6- Transverse vortex test case 3 - working section velocity 20 m/s, rotational speed approximately 520rpm. Sampling frequency 5000Hz for 0.4seconds.

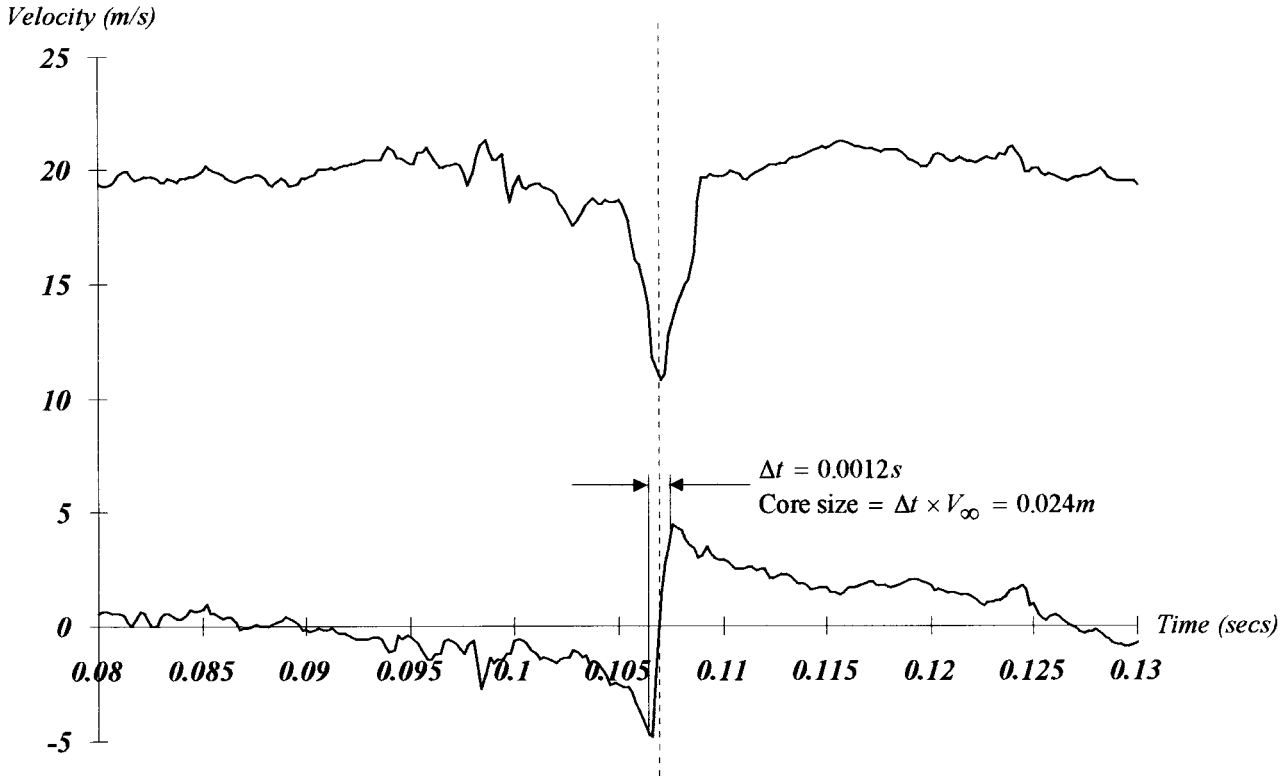

Figure R6.7- Close-up of first vortex in Fig. 6.6 illustrating peak to peak change in time (Δt) and corresponding core size.

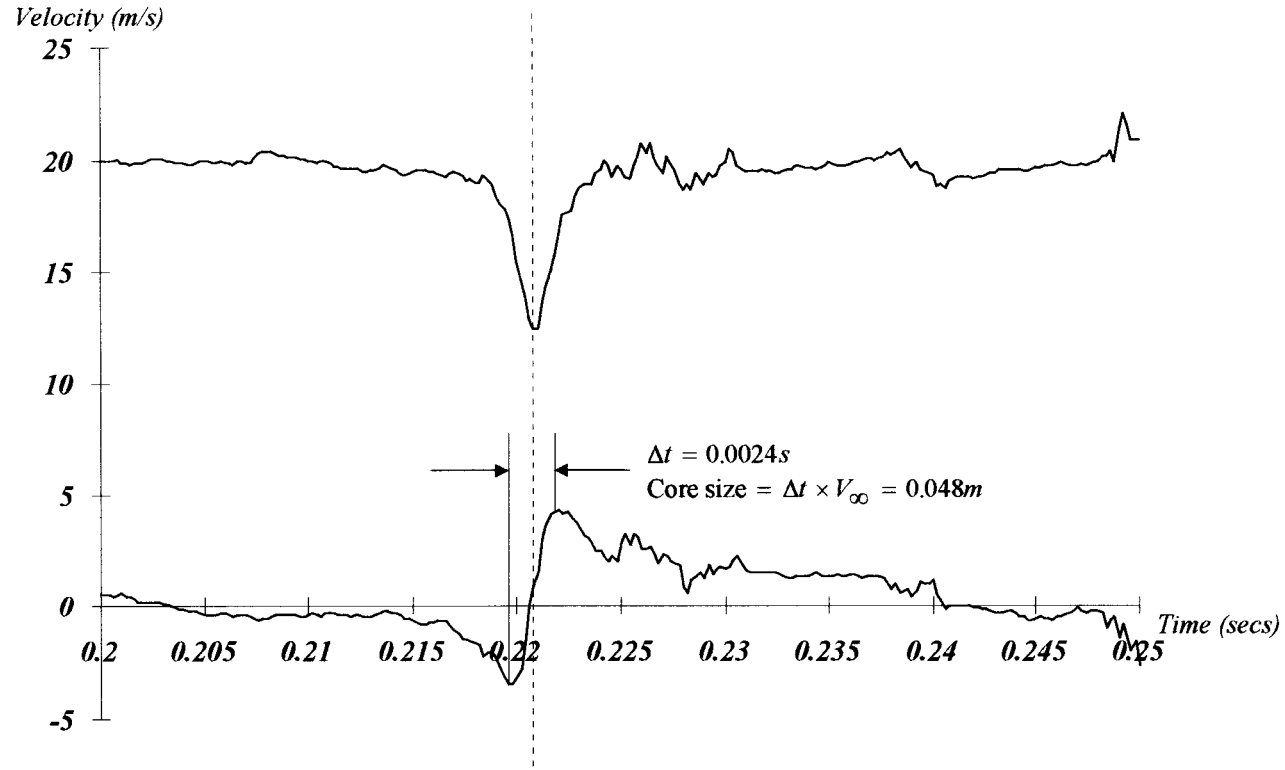

Figure R6.8- Close-up of second vortex in Fig. 6.6 illustrating peak to peak change in time (Δt) and corresponding core size.

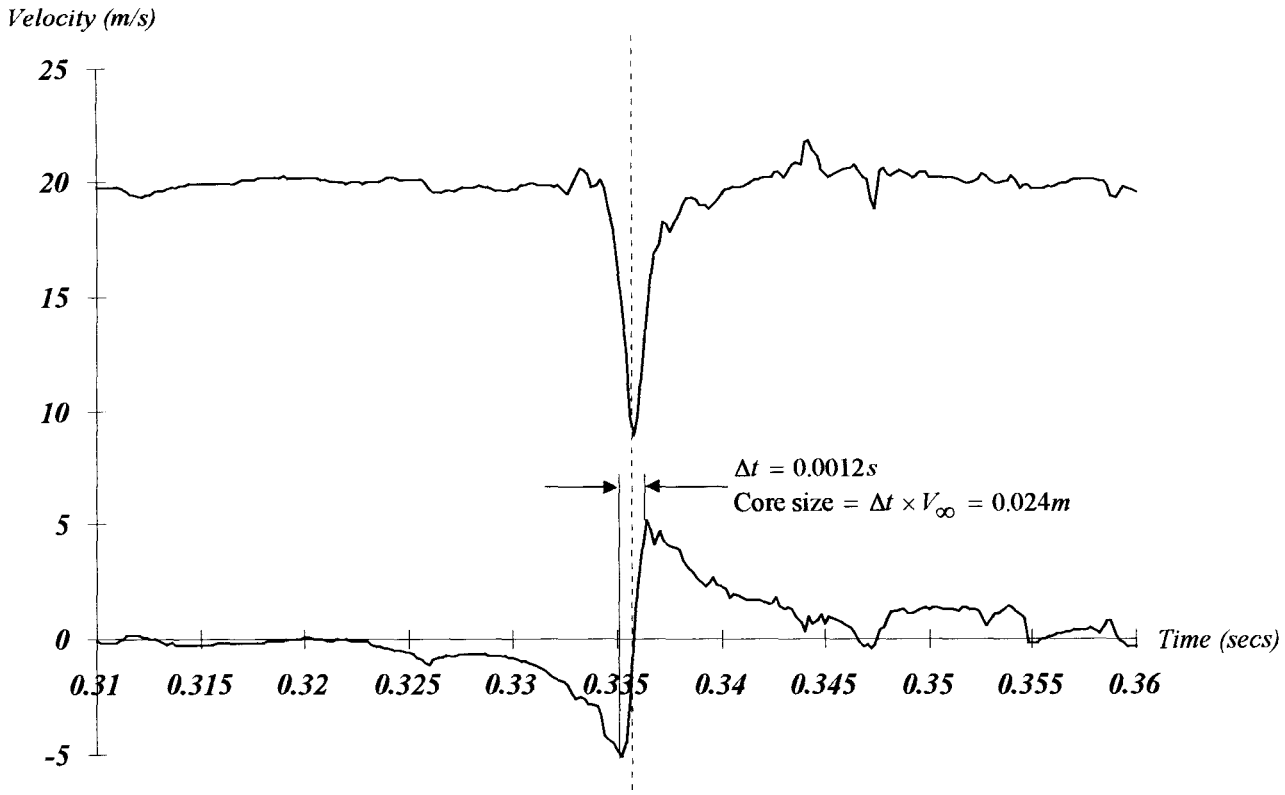

Figure R6.9- Close-up of third vortex in Fig. 6.6 illustrating peak to peak change in time (Δt) and corresponding core size.

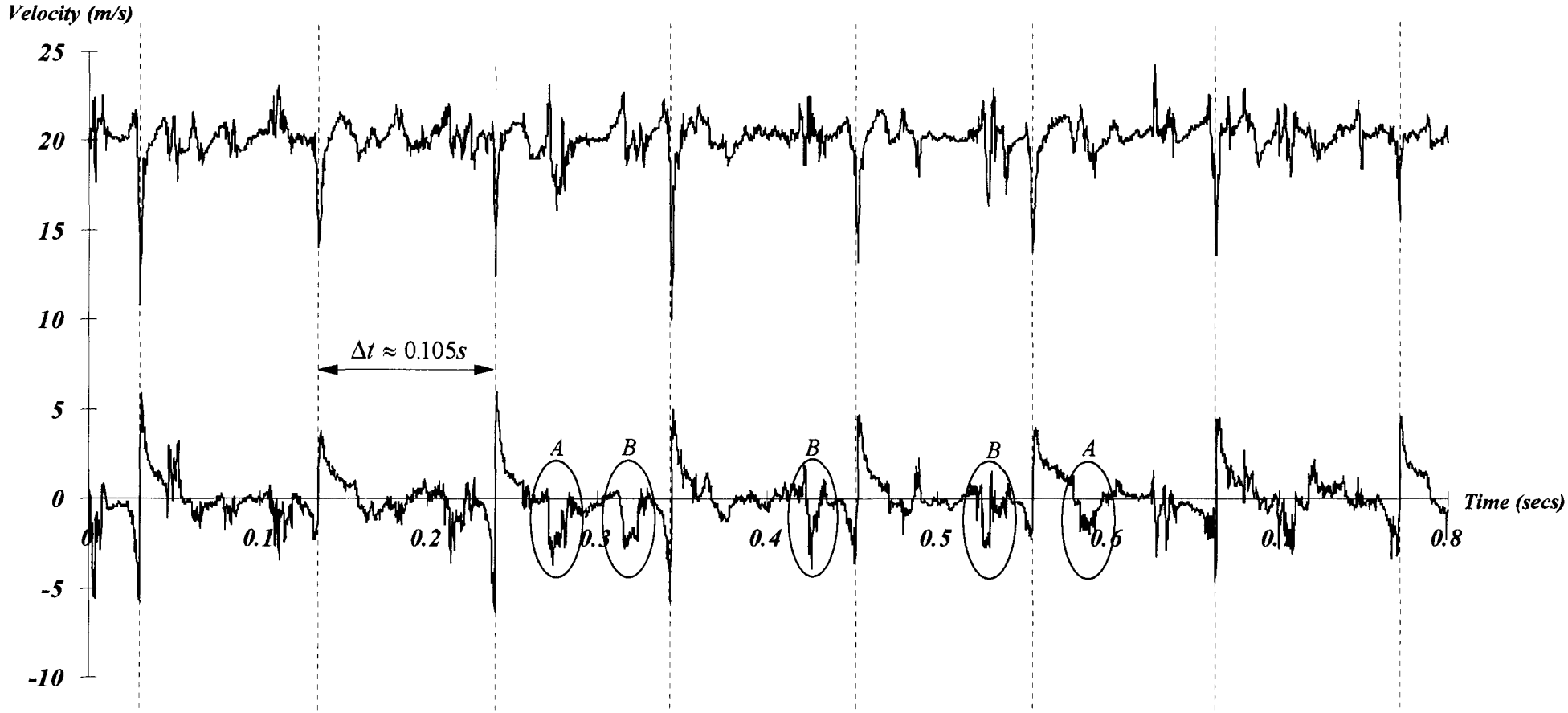

Figure R6.10- Transverse vortex test case 4 - working section velocity 20 m/s, rotational speed approximately 600rpm. Horizontal measurement location of 150mm (on the right of the centre line when looking upstream). Sampling frequency 5000Hz for 0.8seconds.

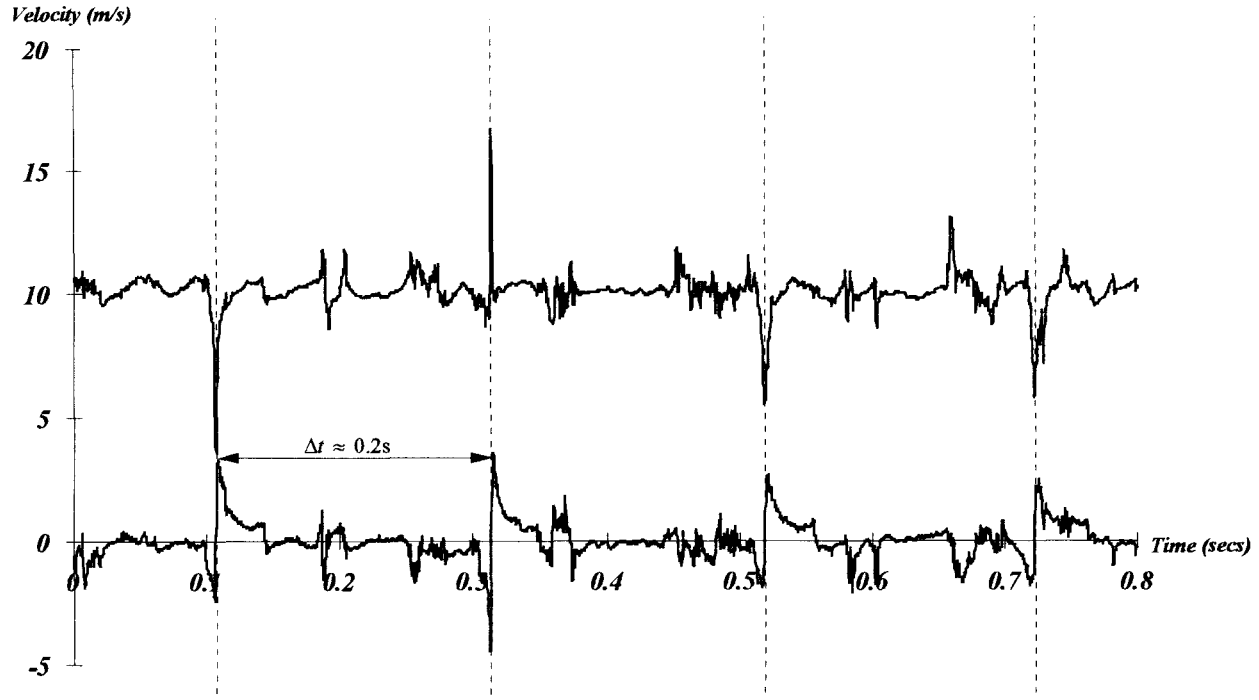

Figure R6.11- Working section velocity 10 m/s rotational speed approximately 300rpm.

Test case 6.

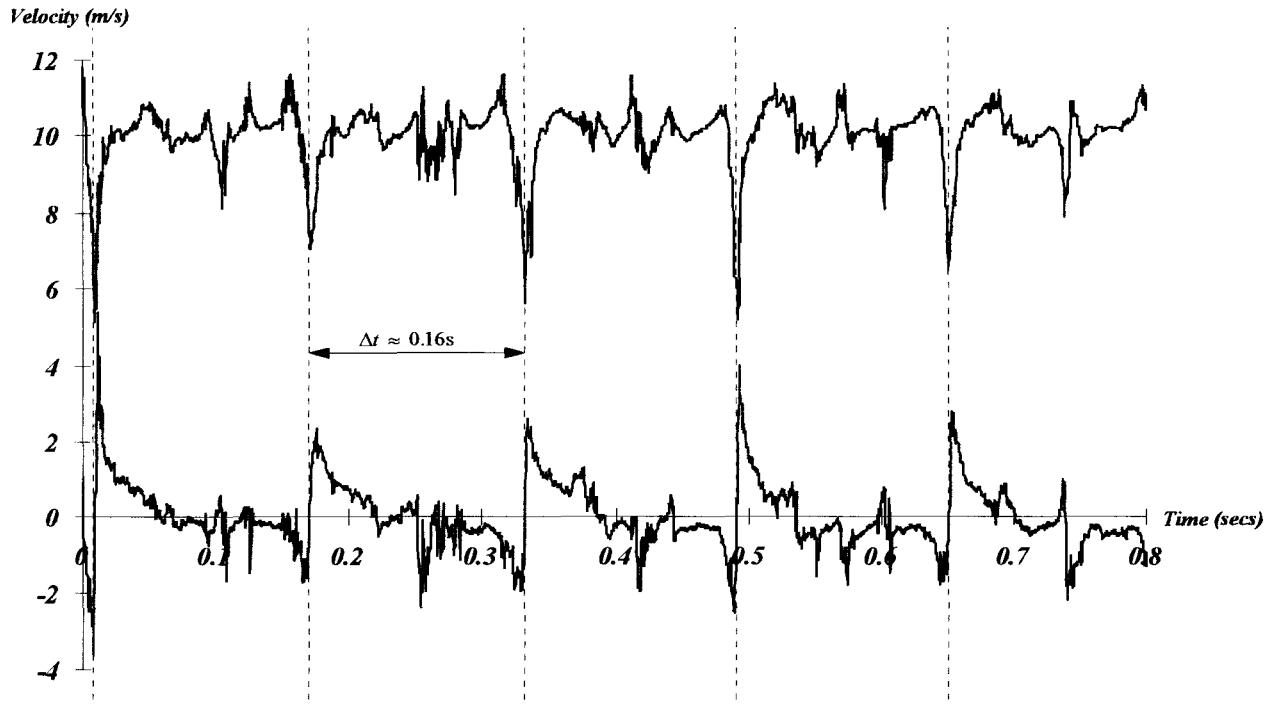

Figure R6.12- Working section velocity 10 m/s rotational speed approximately 375rpm.

Test case 7.

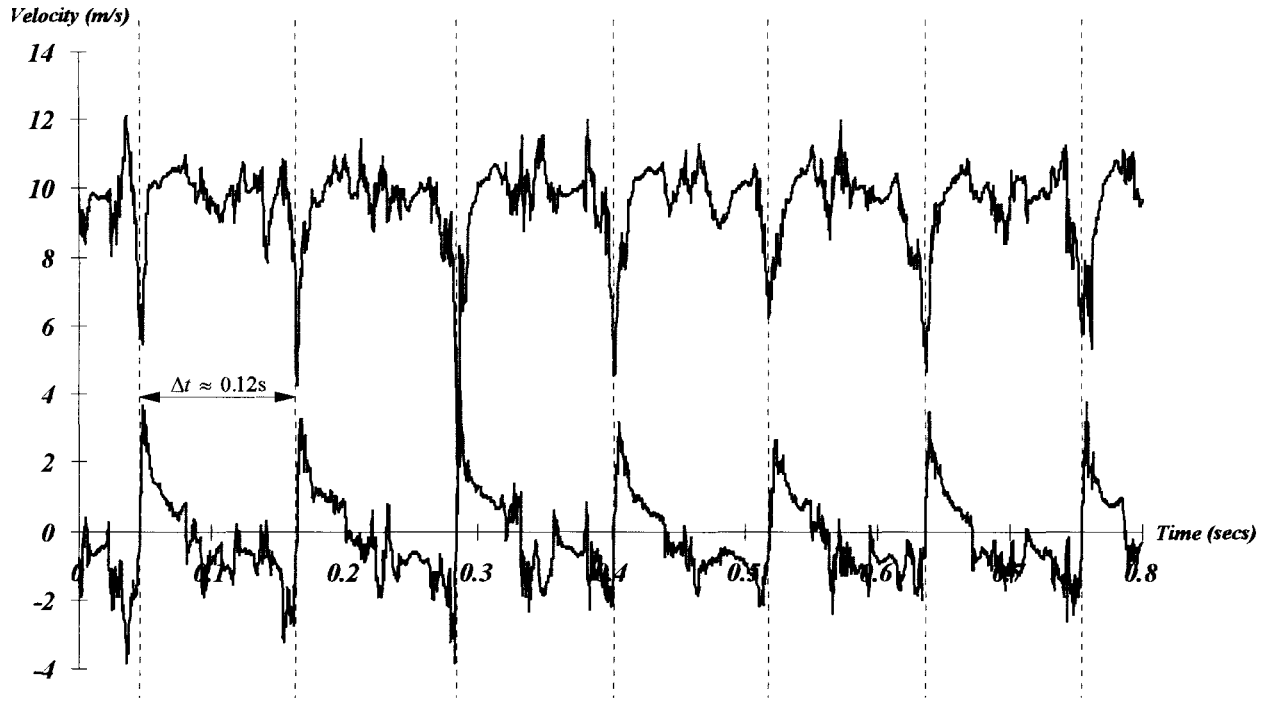

Figure R6.13- Working section velocity 10 m/s rotational speed approximately 500rpm.

Test case 8.

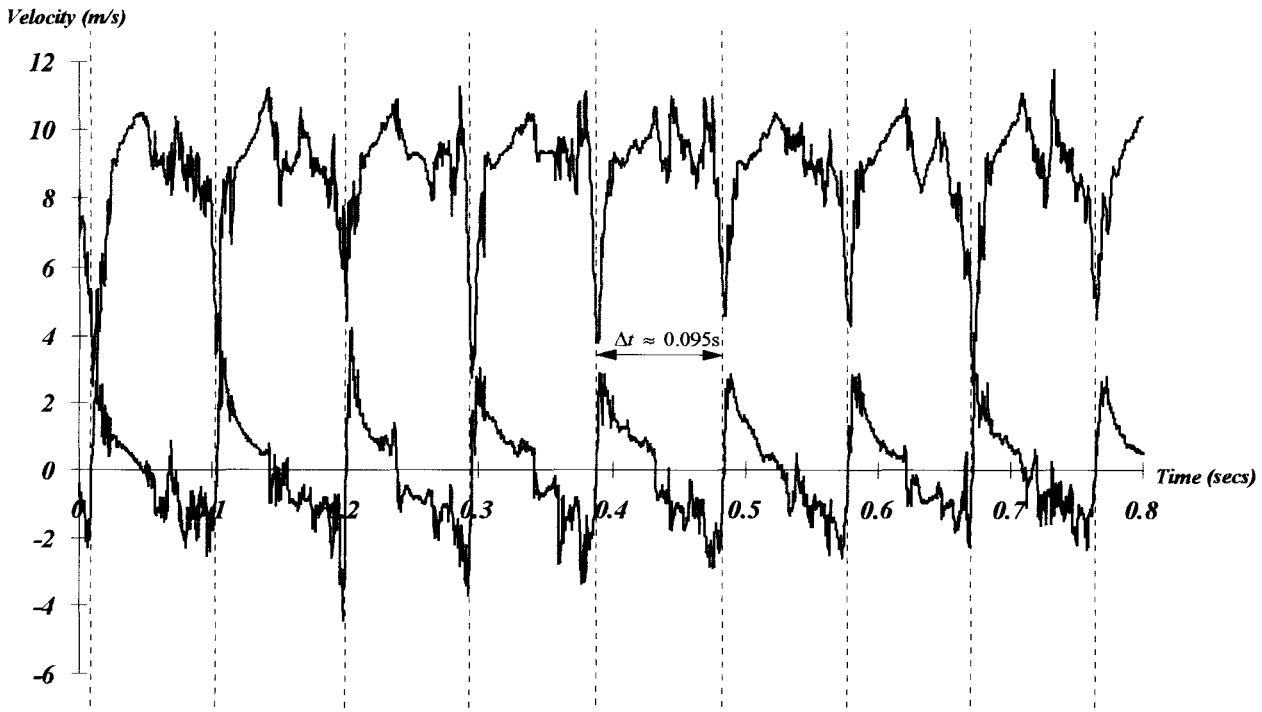

Figure R6.14- Working section velocity 10 m/s rotational speed approximately 600rpm.

Test case 9.

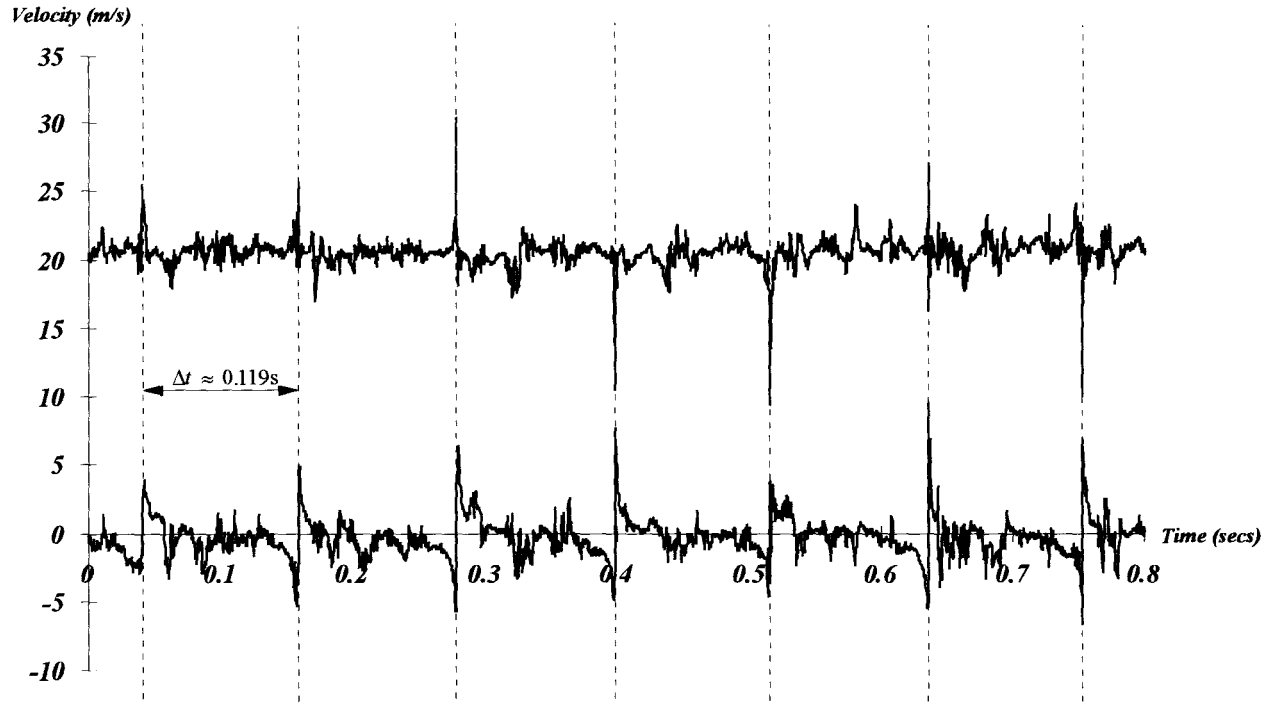

Figure R6.15- Working section velocity 20 m/s rotational speed approximately 500rpm.

Test case 24 - horizontal measurement location of -150mm.

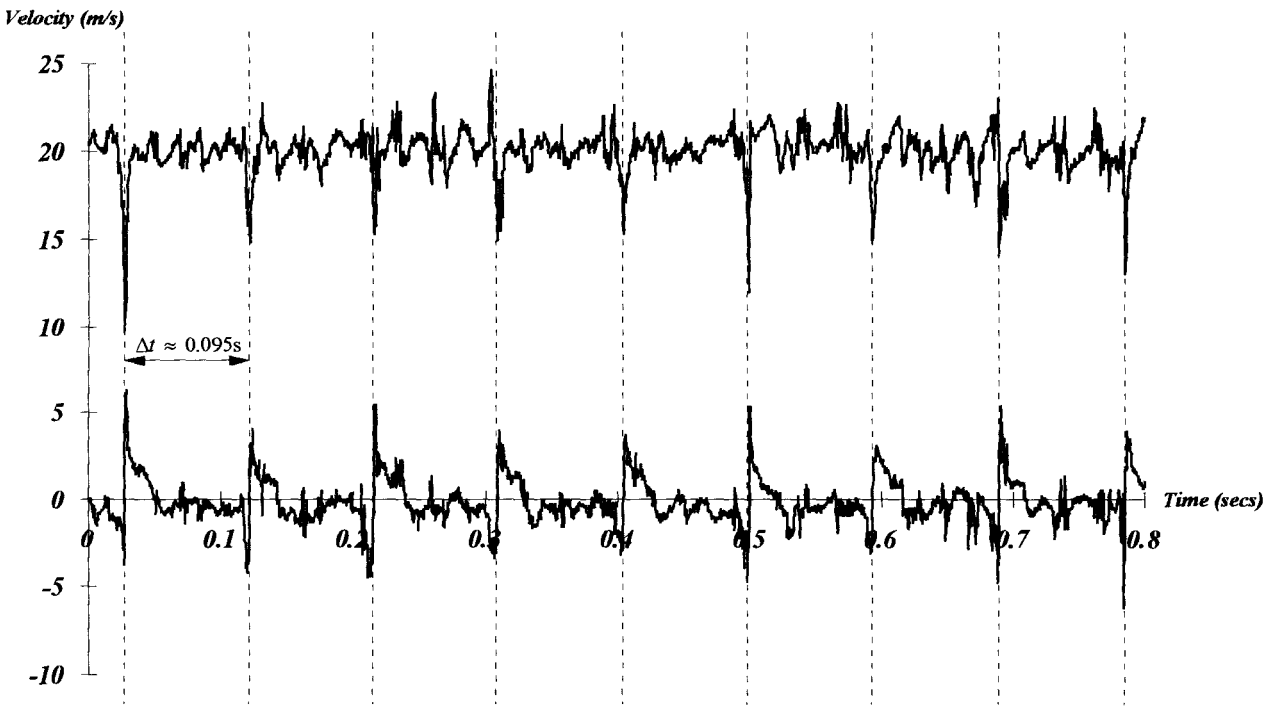

Figure R6.16- Working section velocity 20 m/s rotational speed approximately 600rpm.

Test case 19.

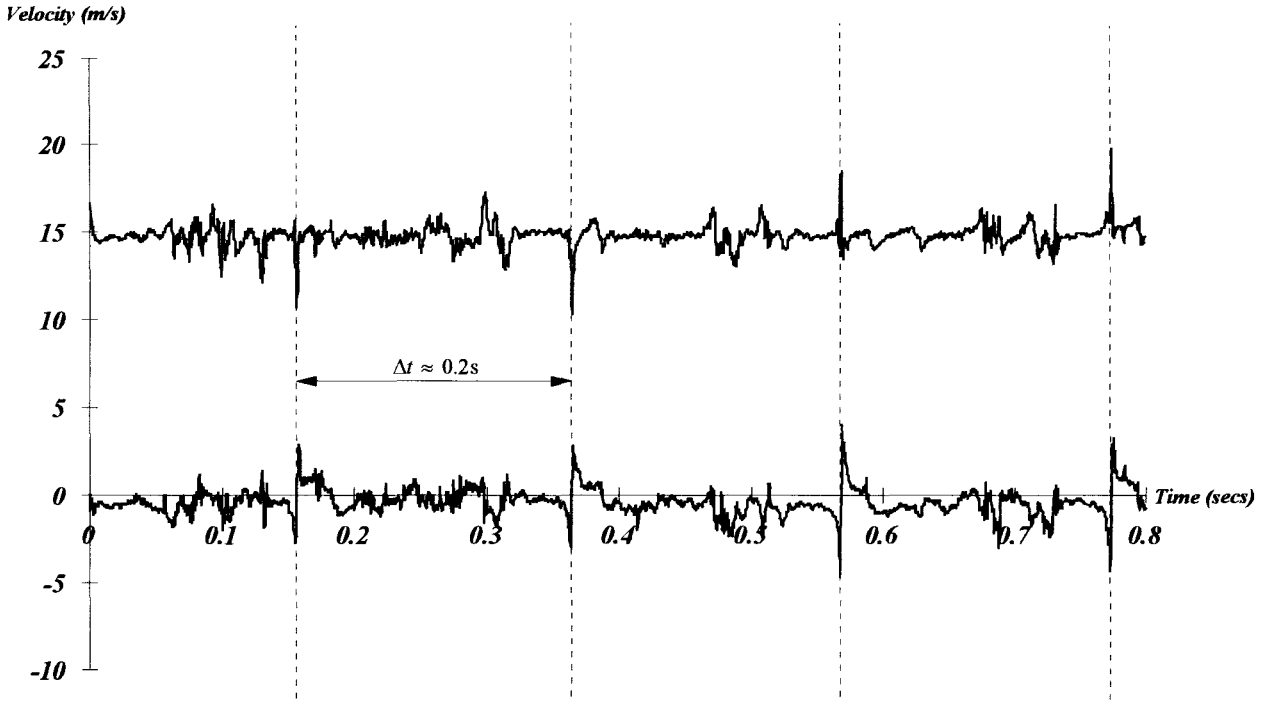

Figure R6.17- Working section velocity 15 m/s rotational speed approximately 300rpm.

Test case 26.

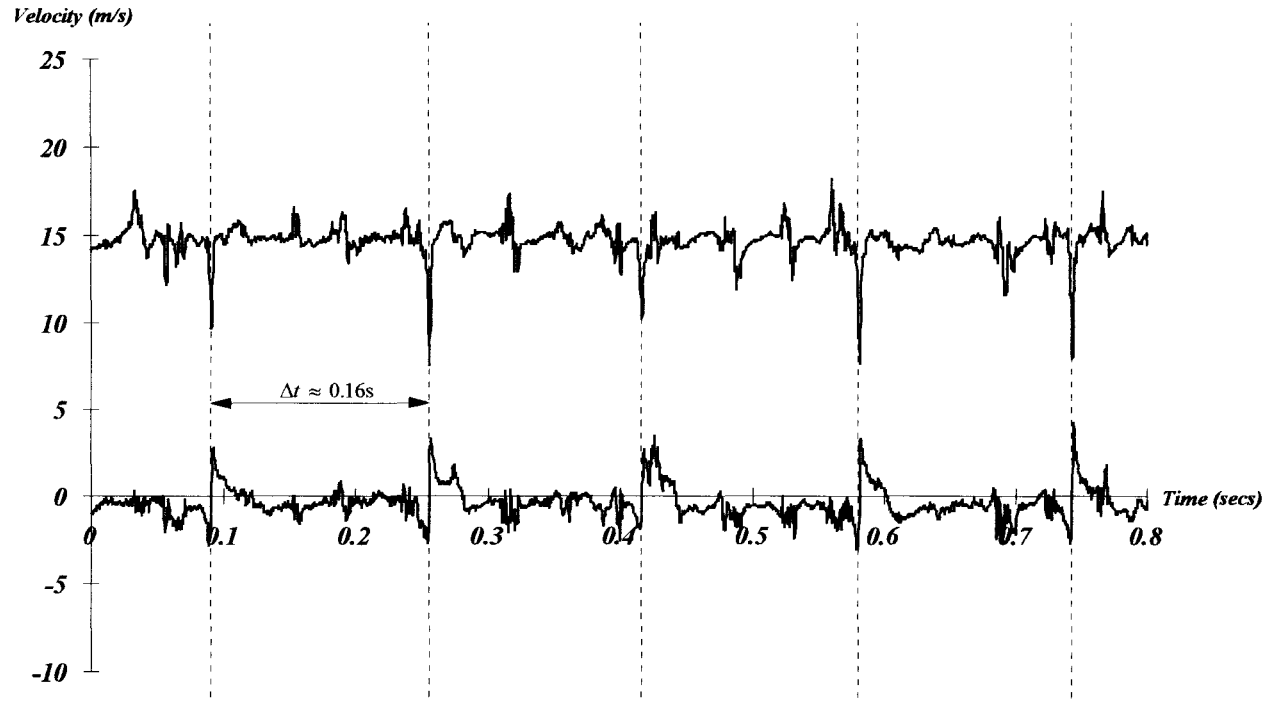

Figure R6.18- Working section velocity 15 m/s rotational speed approximately 375rpm.

Test case 27.

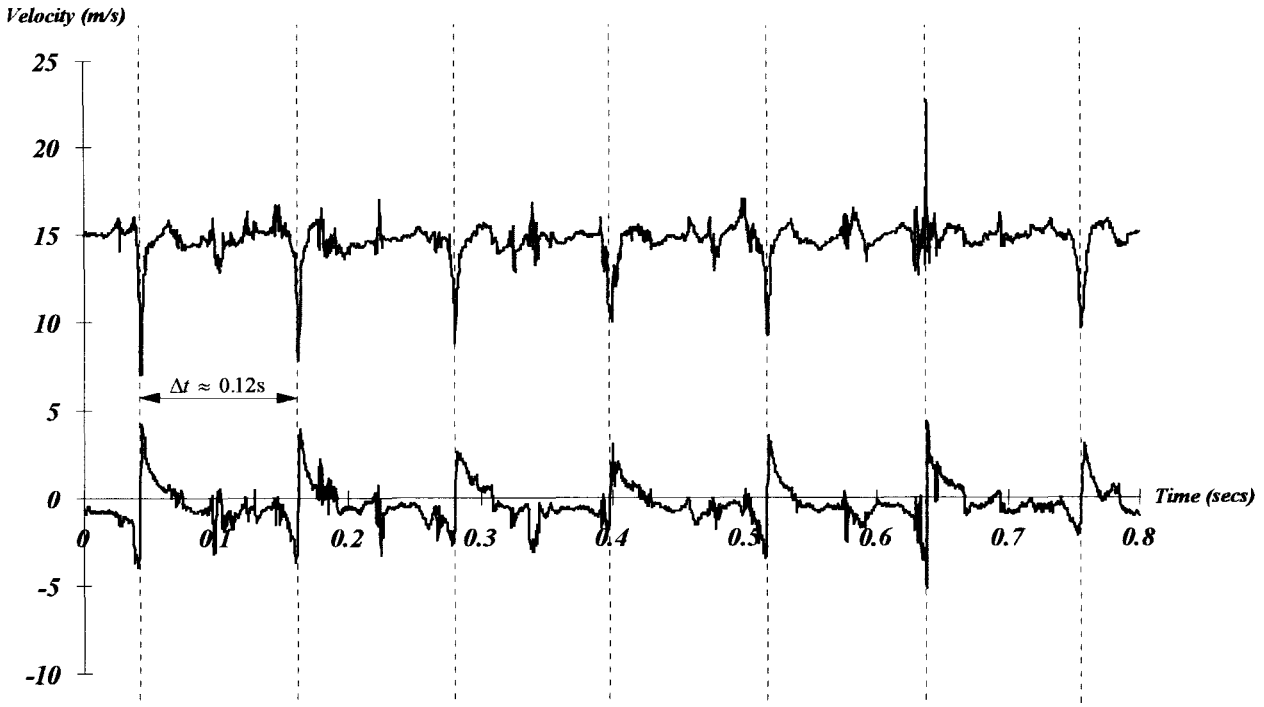

Figure R6.19- Working section velocity 15 m/s rotational speed approximately 500 rpm.

Test case 28.

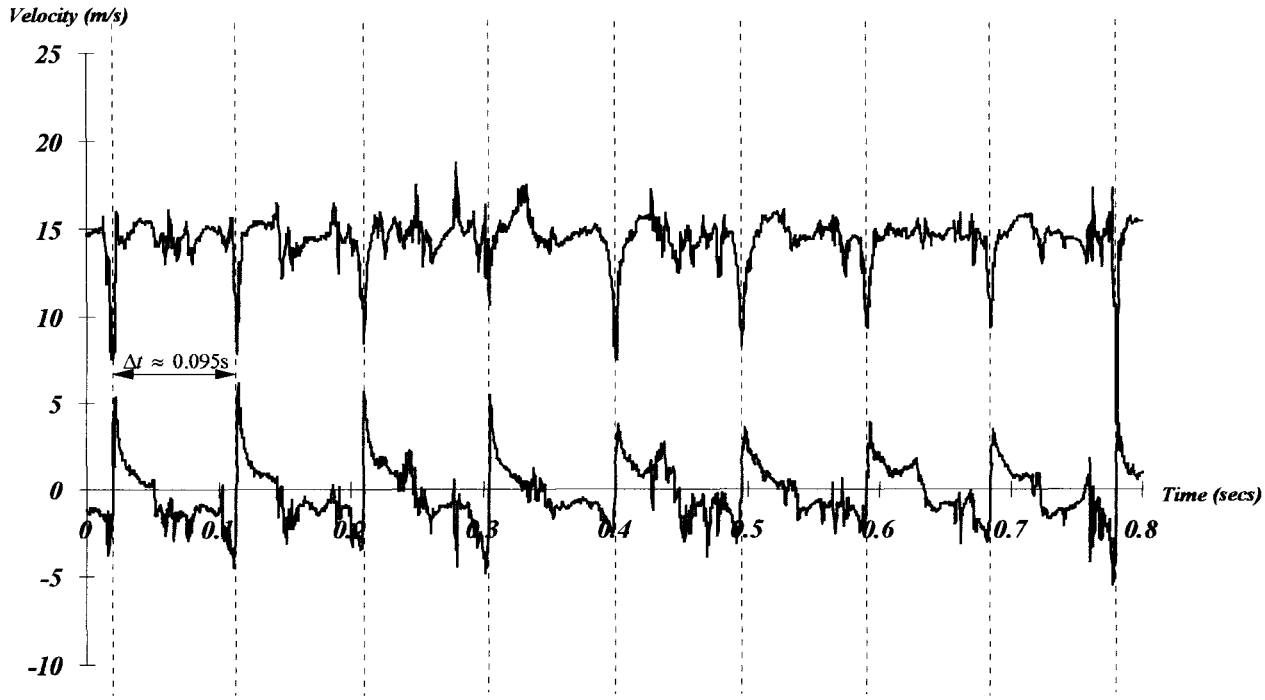

Figure R6.20- Working section velocity 15 m/s rotational speed approximately 600 rpm.

Test case 29.

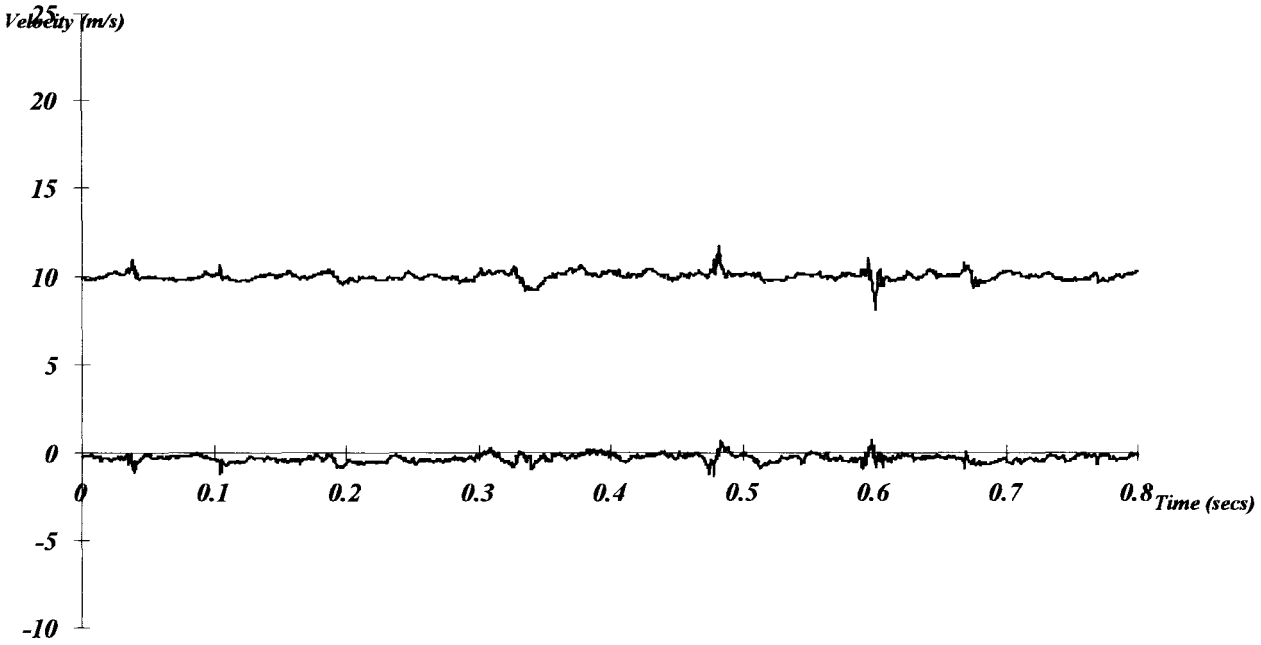

Figure R6.21- Working section velocity 10 m/s rotational speed 0 rpm.

Test case 5. Streamwise turbulence intensity approximately 2%.

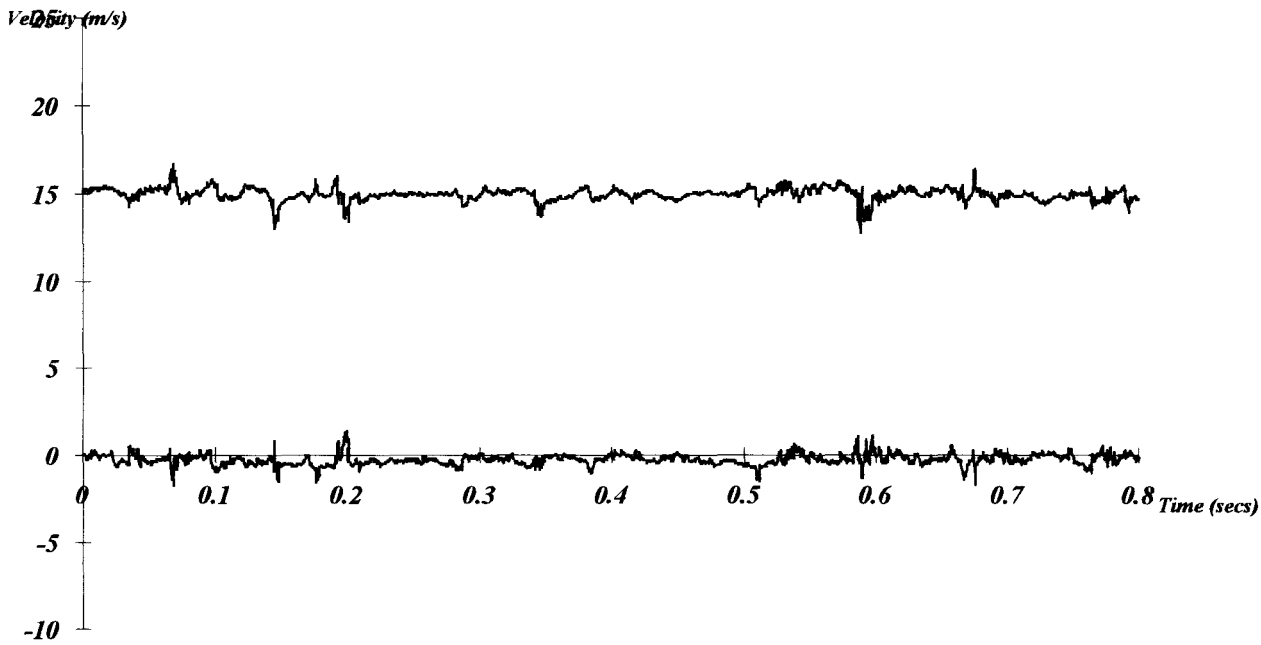

Figure R6.22- Working section velocity 15 m/s rotational speed 0 rpm.

Test case 25. Streamwise turbulence intensity approximately 2%.

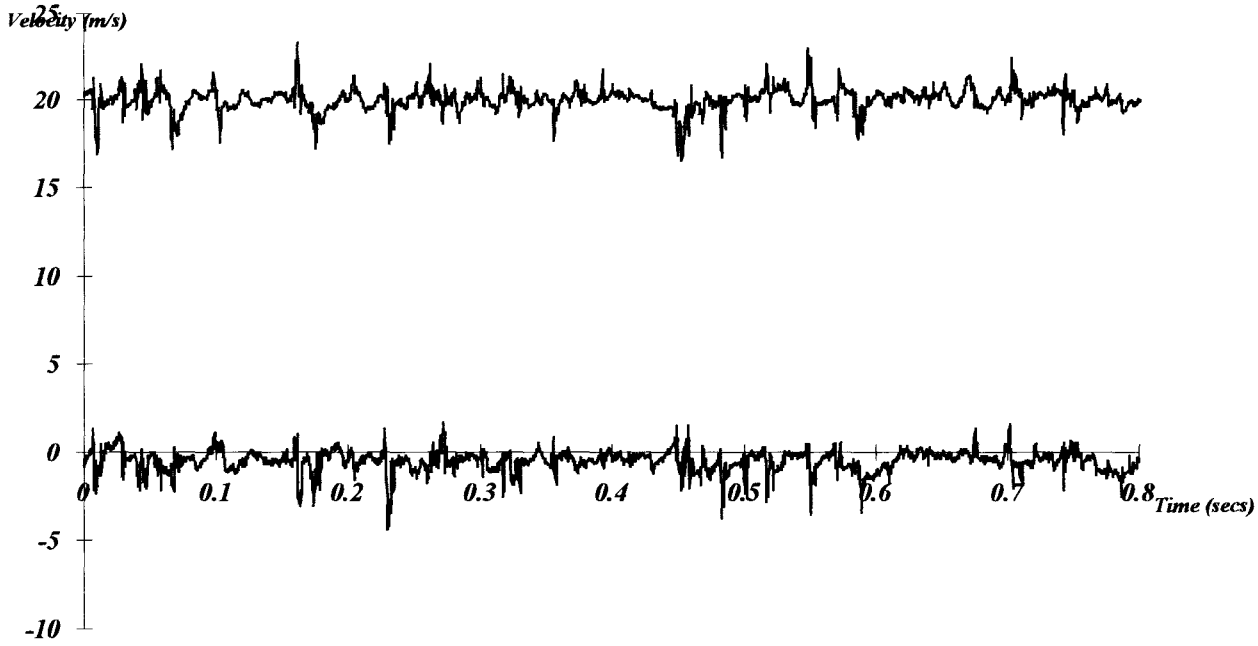

Figure R6.23- Working section velocity 20 m/s rotational speed 0 rpm.

Test case 15. Streamwise turbulence intensity approximately 4.9%.

Appendix A

Calibration and Experimental Procedures

Calibration Procedure for X-wire Probes (Chapter 4)

The procedure for the calibration of x-wire probes is detailed below. The actual use of the calibration software is adequately detailed in the IFA300 manual but the specific calculations for the determination of operating and signal conditioning parameters are not. This method was derived for the calibration facility at Glasgow University and the information is provided for future users of the system. Table 4.1 is used for the calibration of single (neglect column for sensor 2) and x-wire probes and is filled in by hand after each value is measured/calculated. The calibration procedure is,

1. Select calibration and Probe Data from the main menu.
2. Type in probe serial usually 55P61X* where * represents the x-probe being calibrated (probe numbers 1-6) and specify Wire probe as opposed to Film.
3. Insert shorting probe into probe support and measure the cable resistance for each channel (in ohms).
4. Insert x-wire probe into probe support and measure the total resistance for each channel (in ohms).
5. Determine operating resistance. Simply subtract the cable resistance from the total resistance and multiply by 1.8.
6. Specify an offset of 0 and gain of 1 for signal conditioning and select calibrate. This sets the measured voltage after signal conditioning equal to the bridge voltage.
7. In the Conditions Setup press Test. This displays the bridge voltages for the determination of each sensors maximum and minimum voltage.
8. With the calibration tunnel shut off read the minimum bridge voltages E_o for each channel.
9. With the tunnel at maximum velocity and probe sensor 1 angled at 15 degrees to the flow note E_m for sensor 1.
10. With the tunnel at maximum velocity and probe sensor 2 angled at 15 degrees to the flow note Em for sensor 2.

11. From the equations in Table 4.1 determine appropriate settings for the offset and gain.

12. Exit from Conditions Setup and re-enter Probe Data. Replace the original offsets and gains with the new calculated values.

13. In Conditions Setup press Test and note the difference between the bridge voltage and signal conditioner voltage. Make sure, with tunnel off, the minimum signal conditioner voltage for channels 1 and 2 (for x-wires) are not reading -5V. If one or both read -5V a reduced offset or gain may be required.

14. Set tunnel to maximum velocity and make sure channels 1 and 2 are not reading +5V from the signal conditioner. If so a change in the offset/gain for the appropriate channel/s may be required.

15. If signal conditioner voltages need changing return to 12 otherwise continue.

16. Set (first) calibration velocity. Supply software with calibration velocity and acquire velocity calibration point.

17. Repeat 16 until all velocity calibration points are acquired. The velocity calibration points usually range from 0 to 42 m/s with 17-25 points being acquired. Usually the velocity is changed every 1m/s up to 14 m/s then every 2m/s up to 42m/s.

18. Once all velocity calibration points are acquired set yaw calibration velocity (Usually set at the velocity at which the wind tunnel tests will be conducted).

19. Set first yaw angle by rotating probe anti-clockwise 30 degrees. Lock probe in position and acquire yaw calibration point.

20. Move probe 6 degrees clockwise and acquire next yaw calibration point.

21. Repeat 20 until all 11 yaw calibration points are acquired.

22. Pop Up screen appears stating that the calibration is complete. Press Next Screen. A table comes up depicting the velocity calibration points, bridge voltages and actual velocity set. Press Curves to show the curve fit of the

predicted effective velocities using the calculated yaw coefficients *k* for each sensor.

For the majority of velocity measurements in air it is not necessary to know the exact value of the overheat ration.. For a tungsten wire probe the overheat ratio is usually set at a recommended value of 1.8 i.e.

$$\frac{R_W}{R_a} = 1.8$$

The manufacturers of hot-wire probes usually supply the probes with values of R_{20} and α_{20} with the equation,

$$R_W = R_{20}\left[1 + \alpha_{20}\left(T_W - T_{20}\right)\right]$$

and so the temperature of the sensor can be calculated from the overheat ratio of the hot-wire resistance can be calculated for a specified hot-wire temperature. It is usual to assume $R_a = R_{20}$ and $\alpha_{20} = 0.0036/°C$ for calibration temperatures close to $20°C$.
As state by Bruun, to avoid oxidation it is essential that the wire temperature at any point along the wire element is kept well below $350°C$ to avoid oxidation. A typical value for the sensor temperature is around $250°C$.

If incorrect (high) values of cable resistance or operating resistance are set, the operating temperature may be too high. This can easily burn out the sensor.

The calculation of the offset and gains is very important but. is of particular importance when measurements are being conducted at or above the highest calibration velocities. If the specified offset and gains used in calibration are used in measurement the signal conditioner voltage could read +5V and so render any measurements useless.
The signal conditioned voltage E_s is related to the bridge voltage E_b via the relationship,

$$E_s = \left(E_b - Offset\right) \times Gain$$

The method for calculating the offsets and gains, to best use the range of the A/D converter for each wire, is documented on Table 4.1 from the measurement of the minimum and maximum bridge voltages which would be experienced in the calibration.

Experimental Procedure for Twin or Single Vortex Measurements (Chapter 5)

The procedure for the acquisition of one complete measurement grid in the cross flow plane is presented below. To acquire the in plane velocity components this procedure must be conducted twice, once with plane of the x-wires horizontal and once with the sensor plane vertical. This measures the horizontal and vertical velocity components respectively. The data acquisition record for each individual grid is presented in Table 5.1.

1. Repair/Calibrate Probe (see Chapter 4).
2. Set blade incidence and separation on vortex generators.
3. Set downstream measurement position of the traverse.
4. Place probe in tunnel and align.
5. Move probe to origin of grid to be traversed (corresponds to centre line of tunnel) and check location with respect to tunnel walls.
6. Start acquisition system.
7. Start wind tunnel and set required velocity.
8. Check probe operation by traversing probe out of influence of vortex generators and acquiring a data point. This will highlight any problems with calibration and probe alignment.
9. Traverse probe to starting grid point.
10. Take data point
11. Repeat steps 8 and 9 until all (usually 289) grid points are acquired (then switch off tunnel).
12. Analyse data to calculate the required statistical quantities for each measurement locations.
13. Build complete file of all the measurement points in the grid in ASCII format for transfer over network to Sun SPARC Station.

Probe calibration is not conducted prior to every acquisition. It is recommended that a probe should be re-calibrated once a week. After calibration, a few representative grid

points are, usually, acquired to make sure the probe and all the equipment/software are operating correctly.

Unfortunately, there is a limitation in the software when acquiring one grid. Under each filename only 99 points may be taken. So, in the case of the larger 17x17 grid, 3 file names must be used to cover one grid. This is not a problem when acquiring the data, but, afterwards the three sets of data must be combined into a single data set for analysis. Care must be taken when acquiring the measurement grid so as not to omit any points. If this occurs these relevant points must be acquired at the end to complete the grid. It is better to acquire too many points than miss one.

During acquisition the change over between the data files enables a spot check to be conducted on the probe condition. There are no warnings if a wire has broken and, so as a precautionary measure, it is advisable to conduct routine checks. If the wire breaks during acquisition, the complete grid should be re-acquired and the incomplete grid data stored to compare with the new data (with a different calibration). The comparison is usually good and the previous grid data are deleted. This minimises any errors between changing probes and re-calibration. Each grid takes approximately 2 hours and one configuration can be conducted in a day (with analysis and transfer of data). Post (graphical) analysis of one grid takes approximately one hour and is usually conducted after a series of configurations have been acquired. Only in exceptional circumstances, when problems occur during acquisition , is the data analysed immediately for one cross flow plane.

Experimental Procedure for Transverse Vortex Measurements (Chapter 6)

In this investigation, the data acquisition system can be activated either remotely or manually from the electronic trigger circuit designed to link with the BNC interface board. Remotely, the system is connected through an external trigger circuit to the rotating shaft. The optical switch activates the data acquisition when a reflective object positioned on the shaft passes in front of the sensor. This provides a trigger signal which the electronic circuit converts into a TTL High/Low pulse to activate the A/D converter in the PC (via the BNC interface board). This consistent trigger is activated when the rotating blade is pointing into the settling chamber along the centre line of the wind tunnel.

Table 6.1 shows the transverse vortex data acquisition record and the procedure for the acquisition of one measurement point, with the manual trigger, is presented below.

1. Repair/Calibrate Probe (see Chapter 4).
2. Set downstream measurement position of the traverse.
3. Place probe in tunnel and align.
4. Move probe to origin of grid to be traversed (corresponds to centre line of tunnel) and check location with respect to tunnel walls.
5. Start acquisition system.
6. Start wind tunnel and set required velocity.
7. Check probe operation by traversing probe out of influence of vortex generator and acquiring a data point. This will highlight any problems with calibration and probe alignment.
8. Traverse probe to measurement location.
9. Set rotational speed of transverse vortex generator.
10. Take data point by pressing the Acquire button in the Acquisition - Conditions Setup screen.
11. Repeat steps 8 to 10 until all test configurations have been conducted (then switch off rotating blade control and tunnel).
12. Analyse data to calculate the required time histories.

13. Transfer time series files, in ASCII format, over network to Sun SPARC Station.

If external triggering is being conducted, step ten is slightly altered. In the Acquisition-Conditions Setup screen the Trigger Source should be set to Ext (as opposed to Int). When this is done the Manual Trigger button changes and reads [Arm] and below the Trigger Source switch another toggle switch appears which allows the user to select single event triggering or continuous triggering.

With single event triggering (which should be used in an investigation into wake curvature),

1) Select the [Single] position.
2) Press the manual Trig Reset button on the trigger box (which connects to the BNC interface board).
3) Click on the [Arm] button with the mouse. This writes the header of the raw data file to the disk. The A/D board is now waiting for the external trigger to start the data acquisition.
4) Activate Trigger on the BNC interface board. This is either done with the external manual trigger or with the reflective opto sensor on the rotating shaft.
5) To acquire another file repeat steps 2-4
6) Analyse data but remember to select the [Text] option. This produces a file with a *.W* extension which contains the velocity time history. This file can be exported to spreadsheet (Excel) and graphics (PV-WAVE) programs for analysis.

With continuous triggering (for acquisition of a larger amount of files),

1) Select the [Cont]inuous position.
2) Click on the [Arm] button with the mouse. A series of raw data files will be acquired and the file number will increment.
3) To stop acquiring click on the [Arm] button again and a pop-up message will appear stating that "Automatic Trigger and Acquire Stopped".

4) Analyse data but remember to select the [Text] option. This produces a file with a *.W* extension which contains the velocity time history. This file can be exported to spreadsheet (Excel) and graphics (PV-WAVE) programs for analysis.

The continuous mode is misleading. When conducting external manual triggering with the continuous mode the software does not wait for another trigger pulse before acquiring data. It seems to acquire a series of files without any reference signal. This, unfortunately, means that only the single event triggering mode can be used to acquire the files required for phase locked averaging which will increase acquisition time for the large number of files required (Bruun states that usually 100-300 files are used for averaging).

Appendix B

Illustrations and Technical Drawings of the Twin Vortex Generators

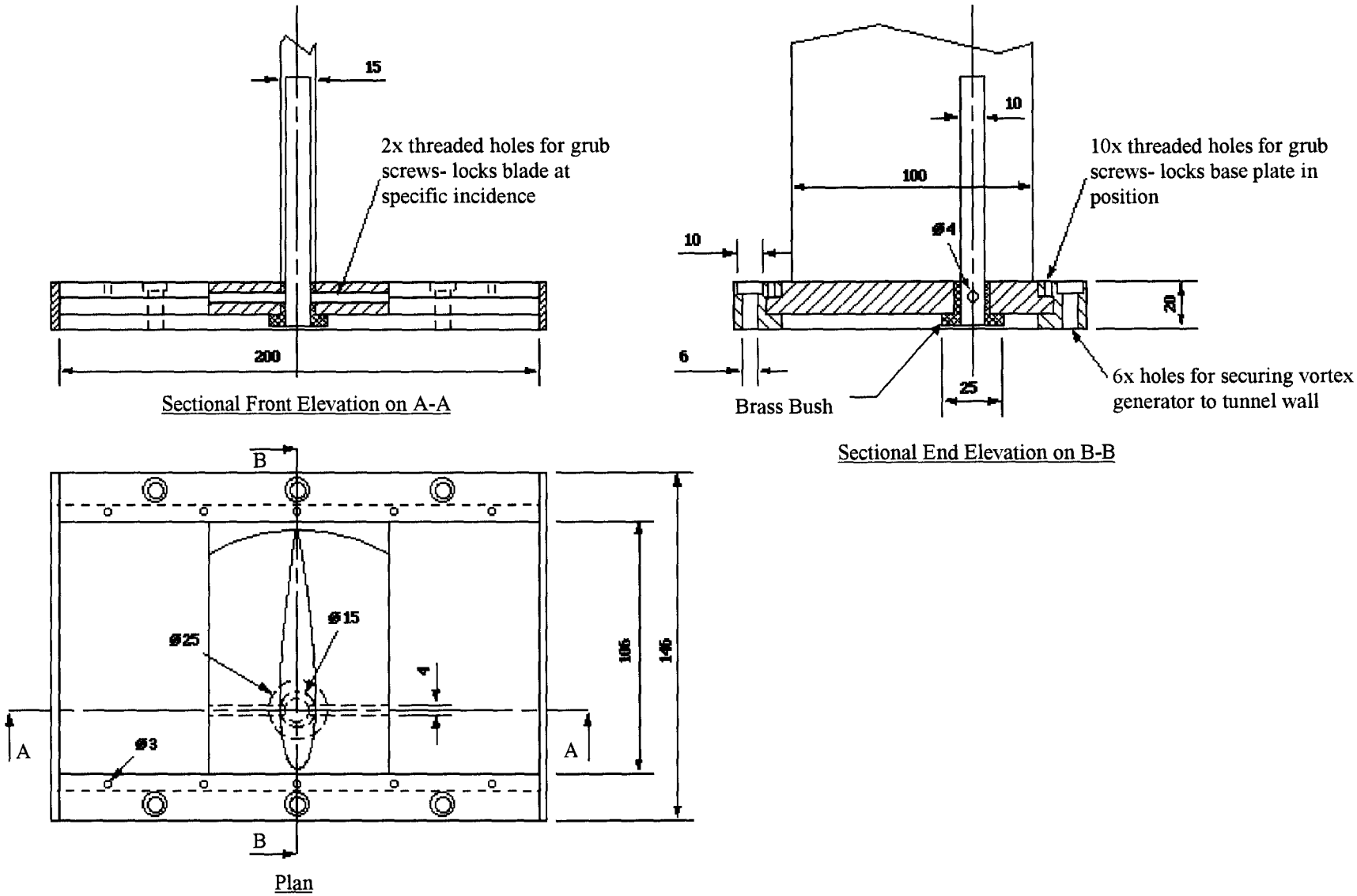

Figure B.1- Technical drawing of twin vortex generator for the 1.15m x 0.8m low speed wind tunnel.

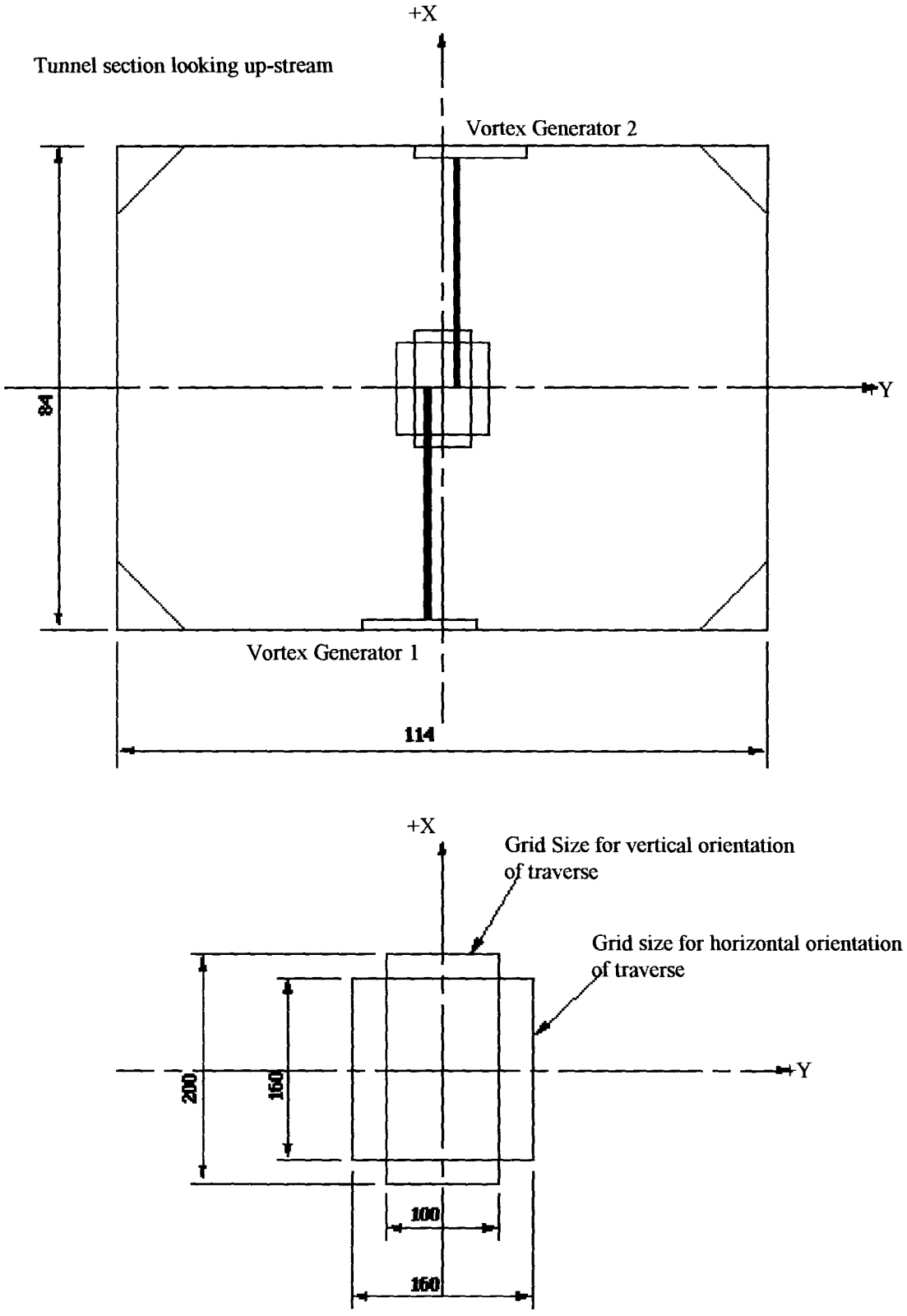

Figure B.2- Illustration of twin vortex generators and measurement grid/co-ordinate system for the 1.15m x 0.8m wind tunnel.

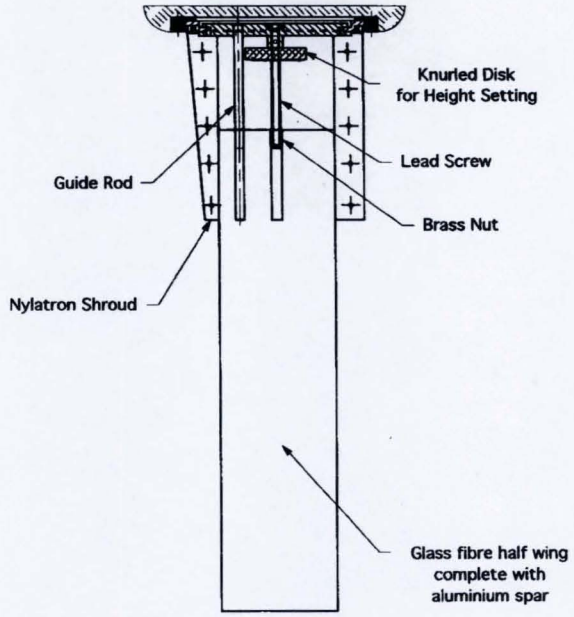

Figure B.3- Technical illustration of 2.1m x 1.6m twin vortex generator.

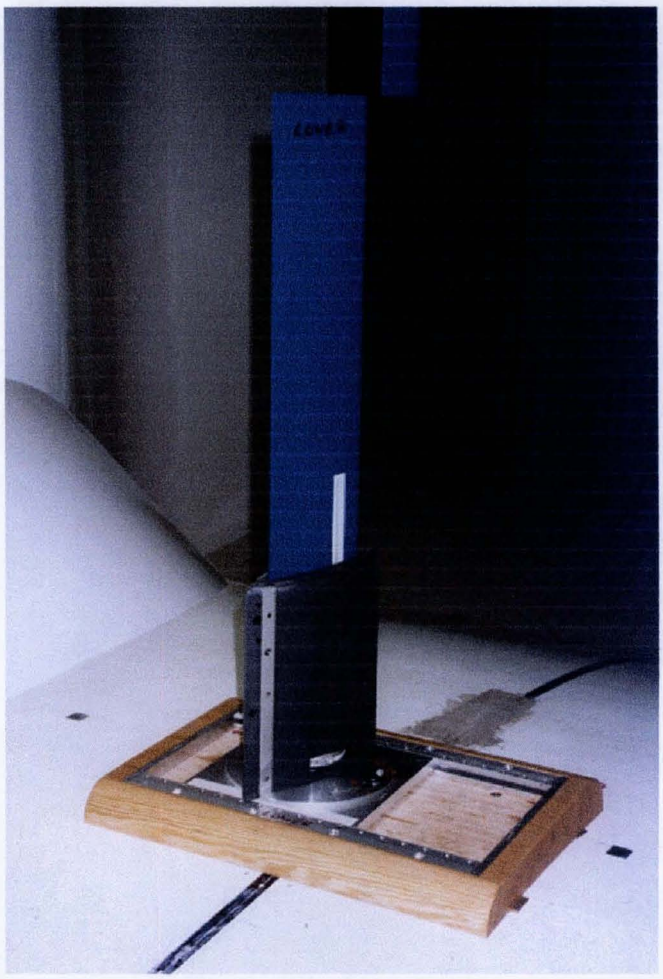

Figure B.4- Photograph of the 2.1m x 1.6m lower vortex generator.

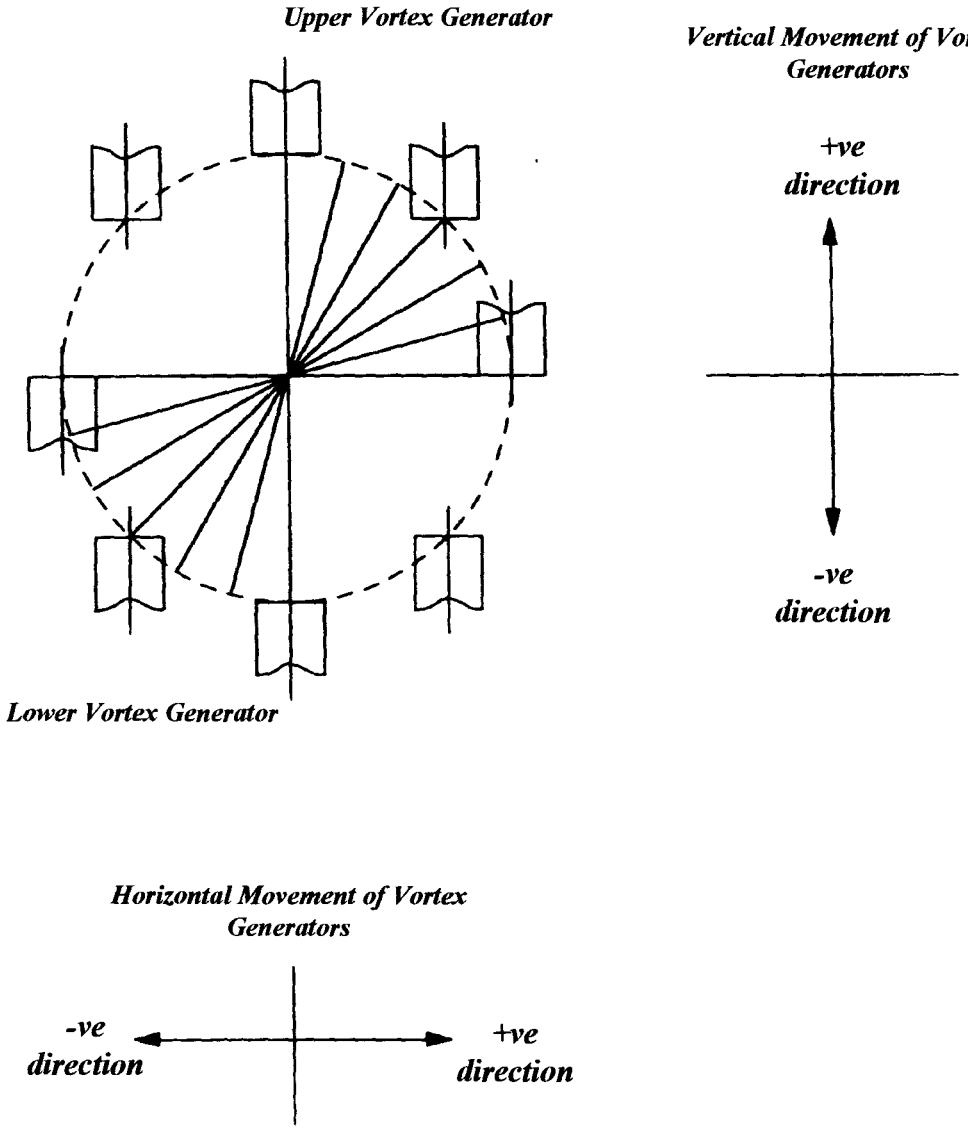

Figure B.5- Illustration of the movement of the 2.1m x 1.6m twin vortex generators looking upstream.

Appendix C

Calculation of Streamwise Vorticity

Vorticity resulting from wing lift is generally considered to be the most important quantity responsible for wake characteristics. Wake vorticity is frequently described by the streamwise component of the vorticity vector which can be expressed as

$$\omega_z = \frac{\partial v}{\partial x} - \frac{\partial u}{\partial y}$$

where u and v are the cross-flow components of the velocity vector and x,y define the Cartesian co-ordinates (with x horizontal and y vertical). This is different to the measurement grid co-ordinate system of the surveyed plane, where x_G is the vertical axis and y_G the horizontal. The above equation can, therefore, be transformed into the grid co-ordinate system and expressed as,

$$\omega_z = \frac{\partial u_G}{\partial y_G} - \frac{\partial v_G}{\partial x_G}$$

The streamwise vorticity component as expressed above was calculated, using a simple finite difference representation, at the centre of four (measured) corner points as depicted below.

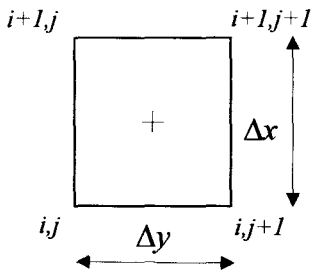

Here, i,j =1,....,17 and represent the appropriate grid points in the 17 x 17 grid starting from the bottom left of the measurement grid when looking upstream and Δy=Δx=0.01m.

An estimate of the change in the vertical velocity , u, with respect to a change in horizontal position ,y, can be determined from,

$$\left[\frac{\Delta u}{\Delta y}\right]_i = \frac{u_{i,j+1} - u_{i,j}}{\Delta y}$$

for the vertical measurement position i.

Similarly, at the vertical location $i+1$, another estimate for the change in vertical velocity with respect to a change in horizontal position can be determined from

$$\left[\frac{\Delta u}{\Delta y}\right]_{i+1} = \frac{u_{i+1,j+1} - u_{i+1,j}}{\Delta y}$$

The final value of $\partial u_G / \partial y_G$ at the centre point of the four measured values of u is simply the average of the two above estimates which can be expressed as,

$$\frac{\partial u_G}{\partial y_G} = \frac{1}{2}\left(\left[\frac{\Delta u}{\Delta y}\right]_i + \left[\frac{\Delta u}{\Delta y}\right]_{i+1}\right)$$

The same procedure is used to calculate the change in horizontal velocity, v, with respect to a change in vertical position, x, via,

$$\left[\frac{\Delta v}{\Delta x}\right]_j = \frac{v_{i+1,j} - v_{i,j}}{\Delta x}$$

$$\left[\frac{\Delta v}{\Delta x}\right]_{j+1} = \frac{v_{i+1,j+1} - v_{i,j+1}}{\Delta x}$$

$$\frac{\partial u_G}{\partial y_G} = \frac{1}{2}\left(\left[\frac{\Delta v}{\Delta x}\right]_j + \left[\frac{\Delta v}{\Delta x}\right]_{j+1}\right)$$

All the vorticity plots depicted in this thesis, for both the experimental and the numerical model data, use the above method and, so, a direct comparison can be made between these two sets of data. This provides additional verification of the vortex parameters which were determined with comparison of the velocity data.

Appendix D

Technical Drawings of Transverse Vortex Generator

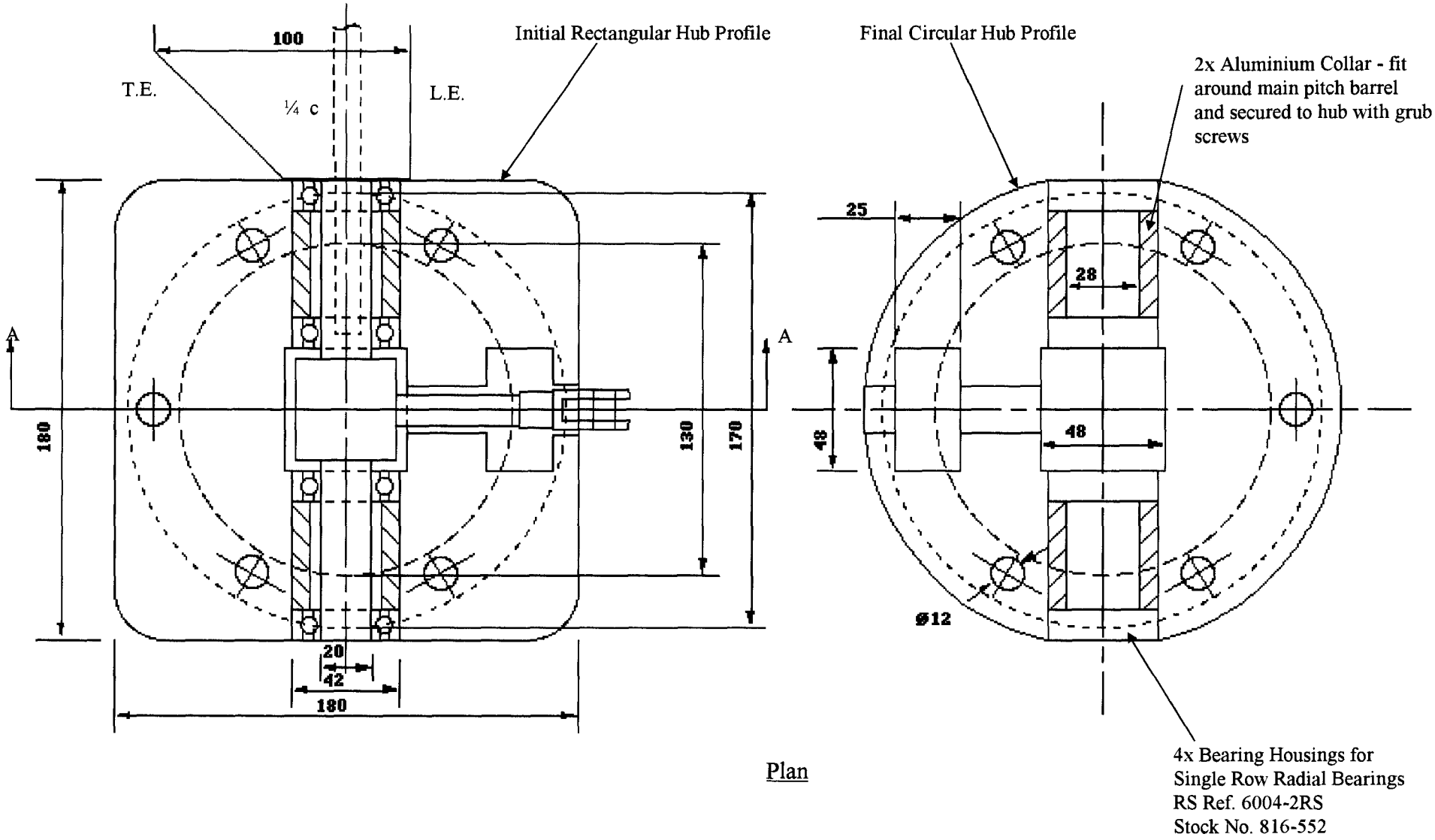

Figure D.1- Technical drawing of hub internal arrangement.

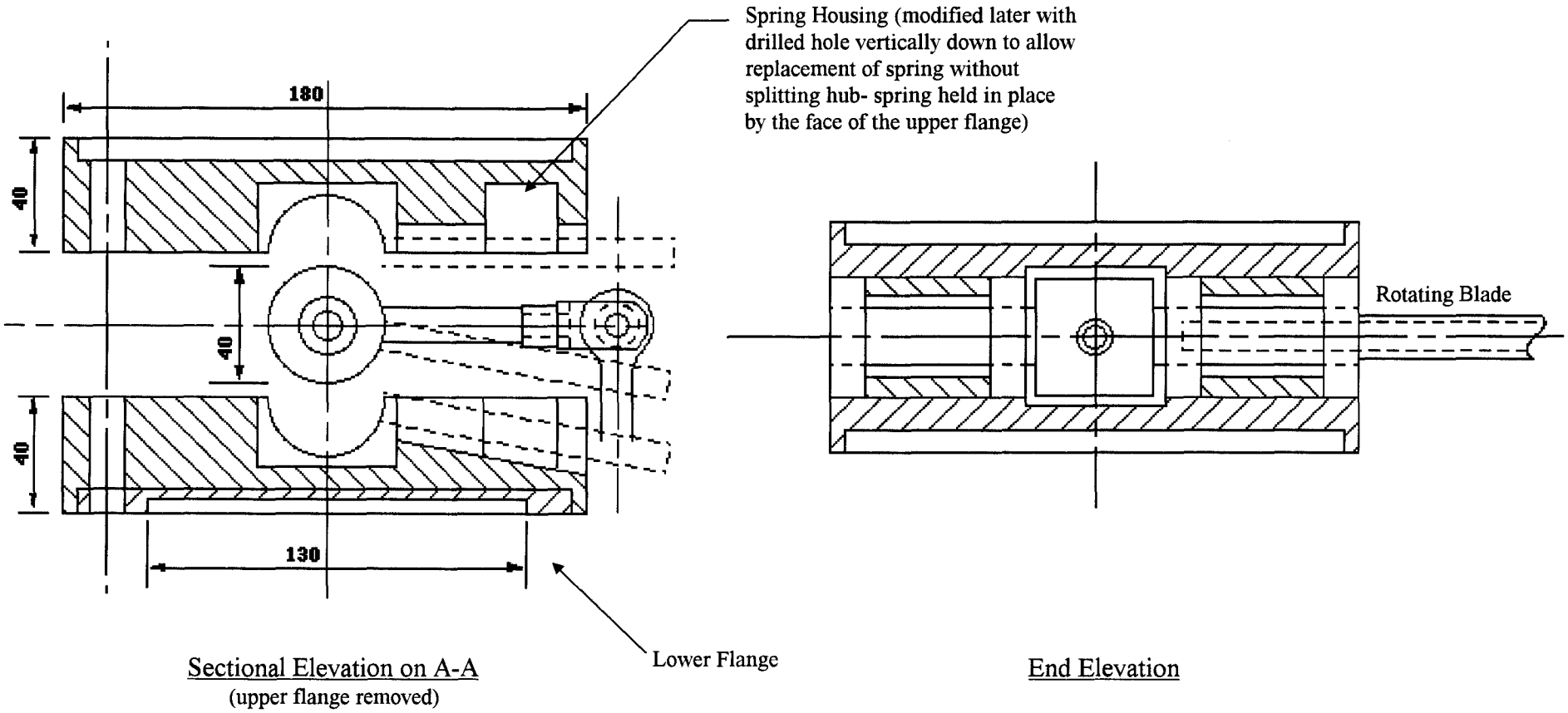

Figure D.1- Technical drawing of hub internal arrangement (continued).

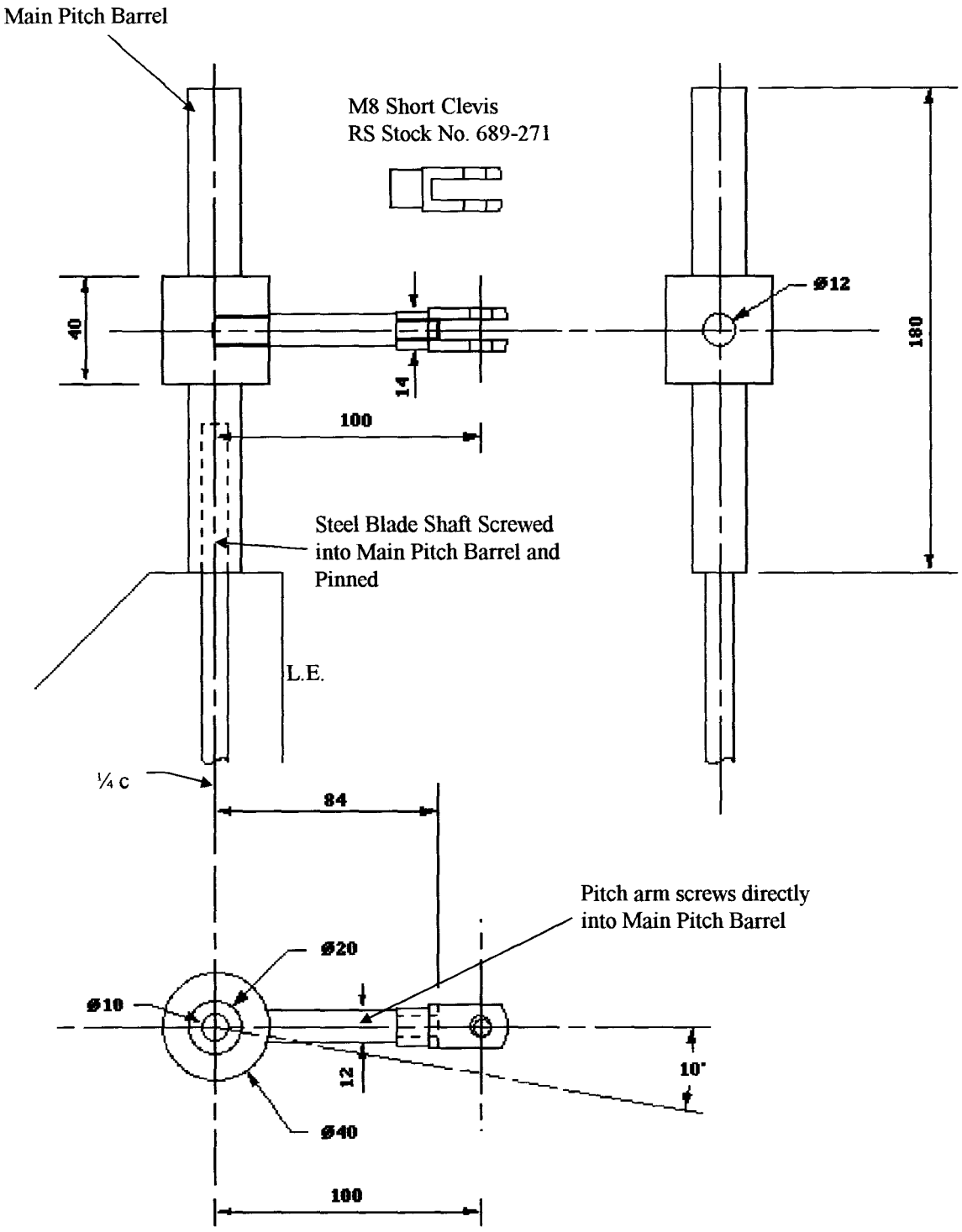

Figure D.2- Technical Drawing of pitch barrel and pitch arm.

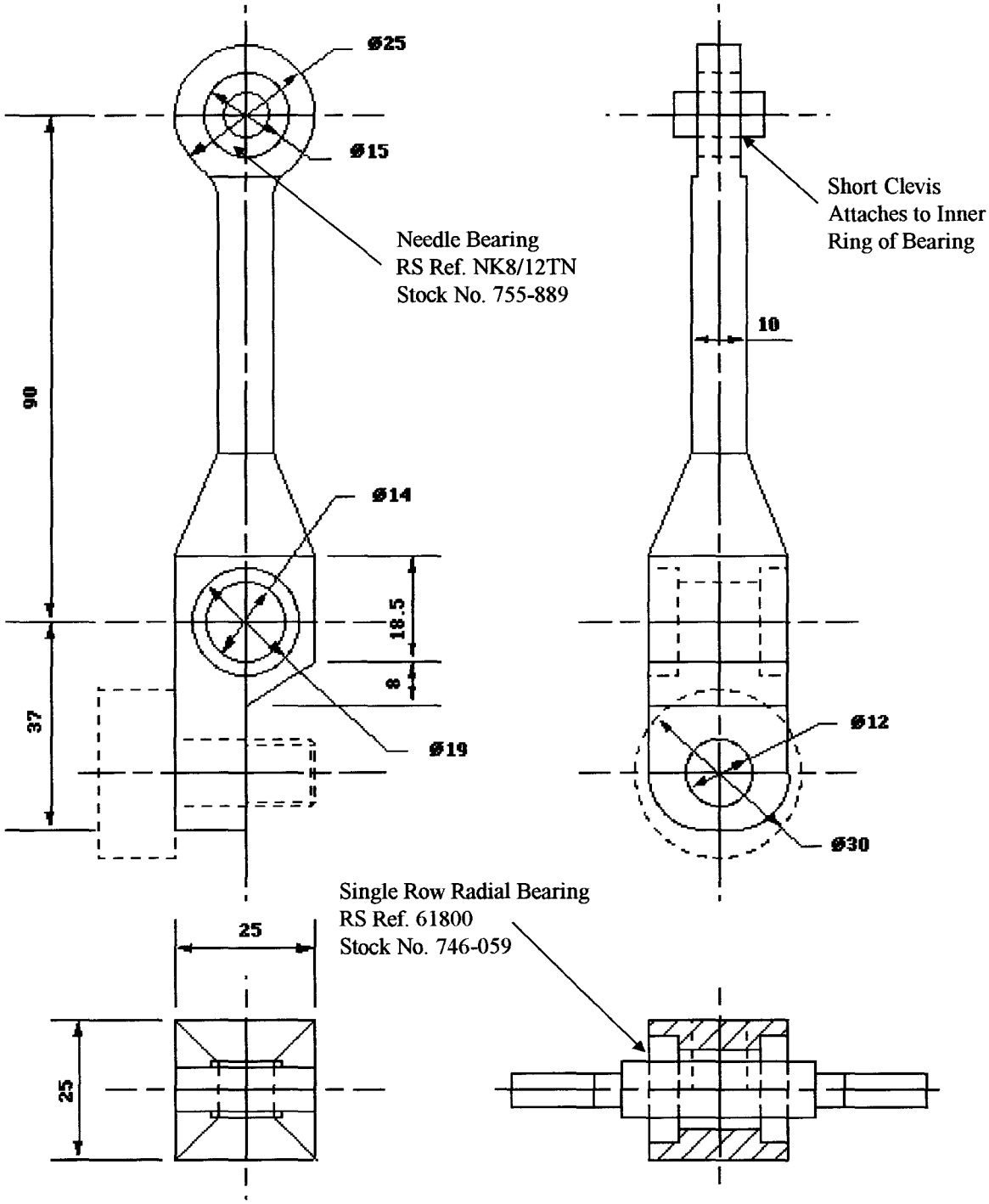

Figure D.3- Technical Drawing of Pitch Link (roller in hidden detail).

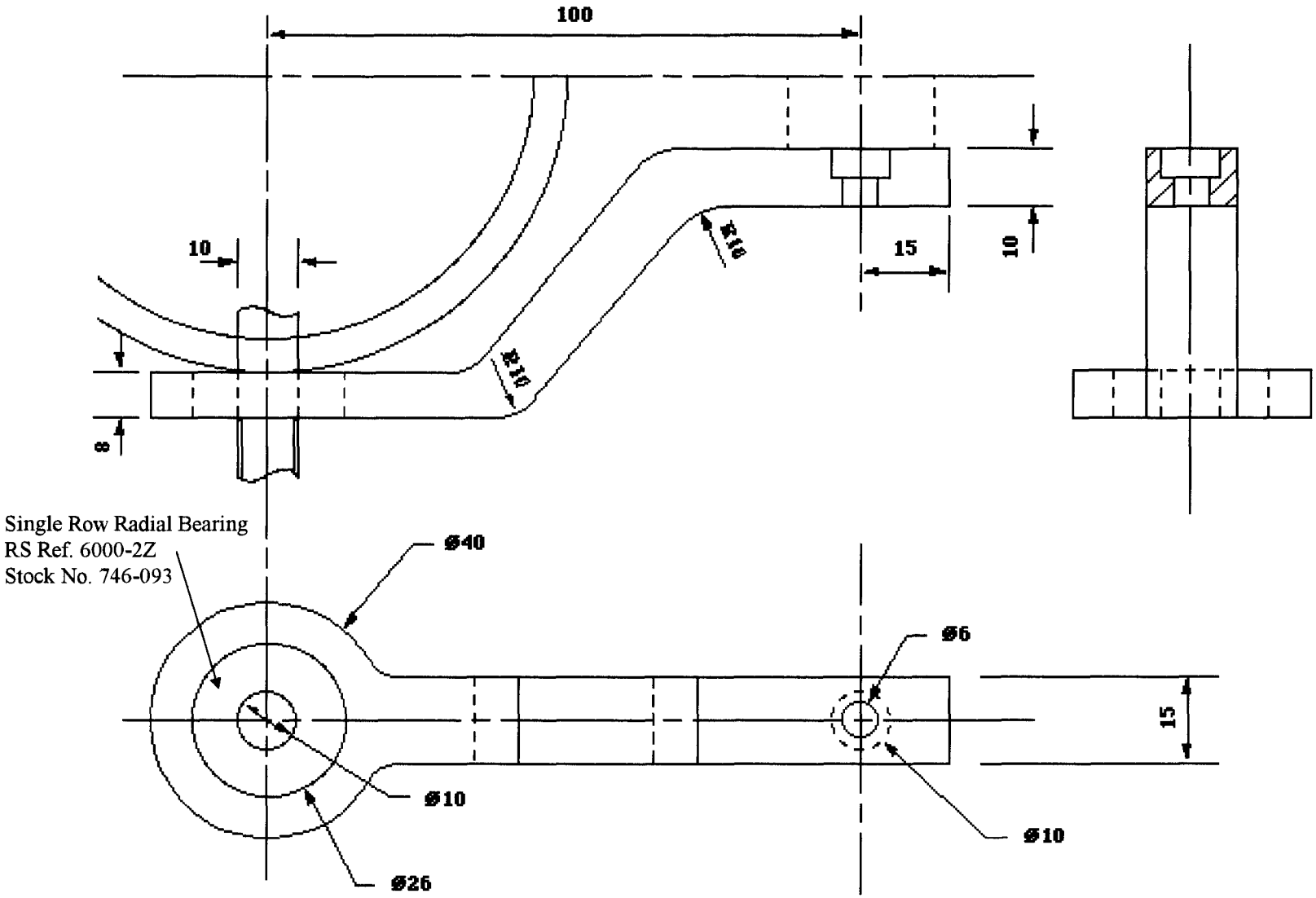

Figure D.4- Technical drawing of constraining arm.

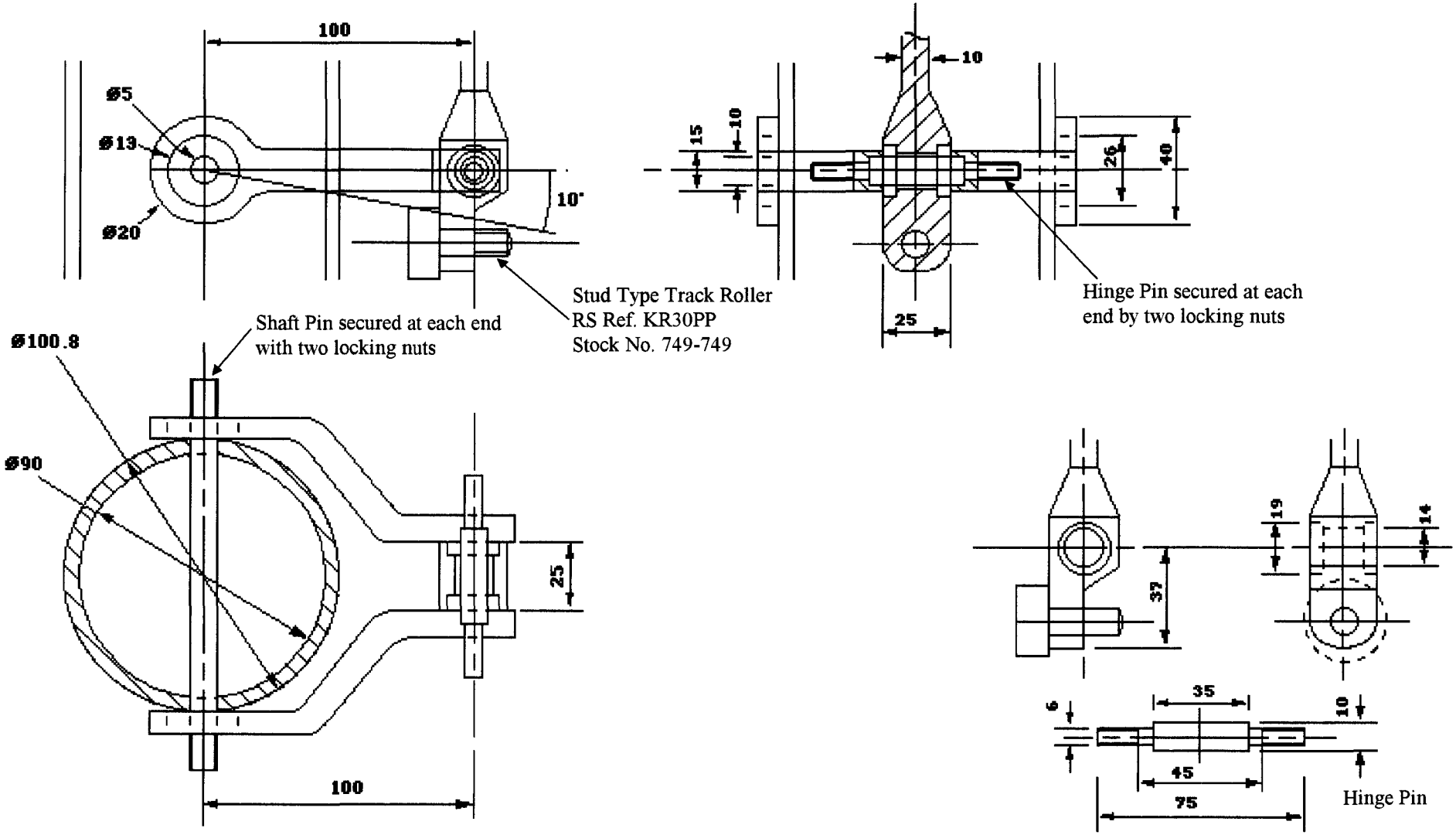

Figure D.5- Construction drawing of lower pitch assembly.

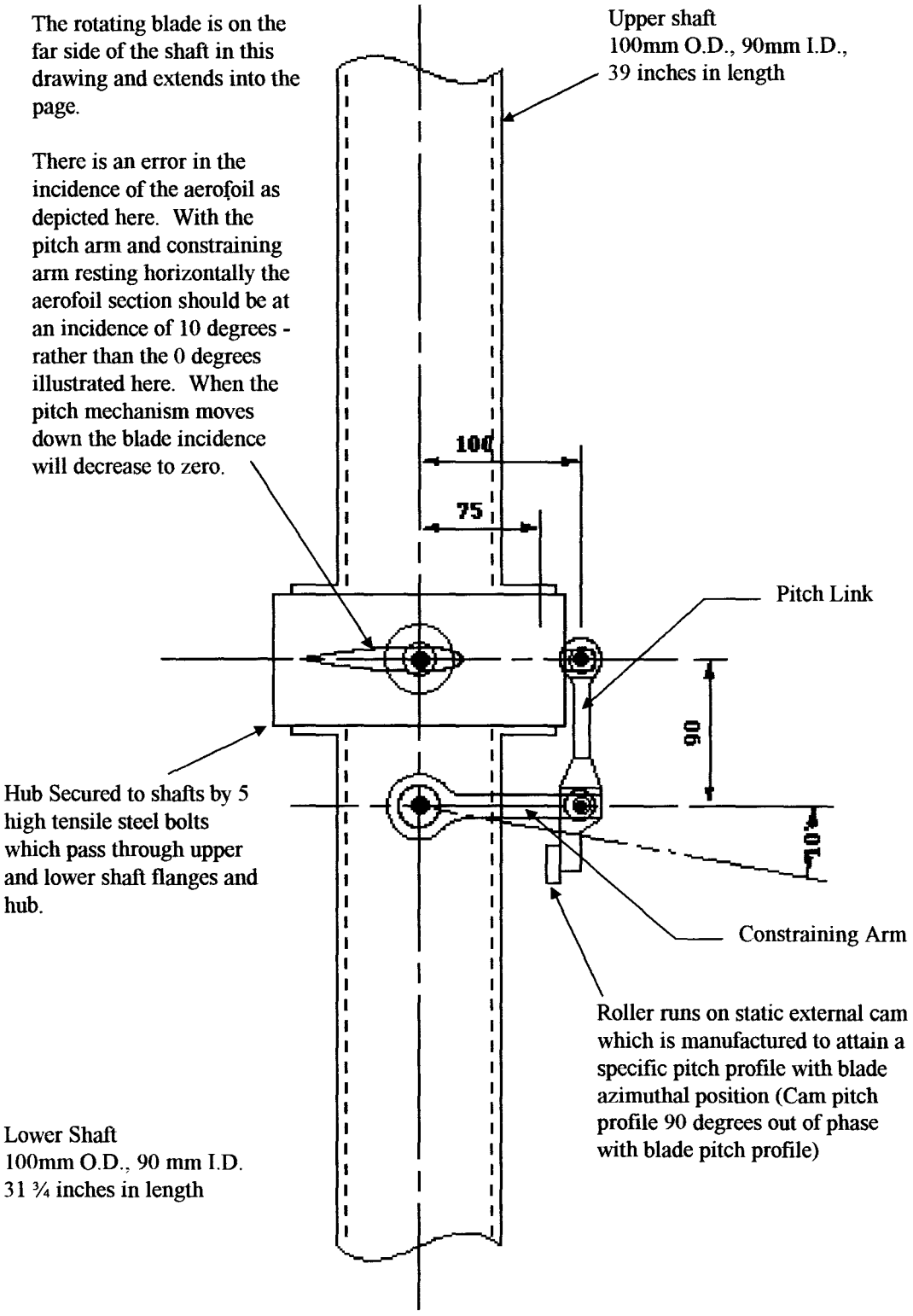

Figure D.6- Construction drawing of hub, pitch mechanism and rotating shafts.

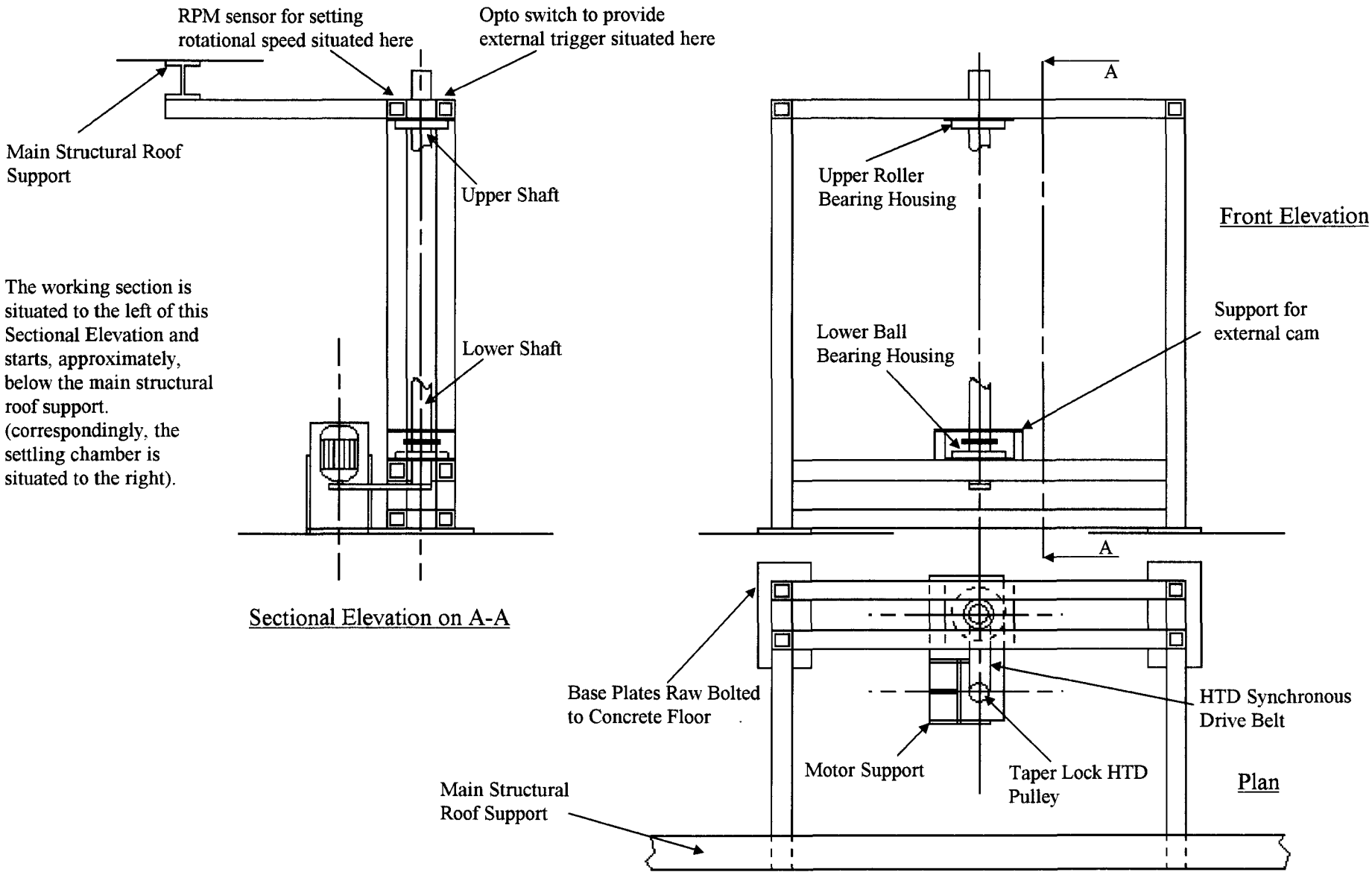

Figure D.7- Drawing of rotating blade support structure illustrating motor support and position.

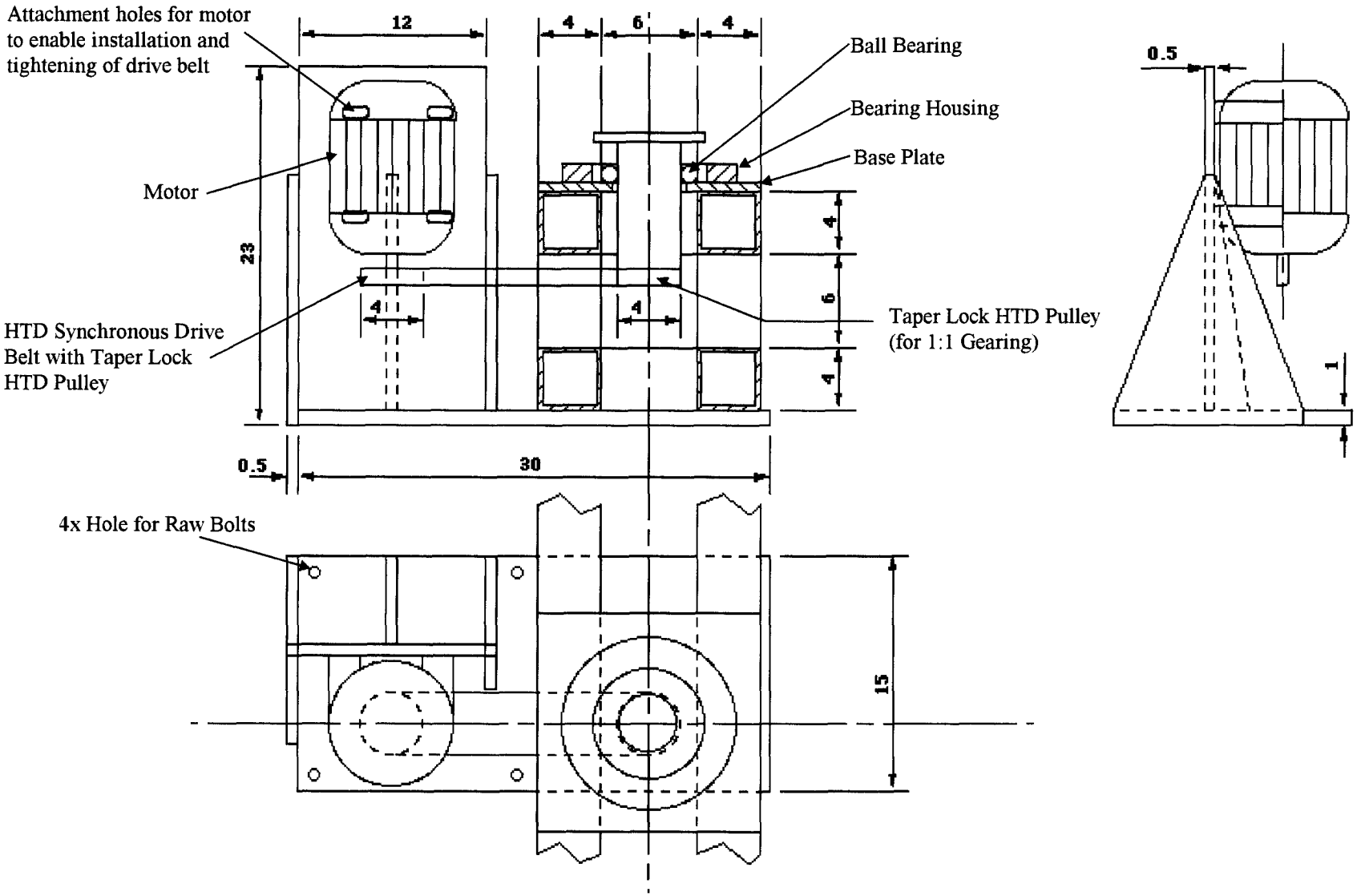

Figure D.8- Technical drawing of the lower part of the main rotor support structure and motor support.

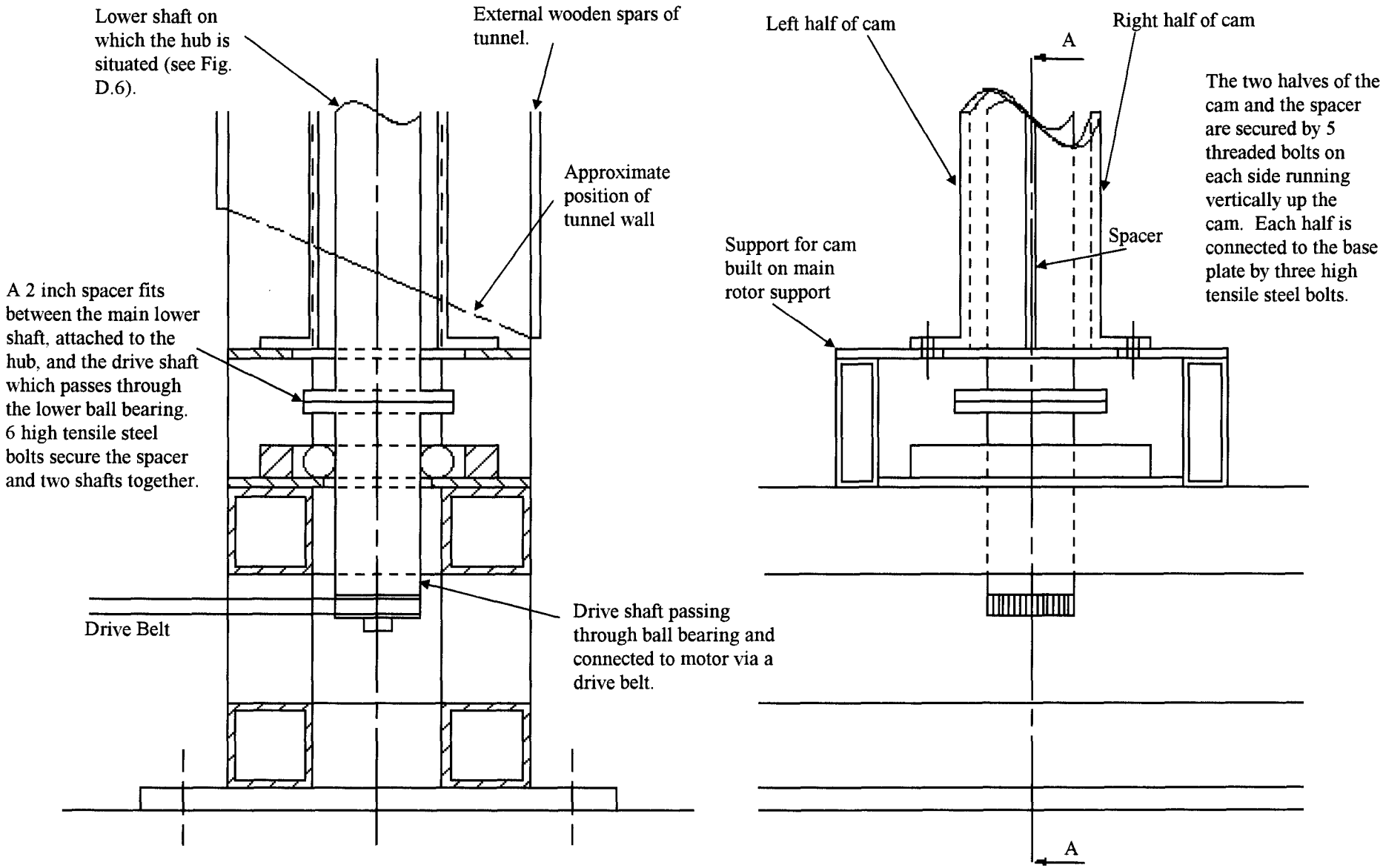

Figure D.9- Technical Drawing of lower rotating assembly illustrating position of the cam for providing cyclic pitch.

Appendix E

Results from Previous Single Vortex Generator Tests

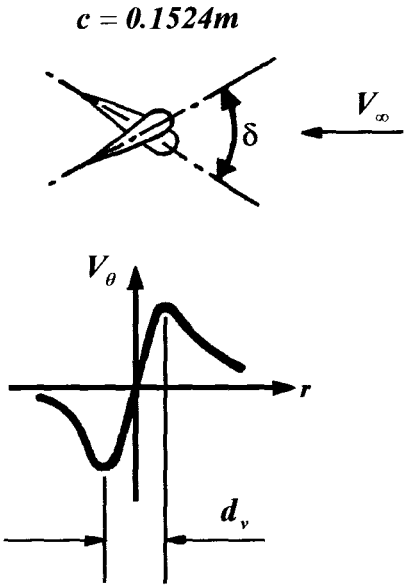

δ(°)	$\Gamma(m^2/s)$	$\overline{\Gamma} = \frac{\Gamma}{V_\infty c}$	d_v/c
5	1.1	0.16	0.34
10	2.2	0.32	0.28
15	3.4	0.49	0.27
20	5.1	0.73	0.26
25	6.7	0.96	0.26

Figure E.1- Tabulated single vortex results from determined from the triple-wire data of Kokkalis (1988).

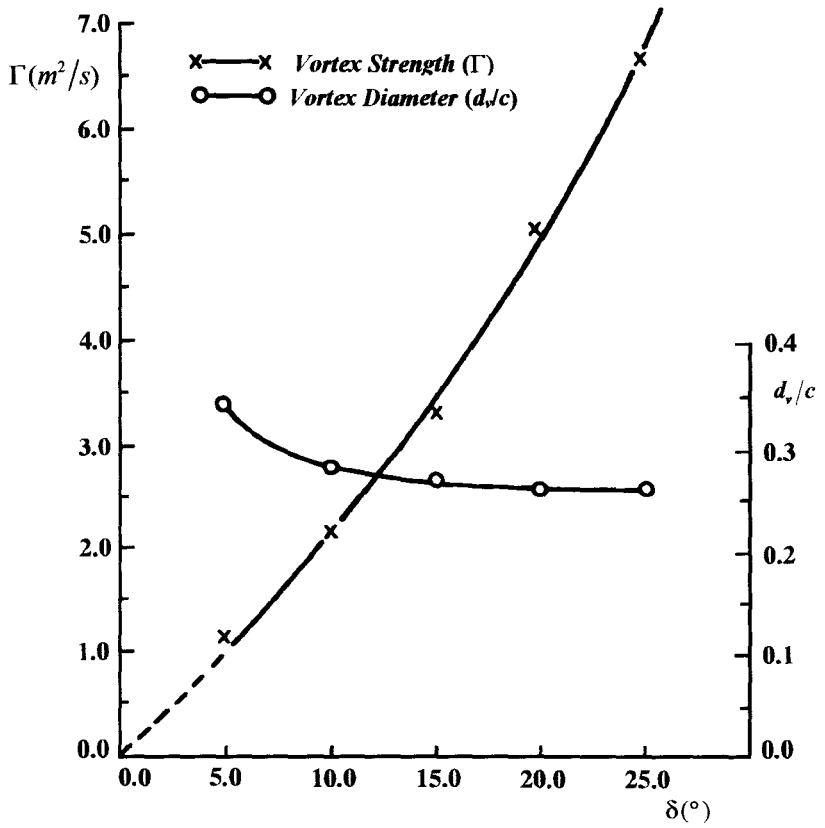

Figure E.2- Variation of vortex strength and core diameter with differential angle of incidence δ (Kokkalis (1988)).

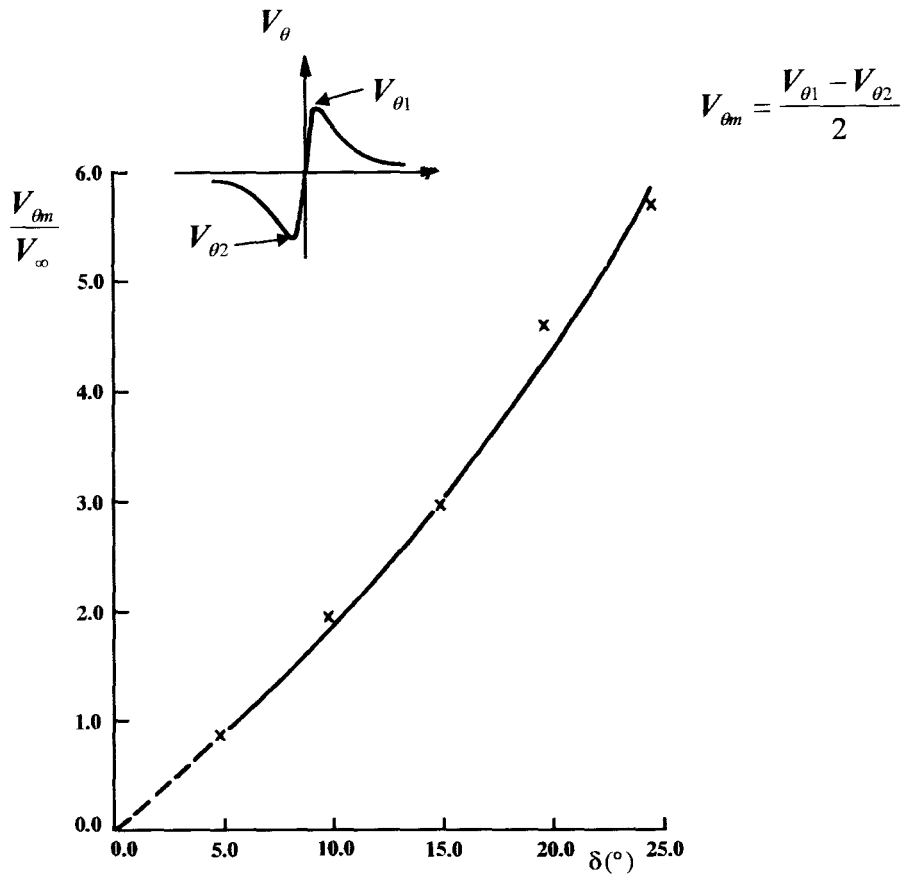

Figure E.3- Variation of the maximum normalised tangential velocity with differential angle of incidence, δ (Kokkalis (1988)).

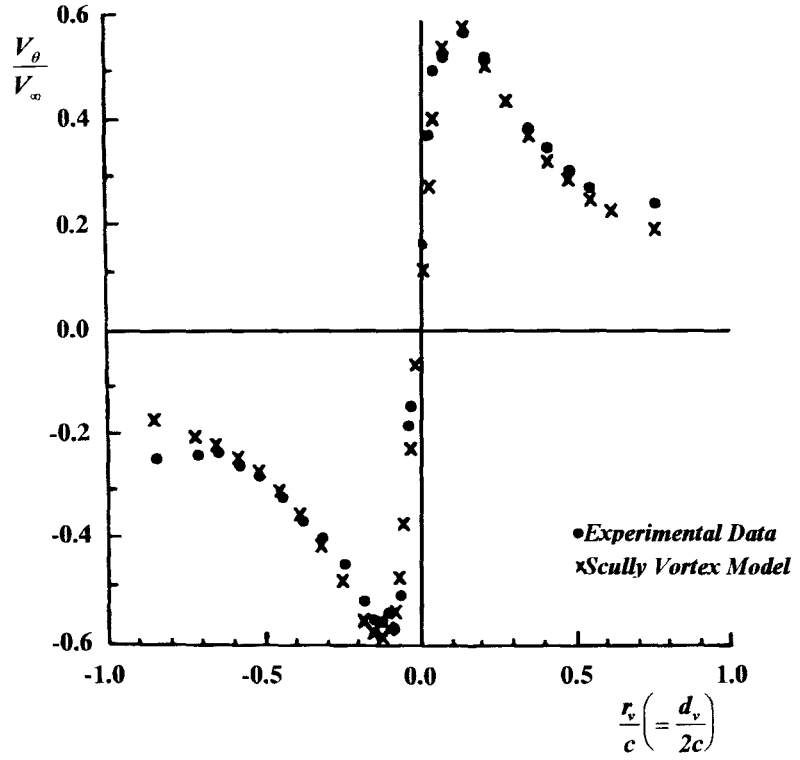

Figure E.4- Variation in the normalised tangential velocity across the vortex core δ=25° (Kokkalis (1988)).

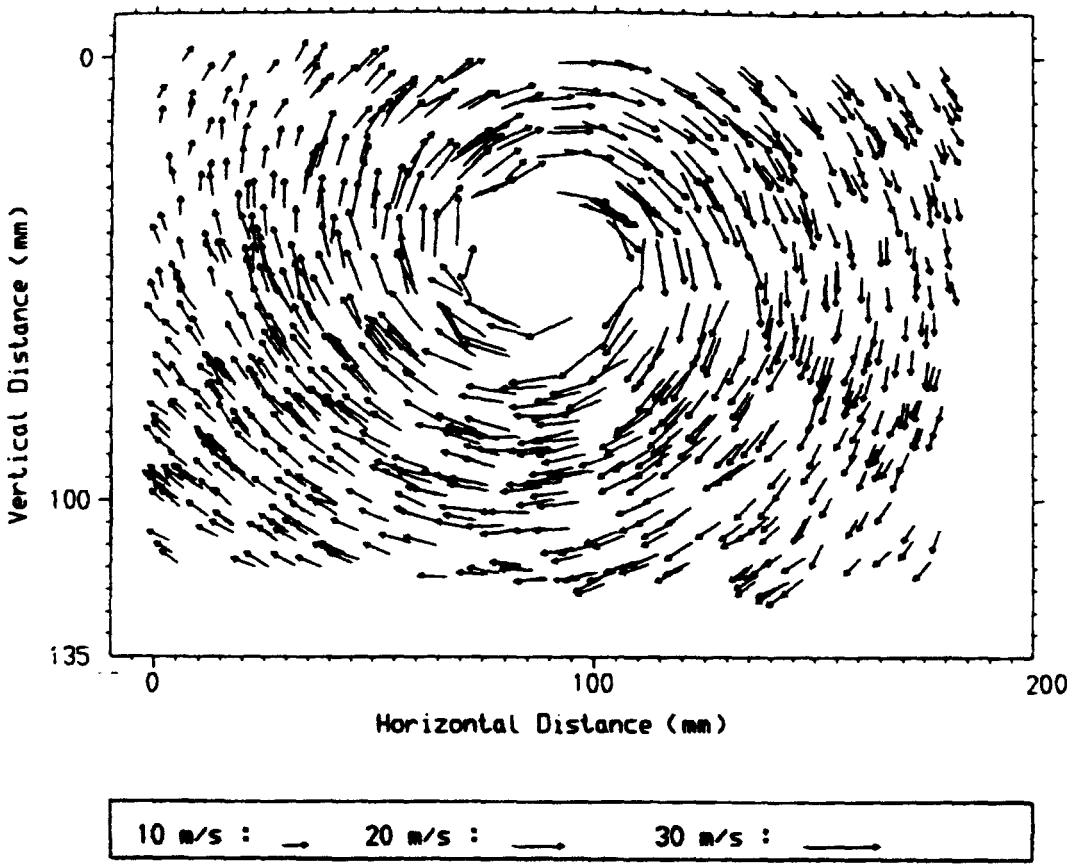

Figure E.5- Vector plot of the PIV data characterising the interacting vortex δ=25° (Horner et al. (1994)).

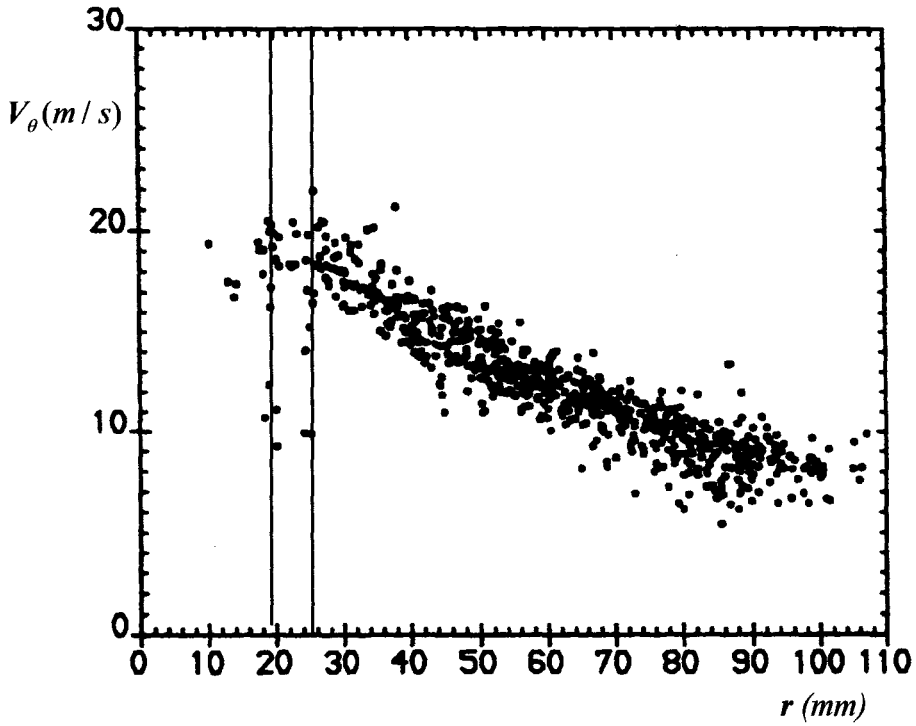

Figure E.6- The complete set of PIV tangential velocity data for the strongest vortex δ=25° (Horner et al. (1994)).

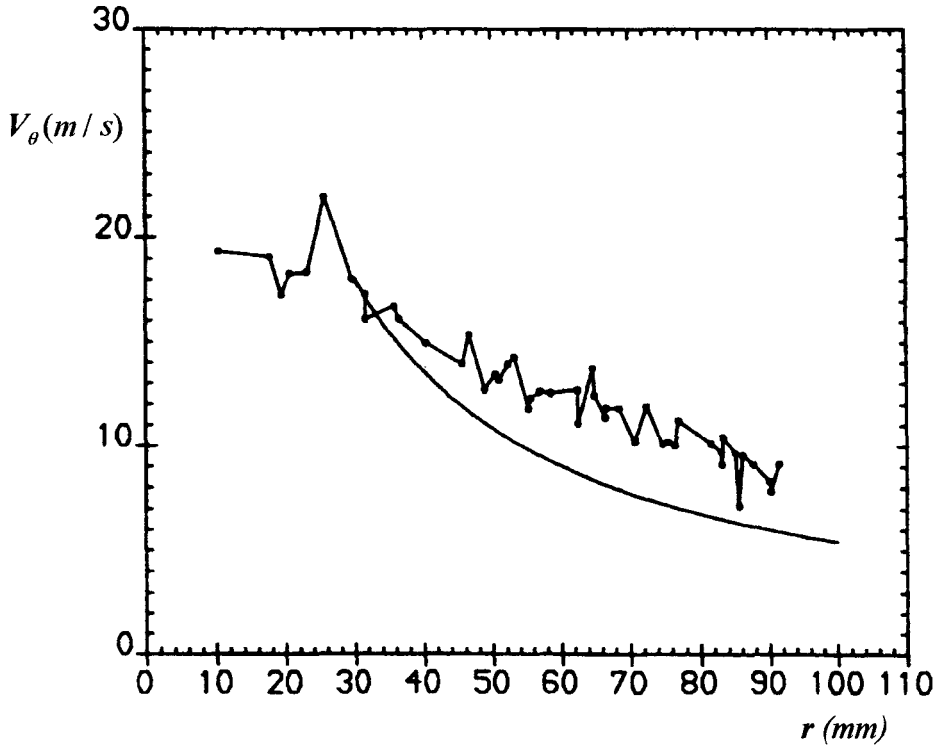

Figure E.7- A selected set of tangential velocity data collected about the strongest interaction vortex with curve fit, Biot-Savart law for a vortex strength of Γ=3.2m^2/s (Horner et al. (1994)).

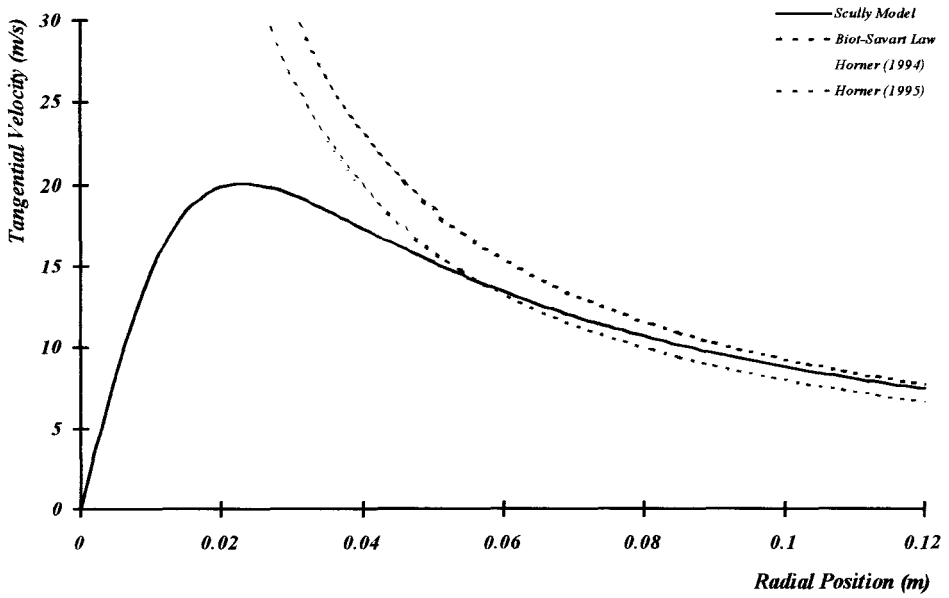

Figure E.8- Comparison of the Scully model (with a core size of 0.023m) and Biot-Savart Law for a vortex strength of Γ=5.8m^2/s. Additional lines represent the Biot-Savart law curve fits (Γ=3.2 and 5.0 m^2/s) documented by Horner (1994,1995 respectively) to the PIV data.